Universitat de València

Facultat de Física

Departament de Física Atòmica, Mol·lecular i Nuclear

Doctorat en Física

Silicon Strip Detectors for the ATLAS End-Cap Tracker at the HL-LHC

TESI DOCTORAL PRESENTADA PER

Urmila Soldevila Serrano

DIRIGIDA PER

Dr. Carlos Lacasta Llàcer

València, Gener 2017

El Dr. CARLOS LACASTA LLÀCER, Investigador Científico del Consejo Superior de Investigaciones Científicas (CSIC)

CERTIFICA:

Que la presente memoria: **"*Silicon Strip Detectors for the ATLAS End-Cap Tracker at the HL-LHC*"** ha sido realizada bajo mi dirección en el Departamento de Física Atómica, Molecular y Nuclear de la Universidad de Valencia por Urmila Soldevila Serrano y constituye su tesis para optar al grado de Doctora en Física.

Y para que así conste, en cumplimiento de la legislación vigente, firmo el presente Certificado.

Firmado

Dr. Carlos Lacasta Llàcer

Declaration

This dissertation is the result of my own work, except where explicit reference is made to the work of others, and has not been submitted for another qualification to this or any other university.

Urmila Soldevila Serrano

a Carles, el motor que mueve mi alma.

Contents

Preface **1**

1 Theoretical Physics Motivation **3**

1.1 The Standard Model . . . 3

1.2 Limitations of the SM . . . 7

1.3 Beyond the Standard Model . . . 10

1.3.1 Supersymmetry . . . 10

1.3.2 Extra Dimensions . . . 11

1.4 The search of the Higgs Boson . . . 12

2 The discovery machine **13**

2.1 CERN facilities and The Large Hadron Collider . . . 13

2.2 The LHC Experiments . . . 18

2.3 The ATLAS Detector . . . 21

2.3.1 The ATLAS Magnet System . . . 23

2.3.2 The Inner Detector . . . 31

2.3.3 The ATLAS Coordinate System . . . 37

2.3.4 Radiation levels . . . 38

2.4 High Luminosity LHC: Upgrading the ATLAS detector . . . 40

2.4.1 Inner Tracking System upgrade for the Phase-II . . . 47

2.4.2 Strip System for the Phase-II . . . 51

3 Silicon detectors for HL-LHC **59**

3.1 Semiconductor Theory . . . 59

3.1.1 Creation of electron-hole pairs in Silicon. . . . 60

3.1.2 Impurities in the material. Doped silicon. . . . 63

3.1.3 Carrier Transport. . . . 64

3.1.4 The reverse biased p-n junction. . . . 67
3.2 Silicon Detectors Technology . . . 74
3.2.1 Sensor types . . . 74
3.2.2 Isolation methods . . . 77
3.2.3 Spatial resolution . . . 81
3.2.4 Sources of noise . . . 82
3.3 Radiation damage on Silicon Detectors . . . 84
3.3.1 Bulk Damage . . . 84
3.3.2 Surface Damage . . . 86
3.3.3 Effect of Radiation Damage on Sensor Properties . . . 87
3.4 Experimental techniques for the characterization of Silicon Microstrip Detectors . . . 95
3.4.1 Current-Voltage (IV) characterization . . . 97
3.4.2 Capacitance-Voltage (CV) characterization . . . 100
3.4.3 Charge Collection measurement system . . . 104
3.4.4 Strip Integrity: Laser measurements . . . 107
3.4.5 Data analysis with ALiBaVa . . . 112

4 Strip Petals for HL-LHC 121
4.1 Petal core assembly . . . 121
4.2 Thermo-mechanical Tests: Simulation and Experimental results . . . 129
4.3 Metrology of Petal prototypes . . . 145
4.4 Microstrip silicon detectors from Hamamatsu (ATLAS12A) . . . 150
4.4.1 Electrical tests: IV/CV measurements . . . 156
4.4.2 Charge Collection pre and post-irradiation . . . 163
4.4.3 Laser measurements on ATLAS12A . . . 170
4.4.4 Annealing studies . . . 187

5 First Petal prototype: The Petalet Project 199
5.1 Structure description . . . 201
5.2 Petalet Sensors . . . 201
5.2.1 Embedded pitch adaptors . . . 203
5.2.2 Tests with minis and full-size sensors . . . 204
5.3 Electronics description . . . 221
5.3.1 Split readout configuration . . . 222

5.3.2 Common readout configuration 223
5.3.3 Electrical tests and results 223
5.3.4 Petalet readout decision 227

6 Conclusions **229**

Resumen en castellano **235**

References **273**

List of Figures **285**

List of Tables **305**

Preface

The start-up of the *LHC* on 2009 meant the beginning of a new high energy physics experiments era. The *LHC* has become the most powerful particle accelerator of all times and its high luminosity will allow to elucidate open questions in particle physics. The work presented in this thesis is focused on the second upgrade of the *ATLAS* detector at *LHC* (in particular in the End-caps tracker region). This second upgrade marks the beginning of the *High Luminosity LHC* period (*HL-LHC*) where the luminosity will be increased up to 5×10^{34} cm^{-2} s^{-1}.

A brief overview of the *Standard Model* will be given in chapter 1. The *Standard Model* is the actual theory that describes elementary particles and their interactions. In this chapter the limitations and the physics beyond the *Standard Model* will be also reviewed.

This theory introduction will give way to a general descripcion of the *LHC* aims and experiments in chapter 2. The *ATLAS* detector and its parts will be introduced. We will then look over the different detector upgrades, emphasizing in the strip tracker system for the *HL-LHC* period.

Chapter 3 is dedicated to the silicon sensors technology preceded by a general semiconductor theory introduction. Different types of silicon strip sensors will be explained and *p*-type sensors (which will be used for *HL-LHC*) will be described in detail. After that, we will go through the different effects of radiation damage in silicon sensors and the experimental techniques used for the characterization of *p*-type sensors.

The next two chapters will be devoted to the experimental measurements carried out. In particular, in chapter 4 the Petal structure will be introduced. First, we will briefly summarize the Petal fabrication steps and then we will comment on the different thermo-mechanical studies performed. The results regarding the Petal deformations and strains will be presented, as well as the minimum temperature achieved at the

Petal surface. The Petal planarity after the fabrication process will be also analized. After that, we will present the electrical characterization carried out with the Petal silicon strip sensors and the comparison of the results before and after irradiation.

Chapter 5 will be dedicated to the studies performed with the first Petal prototype, the so-called Petalet. After a brief project introduction, the electrical characterization results of the Petalet sensors will be presented. The two possible configurations for the Petalet readout electronics will be discussed and the electrical tests with the complete Petalet will be shown.

This thesis will conclude with chapter 6 which is dedicated to the main conclusions derived from this work.

Chapter 1

Theoretical Physics Motivation

1.1 The Standard Model

During the last 25 years of the 20th century our progress in particle physics knowledge led to the development of the *Standard Model* (*SM*). The *Standard Model* is a gauge quantum field theory which describes the properties of the fundamental particles and their interactions up to scales of O(200 GeV) [1]. It is the theoretical framework that provides the most accurate description of the interactions among elementary particles and it is consistent with quantum mechanics and the special theory of relativity. According to the *SM*, the matter constituents are point-like particles with half-integer spin (fermions) which are described by the Fermi-Dirac statistics and their interactions are mediated by integer spin gauge particles (bosons) which follow the Bose-Einstein statistics. In addition, each particle has an antimatter counterpart with exactly the same properties except the electric charge (which has an opposite sign). Thus the *SM* is a gauge theory based on the $SUC(3) \bigotimes SUL(2) \bigotimes UY(1)$ symmetry group [1].

Particles can be divided in two big groups: elementary and non-elementary particles, as shown in figure 1.1.

Regarding fermions group, there are three families of leptons and three of quarks.

On one side, leptons interact by the electroweak force only and they are electrically charged (electron (e) , muon (μ) and tau (τ)) or neutral (the corresponding neutrinos). On the other side, quarks are mathematically triplets of the *SUC(3)* gauge group and they carry the charge of the strong interaction , known as color (Quantum Chromo Dynamics theory, *QCD*). There are three quarks with electric charge $+\frac{2}{3}$ (up (u), charm (c) and top (t)), and three with electric charge $-\frac{1}{3}$ (down (d), strange (s)

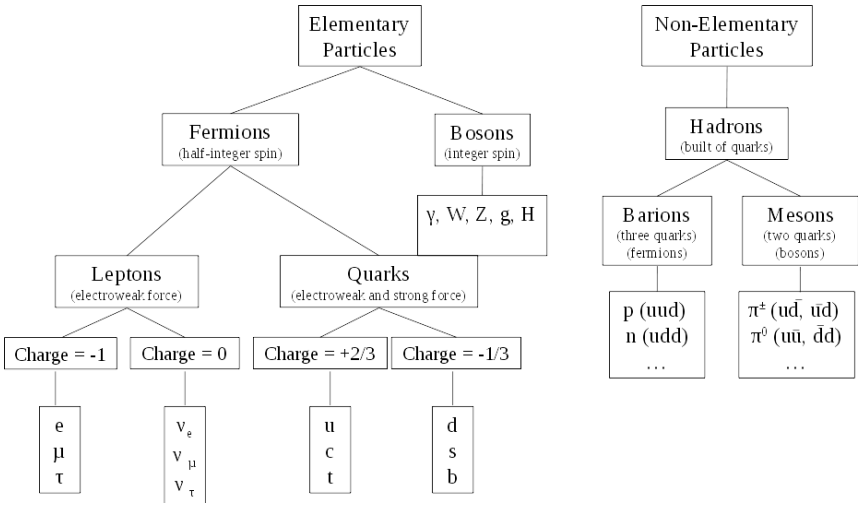

Figure 1.1: The fundamental matter particles of the Standard Model.

and bottom (b)). In ordinary matter only the first generation particles (*u*, *d*, *e* and ν*e*) are found. High energy experiments have proven the existence of the other generations of particles. The quark model was first postulated in 1964 and four years later the up quark was found in deep inelastic scattering experiments at Stanford Linear Accelerator Center $(SLAC)$ [2]. From this discovery different experiments have worked hard to find the different pieces of the theory. The latest discovered quark was the top which was found in 1995 at Fermilab $(FNAL)$ by the *Collider Detector at Fermilab* (CDF) experiment [3].

In addition, there are fundamental bosons which mediate the different interactions. The massless photon (γ) for the electromagnetism, the massive *W*± and *Z* bosons which were directly observed at the *CERN Super Proton Synchrotron* (SPS) collider [4] and are mediators of the weak force, the 8 massless gluons for the strong force (which carry color charges themselves, thus self-interacting) and the Higgs boson which has been recently discovered [5, 6] and explains the difference between the massless photon and the relatively massive *W* and *Z* bosons through the *Spontaneous Symmetry Breaking* (SSB) mechanism [7].

The other big group is the non-elementary particles group with *Hadrons* in the first stage. *Hadron* is the name of a non-elementary particle which is built of quarks held together by the strong force. They are sub-classified in *baryons* (formed by three quarks) and *mesons* (form by two quarks). Barions have half-integer spin therefore they are fermions. Mesons have integer spin so they are bosons.

Due to the property of the *color confinement* quarks are never observed freely, they are always confined in bound states (i.e. in hadrons since they are color singlets). Gluons interact with each other leading to an increase of the strong coupling constant (α_S) at large distances and thus produces the confinement. On the contrary, at small distances (i.e. high energy) the strong coupling constant decreases and therefore quarks and gluons can be understood as free particles. This property is called the *asymptotic freedom*. Quarks in that state of freedom, can exchange gluons which can produce additional *qq* pairs. Collimated groups of hadrons can be produced due to the interaction between all these quarks and gluons. These are the so-called *jets*.

The *SM* can be described in terms of fields that can be divided in three types: the matter field, which corresponds to the fermionic leptons and quarks; the gauge fields, from which the gauge bosons appear and the Higgs scalar fields, which explain the generation of particles and gauge bosons ($ZandW$) masses.

Particles interact with each other through four fundamental interactions or forces: the electromagnetism, the weak interaction, the strong interaction and the gravitation. Every observed physical phenomenon is explained by these interactions. Classically, two particles interact due to the field created between them. For quantum physics, this interaction is due to a field particle exchange, as explain before.

- **Electromagnetic Interaction**: In this interaction, the physical magnitude that comes into play is the electric charge of the constituents. The interaction is described by the photon exchange (*gauge* invariant), that couple with the electric charge. The quantum approach to the electromagnetic force is called Quantum *Electro Dynamics* theory (*QED*). *QED* is the simplest, well-known and studied theory and its predictions are verified experimentally until several decimal order. It has been used as a model for other field theories. This is a local gauge invariant theory due to the invariant interaction of the *Lagrangian* under phase transformation. This invariance leads the possibility of renormalization of the theory. Moreover, it is an abelian gauge theory, and therefore the no existence of the double photon coupling $(\gamma\gamma)$, and this does not happen in other theories. The intensity of the interaction is carried by the fine-structure constant (α) and the probability of photon emission or absorption is proportional to the coupling constant. Since the photon is a massless boson, the interaction has infinite range.

- **Weak Interaction**: is the responsible of the beta decay of nuclei and the processes between leptons and quarks. The beta decay was early associated with the most elementary process of neutron disintegration: $n \rightarrow p + e^- + \bar{\nu}_e$.
  The weak interaction is the only one that neutrinos can suffer and it explains the quark flavour exchange. It is very important at cosmic scales since it controls thermonuclear reactions where deuterium is created. For the weak interaction all the matter particles may carry isospin charge. The weak interaction can be unified with the electromagnetic interaction into the electroweak interaction (EW) [8]. This interaction is mediated by the $W^{\pm}$ and Z^0 bosons. These particles were postulated by the theory to be massless but experimentally they were found massive ($\backsim 80\ \ \mathrm{GeV}/c^2$ and $\backsim 90\ \ \mathrm{GeV}/c^2$, respectively). This is explained by the spontaneous symmetry breaking where an additional scalar field that breaks the electroweak symmetry has to be introduced. The scalar field will not only provide masses for the gauge bosons but also predicts an additional scalar particle, the Higgs boson[9]. The high masses of these bosons establish the low range of the interaction (10^{-18}m, which is about 0.1% of the diameter of a proton).

- **Strong Interaction**: Historically the strong interaction is the responsible of nuclei formation by nucleon union. The first attempt to explain the interaction between nucleons was done by Yukawa and it was described due to meson exchanged. Nowadays, after the huge success of quarks models, it is known that the strong interaction is the one that exist between quarks and holds them together inside hadrons. The quantum representation of the strong interaction is the *Quantum Chromo Dynamics* (*QCD*) and the field boson is the *gluon*. This interaction affects particles that have color charge, i.e, gluons and quarks. Gluons carry color charge themselves which makes that they are self-interacting. This limits the range of the interaction to 10^{-15}m (which is the diameter of a medium size nucleus).

- **Gravity**: This interaction affects all particles and it is described by the *General Relativity* (*GR*). It has infinite range as the hypothetical graviton (*G*), which is supposed to be its massless mediator.

The *SM* has achieved unifying the electromagnetic, nuclear weak and strong interactions under the same framework[1]. It has been a highly successful theory but it is not a complete description of observed physical phenomena. It contains no treatment of gravity or general relativity nor it includes any mathematical mechanism to solve the hierarchy problem.

1.2 Limitations of the SM

The *SM* has been very successful describing the strong and electroweak interactions of elementary particles. Despite the fact that the *SM* apparently comply with most experimental data up to this day, there is still some issues unresolved within this theory which can point to new physics beyond the *SM*. Some of the unsolved problems in the *Standard Model* of elementary particles are enumerated below.

- **Grand Unification**: The description of the strong force in the *SM* framework is not as good as the *EW* force is. The *Grand Unifying Theory* (*GUT*) is the one that really unifies these forces [10]. However some implications must be considered such as the proton decay in *GUT*. Proton lifetime depends on the *GUT* scale. Lower limits on the proton lifetime have been established by very precise experiments and up to now no proton decays has been observed, implying that at least the proton lifetime is longer than the one predicted by *GUT*. Furthermore, gravity is not included. Thus, new theories should be proposed.

- **Renormalization**: The *SM* is a renormalizable theory. This implies that infinites on measurable quantities can be absorbed into non-measurable quantities. So that, all quantities predicted by the theory are well defined and have a finite value. This leads to the fact, that these quantities depend on the energy scale at which they are measured. Therefore, the interaction coupling constants, which set the strength for the interactions, present the so-called *running coupling constants* [11]. This principle applies to the coupling constants of the *SM* as well as to masses. As the three coupling constants (electromagnetic, weak and strong) are all running, one could assume that they all cross at one point and are unified there. But this is not the case for *SM* as seen in Fig.1.2 (left). However, with some possible extensions of the *SM* such as the minimal

[1] Gravity, the fourth interaction, is not contained in the *SM* and is extremely weak when compared to the other interactions at the high energy scales.

supersymmetric standard model (*MSSM*) [11], with particles of masses around 1 TeV, an unification of the three forces of the *SM* is possible as seen in figure 1.2 (right).

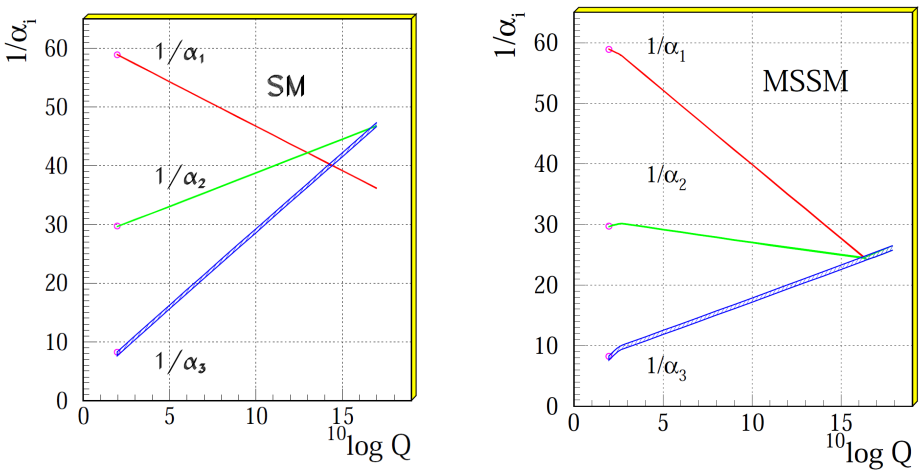

Figure 1.2: Running coupling constants of the three Standard Model interactions. It is shown the inverse of the three Standard Model couplings α_i with i =1, 2, and 3 for the U(1)Y, SU(2)L and SU(3)C symmetry groups respectively as a function of the sliding scale Q (in GeV) in left for the StandardModel and in right for the minimal supersymmetric extension of the StandardModel (*MSSM*). The gauge couplings meet almost exactly in one point, somewhere around 10^{16} GeV, usually referred to as the *GUT* scale (*Gran Unification Theory*).

- **Hierarchy problem**: It is related to the huge gap between two fundamental scales of physics: the electro-weak scale $\left(\Lambda_{EW} \backsim 10^2 \text{ GeV}\right)$ and the Planck scale $\left(\Lambda_P \backsim 10^{19} \text{ GeV}\right)$ where the gravitational interaction becomes important. One of the consequences is that, if no new physics exists between these two scales then the Higgs mass diverges, unless it is unnaturally fine tuned.
  The observable Higgs mass is composed of a bare mass (M_{H0}) and radiative corrections (δM_H) and the correct physical value M_H may be obtained as:

$$M_H^2 \backsim M_{H0}^2 + \delta M_H^2 \tag{1.1}$$

  The leading term of the radiative corrections is quadratically dependent on the coupling constant of the corresponding interaction [12] and thus on the energy scale. This can be associated to the *Grand Unification Theory* (*GUT*) scale $\left(\Lambda_{GUT} \backsim 10^{16} \text{ GeV}\right)$ in order to be consistent with a relatively light *Higgs boson*

($M_H < 1\ \mathrm{TeV}/c^2$). It is required to be accurate in one part in 10^{16} in order to compensate the divergent corrections. This is the so-called *fine tuning problem*.

As we will explain later on this chapter, the *ATLAS* and *CMS* experiments observed a particle at the *LHC* with a $mass \approx 126$ GeV, which is compatible with the Higgs boson of the Standard Model. This value for the mass is really below the Planck scale. Therefore the fine tuning problem is still unresolved. This could mean that the *SM* is incomplete at the TeVscale and therefore is an effective theory valid up to the Planck scale. Different theories propose elegant solutions to explain this hierarchy such as *Supersymmetry* and *Extra Dimensions* which will be introduced in the next section.

- **The fermion mass hierarchy problem**: The *SM* can't explain the reason why fermions are grouped in three generations. There are no predictions of their masses which are observed to have hierarchical pattern. The mass difference of each generation is not described by the *SM* and therefore it is still unknown.

- **Neutrino masses**: In the *SM* the neutrinos are massless particles. However, from different experiments it is known that these particles have masses. The new models have to explain this fact.

- **Cosmological consideration**: The theory predicts that the baryon matter density is $\backsim 4\%$. The rest of the universe is made up of $\backsim 24\%$ dark matter and $\backsim 72\%$ dark energy [13]. The *SM* does not provide any explanation for dark matter and dark energy observed in cosmology and possible candidates are proposed by new models beyond the *SM*. Similarly, the existence of an asymmetry between matter and anti-matter in the universe cannot be explained within the framework of the *SM*.

- **The down-quark mass eigenstates**: i.e. *d*', *s*', *b*', which couple to the gauge bosons are not the same as the eigenstates for the weak interaction.
  In other words, the quark mass eigenstates are not the same as the physical masses, with mixing between the three generations of quarks, which in the *SM* is parametrized by the *Cabibbo-Kobayashi-Maskawa* (CKM) matrix (V_{CKM}) where V_{ij} is the matrix element coupling the *ith* up-type quark to the *jth* down-type quark. The problem is that although this is already parametrized in the *SM* it is not explained.

All these problems need new theories which should solve them. The *LHC* physics program includes these theories as subject of extensive searches and studies at the *LHC* experiments.

1.3 Beyond the Standard Model

Several theoretical models have tried to solve the abovementioned problems. *Supersymmetry* and *Extra Dimensions* stand out above others. They are briefly described in this section.

1.3.1 Supersymmetry

SUSY is a gauge theory that assumes that every particle on the *SM* would have its own *superpartner* with the same quantum numbers but with the spin differing by $\pm\frac{1}{2}$ [14]. A simple extension of supersymmetry is the *Minimal Supersymmetric Standard Model* $(MSSM)$ [11]. In this supersymetric world each fermion has a bosonic counterpart (the squarks and sleptons) and the bosons have fermionic superpartners (called *gluinos* and *gauginos*). For example, the electron with spin $\frac{1}{2}$ would have a bosonic partner with spin 0 and the same mass. An exact unbroken *SUSY* predicts that a particle and its superpartner have the same mass. But as these superpartners have not been observed, if *SUSY* exists, it must be broken allowing the sparticles to be heavy.

SUSY is one of the best candidates which will solve many of the *SM* problems, if it exists.

- Within the contribution of the *SUSY* particles to the running of the coupling constants, it is possible to unify the gauge couplings for the strong, weak, and electromagnetic interactions at the *GUT* energy scale. Moreover, the origin of the large hierarchy scale from the W and Z masses to the Planck scale (the gauge hierarchy) could be also explained by *SUSY*. It is possible to maintain the stability of the gauge hierarchy in the presence of radiative quantum corrections in supersymmetric theories. Figure 1.2 shows the inverse of running coupling constants where α_1^{-1}, α_2^{-1} and α_3^{-1} refer to the electromagnetic, the weak and the strong interaction, respectively. Figure 1.2 (right) shows the case for the *MSSM* where unification of the coupling constants is achieved at *GUT* scale ($\backsim 10^{16}$GeV) in contrast to the case for the *SM* shown in figure 1.2 (left).

- Another issue that cannot be explained within the *SM* is dark matter which constitutes the 90% of the matter in the Universe and is undetectable by its emitted radiation. Dark matter would be formed by weakly interactive massive particles $(WIMPs)$. The neutralino (χ_0) is the lightest neutral weakly-interacting supersymmetric particle and it is considered as good candidate for dark matter. It is considered to be stable in the *MSSM* and hence expected to exist in the universe today. The neutralino would be present in the resultant cascades of supersymmetric particles decay.

- The fine tunning problem of the *SM* can also be solved due to the radiative corrections introduced by the supersymmetric partner particles which cancel the quadratically divergent terms of the *Higss* mass.

All the arguments mentioned above imply the discovery, identification and the study of a whole new spectrum of particles. This amount of parameters of the *MSSM* can be studied at *LHC*. *ATLAS* and *CMS* experiments will search for the range of particles predicted by *SUSY*: *squarks*, *gluinos*, *supersymmetric Higgs*, etc... which may verify the theory.

1.3.2 Extra Dimensions

Extra dimensions models are based on the idea of adding more space dimensions on top of the usual three spatial dimensions. *SM* would be confined to a 4-dimensional manifold while gravity could propagate through all the dimensions. Then, the observed weakness of the gravitational interaction (compared with other interactions) is not fundamental, it is merely a consequence of the existence of the extra dimensions. These extra dimensions would not be visible to us due to their curled up nature but they may become detectable at very high energies. If extra dimensions exist they could be studied in the *ATLAS* and *CMS* detectors through the emission of *gravitons* which scape into extra dimensions and therefore generate E_T^{miss} or the creation of microscopic black holes at the *LHC* [15]. The *String theory* predicts seven undiscovered dimensions of space and considers particles as tiny vibrating strings instead point-like objects. All the different particles and forces are just different oscillation modes of a unique type of string.

There are other important models. For example, the 2 *Higgs-Doublet* Models $(2HDM)$ [16] or the *Super String* theory $(M-theory)$ which combines *SUSY* and *Extra Dimensions*. Nevertheless, the *LHC* experiment will give the chance to confirm these models and theories and also to search for unpredicted signals in unexplored energy regions.

1.4 The search of the Higgs Boson

As mentioned before, the *SM* treats the *Higgs* boson as the physical representation of the Brout-Englert-Higgs field which permeates the space and is responsible for the generation of the masses of the fundamental particles. Within the *SM*, the *Higgs* boson is unique since it is the only physical scalar in the theory. Its mass is undetermined by the *SM* thus it is free parameter of the model. Theoretically it must be below the TeV range, as required by partial wave unitarity in gauge boson scattering.

On July 4th 2012 *ATLAS* [17] and *CMS* [18] (the two main experiments at *LHC*) announced that they had found a new state compatible with the properties of the *Higgs* boson. The measured mass was about 125 GeV/c^2, and some months later it was confirmed the particle was "consistent with the *Higgs* boson". With this mass value, the *Higgs* boson is the second heaviest elementary particle discovered so far, after the top quark, which measured mass is $m_t \simeq 173$ GeV [19].

Despite the fact that the *SM* still has unsolved problems, the *Higgs* boson discovery has shed light on other aspects of the theory as the *EW* symmetry breaking. This was the only fundamental particle predicted by the *SM* not experimentally discovered until 2012. The *Higgs* mechanism explains the generation of *W*, *Z*, quark and lepton masses. A key feature of the *SM* mechanism of the *EW* symmetry group $SU(2)L \bullet U(1)Y$. However, all the arguments given above tend to indicate that the *SM* may be an approximation describing low-energy aspects of a more fundamental theory. The difference between the approximation and the absolute theory would then start to appear when the energies involved become large.

The experimental study of the *Higgs* boson at the *LHC* has become one of the most exciting areas in contemporary particle physics. Now that it has been discovered, the emphasis is on a more precise measurement of its mass and properties to understand whether the observed particle is the *SM Higgs* boson or something more exotic.

Chapter 2

The discovery machine

9-December-1949: At the end of the Second World War a group of european scientists proposed creating an European atomic physics laboratory (Pierre Auger, Edoardo Amaldi and Niels Bohr were among these pioneers). This new laboratory would unite European scientists and also allow them to share the increasing costs of nuclear physics facilities. 11 countries signed an agreement establishing the European Council for Nuclear Research - the acronym *CERN* was born. Geneva was selected as the site for the CERN Laboratory and after 5 years of bureaucracy on September 1954 the European Organization for Nuclear Research officially came into being (with 12 founding member states). The provisional CERN was dissolved but the acronym remained. Since CERN Laboratory started-up in 1957, it has been witness to large revolutionary discoveries and technolgy developments, such as the W and Z particles discovery (1983) or the Web creation (1990). Nevertheless, the most challenging period came with the beginning of the *Large Hadron Collider* (LHC) era (2008). The LHC has become the most powerful particle accelerator of all times.

2.1 CERN facilities and The Large Hadron Collider

The LHC [20][21] is assembled in the existing 27 km tunnel that was constructed for the Large Electron-Positron Collider (*LEP*).
The prime motivation of the LHC is to shed light on the mathematical consistency of the Standard Model at energy scales above 1 TeV. It should perform precision measurements of the already known phenomenology and elucidate the nature of electroweak symmetry breaking for which the Higgs mechanism is presumed to be responsible. It also aims at revealing the Physics beyond the *SM*, with proton-proton

(pp) collisions with a nominal centre-of-mass energies of 14 TeV[1] and a luminosity (L) peak of 10^{34} cm^{-2} s^{-1}. It will lead to the investigation of various alternatives to the *SM* which invoke new symmetries, new forces or new constituents.

The considerable amount of Bremsstrahlung radiation for the required high energies, excludes the use of electrons in this collider. In addition, the high beam intensity required for a luminosity of 10^{34} cm^{-2} s^{-1}excludes the use of anti-proton beams, and hence excludes the particle-anti-particle collider configuration of a common vacuum and magnet system for both circulating beams, as used for example in the Tevatron. A total integrated luminosity of $300\ fb^{-1}$ is expected to be collected. For this luminosity, some of the most relevant LHC parameters are summarized in Table 2.1.

Parameter	**Nominal**
Intensity per bunch	1.15×10^{11} proton per bunch
Number of bunches per beam	2808
Bunch spacing	25 ns
Average radius of a beam at interaction point (IP)	$16\ \mu m$
Crossing angle	$16\ \mu rad$
Magnet field strength	8.33 T
Dipole magnet temperature	1.9 K
Total beam current	0.584 A
Inelastic proton-proton cross section	80 mb
Collisions per bunch crossing	23
Track multiplicity	700

Table 2.1: LHC general parameters at the high luminosity of 10^{34} cm^{-2} s^{-1}

The number of events per second generated in the LHC collisions is given by:

$$N_{event} = L\sigma_{event} \tag{2.1}$$

where σ_{event} is the cross section for the event under study and L the integrated luminosity which is defined by

$$L = \int \mathcal{L} \mathrm{d}t \tag{2.2}$$

[1] At the time of writing the nominal centre-of-mass energy reached at *LHC* is 13 TeV.

$\mathcal{L}$ is the machine instantaneous luminosity which depends only on the beam parameters. It can be written for a Gaussian beam distribution as:

$$\mathcal{L} = \frac{N_b^2 n_b f_{rev} \gamma_r}{4\pi\varepsilon_n \beta^*} F \tag{2.3}$$

where N_b is the number of particles per bunch, n_b the number of bunches per beam, f_{rev} the revolution frequency, γ_r the relativistic gamma factor, ε_n the normalized transverse beam emmittance, β^* the amplitude function at the collision point. The latter two parameters together describe the beamsize at interaction: ε_n is a beam quality concept reflecting the concept of bunch preparation and β^* is a beam optics quantity and is determined by the accelerator magnet configuration at the interaction point. F is the geometric luminosity reduction factor due to the crossing angle at the interaction point. It is dependent on the full crossing angle, Θ_c, and the bunch length, σ_z.

$$F = \frac{1}{\sqrt{1 + (\frac{\Theta_c \sigma_z}{2\sqrt{\varepsilon_n \beta^*}})^2}} \tag{2.4}$$

Theoretically, the luminosity can be increased by increasing both the number of particles per bunch and the number of bunches, and by reducing the intersection area between them. Nevertheless, this is hard to achieve in practice since the major limitation comes from beam-to-beam effects. The proton bunch creates a hugely non-linear electromagnetic field which modifies the trajectory of particles from their ideal orbits. The force on the particle is proportional to the number of protons on the bunch, and limits the bunch intensity to $\sim 10^{11}$ protons.

The protons are obtained by removing electrons from hydrogen atoms and they pass through the LINAC2 linear accelerator and then injected into the booster with an energy of 50 MeV. The Proton Synchroton Booster (PSB) increases the energy to 1.4 GeV before the SPS accelerates the beam to 450 GeV and injects it into the LHC. The maximum energy that can be transferred to the beams is proportional to the radius of the accelerator as can be deduced from equation 2.5

$$p_T \ (\text{GeV}/c) = 0.3qBr \tag{2.5}$$

where p_T is the transverse momentum of the particles, B the strength of the magnetic field (in Tesla) and r the radius of curvature of the circular accelerator (in

meters).

There are two transfer tunnels, approximately 2.5 km in length, linking the LHC to the CERN accelerator complex that acts as injector. To keep the two circulating proton beams in their orbits a total of 1232 superconducting dipole magnets are needed. To reach the required field strength of 8.33 T the magnets are cooled down to 1.9 K using super-fluid helium (He) [21]. A detailed cross section of a dipole magnet is shown in figure 2.1 where all its parts are depicted.

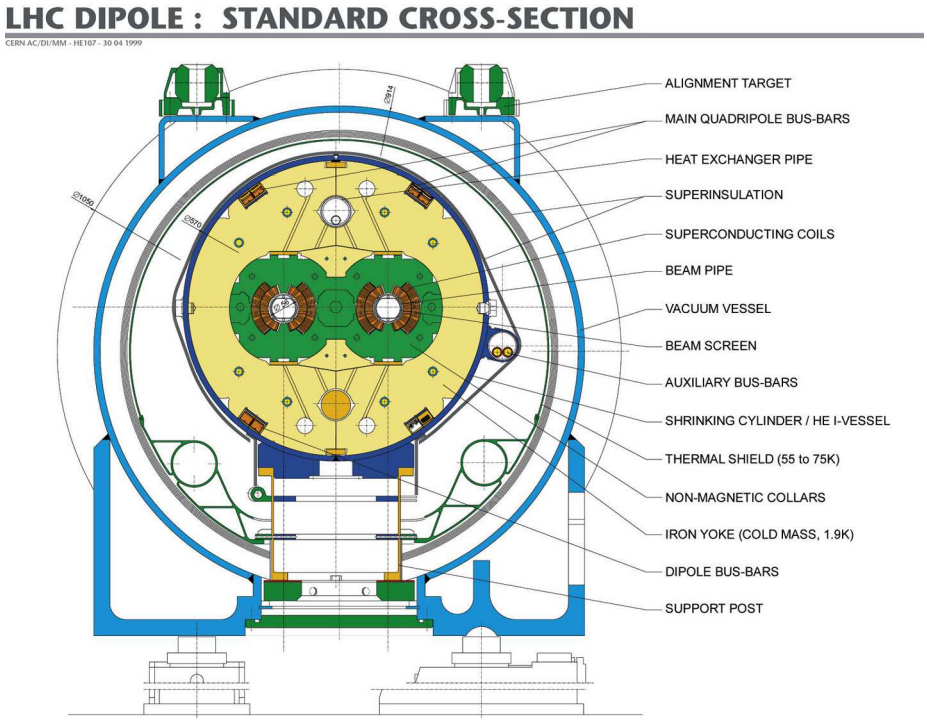

Figure 2.1: Cross section of a LHC dipole magnet design showing its components

Each beam has an internal structure as they are arranged in bunches separated in space. At design luminosity the protons are accelerated in bunches of 1.15×10^{11} $protons$ each, with 40 MHz bunch spacing (i.e. one collision every 25 ns). The main LHC design parameters are summarized in Table 2.2.

In addition to the pp collisions, shorter running periods (typically one month per year) with heavy-ion collisions are included in the program (with an energy of 2.8 TeV per nucleon). This will allow the LHC to study physics of strongly interacting matter and the quark-gluon plasma.

During 2010 and 2011, the accelerator has been working at 3.5 TeV per beam,

LHC parameter	**proton-proton collisions**
Beam energy	7 TeV (up to now: 3.5-4 TeV)
centre-of-mass energy $\sqrt{s}$	14 TeV (up to now: 7-8 TeV)
Injection energy	450 GeV
Luminosity (L)	10^{34} cm^{-2} s^{-1}
Frequency (f)	40 MHz
Bunch separation	25 ns
Number of particles per bunch (N_b)	$1.15 \cdot 10^{11}$
Average radius of a beam	16 μm
Beam current	0.58 A

Table 2.2: Design accelerator parameters of the LHC collider

and at 4 TeV per beam in 2012[1]. The existing CERN accelerator complex is used to accelerate the proton beams (see figure 2.2). The conditions of 2010-2012 proton runs are presented in Table 2.3.

Parameter	**2010**	**2011**	**2012**	**Nominal**
Beam energy (TeV)	3.5	3.5	4.0	7
centre-of-mass energy $(\sqrt{s})$ (TeV)	7	7	8	14
Maximum bunch pairs colliding	368	1380	1380	2808
Bunch separation (ns)	150	75/50	50/25	25
Maximum bunch intensity (10^{11} proton/bunch)	1.2	1.45	1.7	1.15
β^* (m)	3.5	1.5/1.0	0.6	0.55
ε_n $(\mu mrad)$	2.0	2.4	2.5	3.75
Peak luminosity $(10^{33}\ cm^{-2}\ s^{-1})$	0.2	3.7	7.7	10.0
Mean interactions per crossing	8	17	38	~ 23
Total integrated luminosity delivered	48 pb^{-1}	5.6 fb^{-1}	23.3 fb^{-1}	

Table 2.3: LHC parameters for proton-proton collisions for nominal design and for 2010 and 2011 runs at 7 TeV and 2012 runs at 8 TeV. Source:[22]

The collisions of high energetic beams at the LHC produces tones of particles. They are recorded by particle detectors, the so-called LHC experiments, which are placed just at the collision points. A brief description of them is given in section 2.2.

[1] At the time of writing the LHC has achieved a nominal energy of 13 TeV

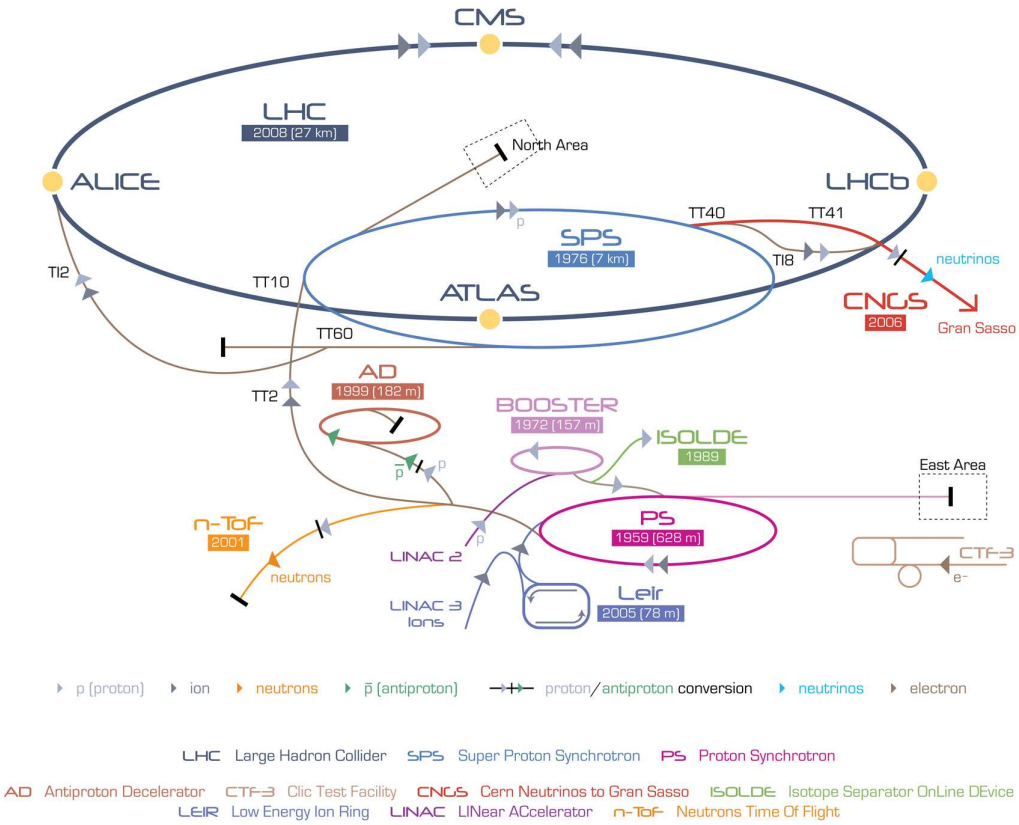

Figure 2.2: Layout of the full CERN accelerator complex and locations of the four LHC experiments

2.2 The LHC Experiments

The LHC is located 100 m below ground as can be seen in figure 2.3. All of its experiments are run by international collaborations bringing together scientists from all over the world.

The LHC ring houses four huge detectors (see figure 2.4) which are located, each of them, in an interaction point around the LHC where the two beams are brought to collision.

These experiments are:

- **A Toroidal LHC Apparatus (ATLAS) [17]**: It is a general purpose experiment for high luminosity (up to 10^{34} cm^{-2} s^{-1}) for proton-proton operation. It will perform high precision measurements on *SM* parameters and the *Higgs boson* search. It has also been designed to be able to account for several new physics processes that may be expected at the TeV scale. ATLAS is the largest LHC

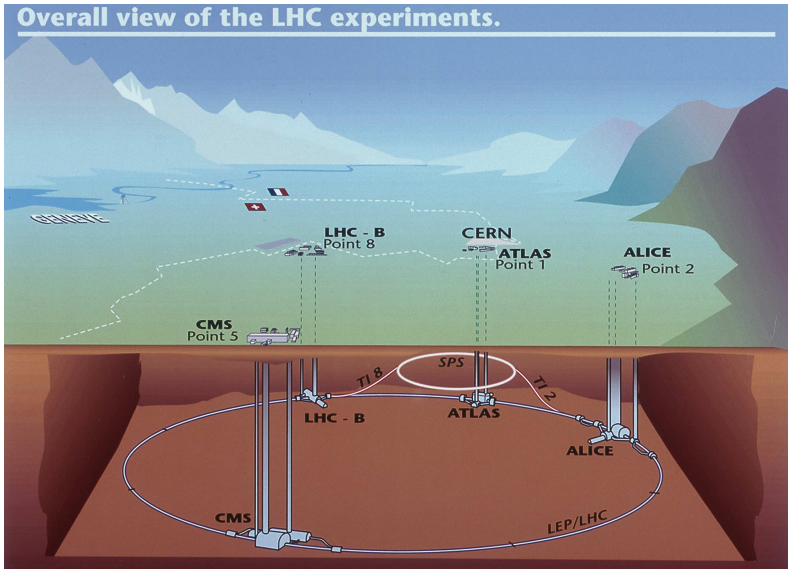

Figure 2.3: Representation of the LHC ring with its detectors and all its services

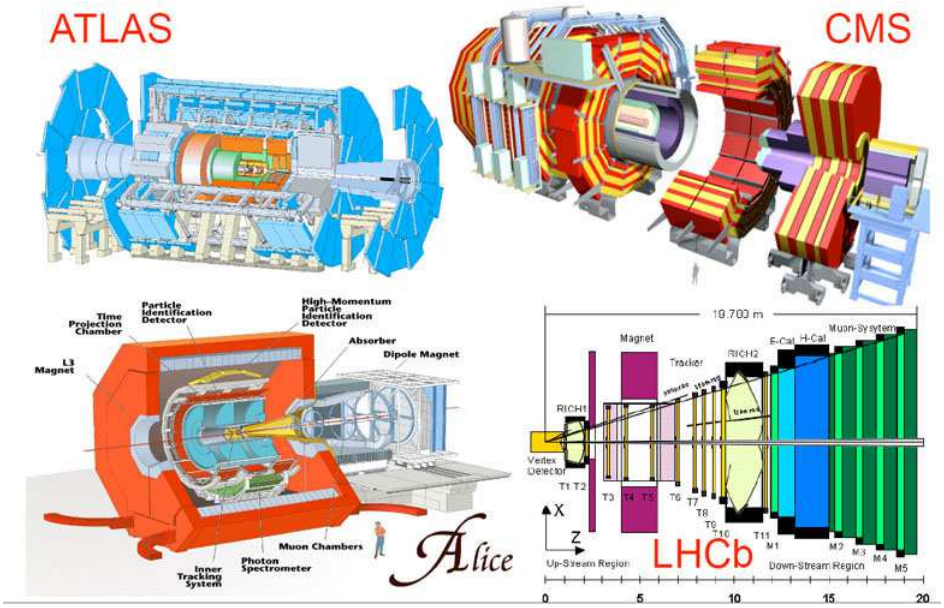

Figure 2.4: Detectors deployed at the four LHC interaction points [23]

detector with $44 \times 25\ m^2$ and 7000 tons. It has two magnets, one 2 T solenoid for the inner detector and a toroid which generates up to 6 T/m for the muon spectrometer. The advantage of a toroidal magnetic field is that its direction is almost perpendicular to the direction of flight of the particles.

- **Compact Muon Solenid (CMS) [18]**: It is the other general purpose experiment

for high luminosity (up to 10^{34} cm^{-2} s^{-1}) and it has the same discovery potential as ATLAS although its hardware and software design is different. It is smaller than ATLAS ($21 \times 15\ m^2$) although heavier with 12.500 tons and it can generate a unique non-linear magnetic field up to 4 T.

- **Large Hadron Collider beauty (LHCb) [24]**: Aiming at a peak luminosity of $10^{32}\ cm^{-2}s^{-1}$ for measuring the parameters of CP violation in the interactions of b-hadrons. The LHCb detector is a single arm spectrometer stretching for 20 metres along the beam pipe, with its subdetectors stacked behind each other like books on a shelf.

- **A Large Ion Collider Experiment (ALICE) [25]**: This experiment is focused on heavy ions and quark-gluon plasma studies (peak luminosity of L = $10^{27}\ cm^{-2}s^{-1}$). It works mainly with Pb-Pb ion nuclei collision.

In addition to this, other smaller experiments are placed along the ring [23]. Such is the case of:

- **Total Cross Section, Elastic Scattering and Diffraction Dissociation (TOTEM) [26]**: It is integrated into CMS and the aim of this experiment is to measure total cross sections, elastic scatterings at small angles and diffractive processes at the LHC at low luminosities (peak luminosity of $2 \times 10^{29}\ cm^{-2}s^{-1}$).

- **Large Hadron Collider forward (LHCf) [27]**: It is a special purpose experiment for low luminosity (up to $2 \times 10^{28}\ cm^{-2}s^{-1}$) which will study neutral pions produced in the forward region of collisions. It shares cavern but now with ATLAS and it consists of two detectors, 140 m on either side of the intersection point.

To carry through the ambitious LHC physics program all the detectors mentioned above must accomplish a set of general requirements such as:

- Fast, radiation hard electronics and sensor elements in order to cope with the harsh radiation environment. High detector granularity with good time resolution, resulting in low occupancy, to reduce the overlapping events, avoiding the products of an interaction to be confused with the products of another one.

- Good charge-particle momentum resolution and reconstruction efficiency in the inner tracker are essential to observe secondary vertices.

- Very good electromagnetic calorimetry for electron and photon identification complemented by full-coverage hadronic calorimetry for accurate jet and missing transverse energy measurements.
- Good muon identification and momentum resolution over a wide range of momenta.
- Highly efficient triggering on low transverse momentum objects with sufficient background rejection.

A more detailed description will be focused on the high luminosity experiment ATLAS and in particular its silicon tracker which constitutes the main subject of this thesis work.

2.3 The ATLAS Detector

The ATLAS experiment is a general-purpose detector which records the particles created in LHC collisions through different detecting subsystems that allow to identify particles and measure their momentum and energy. The ATLAS layout has cylindrical shape (4π coverage) and layers of subdetectors. It follows a similar scheme to other general purpose high energy collider detectors that aims at an hermetic coverage. A cut-away view of the overall layout of the ATLAS detector is shown in figure 2.5. The ATLAS detector is nominally forward-backward symmetric with respect to the interaction point.

The detecting technologies present at ATLAS are: a precision tracking system (for measuring the momentum of charged particles), calorimeters (for the determination of the energy of the electromagnetic and strongly interacting particles) and muon chambers (for measuring the momentum of muons).
Therefore, ATLAS consists of three main subsystems: the tracking system, the two calorimeters (electromagnetic and hadronic) and the muon chambers, all embedded in a huge magnetic field generated by a solenoidal and a toroidal magnet that bends the paths of charged particles in order to measure their momentum. To deal with the large amount of data that interactions create in the ATLAS detectors, they need an advanced trigger and data acquisition system and a large computing system.

From the inside out:

- **The Inner Detector** (ID) combines high resolution discrete silicon detectors in the innermost layers (pixel and microstrips detectors) with a continuous gaseous

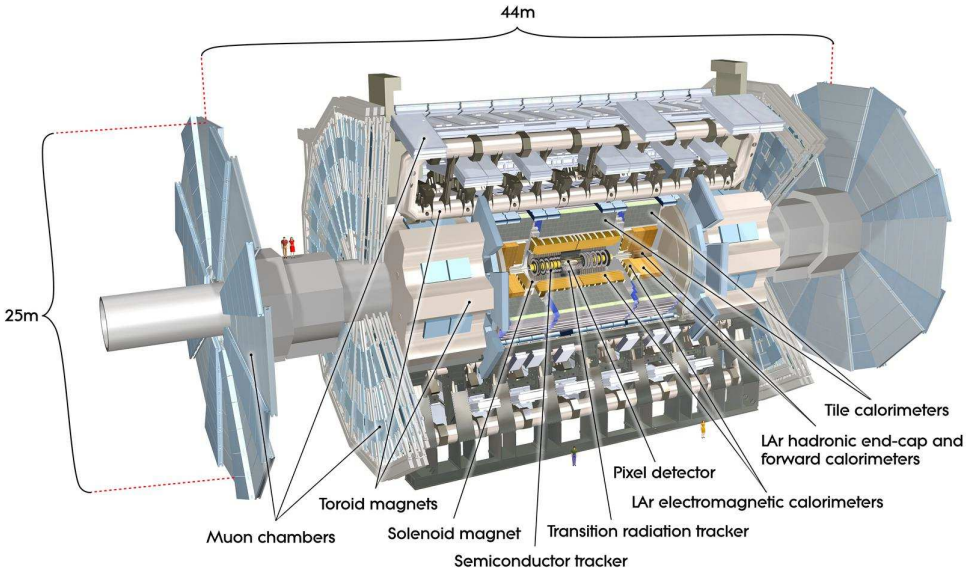

Figure 2.5: General view of the ATLAS detector (25 m in height and 44 m in length). The overall weight of the detector is approximately 7000 *tons*

straw drift-tube detector in the outermost radii. Together with the solenoidal magnet, ensures a robust pattern recognition and momentum determination, precise vertex measurements, electron identification, and electron-pion separation. The ID will be described in more detail later.

- **The Electromagnetic Calorimeter** $(ECAL)$ for the identification and energy measurements of electrons and photons. With an hermetic coverage, it uses liquid argon (LAr) as an ionization medium (it is also known as LAr calorimeter), with lead absorbers arranged in an accordion geometry. The high granularity of the detector elements allows to work with excellent performance in terms of energy and position resolution. It is surrounded by a cryostat as it needs very low temperatures to operate.

- **The Hadronic Calorimeter** $(HCAL)$ The Hadronic Calorimeter (HCAL) for the measurements of hadronic jets and missing energy (E^T_{miss}). HCAL is separated into a large barrel $(TileCal)$ which is provided by an iron absorber and plastic scintillator plates (called $tiles$) and two smaller extended barrel cylinders, one on either side of the central barrel. In the end-caps, LAr technology is also used for the hadronic calorimeters providing both electromagnetic and hadronic

energy measurements. The showers produced by particles such as the γ and $e^{\pm}$ are practically contained in the electromagnetic calorimeter, as they can penetrate much less than hadrons and produce narrower showers. Often a hadronic shower will start in the electromagnetic calorimeter and most of which will be absorbed in the hadronic calorimeter.

- **The Muon Spectrometer**, a stand-alone tracking device for muon detection including:
  - High precision tracking chambers: the *Monitored Drift Tubes* (MDT) and the *Cathode Strip Chambers* (CSC), for an excellent measurement of the muon momenta.
  - Trigger chambers with very fast response (timing resolution $\sim 1.5-4$ ns) and bunch crossing identification: the *Resistive Plate Chambers* (RPC) and the *Thin Gap Chambers* (TGC).

In order to select events of interest, a three-level trigger system is used. The hardware-based level-1 $(L1)$ uses a subset of detector information to reduce the event rate to a design value of 75 kHz. It uses information from the calorimeters and muon trigger chambers. The two software-based trigger levels, level-2 and the event filter, are collectively known as the High Level Trigger (HLT) and reduce the event rate to about 200 Hz. This reduction is possible because the HLT uses seeded, step-wise and fast selection algorithms based on the reconstruction of potentially interesting physical objects like electrons, muons, jets, tracks, and missing E_{T} and can provide the earliest possible rejection of background events.

2.3.1 The ATLAS Magnet System

Charged particles are deflected in a magnetic field due to the Lorentz force. The resulting path is helical propagating along a circular path in the bending plane and following the field direction (figure 2.6).

The ATLAS magnet system uses superconductive magnets to provide high fields to the detector (above 2 T). To provide the optimised magnetic field configuration for particle bending in a light and open structure, ATLAS chose different types of magnets: a central solenoid with small radius and thin walls, surrounded by three large air-core toroids, generating the magnetic field for the muon spectrometer.

A scheme of the complete system can be seen in figure 2.7.

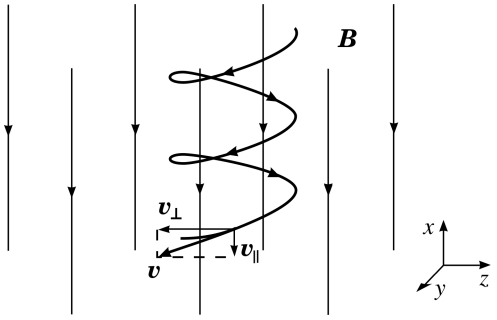

Figure 2.6: Inside a magnetic field the trajectories of the particles are deflected due to the Lorentz force describing a helical path.

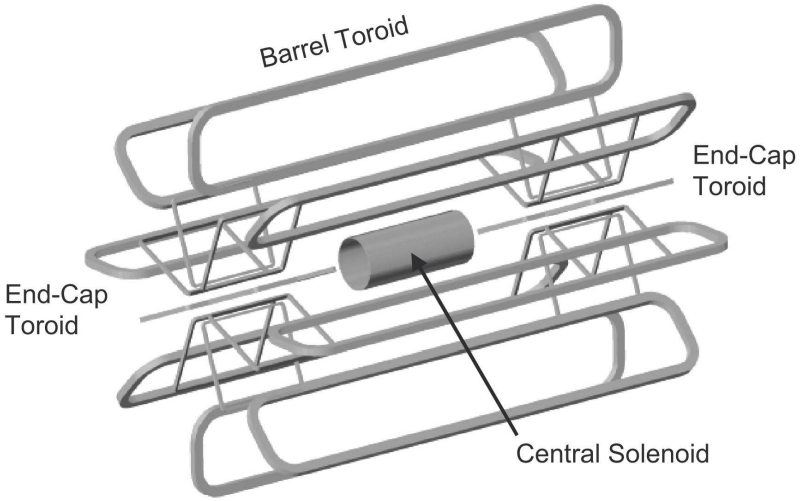

Figure 2.7: Three-dimensional view of the bare windings of the ATLAS magnet system: the central solenoid, the 8 coils of the barrel toroid and the 2×8 coils of the end-cap toroids.

- **Central Solenoid:** Surrounding the Inner Detector, the solenoid produces a 2 T magnetic field in the central tracking volume . This high magnetic field bends particles around the direction of the incoming LHC beams (even very energetic particles). Below 400 MeV of momentum, particles will be curved so strongly and they will loop repeatedly in the field and most likely not be measured; however, this energy is very small compared to the several TeV of energy released in each proton collision.

  To decrease particle scattering effects, the superconducting solenoid is based on a thin-walled construction and the material of the system is reduced sharing its cryostat with the liquid argon calorimeter. The solenoid is made as a single

layer coil so it generates a nearly uniform field inside the windings and a comparably weak and divergent field outside. The direction of the magnetic field and the field lines can be seen in figures 2.8 and 2.9 respectively.

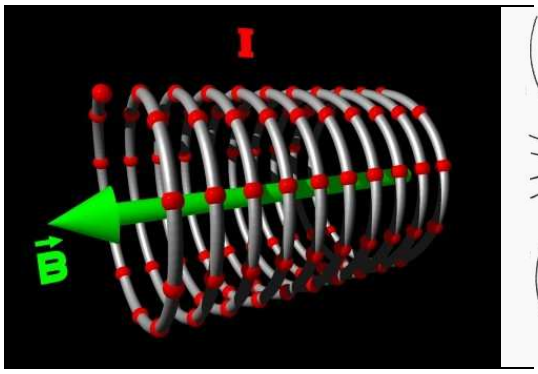

Figure 2.8: Magnetic field (B) inside a solenoid.

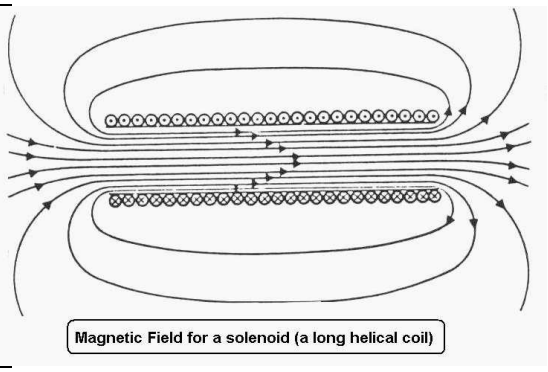

Figure 2.9: Field lines inside a solenoidal magnetic field.

An schematic bird's eye view of the solenoid is depicted in figure 2.10. Solenoidal fields give very good momentum resolution at large angles.

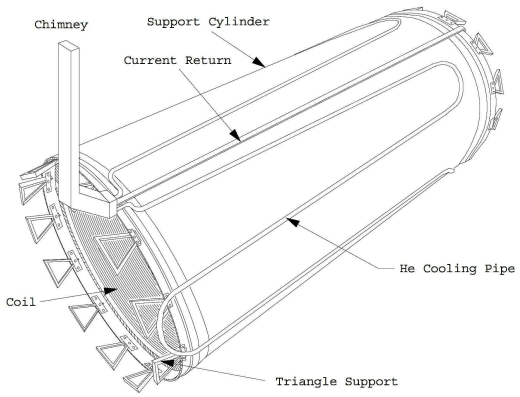

Figure 2.10: Schematic bird's eye view of the ATLAS central solenoid.

- **Toroid Magnets:** Each of three ATLAS toroid systems consists of eight coils, assembled radially and symmetrically around the beam axis. A scheme of the complete system design can be seen in figure 2.11. In order to obtain a better momenta and position measurement, the toroids have been built "in air".

  The magnetic field inside a toroid is directed tangentially and depends on the radius of the toroid (figure 2.12). The field lines created by a toroidal magnet

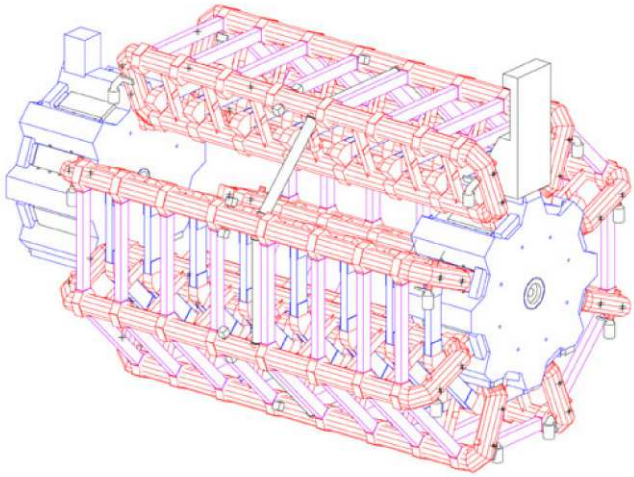

Figure 2.11: Schematic view of the ATLAS toroid magnet system design. It consists of two inserted end-cap toroids and a long barrel toroid that comprises eight separate cryostats.

can be seen in figure 2.13.

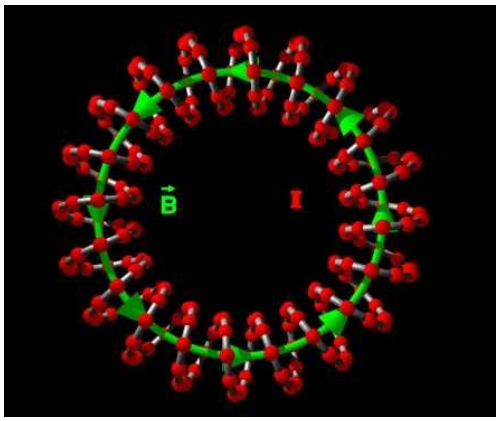

Figure 2.12: Magnetic field (B) inside a toroid.

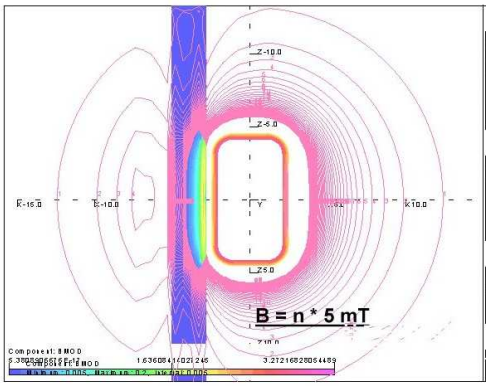

Figure 2.13: Field lines inside a toroidal magnetic field.

Toroids contain closed B field lines (figure 2.14), thus there is no need for extra yokes, avoiding the resulting multiple scattering.

With a toroid field particles will cover the complete pseudorapidity range being almost perpendicular to the field. This means that the field integral $\int BdL$, which is the important factor for momentum resolution, can be kept high even in the forward direction.

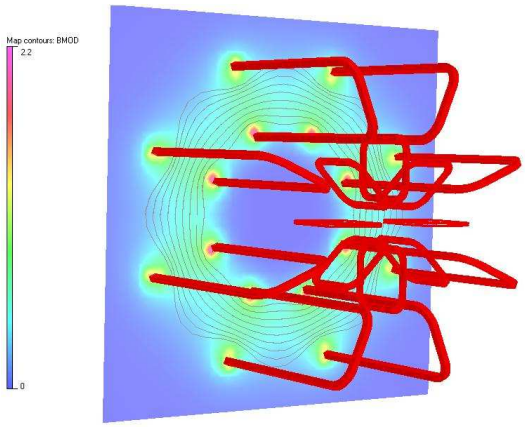

Figure 2.14: Simulation of the magnetic field lines generated by the magnet system. The magnet system provides an optimised magnetic field configuration for particle bending in the inner detector and the muon spectrometer.

The system is composed by two end-cap toroids (figure 2.15) and a 25 m long barrel toroid (figure 2.16). The Barrel system comprises eight separate cryostats. Each of the toroids carries a current of 20 kA, generating a magnetic field of 4 T. This magnet system provides strong bending power in a large volume (3 Tm in the barrel and 6 Tm in the end-caps) and this force is independent on the track angle since the magnetic field acts on p and not p_T.

The type of the magnets used is one of the differences between CMS and ATLAS. CMS is smaller and heavier than ATLAS, for this reason CMS uses a strong solenoidal magnetic field to bend the trajectories of the particles. On the contrary, ATLAS opts for a larger and lighter configuration using a smaller central solenoid but adding toroidal magnets in the outer part.

The combination of the solenoid and the toroid magnets provides a high-precision stand-alone momentum measurement of muons. In collider experiments often the sagitta *s* is measured inside the magnet region. The precision of the sagitta measurement is a direct measure for the precision of the muon momentum. The sagitta method is depicted in figure 2.17.

In general a charged particle track is measured using several (N) position-sensitive detectors. At least three coordinate measurements are necessary. For N equidistant measurements, the momentum resolution is described by the *Gluckstern formula*

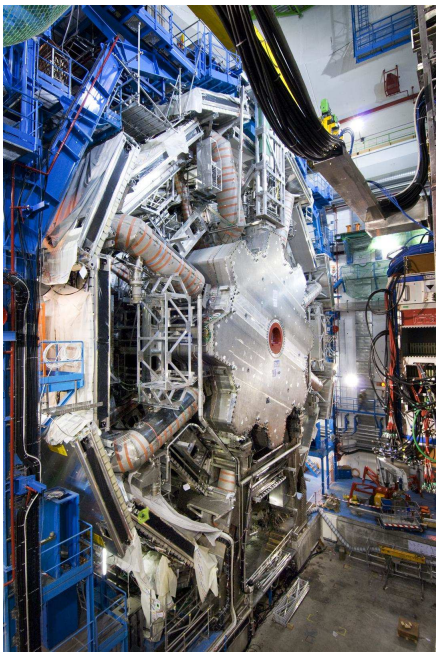

Figure 2.15: Endcap toroid system inserted in ATLAS. It consists of eight flat coils assembled radially and symmetrically around the beam axis. The magnet system provides a peak field of 4.1 T.

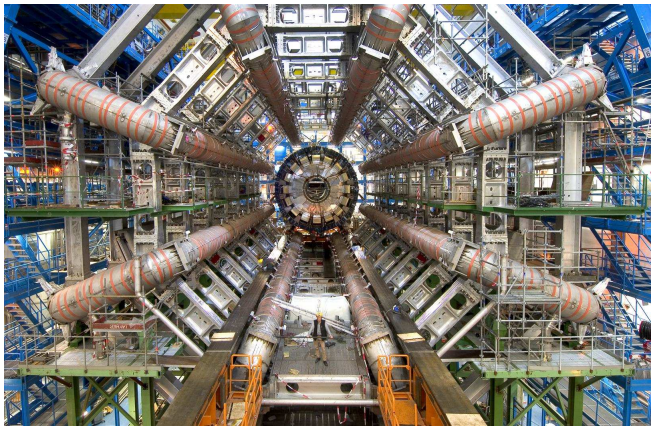

Figure 2.16: Barrel toroid system inserted in ATLAS. It consists of eight flat coils assembled radially and symmetrically around the beam axis. The magnet system provides a peak field of 3.9 T.

(1963) [28]. Assuming that each detector measures the coordinates of the track with a precision of σ_x, the approximate parametrization of the resolution is:

$$\frac{\sigma_{p_T}}{p_T} \approx \sqrt{\frac{A_N}{N+4}} \left(\frac{\sigma_x p_T}{0.3BL^2} \right) \tag{2.6}$$

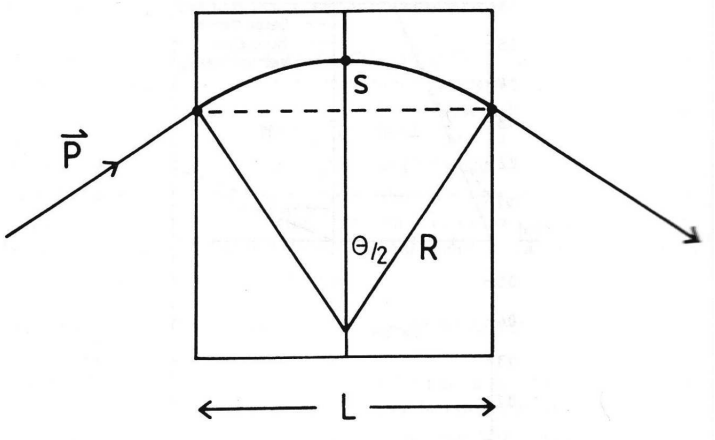

Figure 2.17: The sagitta *s* of the curvature of the track is often measured on collider experiments. The precision of the sagitta measurement is a direct measure for the precision of the muon momentum *p*.

with A_N statistical factor equal to 720 [28].

According to the above equation, the momentum resolution depends on the amount of material the particle has to traverse (L), the magnetic field strength (B) and the position resolution (σ_x). A sketch of two muon tracks bending under the presence of the ATLAS magnet system can be seen in figure 2.18.

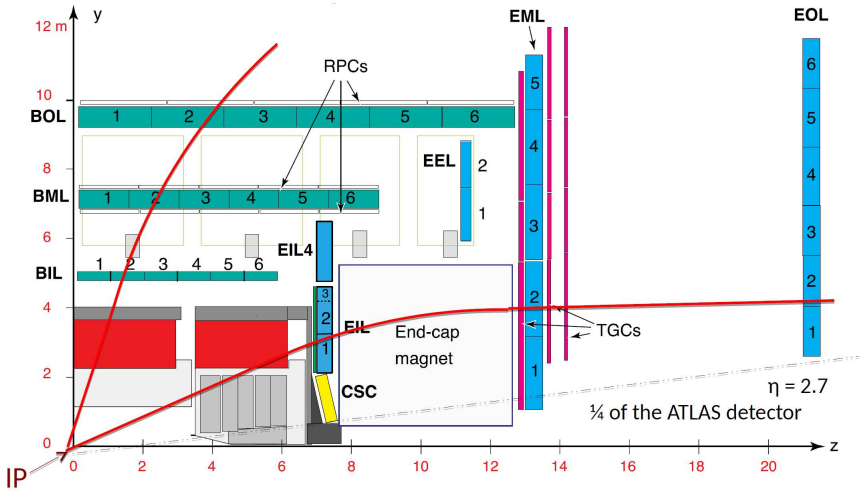

Figure 2.18: Sketch of two muon tracks bending under the presence of the ATLAS magnet system.

The ATLAS magnet system generates a stable, precise and predictable magnetic field in an enormous volume and is fully integrated with the detectors in an overall

$20 \times 20 \times 25\ m^3$ assembly. In table 2.4 the main parameters of the CMS and ATLAS magnet systems are presented.

	CMS	ATLAS		
Parameter	**Solenoid**	**Solenoid**	**Barrel Toroid**	**End-cap Toroids**
Inner diameter	5.9 m	2.4 m	9.4 m	1.7 m
Outer diameter	6.5 m	2.6 m	20.1 m	10.7 m
Axial length	12.9 m	5.3 m	25.3 m	5.0 m
Number of coils	1	1	8	8
Number of turns per coil	2168	1173	120	116
Conductor size (mm^2)	64 x 22	30 x 4.25	57 x 12	41 x 12
Bending power	4 Tm	2 Tm	3 Tm	6 Tm
Current	19.5 kA	7.7 kA	20.5 kA	20.0 kA
Stored energy	2700 MJ	38 MJ	1080 MJ	206 MJ

Table 2.4: Main parameters of the CMS and ATLAS magnet systems. CMS uses strong solenoidal magnets on a compact structure while ATLAS combines lighter solenoidal and toroidal magnetic fields in an open structure.

Table 2.5 shows a summary of the expected combined[1] and stand-alone[2] performance at two typical pseudorapidity values (averaged over azimutal) of the CMS and ATLAS experiments. The ATLAS muon stand-alone performance is excellent over the whole pseudorapidity[3] (η) range.

Combined (stand-alone) momentum resolution at	**ATLAS**	**CMS**
- p = 10 GeV and $\eta \approx 0$	1.4% (3.9%)	0.8% (8%)
- p = 10 GeV and $\eta \approx 2$	2.4% (6.4%)	2.0% (11%)
- p = 100 GeV and $\eta \approx 0$	2.6% (3.1%)	1.2% (9%)
- p = 100 GeV and $\eta \approx 2$	2.1% (3.1%)	1.7% (18%)
- p = 1000 GeV and $\eta \approx 0$	10.4% (10.5%)	4.5% (13%)
- p = 1000 GeV and $\eta \approx 2$	4.4% (4.6%)	7.0% (35%)

Table 2.5: Summary of the expected combined and stand-alone performance at two typical pseudorapidity values (averaged over azimutal) of the CMS and ATLAS experiments.

[1] Muons are reconstructed with the muon spectrometer and the inner detector.

[2] Muons are reconstructed with the muon spectrometer stand-alone; the muon momentum is corrected for the energy loss in the calorimeters by the expected energy loss.

[3] In experimental particle physics, pseudorapidity (η) is related with the azimuthal angle θ (i.e. it is related with the angle of a particle relative to the beam axis) as follows: $\eta = -\ln[\tan\frac{\theta}{2}]$

2.3.2 The Inner Detector

The Inner Detector (*ID*) [29] is the precision tracker of ATLAS and it is a 6.2 m long cylinder with a radius of 1.15 m. A sketch of its layout is shown in figure 2.19. The ID is the closest detector to the interaction point and, as mentioned in the previous section, its task is to reconstruct the trajectories of charged particles that are produced in the proton-proton collisions. It performs the pattern recognition, momentum and vertex measurements together with electron identification. The design of the Inner Detector provides pseudorapidity coverage up to $|\eta| < 2.5$. Pseudorapidity is a parameter commonly used due to the fact that only depends on the polar angle of the particle's trajectory and not on the energy of the particle.

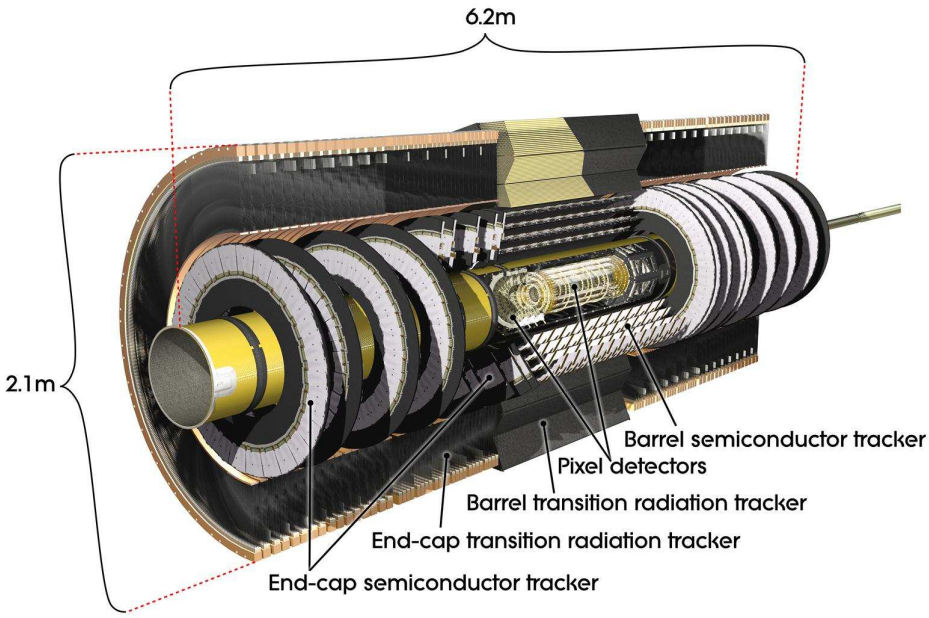

Figure 2.19: A sketch of the ATLAS Inner Detector, showing the various subdetectors

Mechanically, the ID is divided in three parts: a central barrel region and two symmetric end-caps. The barrel extends over ± 80 cm along the Z-axis. The components of the ID are summarized in the Table 2.6. It combines high-resolution silicon detectors in the inner radii with continuous tracking detectors at outer radii. It is composed by three sub-systems: the Pixel Detector, the Semiconductor Tracker (SCT) and the Transition Radiation Tracker (TRT).

Due to the large track density expected at the LHC (around 1500 charged particles crossing the ID every 25 ns), high precision measurements with fine-granularity detectors

Detector	Distance from beamline	Section	Layers	Area [m^2]	Channels [M]
Pixel	R 5.1 cm	B-Layer	1	0.2	13.2
	9.9 <R <12.3 cm	Barrel	2	1.4	54
	8.9 <R <15 cm	End-cap	3	0.7	6.6
SCT	25.5 <R <55 cm	Barrel	4	34.4	3.2
	25.1 <R <61 cm	End-cap	9	26.7	3.0
TRT	55.4 <R <108.2 cm	Barrel			0.1
	31.7 <R <110.6 cm	End-cap			0.32

Table 2.6: Main parameters of the Inner Detector

need to be performed to handle the particle fluxes and to reduce the influence of overlapping events. For this purpose the ID has 5832 individual silicon modules (with about 86 million of readout channels).The ID electronics and all the sensor elements must be fast enough and radiation hard.

Finally, figures 2.20 and 2.21 show the nominal positions of each barrel layer and end-cap disc in the radial and transverse plane, respectively.

- **Pixel Detector:**

  The Pixel Detector occupies the radii between 5 and 15 cm from the interaction point and it is designed to provide a very high granularity (with 80.4 million channels) as well as high precision set of measurements as close as possible to the interaction point. This system is based on silicon pixel technology as a detection medium and it consists of one B-layer (for its importance in B-physics), two cylindrical barrel layers and two endcaps, with three discs on each side of the central barrel [30]. A 3D model of the Pixel detector can be seen in figure 2.22. The pixel modules (identical for all regions) are single silicon sensors of 6.08$\times$1.64 cm^2 divided in 46.080 pixels and a size of $50\ \mu m \times 400\ \mu$m resulting in an intrinsic resolution resolution of 10 μm in the R (transversal) direction and 115 μm in the Z (longitudinal) direction with a direct 2D readout. Each single silicon sensor has highly doped n^+ implants on a n-type substrate. The pn junction is located on the back-side, with a multi-guard structure controlling the potencial drop towards the cutting-edges. These sensors have $250\ \mu m$ of thickness and a sensitive area of 16.4$\times$60.8 mm^2. There are 1456 modules in the barrel and 288 in the end-caps.

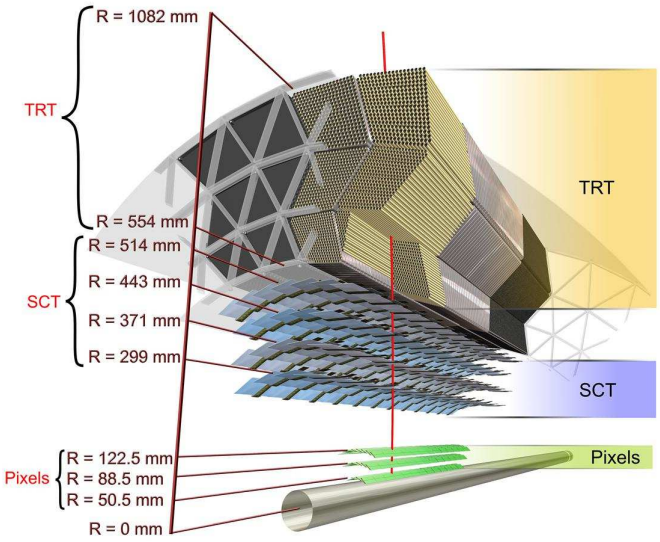

Figure 2.20: Drawing showing the sensors and structural elements traversed by a charged track of 10 GeV p_T in the barrel inner detector (η = 0.3). The track traverses successively the beryllium beam-pipe, the three cylindrical silicon-pixel layers with individual sensor elements of $50 \times 400\ \mu m^2$, the four cylindrical double layers (one axial and one with a stereo angle of 40 mrad) of barrel silicon-microstrip sensors (SCT) of pitch $80\ \mu m$, and approximately 36 axial straws of 4 mm diameter contained in the barrel transition-radiation tracker modules within their support structure

Much more information about the pixel module components and its electronics can be found in reference [31].

- **Semiconductor Tracker (SCT):**

  The SCT surrounds the pixel detector and consists of four barrel layers and two end-caps.

  On each barrel, the modules are placed in rows parallel to the beam axis. There are 12 modules in each row with a total of 2112 modules [32]. A barrel module consists of two pairs of single-sided p^+n silicon detectors glued back-to-back at 40 mrad angle and separated by a heat transport plate. Each silicon wafer is $6 \times 6\ cm^2$, $285\ \mu m$ thick, and has 768 readout strips with $80\ \mu m$ pitch. On each side of the module, two wafers are wire-bonded together to form 12 cm long strips. Combining the measurements from both sides, a two-dimensional

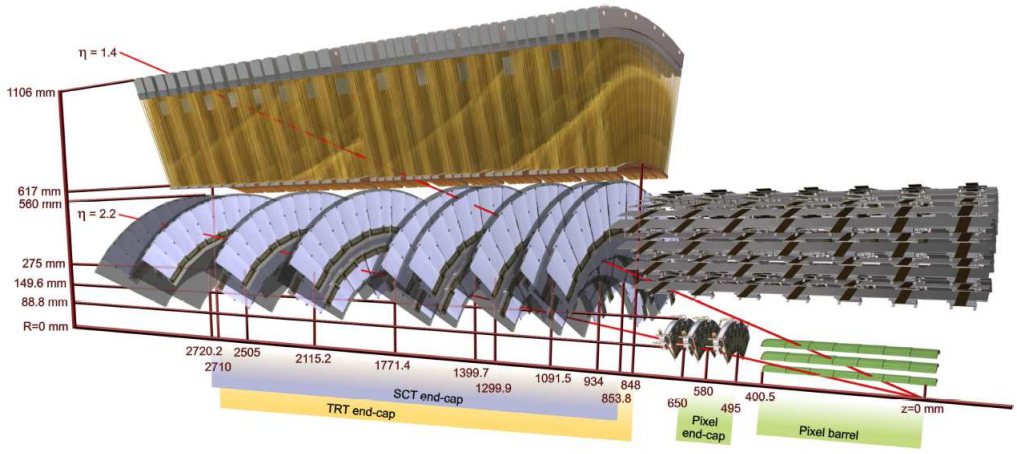

Figure 2.21: Drawing showing the sensors and structural elements traversed by two charged tracks of 10 GeV p_T in the end-cap inner detector (η = 1.4 and 2.2). The end-cap track at η = 1.4 traverses successively the beryllium beam-pipe, the three cylindrical silicon-pixel layers with individual sensor elements of $50 \times 400\,\mu m^2$, four of the disks with double layers (one radial and one with a stereo angle of 40 mrad) of end-cap silicon-microstrip sensors (SCT) of pitch $\sim 80\,\mu m$, and approximately 40 straws of 4 mm diameter contained in the end-cap transition radiation tracker wheels. In contrast, the end-cap track at η = 2.2 traverses successively the beryllium beam-pipe, only the first of the cylindrical silicon-pixel layers, two end-cap pixel disks and the last four disks of the end-cap SCT. The coverage of the end-cap TRT does not extend beyond $|\eta| = 2$

spacepoint is created. The readout is performed by means of 12 binary $ABCD$ [33, 34] front-end chips and mounted above the detectors on a $hybrid$. The readout chain consists of a front-end amplifier and discriminator, followed by a binary pipeline which stores the hits above threshold until the level-1 trigger decision.

Each end-cap consists of 9 disks supported by a cylinder with modules arranged in rings within a disk. The disks are located at a 27.5 $<$ R $<$ 56 cm from the beamline. A disk may have up to three rings, therefore three types of end-cap modules (namely inner, middle, and outer) are needed [35]. The end-cap modules are similar to the barrel modules in electronics and readout, except in their shape. The coverage of each disk is required to be fully hermetic for tracks above a transverse momentum of 1 GeV, except for the unavoidable dead area between the two sensors in each plane for outer and middle modules. Moreover, the layout allows sufficient overlapping active area between neighbouring modules

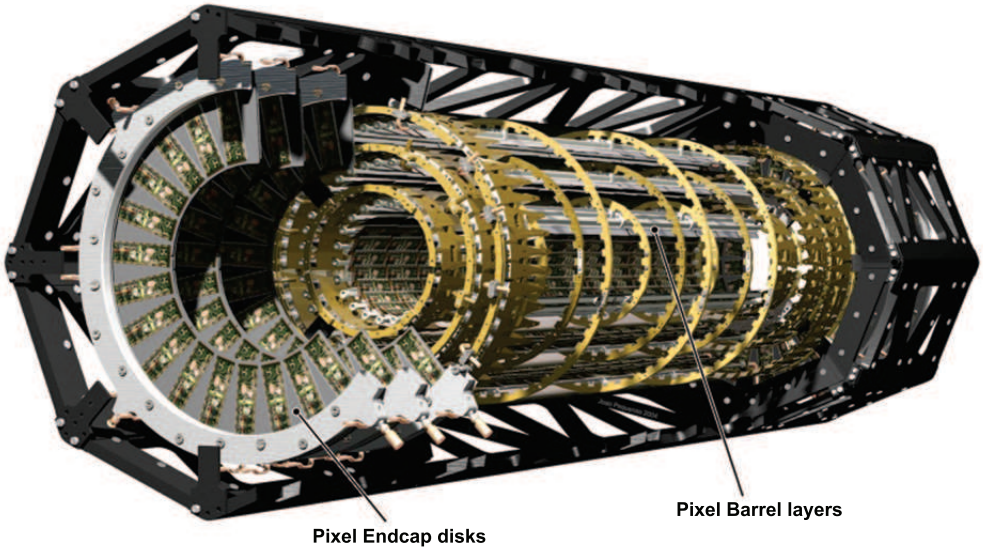

Figure 2.22: A 3D model of the Pixel Detector and it's framework.

for the module alignment parameters to be efficiently determined.
As a consequence, the shape of the modules is trapezoidal, resulting in a variable strip pitch. The effective strip length after bonding is around 12 cm for middle and outer modules, and half this value for inners (with only one sensor per side). The strip pitch varies from 55 to $95\ \mu m$ depending on the end-cap module type.

With this performance the system fulfils the required intrinsic resolution of $17\ \mu m(r\phi)$ and $580\ \mu m(z)$ for the barrel and $17\ \mu m(r\phi)$ and $580\ \mu m(r)$ for the disks. The SCT is constructed so that on average four space points are measured for particles up to a pseudorapidity of $|\eta| < 2.5$ as shown in figure 2.23.

The SCT has 4088 modules in total which means 61 m^2 of silicon sensors with 6.3 million channels.

- **Transition Radiation Tracker (TRT):**

  The TRT is based on the use of straw detectors with the capability to generate and detect transition radiation in its outerpart.
  It surrounds the other two subsystems and consists of about 300 000 gaseous straw tubes arranged in 73 layers in the barrel region and 2$\times$160 straw planes in the end-cap regions. A picture of the barrel part can be seen in figure 2.24.

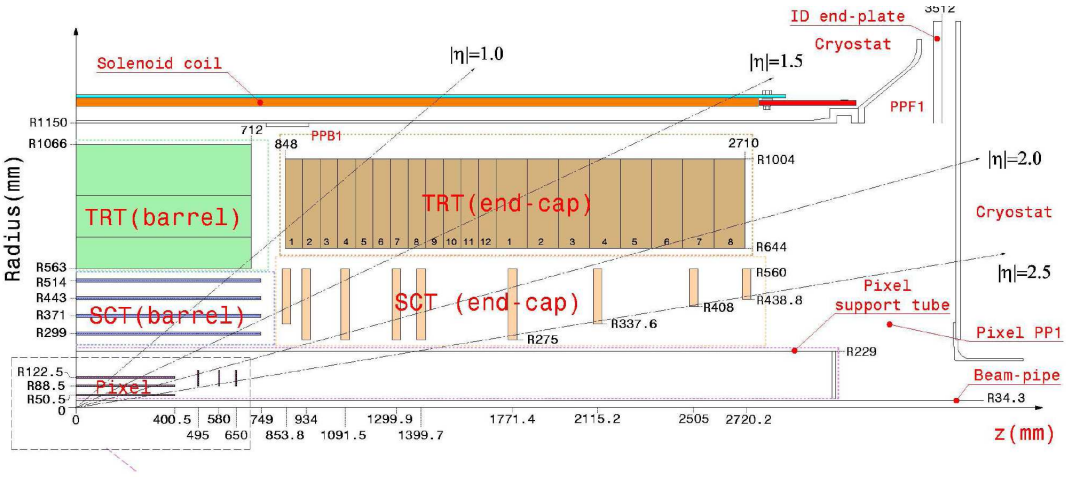

Figure 2.23: Schematic of the ATLAS inner detector

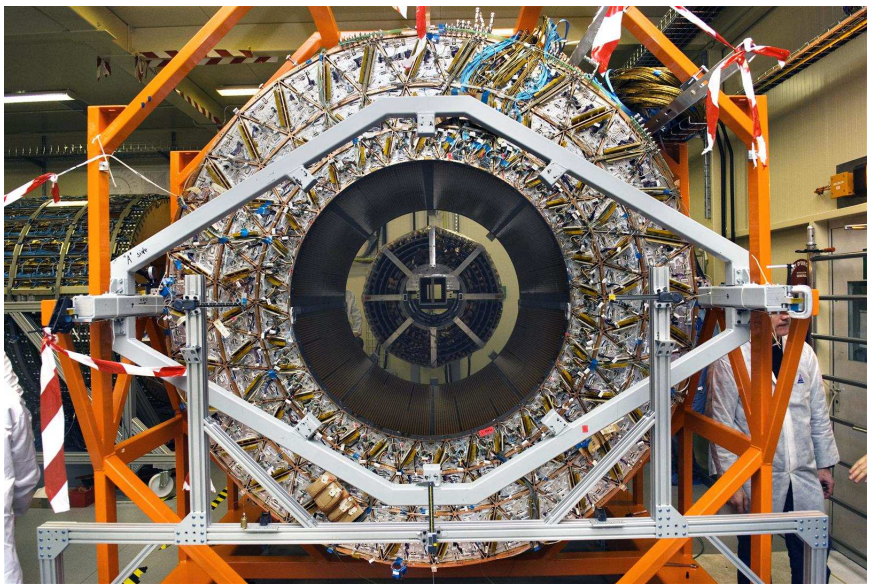

Figure 2.24: TRT barrel, just before SCT barrel insertion

One of the main reasons to build the TRT in straws filled with a gas mixture was to minimize the material used to build the ID. The pixel and strip detectors require a lot of material in the form of support structures and services (cables and cooling pipes). This material has a negative effect on the performance of the tracker [36].

An average number of 36 hits per track its provided (in the transverse plane to the beam pipe). The TRT gas mixture *Xe/CF4/CO2* (70%/20%/10%) provides an efficient X-ray absorption, a fast charge collection and a stable operation over a sufficient high-voltage range even at high particle rates. The total number of channels that are read out is 420.000 and each channel provides a drift time measurement. Its technology allows to have an intrinsic resolution of $130\ \mu m$ per straw (i.e. in the direction perpendicular to the wire) where each straw tube has a diameter of 4 mm.

2.3.3 The ATLAS Coordinate System

The origin of the coordinate system in ATLAS is the nominal interaction point (IP). In the Cartesian coordinate system the z-axis is oriented parallel to the beam line in anti-clockwise direction, the x-axis points horizontally to the centre of the LHC ring and the y-axis is perpendicular to the x-axis and z-axis and points upwards. The detector is symmetric about the perpendicular plane spanned by the x and y axis. The symmetry of the detector makes cylindrical coordinates with (r, ϕ, θ) useful. R is the transverse radius from the beam axis and the azimuthal angle (ϕ) is the angle in the perpendicular plane to the beam axis (z-axis). The polar angle (θ) is defined as the angle with the positive z-axis and is measured from the beam-axis.

The side of the detector at positive z values is called the $A-side$ of the detector whereas the detector half with negative z values is defined as the $C-side$.

The pseudorapidity is often used instead of polar angle θ, as the particle multiplicity is approximately constant as function of η. With these coordinates η is defined as:

$$\eta = -\ln[\tan\frac{\theta}{2}] \tag{2.7}$$

This dependence is derived from the definition of the rapidity, y, used for describing tracks of particles in a detector. This parameter is especially useful because Δy is

invariant under longitudinal (in z) Lorentz boosts. Rapidity is defined as

$$y = \frac{1}{2}\log\frac{E + p_L}{E - p_L} \tag{2.8}$$

where E is the energy of the particle and p_L is the longitudinal component of the momemtum of the particle. By assuming massless particles equation 2.8 can be reduced to 2.7. η is also a good approximation for y in the relativistic limit. This parameter is convenient for describing the coverage of a detector. A high η coverage, meaning $\eta \gg 1$, means that a detector has good coverage in the forward regions.
The Inner Detector layout provides full tracking coverage over $|\eta| \leq 2.5$ (figure 2.23), including impact parameter measurements and vertexing for heavy-flavour and τ tagging. The secondary vertex measurement performance is enhanced by the innermost layer of pixels.

2.3.4 Radiation levels

Detectors working at high luminosity scenarios are exposed to high radiation levels. These levels increase as we are closer to the interaction point. So, the radiation levels in the inner tracker region will be extremely high.

At small radii the radiation backgrounds are dominated by charged hadron secondaries (mainly pions) from inelastic proton-proton interactions, as seen in figure 2.25.

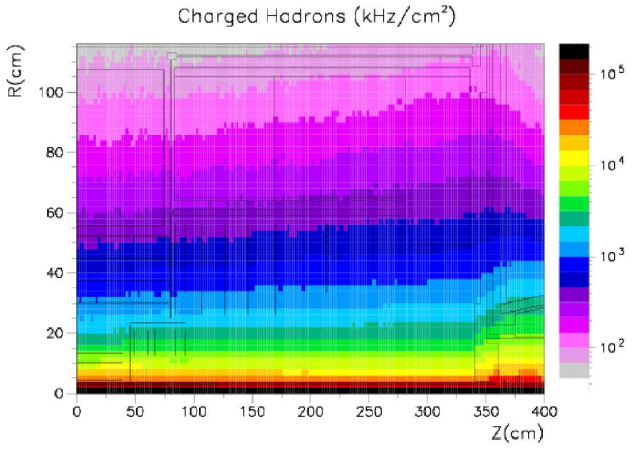

Figure 2.25: Charge hadron fluence rates in the inner detector.

It can also be seen that the charged hadron fluence contours run parallel to the beamline, which is a consequence of the flatness of the charged particle rapidity

plateau of minimum bias events. Close to the interaction point, charged pions dominate the bulk damage in silicon. However, further out in the SCT and TRT systems, neutrons are dominant.

Figure 2.26 highlights the importance of neutron fluence. Despite some neutrons are originated from the interaction point, as well as secondaries from the beampipe, most of them come from albedo (backsplash from the surfaces of the electromagnetic calorimeter).

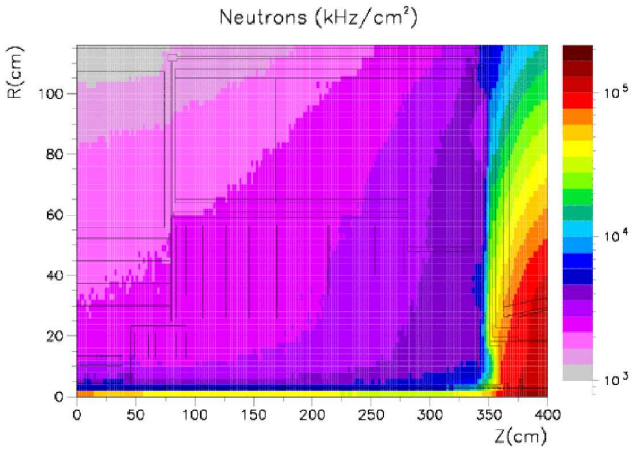

Figure 2.26: Total neutron fluence rates in the inner detector.

Due to the effects of the background radiation in the detectors, the performance of the tracking is degraded. They fall into a number of general categories:

- The occupancy is increased (figure 2.27) leading to inefficiencies, worsened resolutions and fake tracks.
- Radiation damage and ageing of detector components and electronics (figures 2.25 and 2.26).
- Interactions leading to anomalous deposits of local radiation can disrupt electronic signals (single events upsets) or destroy components (single event damage).

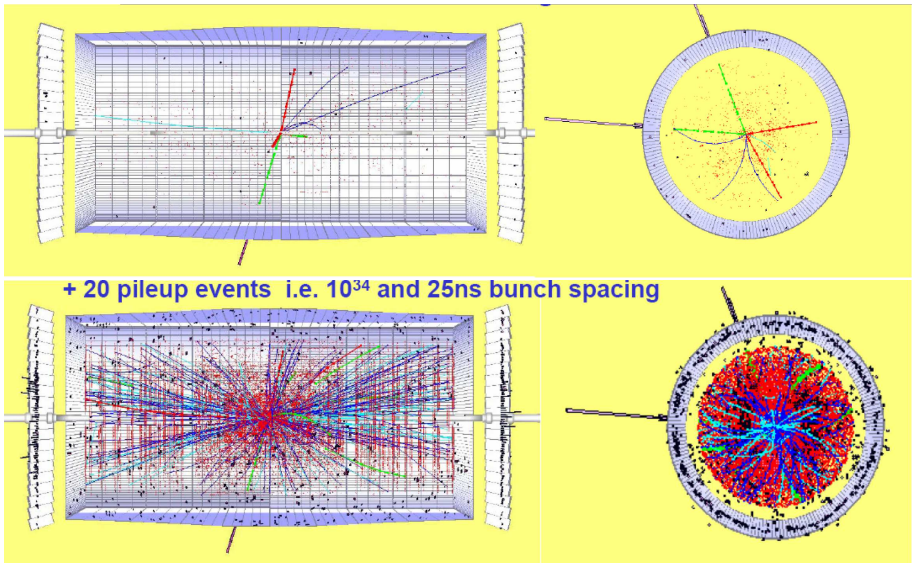

Figure 2.27: Higgs event: $H \to 2e\,2\mu$. In the upper part a "clean" event is shown. In the picture below, the same event is shown with the expected background for LHC design luminosity (from [37]).

2.4 High Luminosity LHC: Upgrading the ATLAS detector

At the moment the LHC machine has brought to light its excellent performance. Figure 2.29 shows the evolution of the increasing luminosity during 2011 and 2012 in ATLAS. Within a few weeks the machine ramped to standard performance at a higher energy than before (8 TeV centre of mass).

In the next years, the LHC will undergo a series of upgrades leading ultimately to five times increase of the instantaneous luminosity (5×10^{34} cm^{-2} s^{-1}) in the *High-Luminosity LHC* (HL-LHC) project [38]. The main accelerator parameters of the HL-LHC are shown in table 2.7.

This increase turns into higher collision rates extending the sensitivity to new physics and allowing additional and more precise measurements to be performed. The large luminosity extends the energy scales that can be studied in high energy experiments as for example studying the EWSB mechanism, and to probe for signatures of new physics predicted by models such as SUSY and extra dimensions. Precision measurements of the Higgs boson properties will be possible with larger data sample, in particular the Higgs couplings to fermions and bosons, rare decays and self-couplings (precisions in a range between 5% and 30%). For instance, the full luminosity should

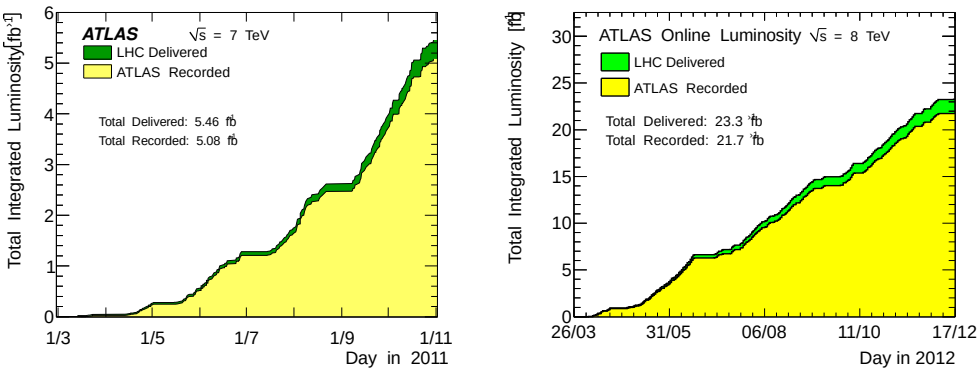

Figure 2.28: Cumulative luminosity versus day delivered to (green), and recorded by ATLAS (yellow) during stable beams and for pp collisions in 2011 (left) and 2012 (right). The delivered luminosity accounts for the luminosity delivered from the start of stable beams until the LHC requests ATLAS to turn the sensitive detector off to allow a beam dump or beam studies. Given is the luminosity as determined from counting rates measured by the luminosity detectors. These detectors have been calibrated with the use of the van-der-Meer beam-separation method, where the two beams are scanned against each other in the horizontal and vertical planes to measure their overlap function.

allow studying Higgs self-coupling in channels HH$\rightarrow \tau\tau$bb [39]. More details on the HL-LHC physics potential can be found in references [38, 40, 41, 42]

The goal of the project is to extend the dataset from about 300 fb^{-1}, expected to be collected by the end of the LHC run (in 2022), to 3000 fb^{-1} by 2035. The HL-LHC will begin collisions around 2024 and will deliver an additional 2500 fb^{-1} to ATLAS over ten years [43]. This factor of ten increased in the luminosity is beyond the design specifications of the LHC and its experiments. To deal with this new scenario the detectors will require significant optimizations, changes and improvements.

The number of particles produced in each bunch crossing would increase by a factor of 10. The proton-proton (pp) collisions at the Large Hadron Collider (LHC) result not only in hard-scatter (signal) interactions, but also in additional collisions accompanying the signal. Such additional low transverse momentum pp collisions are referred to as pileup interactions. When a collision occurs, computers above the machine decide whether the data are interesting and, if so, reconstruct the collision from the tracks. But when dozens of collisions occur at once, the computers must disentangle them. We differentiate between *in-time* and *out-of-time* pileup. While *in-time* pileup arises from additional *pp* interactions in the current bunch-crossing, *out-of-time* pileup refers to energy deposits in the ATLAS calorimeter from previous and following bunch crossings

Protons per bunch	2.2×10^{11}
Number of bunches	2750
Normalized emittance	2.5 micron
$Beta^*$	15 cm
Crossing angle	590 μrad
Geometric reduction factor	0.305
Virtual luminosity	$2.4 \times 10^{35} cm^{-2} s^{-1}$
Levelled luminosity	$5 \times 10^{34} cm^{-2} s^{-1}$
Levelled $\langle$pile-up$\rangle$	140

Table 2.7: Design accelerator parameters of the HL-LHC collider

relative to the triggered event to which the calorimeter is susceptible. In the ATLAS detector, many of the subsystems have sensitivity windows longer than 25 ns, which is the interval between proton-proton bunch crossings. As a result, every physics object is affected by pile-up in some way, from additional energy contributions in jets to the mis-reconstruction of background as high-momentum muons.

Therefore, in order to reliably distinguish between the tracks produced by these particles within a HL-LHC scenario, the granularity of many of the detectors would need to be increased. This also requires a detector able to operate after exposure to large particle fluences. The design of the detectors must also function within a much harder environment in terms of radiation damage received. In preparation for this, several R&D programs are already working to provide guidelines for new detector technologies, which may be employed at the anticipated high radiation levels, as well as to study and design the new possible detector layouts, in order to be able to cope with the improved physics program. To allow for some safety margin, the design studies for the proposed upgrades assume a maximum instantaneous luminosity of 7×10^{34} cm^{-2} s^{-1}, 200 pile-up events, and an integrated luminosity of 3000 fb^{-1} over ten years where appropriate.

The harsher radiation environment and higher detector occupancies at the HL-LHC imply major changes to most of the ATLAS systems, specially those at low radii and large pseudorapidity, η. The ID, forward calorimeter and forward muon wheels will be affected the most by the higher particle fluxes and radiation damage, requiring replacement or significant upgrade, whereas the barrel calorimeters and muon chambers are expected to be capable of handling the conditions and will not be modified.

In the case of ATLAS, the upgrade is planned in three phases, which correspond to the three long, technical shutdowns (LS) of the LHC towards the HL-LHC. In each shutdown several modifications are introduced to the detectors and the luminosity is increased progressively as can be seen in figure 2.29.

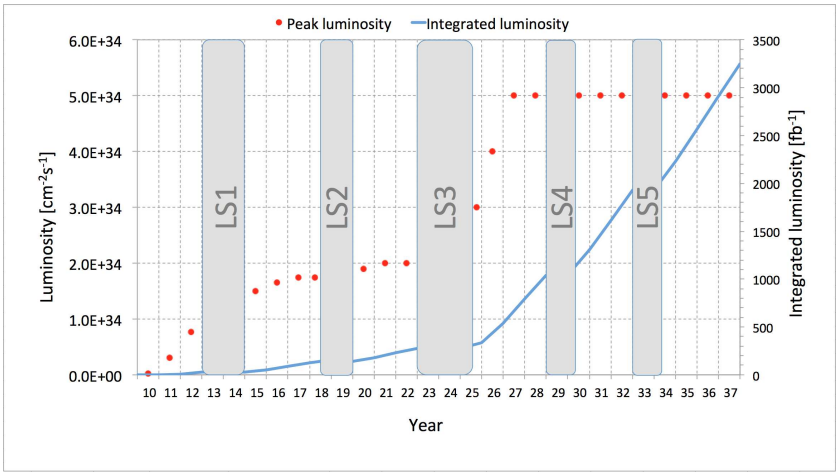

Figure 2.29: Mid-term planning for increasing luminosity at LHC

- **Phase-0:** By the time of writing the LHC has just ended the LS1 and started the first phase of the upgrade. The aim of this new period is to drive the machine to the design energy (nominal luminosity). The number of bunches per beam increases from 1380 to 2808 and the bunch spacing is reduced from 50 to 25 ns. With these modifications, the instantaneous luminosity will reach above 10^{34} cm^{-2} s^{-1}. For that, different changes have been applied such as:

  – Additional Pixel Layer (IBL) has been inserted in the pixel detector at a radius of 33 mm. Due to the IBL position, the beam pipe has been replaced with a small radius one [44]. For this extra pixel layer new front-end electronics, optical transceivers and read-out systems have also been developed. It is expected that the IBL will improve the vertex resolution, secondary vertex finding and b-tagging, hence extending the reach of the physics analysis.

  – The cooling plant for the pixel and the SCT will be modified to an evaporative cooling system and the IBL will use CO_2 based cooling.

  – A new diamond beam monitor has been installed.

  - Improved coverage of Muon spectrometer between the barrel and the endcap region.
  - On the calorimeters, all low voltage power supplies will be changed.

  Firts proton collisions (at 13 TeV) began on May 2015 and the machine seems to be working as expected. The instantaneous luminosity reached at 2016 was around 1.5×10^{34} cm^{-2} s^{-1}.

- **Phase-I:** In 2018, the LHC will be stopped for the second long shutdown. During this period, ATLAS intends to accomplish the second stage of its upgrade program, the Phase-I [45]. This phase will imply an upgrade of the injectors and the collimators. An upgrade of the LINAC2 and increase of the Proton Synchrotron Booster output energy are also planned. The data-taking will be resumed after one year shutdown with luminosity of 2×10^{34} cm^{-2} s^{-1}. To handle luminosities well beyond the nominal values, installation of new Muon Small Wheels and introducing of new trigger schemes are proposed among others.

  - New Muon Small Wheels: At high luminosity the performance of the muon tracking chambers (in particular in the end-cap region) degrades with the expected increase of cavern background rate.A replacement of the first endcap station of the Muon Spectrometer, the Muon Small Wheel (*MSW*), built of Monitored Drift Tubes (*MDT*) and Cathode Strip Chambers (*CSC*), is proposed. The new Muon Small Wheels must ensure efficient tracking at high particle rate and large $\mid \eta \mid$ with position resolution of $< 100\ \mu m$
  - New Trigger Schemes: At Phase-I, more sophisticated triggers will be required. The objective of this upgrade is to provide higher granularity, higher resolution and longitudinal shower information from the calorimeter to the Level-1 trigger processors. For this, the Fast TracKer (*FTK*) trigger project has been initiated [46]. At the FTK, the track finding and fitting are conducted at a hardware level, which makes it extremely fast. At the current ATLAS, this task is performed by the trigger Level-2 software farm. FTK will provide the track parameters at the beginning of the Level-2 processing. This way, the load on Level-2 will be diminished and extra resources will be available for more advanced selection algorithms, which ultimately could improve the b-tagging, lepton identification, etc. Suggestions

are also in place for combining trigger objects at Level-1 (topological triggers) and for implementing full granularity readout of the calorimeter. The latter will strongly improve the triggering capabilities for electrons and photons at Level-1.

- **Phase-II:** The ATLAS Phase-II upgrade is scheduled for 2022 and 2023. During this time, LHC will be out of operation for furnishing with new inner triplets and crab cavities. As a result, an instantaneous luminosity of 5×10^{34} cm^{-2} s^{-1} should be achieved. As mentioned previously in this section, the goal is to accumulate $3000\ fb^{-1}$ of data by around 2030. The present ATLAS Inner tracker will have several limitations when up to 200 pile-up events per bunch crossing are expected. The gas-based TRT outer tracker has a limit due to instantaneous luminosity because of very high occupancy. ATLAS Phase-II preparations include a new Inner Detector and further trigger and calorimeter upgrades.

  – New Inner Detector: The functionality of the silicon-based parts of the tracker will be deteriorated due to the total radiation dose afecting both sensors and read-out electronics and also by the instantaneous luminosity, too high for the present limited band-width. Due to this factors, ATLAS has decided to replace the entire Inner Detector with a new, all-silicon Inner Tracker (*ITk*).

    The current baseline design of the ITk described in the Letter of Intent (*LOI*) of the phase-II [39]) and is presented in figure 2.30. It consists of 4 Pixel layers and 5 Si-strip layers (3 short-strip layers and 2 long-strip layers) in the barrel part. The two endcap regions are each composed of 6 Pixel disks and 7 strip double-sided disks. Other layouts are currently under study, even extending the coverage at larger pseudo-rapidity.

    The new ITk will improve the material budget, increase the sensor granularity and radiation resistivity of the readout components. Some characteristics of the performance of this layout are listed: robust tracking with at least 11 hits/track for $|\eta| < 2.5$, channel occupancy $< 1\%$ for pile-up up to 200 (figure 2.31), reduced material (factor 5 for $|\eta| < 1$) with respect to current inner detector.

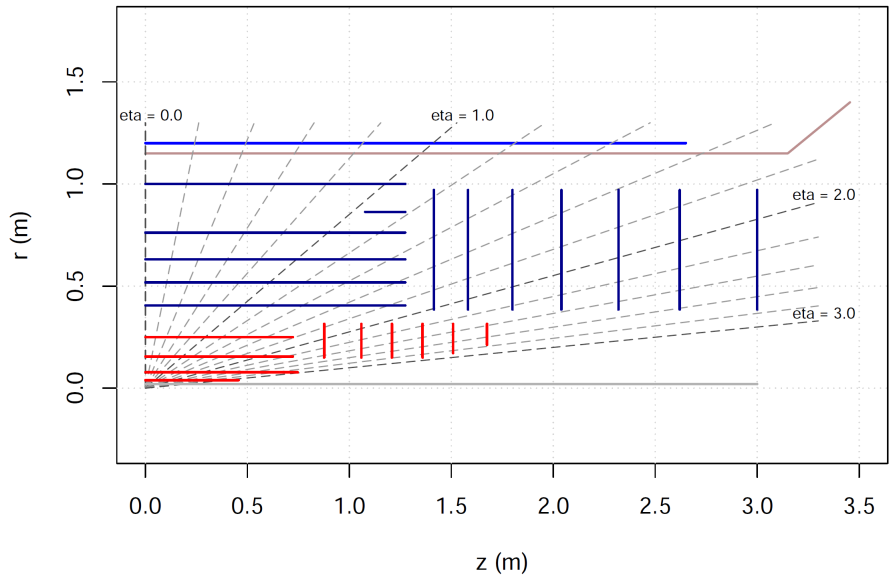

Figure 2.30: The baseline layout of the replacement tracker showing the active areas of silicon detectors arranged on cylinders and disks.

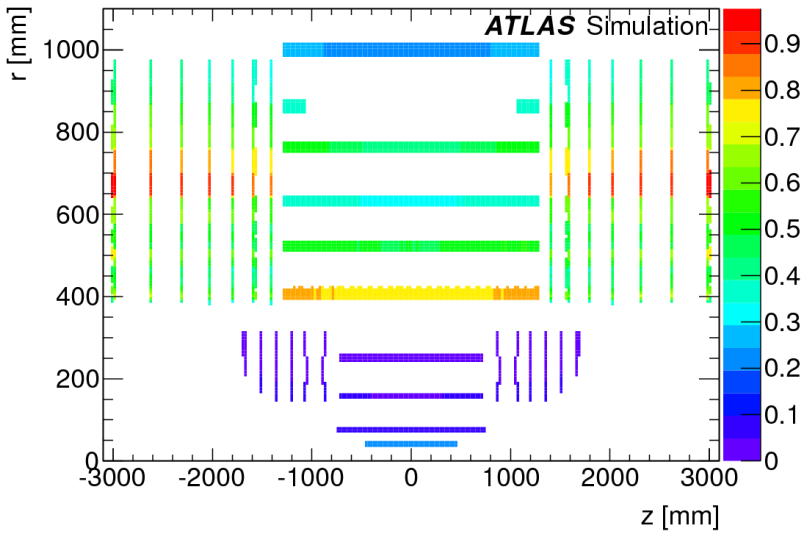

Figure 2.31: Channel occupancies (in percent) with 200 pile-up events.

– Calorimeter upgrades: To ensure an adequate performance of the calorimetry system during the HL-LHC operation, different solutions have been aproved:

  * Replacement of the cold electronics inside the LAr Hadronic endcap and all on-detector readout electronics for all calorimeters.

  * To maintain the FCal functioning at the HL-LHC, two possible solutions

are considered. From one side a complete replacement of the *FCal*, and from the other side the installation of a small warm calorimeter, *Mini-FCal*, in front of the FCal. The Mini-Fcal would reduce the ionization and heat loads of the FCal to acceptable levels.

– Trigger upgrades: A new trigger architecture is being developed that is compatible with the constraints imposed by the detector and provides a fexible trigger with the potential to deliver the required performance. The planned trigger upgrades for Phase-II are connected with implementing a *Track Trigger* at Level-1/Level-2, applying full granularity of calorimeter at Level-1 and improving the muon trigger coverage.

Since the major topic of this thesis is focused on the upgrades proposed for the ITk endcaps in ATLAS, a full description of the considered modifications for the inner tracker will be detailed in the next section. The very high luminosities also present significant challenges to the operation and performance of the rest of the detector systems. A more detailed description of these improvementes can be found in the Letter of Intent of the Phase-II [39].

2.4.1 Inner Tracking System upgrade for the Phase-II

The ID was designed to operate for 10 years at a peak luminosity of 10^{34} cm^{-2} s^{-1}, with an assumed 23 pile-up events per 25 ns bunch crossing, and a level-1 trigger rate of 100 kHz. The current performance cannot survive the planned high luminosity operation. Among other requirements the new tracker must be able to deal with:

- **Radiation damage:** It must use radiation hard sensor and electronics technologies to withstand $10^{16}\ n_{eq}/cm^2$ (inner regions) required at the HL-LHC. The radiation backgrounds close to the interaction point are dominated by particles coming directly from the proton-proton collisions. However, at larger radii the radiation backgrounds which dominate in the inner detector are neutrons from high energy hadron cascades in the calorimeter material. The 1 MeV neutron-equivalent fluences, normalised to $3000\ fb^{-1}$, can be seen in figure 2.32. The radiation background simulations for this layout have been performed using *FLUKA* [47].

  The predictions for the maximum 1 MeV-n_{eq} fluence and ionising dose for $3000\ fb^{-1}$ in the different systems goes from $2.9 \times 10^{14} cm^{-2}$ to $1.4 \times 10^{16} cm^{-2}$ [48].

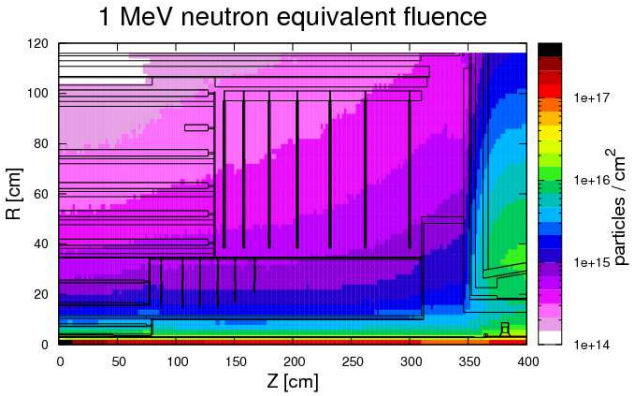

Figure 2.32: *RZ-map* of the 1 MeV neutron equivalent fluence in the Inner Tracker region, normalised to $3000\ fb^{-1}$ of 14 TeV minimum bias events generated using PYTHIA8.

- **Occupancy:** Based on ATLAS measurements from the current LHC running [49], a multiplicity of more than a 1000 tracks per unit of rapidity is expected in the tracker acceptance in the presence of up to 200 pile-up events. Simulations of the pile-up events expected from collisions under LHC and HL-LHC luminosities are compared in figure 2.33.

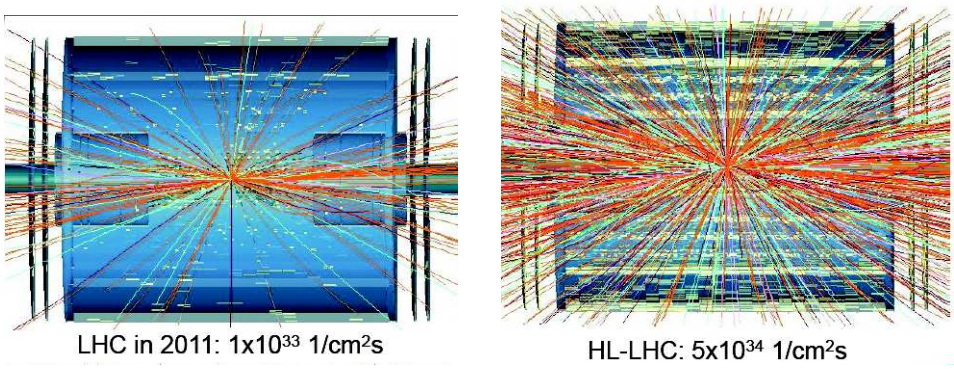

Figure 2.33: Amount of tracks expected in LHC (left) and HL-LHC (right) scenarios.

The current SCT would be unable to resolve particles in close proximity, and the TRT straws will approach 100% occupancy. Actually, some degradation in the TRT performance has already been observed in the most central heavy-ion collisions. To meet the challenges of very high pile-up in the HL-LHC, the sensors must be of finer granularity than the existing tracker.

The finer granularity of the detectors is achieved modifying the size and the width of the pixel and strip sensors. The hit occupancies anticipated in this

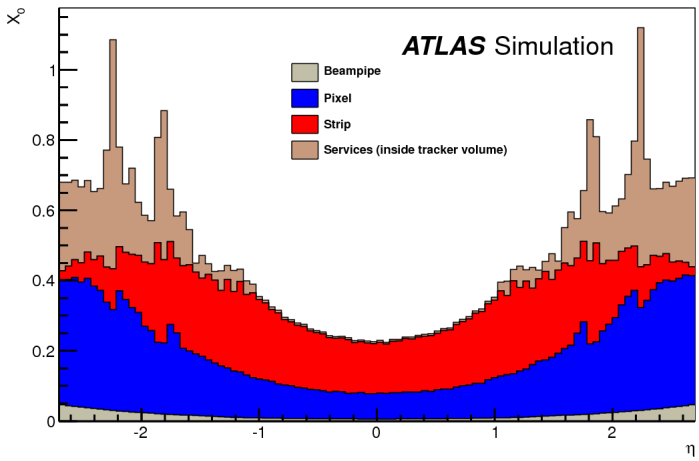

Figure 2.34: The material in X_0 as a function of η for the Phase-II tracker layout.

layout for 200 pile-up were presented in the previous section in figure 2.31. To obtain a good particle separation for highly dense jets but to minimise gaps in the η coverage, the outermost pixel radius is chosen to be 250 mm. For the three innermost layers the strips are only 23.8 mm long and for the outermost layers they are 47.8 mm.

- **Interactions with the material:** To reduce the tracking inefficiency, due to hadronic interactions and Bremsstrahlung effects, the overall tracker material must be minimised. This will contribute to:

  - Reduce multiple scattering. This will lead to better precision in momentum measurements.
  - Having less photon conversions reducing tracking confusion and providing a better photon identification.
  - Reduce the number of secondaries from interactions leading to an increase in the occupancy of the detectors.

Figure 2.34 shows the expected material distribution in the new tracker system. It presents a major improvement with respect to the current ID. The current ID (including the IBL) contributes $> 1.2\ X_0$ for all regions $|\eta| > 1$ [50], while the new tracker remains below $0.7\ X_0$ up to $|\eta| = 2.7$, excepting a few small regions.

- **Space:** The available space is defined by the volume taken by the ID in ATLAS and this is a major constraint on the design. To optimise the process and to allow for supports and services, the gaps between subdetector parts have been preserved. The resulting sensor areas and channel counts are shown in table 2.8.

Detector	**Silicon Area** $[m^2]$	**Channels** $[10^6]$
Pixel Barrel	5.1	445
Pixel End-cap	3.1	193
Pixel Total	**8.2**	**638**
Strip Barrel	122	47
Strip End-cap	71	27
Strip Total	**193**	**74**

Table 2.8: Inner tracker active area and channel count.

In addition to meeting these requirements, the layout must respect constraints from integration, modularity and cost. The extreme conditions at HL-LHC also dictate a more modular concept, being an all-silicon design, based on technologies that are already being prototyped, or are improvements on existing solutions. As mentioned in section 2.4 the proposed inner tracker is presented in figure 2.30 including the overall dimensions.

Table 2.9 highlights some characteristics of the performance of this layout compared with the current inner detector.

Track parameter $\mid \eta \mid < 0.5$	Existing ID with IBL no pile-up $\sigma_x(\infty)$	Phase-II tracker 200 events pile-up $\sigma_x(\infty)$
Inverse transverse momentum $(q/p_T)\,[/\text{TeV}]$	0.3	0.2
Transverse impact parameter $(d_0)\,[/\mu m]$	8	8
Longitudinal impact parameter $(z_0)\,[/\mu m]$	65	50

Table 2.9: Performance of the existing ID with IBL, and of the Phase-II tracker for transverse momentum and impact parameter resolution. $\sigma_x(\infty)$ refers to σ_x for $p_T \to \infty$, to remove the contribution due to material.

In the next section the strip system for the phase-II of the ATLAS upgrade will be detailed.

2.4.2 Strip System for the Phase-II

The system covers approximately 2.5 units of rapidity and it is composed by a central barrel cylinder and two end-cap disks.

- **Central Barrel Region:** The barrel system[1] comprises the region between $\pm$ 1.3 m. It consists of five full length cylinders surrounding the beam-linee.

  To cover the loss of acceptance between the end-cap and barrel a short "stub" barrel is also used. The basic mechanical element of the barrel is the stave and it consists of a low mass central stave core that provides mechanical rigidity, support for the modules, and houses the common electrical, optical and cooling services. As an interface, the stave uses an End-Of-Stave (EOS) card. 472 full length staves populate the layers of the barrel region (236 on each side of $Z = 0$) and each stave has 26 modules (13 on each face). There is a small gap between staves at $Z = 0$. Short strips (23.820 mm long) are used for the three inner cylinders and long strips (47.755 mm long) for the outer two cylinders and stubs. The main components of a stave are shown in figure 2.35(a).

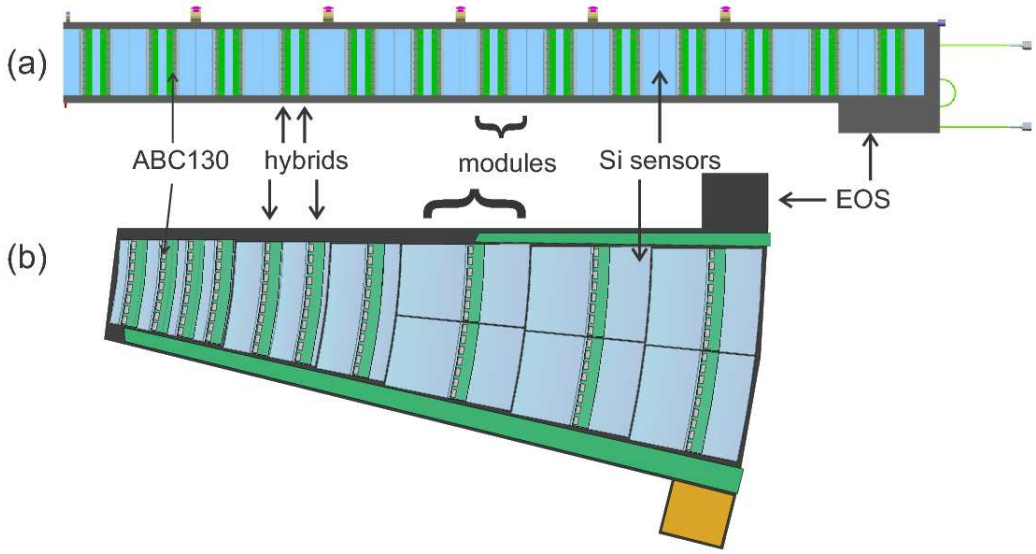

Figure 2.35: Barrel stave (a) and Petal stave (b) components. The basic unit is a module. Each module is composed by a silicon sensor and a hybrid above. The hybrids are made by application specific front-end chips ("ABC130") mounted on kapton circuits.

[1] The Barrel description presented in this thesis corresponds to the layout that was officially in force during 2009 and is included in the Letter of Intent for the phase-II of the ATLAS upgrade [39].

To provide mechanical support to the stave a carbon composite core is used [51]. This structure has built in the cooling system for 26 modules (13 on each side). The cooling pipes are embedded in carbon fibre honeycomb and carbon foam. The system is sandwiched between two carbon fibre facings made from several layers of carbon fibre. Figure 2.36 shows a drawing of the stave core (a) with its main components labeled and a prototype stave core (b) with a copper/aluminum/kapton electrical bus tape co-cured into the facings.

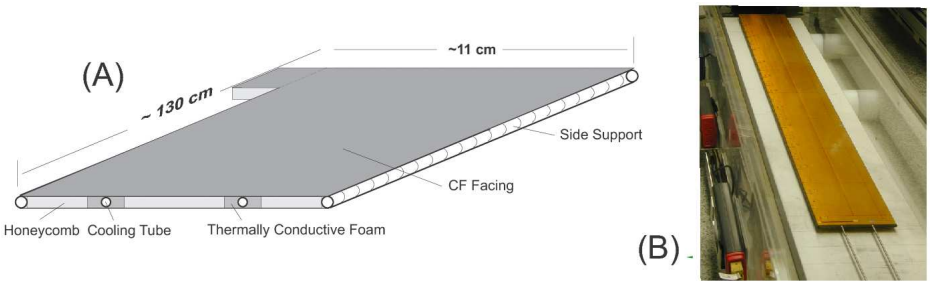

Figure 2.36: (a) Drawing of a stave core. (b) Photo of a stave core with a kapton bus co-cured into facing.

The design of the stave in terms of thermal properties is optimised to avoid thermal runaway in the sensors minimizing the thermal impedance. Due to radiation effects the leakage current of the sensor increases causing an increment in the temperature and entering in a process of positive thermal feedback. The detector current “runs away”. It is a function of the coolant temperature, thermal impedance of any location on the detector to the coolant, and sensor and ABC130 power. To prevent thermal runaway the current designs have a large safety margin ($> 20\ ^{\circ}$ C coolant temperature headroom). This values are obtained by simulations [51].

A program to develop a system for the stave insertion is in progress. Different approaches are being improved. Each option must satisfy the stave insertion in the z-direction rather than the radial direction to permit the replacement of a stave in all but the last stages of testing on the barrels. One option uses an end-insertion of the stave onto five carbon fibre/peek bracket (figure 2.37). A second approach would use cantilevered support to permit smaller stave tilt angles. Both options are under development and a program to compare and choose between them is in place.

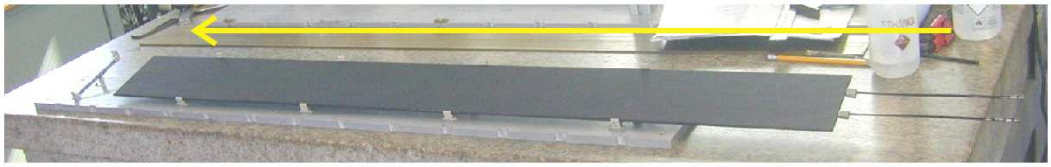

Figure 2.37: Stave being end inserted onto five carbon fibre/peek brackets.

The building of different prototypes is important to optimize the fabrication process, minimize mass and validate simulations. A number of prototype stave cores have been built and tested [51] and figure 2.36(b) shows a stave prototype that would satisfactorily meet the needs of the upgrade. However, further mass minimizations continue to be explored.

The staves are arranged in concentric cylinders (figure 2.38) centred on the beam-line. Each cylinder has a multiple of 4 staves so that each quadrant is identical; this simplifies the routing of services and the design of structure supports between cylinders. The staves are rotated $\geq 10\ ^{\circ}$ (the *tilt-angle*) to allow an overlap in the ϕ direction.

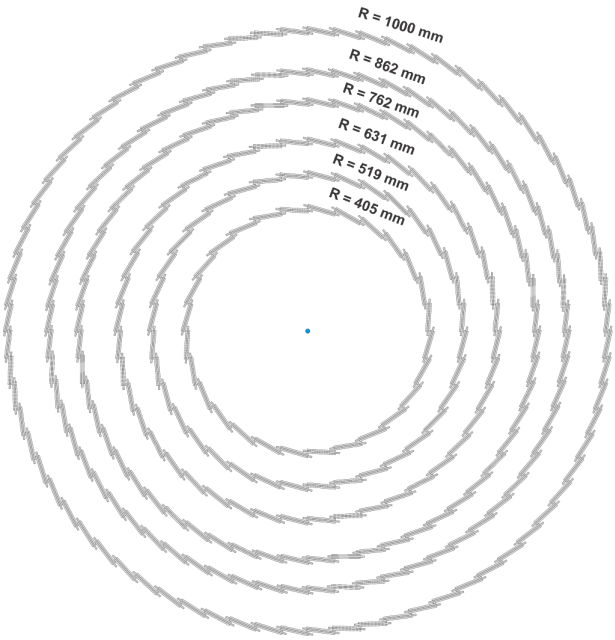

Figure 2.38: Arrangement of staves in barrels. Staves are tilted 10 degrees.

The overlap is sufficient for software alignment, with at least 2% of tracks passing through the edges of two neighbouring staves.

- **End-caps:** The strip End-caps[1] extend the length of the strip detector to $\pm$ 3 m. They have seven disks on each side and each disk is populated with 32 identical Petals with its components also depicted in figure 2.35(b). The Petal is a modular mechanical unit analogous to the stave and is designed to give support and cooling to the endcap sensors, covering a sensitive area that extends radially from 38.5 cm to 97 cm. Each Petal has six different sensor shapes, resulting in 6 rings of detectors. The first three rings have 32 sensors while the outermost three have 64 sensors. Together with the sensors, the Petal houses the bus cable, that brings the voltages and control signals to the ASICS in the hybrids glued on top of the sensors and takes the signal off the hybrid to the End-Of-Petal (EOP) board, located in the *nose* of the Petal, which provides the electrical connection to the outside world.

  The Petal has also a pipe inside for CO_2 circulation right under the sensors, providing the shortest and most efficient thermal path for heat removal from the sensors and their readout electronics. The Petal core design follows quite closely the design of the stave core for the barrel. The main differences are the wedged shape of the Petal with its possible implications in the planarity and mechanical stability, in particular in the widest region, which can be as wide as 20 cm. The bus cable runs underneath the sensors and has a thin kapton layer to isolate electrically the sensors from the carbon fiber core. Apart from that, materials and cooling structure are the same.

  Figure 2.39 shows an exploded view of a Petal. It shows, from top to bottom, the sensors and the bus tape at the sides together with the end of Petal, which provides the electrical connections to the outside world.

  Then we have the carbon fiber facing, the cooling pipes surrounded by carbon foam and the honeycomb filling the rest of the volume. Also shown is a fully populated Petal with the sensors, bus cables and hybrids.

  A major description of the Petal core fabrication and the development of different Petal prototypes will be explained in chapter 4.

[1] The Endcap description presented in this thesis corresponds to the layout that was officially in force during 2009 and is included in the Letter of Intent for the phase-II of the ATLAS upgrade [39].

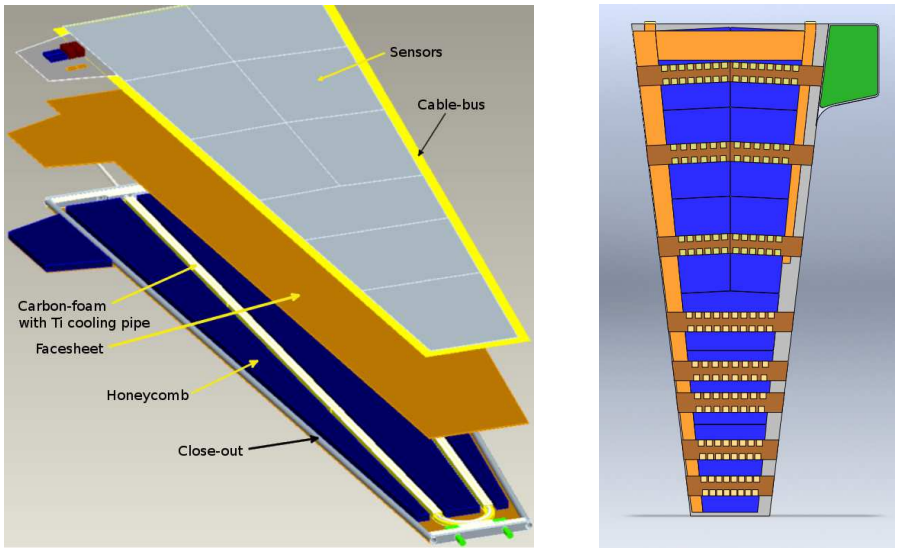

Figure 2.39: Exploded view of a Petal (left) and a fully populated Petal with sensors, bus cable and hybrids (right).

Regarding the Petal insertion in the End-cap disks, the option considered is a castellated layout (figure 2.40). The current version has a large gap all the way along the petal (about 45 mm) but it may be possible to reduce this by moving the support disks out from between the petals and by moving all EOS connectors onto one side of a petal.

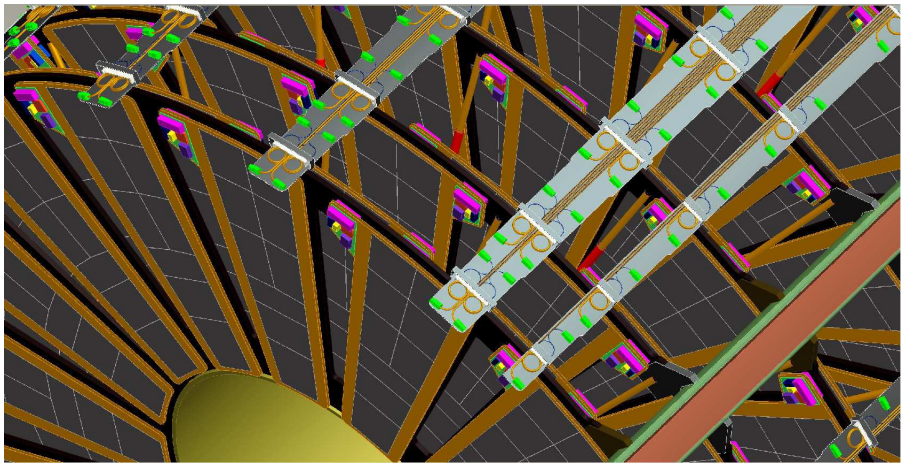

Figure 2.40: In the castellated layout the Petals are arranged on either side of a disk, with services on one ear only.

2.4.2.1 Silicon Sensors

The silicon sensors used for the Barrel and End-cap systems will be microstrip sensors with n-type implants in a p-type float-zone silicon bulk (n-in-p FZ) and AC-coupled. In these type of sensors electrons are collected and they have no radiation induced type inversion. The thickness of the sensors is (320$\pm$15) μm.

In the case of the Barrel staves, the sensors have a size of 97.54$\times$97.54 mm^2. Each sensor is composed by 1280 strips with a strip pitch of 74.5 μm. The strips are parallel to the sides of the sensor. The stereo angle is achieved by rotating the sensors 40 mrad on one side. The other side will be axial. As mentioned before, the sensors of the staves are distinguised by the length of the strips to achieve the proper occupancy for the track density expected at HL-LHC. There are sensors with four rows of short strips (23.820 mm) to be used on the three inner cylinders, and other sensor type with two rows of longer strips (47.755 mm) is used in the outer two cylinders.

In the case of the Petals, the sensors need radial strips to give an accurate measurement of the $r\phi$ coordinate. Therefore, the strips will point to the beam-line and the sensors will have a wedge shape. Each End-cap disk contains 32 Petals (16 each side) covering the radial range required by the layout. Different from the Barrel staves, the sensors in the End-caps achieve the stereo angle by rotating the strips 20 mrad within the sensors thus keeping a total stereo angle of 40 mrad between strips on opposite sides of a Petal. The sensors are divided into pairs of rows of strips (the ABC130 chip is designed to read out two rows of strips). Since the dimensions of the sensors is chosen to use as few 6-inch silicon wafers as possible [52] a Petal has 6 different types of sensors depending on their size and the number of rows of strips in each sensor. A summary of the types of the Petal sensors is presented in table 2.10. The inner-most ring (Ring 0) is in a region of very high track density and radiation damage, and so needs very short strips.

The number of chips on a hybrid, and hence the number of strips, is chosen to keep the strip-pitch at the bond pad region as close to the barrel pitch (74.5 μm) as possible.

To be able to operate under HL-LHC conditions the silicon sensors are required to withstand the expected maximum fluence of 8.1$\times 10^{14}$ n_{eq}/cm^2 and to operate up to 500 V. To allow for uncertainties in fluence calculations, a specification of 2$\times 10^{15}$ n_{eq}/cm^2 is imposed. Prototype short strip sensors have been designed and fabricated and a

Ring	Rows of strips	Hybrids per sensor
0	8	4
1	4	2
2	2	1
3	2	1
4	2	1
5	2	1

Table 2.10: Summary of the number of rows of strips and hybrids per sensor. Each hybrid is designed to read out one pair of strip rows.

detailed description of the design and measurements carried on will be developed in chapter 4.

Chapter 3

Silicon detectors for HL-LHC

3.1 Semiconductor Theory

The field of semiconductor detectors has been in constant progress since the 50's. Semiconductor detectors are based on crystalline semiconductor material and generate electric signals that can be processed with electronic technology. In the case of particle and nuclear physics experiments germanium and silicon are the most frequent semiconductor materials used for particle detection. More precisely silicon is used in tracking detectors and recently also in calorimetry.

The extraordinary properties of semiconductors reside in the structure of their band levels. The band gap of any material is the energy difference between the valence and the conduction band. While conductors, such as copper, have a separation between bands very small or non existent, semiconductors have a larger band gap, a few electronvolts ($\sim 1\ eV$). An insulator has similar band structure to a semiconductor, except that the band gap energy is wider. The difference between their band levels can be seen in figure 3.1.

Silicon has a band gap of 1.12 eV at 300K and it changes with absolute temperature (T) according to the experimental *Varshni equation* [53] that for silicon is given by [54]:

$$E_G(T) = 1.17 - \frac{(4.73 \times 10^{-4}) \cdot T^2}{T + 636} \tag{3.1}$$

where E_G is expressend in electronvolts. With this when temperature rises the band gap in silicon decreases.

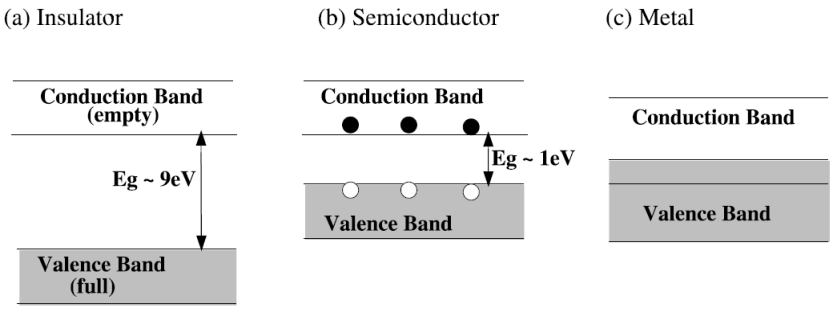

Figure 3.1: Band structures of (a) an insulator, (b) a semiconductor and (c) a conductor.

3.1.1 Creation of electron-hole pairs in Silicon.

Charged particles that are moderately relativistic lose energy in matter primarily by atomic excitation and ionization. From the ionizing energy losses electron-hole[1] pairs are created. This creation is possible when the electron in the valence band receives enough energy to overcome the band gap. Silicon has an ionization energy of 3.62 eV, about three times larger than the band gap (1.12 eV at 300K). This is due to the fact that to create electron-hole pairs the energy and momentum must be conserved. Therefore, excitations of lattice vibrations (phonon creation) are required (see figure 3.2).

The $Bethe - Bloch$ equation allows us to approximate the mean rate of energy loss [56] as:

$$-\frac{dE}{dx} = Kz^2\frac{Z}{A}\frac{1}{\beta^2}\left[\frac{1}{2}ln\frac{2m_ec^2\beta^2\gamma^2T_{max}}{I^2} - \beta^2 - \frac{\delta(\beta\gamma)}{2}\right] \tag{3.2}$$

m_e is the electron mass which is equal to $0.511\ \ \mathrm{MeV}$. β and γ follow from the velocity of the particle: $\beta = v/c$ and $\gamma = 1/\sqrt{1-\beta^2}$. T_{max} is the maximum kinetic energy which can be imparted to a free electron in a single collision and depends on the mass and momentum of the incident particle. K is a constant defined as $K = 0.307\ \ \mathrm{MeV}g^{-1}cm^2$. I is the mean excitation energy of the atoms averaged over all electrons and has been estimated for various materials using experimental measurements of the energy loss [57].

[1] A hole is the lack of an electron. When an electron is excited into a higher state it leaves a hole in its old state.

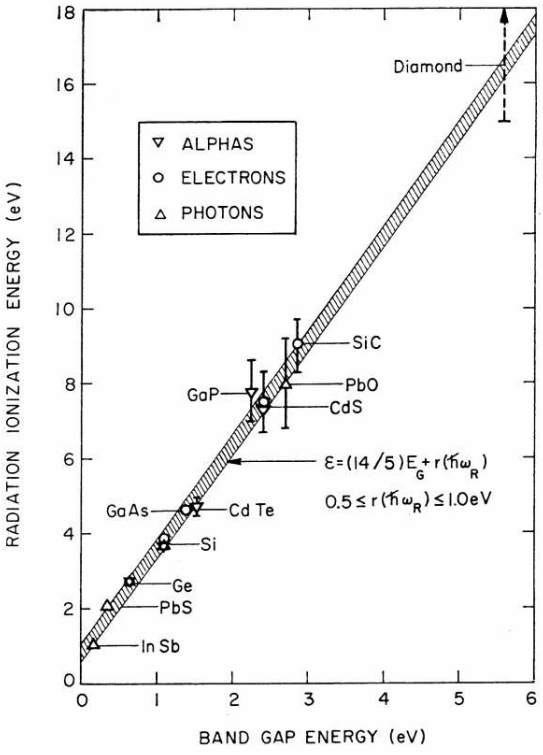

Figure 3.2: Ionization energy as a function of the band gap energy in different materials. Silicon has a band gap of 1.12 eV and an ionization energy of 3.6 eV. Picture taken from [55].

The term $\delta(\beta\gamma)$ is due to the so-called 'density effect' [56], which decreases the average energy loss for highly relativistic particles in dense media. The value of the constants in equation 3.2 for silicon can be seen in table 3.1.

Property	Value
Atomic number, Z	14
Atomic weight, A	28.09 $g \cdot mol^{-1}$
Density, ρ	2.33 g/cm^3
Mean excitation energy, I	174 eV

Table 3.1: Relevant properties of silicon at room temperature.

The $Bethe - Bloch$ distribution can be seen in figure 3.3.

Particles with a value of $\beta\gamma$ that corresponds to the minimum of the Bethe-Bloch equation ($\beta\gamma \sim 3$), are called *Minimum Ionizing Particles* (MIPs).

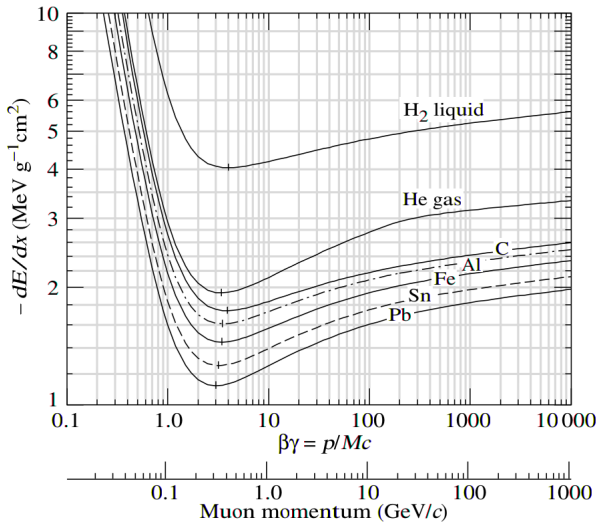

Figure 3.3: Bethe-Bloch distribution for different elements. The minimum of the Bethe-Bloch function correspond to values of $\beta\gamma \sim 3$.

The Bethe-Bloch equation predicts an average energy loss of $388\ \ \mathrm{eV}/\mu m$ for a MIP passing through silicon, resulting in 108 $e-h/\mu m$. This means about 32400 pairs for a typical silicon sensor with a 300 μm thickness. The real case is that the nature of the energy losses is stochastic. Therefore, the Bethe-Bloch formula is essentially useless in describing the behavior of a single particle. It predicts the average value of the energy loss distribution. Since the single collision spectrum is highly skewed, the probability distribution function (pdf) describing the 'straggling' is also highly skewed. The pdf describing the distribution of energy loss in thin absorbers is usually a *Landau* distribution [58]. A Landau distribution has a large tail and peaks well below the value of the average energy loss. For this reason, the most probably energy loss is a more meaningful variable than the average energy loss. Due to the Landau fluctuations the most probable signal is about 23000 pairs (0.7×32400) in a 300 μm silicon sensor.

The thermal excitation of an electron from the valence band to the conduction band creates free charge carriers in both bands (electrons in the conduction band and holes in the valence band). The concentration of electrons in the conduction band and the holes in the valence band are given by:

$$n = N_C exp\left(-\frac{E_C - E_F}{\kappa_B T}\right) \quad (3.3) \qquad p = N_V exp\left(-\frac{E_V - E_F}{\kappa_B T}\right) \quad (3.4)$$

where κ_B is the Boltzmann constant and T is the absolute temperature with $\kappa_B\, T$ (300 K) ~ 0.026 eV. E_F is the Fermi energy and typically corresponds to a point close to the halfpoint of the band gap for intrinsic silicon. It represents the energy level which is occupied with a probability of exactly 0.5.

E_C and E_V are the energy at the bottom of the conduction band and at the top of the valence band, respectively. N_C and N_V are the effective density of states in the conduction and valence bands, respectively, and are given by:

$$N_V = 2\left(\frac{m_h^* \kappa_B T}{2\pi\hbar^2}\right)^{\frac{3}{2}} \qquad (3.5) \qquad N_C = 2\left(\frac{m_e^* \kappa_B T}{2\pi\hbar^2}\right)^{\frac{3}{2}} \qquad (3.6)$$

where m_h^* and m_e^* are the effective mass of the hole/electron in the valence/conduction band[1].

In an intrinsic semiconductor, the concentration of holes is equal to the concentration of free electrons and is called the intrinsic carrier density:

$$n = p = n_i = \sqrt{N_C N_V} exp\left(-\frac{E_G}{2\kappa_B T}\right) \propto T^{3/2} exp\left(-\frac{E_G}{2\kappa_B T}\right) \qquad (3.8)$$

where $E_G = E_C - E_V$ denotes the gap energy also defined in equation 3.1. The only assumption made is that the distance of the Fermi level from the edge of both bands is large in comparison with $\kappa_B T$. These results hold for impurity ionization as well. Multiplying the two distributions results in:

$$np = n_i^2 = N_C N_V exp\left(-\frac{E_G}{\kappa_B T}\right) \qquad (3.9)$$

This property is referred to as the *mass action law* and it is valid for intrinsic or doped material in thermal equilibrium.

3.1.2 Impurities in the material. Doped silicon.

From equation 3.9 the intrinsic concentration of carriers in silicon is $1.45 \times 10^{10}\ cm^{-3}$ at $300\ K$ [59]. Taking into account the density of the material (see table 3.1), this implies that one out of 10^{12} atoms is ionised. To increase the concentration of carriers,

[1] The effective mass takes into account the particle mass and also the effect of the internal forces and is related to the dispersion relation of the energy *E* with the crystal momentum *k*, that is, to the band structure itself. For a 1-D crystal it can be defined as:

$$m^{*-1} = \frac{1}{\hbar^2}\nabla_k \nabla_k E \qquad (3.7)$$

silicon can be doped with impurity atoms. Pure silicon consists of a silicon lattice where the four valence electrons of each atom create bonds with neighboring atoms. The atoms used as impurities in silicon can be of different types depending on the desired effect.

The atoms with three electrons in the valence band, such as Boron (B) will be *aceptors*. Aceptors create electron deficiencies when replace silicon atoms in the lattice. The resulting holes are easily filled by thermally excited electrons coming from silicon atoms. The acceptor atoms create energy levels near to the bottom of the band gap which corresponds to the unoccupied states of the hole left by the acceptor atoms. As the energy gap of the valence band to the new states is rather small, at room temperature they will be occupied and hence the impurity atoms are negatively ionised and holes are created in the silicon. The concentration of free carriers is equal to the concentration N_a of impurities since $N_a \gg n_i$. A crystal doped with acceptors is denoted as *p-type*, and the conduction is mainly due to holes, its majority carriers.

On the other side atoms with five electrons, such as Phosporous (P) are called *donors*. Four of them form covalent bonds with silicon atoms and the fifth one is only weakly bounded so that thermal energy is enough to bring it into the conduction band. From the band point of view, the donor atoms create energy levels near to the top of the band gap which corresponds to the states of the fifth electron apported by the donor atoms. As the energy gap of the new states with respect to the conduction band is rather small, at room temperature, all the donors are positively ionised thus, the concentration of free carriers is equal to the concentration N_d of impurities since $N_d \gg n_i$. A silicon crystal doped with donors is called *n-type* because of the excess of free negative charge carriers. In this case, the conductivity in the crystal is determined by the flow of these electrons. They are the majority carriers while the holes are denoted minority carriers.

The two kinds of doped silicon are ilustrated in figure 3.4.

3.1.3 Carrier Transport.

The electron-hole pairs created by ionization in a semiconductor are constantly undergoing random thermally motion with a thermal velocity of the order $10^6\ cm/s$ [54]. They generate a current when they move under the influence of an externally applied electric field, *E*.

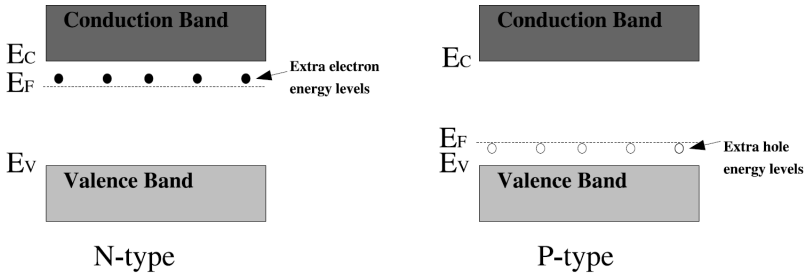

Figure 3.4: The extra levels in the band model created by the impurity atoms are shown for *n-type* and *p-type* silicon. In *n-type* material there are electron energy levels near the top of the band gap so that they can be easily excited into the conduction band. In *p-type* material, extra holes energy levels in the bandgap allow excitation of valence band electrons, leaving mobile holes in the valence band.

The charge carriers will travel at an average drift velocity given by,

$$v_{drift,e} = -\mu_e E \tag{3.10}$$

$$v_{drift,h} = \mu_h E \tag{3.11}$$

where μ_e and μ_h are the mobilities of electrons in the conduction band and holes in the valence band respectively. The electron and hole mobilities are different. The electron mobility in silicon is about 3 times the hole mobility at $300\ K$ as can be seen in table 3.2.

	$\mu_e(cm^{-2}V^{-1}s^{-1})$	$\mu_h(cm^{-2}V^{-1}s^{-1})$
Silicon	1350	480
Germanium	3900	1900

Table 3.2: Mobilities for electrons and holes at $300\ K$ for silicon and germanium materials.

The hole speed is smaller since the holes can be occupied by both free electrons and atomic electrons. Its effect is that the effective mass of holes in silicon is higher than the one of electrons [54] and the mobility is related to the charge carriers effective mass by means of equation 3.12.

$$\mu_{e,h} = e\tau_{e,h}/m^*_{e,h} \tag{3.12}$$

where $m^*_{e,h}$ is the effective mass of the electron or hole and $\tau_{e,h}$ refers to the average time taken between two collisions of the free moving carriers.

As explained before, due to the motion of electrons and holes in silicon, a current is created in presence of an electrical field. The drifft current density, J_{drift}, is given by:

$$J_{drift} = \rho v_{drift} = \rho \mu E \tag{3.13}$$

where ρ is the charge density and is given by $\rho = qn$ for electrons and $\rho = qp$ for holes. The resistivity ρ is the proporcionality constant between the electric field E and the drift current density J_{drift} and it depends on the concentration of both free carriers (electrons and holes) and on their mobilities, μ_e and μ_h:

$$\rho = \frac{E}{J_{drift}} = \frac{1}{q(\mu_e n + \mu_h p)} = \frac{1}{\sigma} \tag{3.14}$$

The conductivity, σ, is also defined in the above equation.
For intrinsic silicon, one obtains $\rho \simeq 235\ k\Omega cm$. The charge neutrality condition governs the number of carriers:

$$n + N_a^- = p + N_d^+ \tag{3.15}$$

When the net impurity concetration $\mid N_d - N_a \mid$ is much larger than the intrinsic carrier concentration n_i, then $n = N_d - N_a$ in the conduction band and $p = N_a - N_d$ in the valence band. So, for p-type silicon,

$$\rho \simeq \frac{1}{q\mu_h N_a} \tag{3.16}$$

and analogously for n-type silicon,

$$\rho \simeq \frac{1}{q\mu_e N_d} \tag{3.17}$$

Both types of silicon are used as bulk material for different detectors. However, for very high radiation environment (as expected at *HL-LHC*) the p-type is preferred and the reasons will be explained in section 3.2.1.

3.1.4 The reverse biased p-n junction.

A semiconductor detector is based, essentially, in a p-n junction which is formed by placing together n-type and p-type silicon. The p and n regions are electrically neutral by themselves, but, when they are part of a p-n junction, electrons from the n-type diffuse to the p-type to fill the holes and vice versa. As explained in the above section the movement of holes and electrons creates a current in presence of an electrical field but also a current is created by the effect of density gradients. The carrier transport is therefore due to two main mechanisms: diffusion and drift.

- **Diffusion current, J_{diff}:** Due to the density gradients, the electrons of the n-side start to diffuse towards th p-side and recombine with the holes. The holes in the p-side diffuse into the other direction and recombine with the electrons in the n-side. It results in a diffusion current:

$$J_{diff} = q(D_n \nabla n - D_p \nabla p) \tag{3.18}$$

  with ∇n and ∇p the charge carrier gradients across the junction and D_n and D_p the diffusion coefficients for electrons and holes respectively given by the Einstein relations [60]:

$$D_{n,p} = \frac{k_B T}{q} \mu_{e,h} \tag{3.19}$$

- **Drift current, J_{drift}:** The diffusion of the electrons (holes) leads to fixed positive charged (negative) ions in the n-type (p-type) silicon. Due to these space charge regions an electric field will be developed from the n-side towards the p-side. The electric potential can form a barrier for further diffusion and it will cause carrier drift in the opposite direction to diffusion. The drift current as explained above is given by:

$$J_{drift} = q(\mu_e n + \mu_h p)E \tag{3.20}$$

The device will reach a state of equilibrium when the net current flow is zero,

$$J_{diff} + J_{drift} = 0 \tag{3.21}$$

The absorption of charge carriers in the originally neutral material leads to a build-up of charge, which creates a potential difference, V_{bi}. This is called the built-in potential and is of the order of a few hundred of milivolts. The height of this barrier potential depends on the purity of the material and can be calculated as:

$$V_{bi} = \frac{kT}{q} ln \frac{N_a N_d}{n_i^2} \tag{3.22}$$

Due to doping, the Fermi level will move towards the valence band for p-type material and towards the conduction band for n-type material. The diffusion of holes and electrons leads to an area free of mobile carriers, named the '*depletion region*'. This region has much lower carrier concentration than the bulk material. Figure 3.5 shows the characterisctics of the pn-junction.

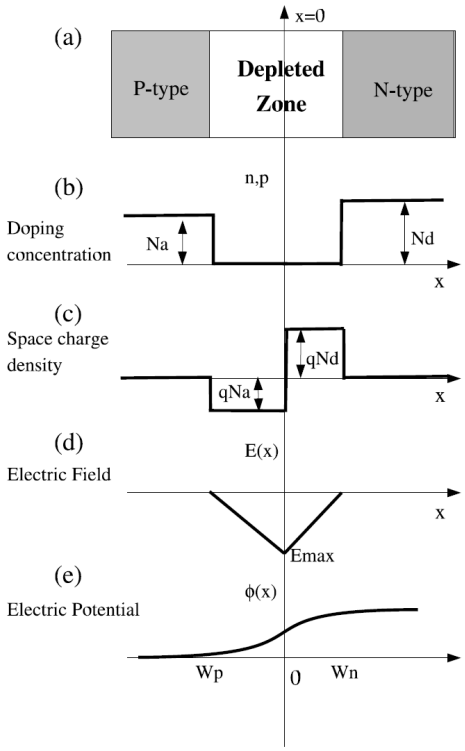

Figure 3.5: Interface region of a pn-junction, each subdiagram shows a variable as a function of distance with $x = 0$ just in the junction. (a) P-type and n-type silicon. (b) Free charge carriers concentration with N_a holes in the p-type side and N_d electrons in the n-type one; note the depletion of carriers in the depletion region. (c) Fixed space charge density. (d) Electric field, E. (e) Electric potential, ϕ.

Incident radiation trough the diode will release free carriers (electron/hole pairs) in the depleted region and they will be accelerated under the built-in electric field. They will move in opposite directions producing a measurable signal. However, the built-in potential is not high enough to generate a large electric field to make the charge carriers move rapidly. Consequently, charges can be readily lost as a result of trapping and recombination, and incomplete charge collection often results. To deal with this effect, an external potential difference will be applied to the junction in order to increase the magnitude of the electric field and enlarge the dimension of the depletion region (see figure 3.6). A wider depletion zone means a wider sensitive volume and this has a clear benefit: a higher pair production leading to a more efficient charge collection.

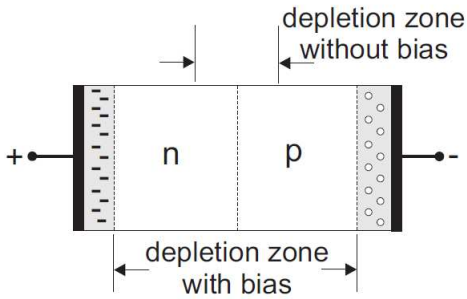

Figure 3.6: Applying an external potential to the pn junction the electron-hole pairs created by passing an ionizing particle through the material are moved rapidly and the dimension of the depletion region is therefore enlarged.

This is the operation principle for radiation detectors in which the free space charge region has to be extended over the full sensitive area to increase the collected signal.

If a negative potential is applied to the p-side (or a positive potential to the n-side), the barrier for electrons moving from n- to p-side is increased and the diffusion current in this direction decreases exponentially resulting in a very small current. In this case the diode will be operating in the reverse bias region as can be seen in figure 3.7 where J is the total current density through the junction of an ideal diode that can be described by the *Shockley* equation [54]:

$$J = J_0(e^{\frac{qV}{k_B T}} - 1) \tag{3.23}$$

The current in reverse bias direction is saturated at saturation current density J_0 given by:

$$J_0 = \frac{qD_p p_{n0}}{L_p} + \frac{qD_n n_{p0}}{L_n} \tag{3.24}$$

where D_p and D_n are the diffusion coefficients for electrons and holes, p_{n0} and n_{p0} are the hole density in the n-side and the electron density in the p-side at thermal equilibrium, and $L_p = \sqrt{D_p \tau_p}$ and $L_n = \sqrt{D_n \tau_n}$ are the diffusion lengths of holes and electrons.

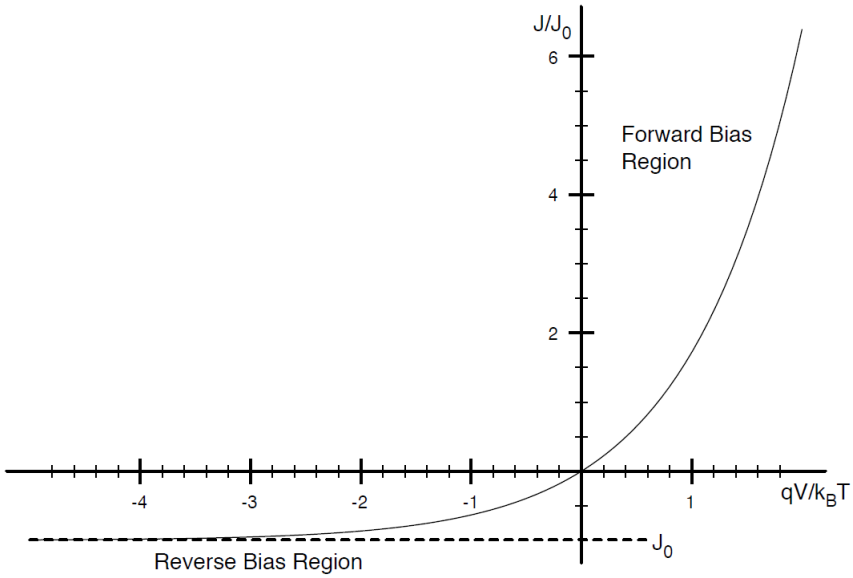

Figure 3.7: Ideal current-voltage characteristics of a pn-junction. The forward and the reverse bias regions can be distinguised. In the case of silicon tracker detectors the sensors operate in the reverse bias region where the total current density is very low.

The width of the depletion zone results in

$$W = W_n + W_p = \sqrt{\frac{2\varepsilon_{Si}}{q \mid N_{eff} \mid}(V_{bi} + V)} \tag{3.25}$$

where W_n and W_p are the width on the n- and p-side respectively. $N_{eff} = N_d - N_a$ is the effective doping concentration. By choosing different doping concentrations on both sides of the junction, the extent of the depletion zone can be controlled. The more highly-doped is one side, the more extent is the depletion zone on the lightly-doped

side. Typically $V \gg V_{bi}$, hence V_{bi} is commonly neglected.
In terms of the silicon resistivity, using equations 3.16 and 3.17, the width of the depleted region can be writen as:

$$W = \sqrt{2\varepsilon_{Si}\rho\mu V} \tag{3.26}$$

where μ indicates the majority carrier mobility.
The depletion region can be increased to the total width of the detector d. The applied voltage required for this purpose is called the *depletion voltage* (V_{fd}) and can be calculated from equation 3.25 resulting in

$$V_{fd} \approx \frac{q}{2\varepsilon_{Si}} \mid N_{eff} \mid d^2 \tag{3.27}$$

According to equation 3.26 the higher the resistivity of the material, the lower bias voltage is necessary to fully deplete a given thickness. In the standard electronics industry the different values of silicon resistivity vary between 0.001 Ωcm and 200 Ωcm. In the case of microstrip sensors for tracking systems a ultra-high resistivity ($>$ 1kΩcm) is needed in order to fully deplete the detector bulk (thickness of about 200-300 μm) by an adequate voltage (around 300 V). Together with the demand for a reasonable price and a homogeneous resistivity distribution *Float Zone* silicon is the best choice of material [61].

A reverse biased pn-junction consists of an insulating layer between 2 conducting regions, therefore it acts as a capacitor. As seen above, an increase of the bias voltage dV enlarges the depletion region, and therefore the active area of the sensor (A) resulting in a charge increment dQ on either sides. A junction capacitance can then be defined as $C = dQ/dV$ and for $W \leq d$ is given by:

$$C = A\sqrt{\frac{\varepsilon_{Si} q \mid N_{eff} \mid}{2V}} \tag{3.28}$$

The capacitance decreases proportionally to $\sqrt{V_{bias}}$ until the depletion region extends to the full width of the junction. For bias voltages higher than V_{fd}, the capacitance saturates and corresponds to the geometrical capacitance being:

$$C_{geom} = \frac{\varepsilon_{Si} A}{d} \tag{3.29}$$

When a silicon detector operates under reverse bias conditions, the resulting current is called the *leakage current*. Ideally, the reverse bias applied for enlarging

the depletion region removes all mobile carriers from the junction volume and no current can flow, however this does not happen in a real device. The current that flows through a pn-junction has several components. The two main contributions are the generation current and the diffusion current through the barrier (*reverse* current). The generation current arises from electron-hole pair generation in the space charge region of the device. This generation is due to thermal excitation of electrons from the valence band to the conduction band. Thermally generated electron-hole pairs in the undepleted region of the device do not contribute to the current as in the lack of electric field they simply recombine.

Although electrons and holes move in opposite directions, their contribution to the signal current is of the same polarity since they have opposite charge. The total induced charge, that is the signal charge, Q, will be therefore the sum of the induced currents by the moving electrons and holes:

$$Q = \int_0^{t_c(e)} i(t)dt + \int_0^{t_c(h)} i(t)dt \tag{3.30}$$

where $t_c(e)$ and $t_c(h)$ are respectively the collection times for electrons and holes. The collection time[1] is the time required for a charge carrier to traverse the sensitive volume [54]. Integration times in the electronics larger than the collection time of all charge carriers yield the full charge. In *ATLAS* the integration time (25 ns) is near the electron collection times. A shorter integration time yields a fractional charge. Due to their different mobility values, the collection of electrons is much faster than that of holes (roughly a factor $\sim$3). Despite we have also holes current contribution, for short integration times, as in the case of *ATLAS*, the signal current corresponds basically to the electron current. If charge is generated in the neutral silicon but in the proximity of the depletion region, diffusion of electrons and holes occurs due to the existing large doping gradient. Under normal conditions, silicon detectors operated under reverse bias are fully depleted, and the generation current J_g dominates. It is given by [54]

$$J_g = \frac{qn_iW}{2\tau_g} \propto \sqrt{V} \tag{3.32}$$

[1] The collection time is given by [62]:

$$t_c = \frac{d^2}{2\mu V_{dep}} ln\left(\frac{V_{bias}+V_{dep}}{V_{bias}-V_{dep}+2V_{dep}(1-x/d)}\right) \tag{3.31}$$

where V_{dep} is the depletion voltage, V_{bias} is the bias voltage, d is the detector thickness, and x is the distance where the carrier was created with respect to the readout side.

where τ_g is the carrier generation time in the space charge region. Equation 3.25 shows that the generation current is also proportional to the square root of the applied bias. The generated charge carriers are to be considered as a noise source for semiconductor sensors. The temperature dependence is given via the intrinsic carrier concentration n_i (see equation 3.9). Therefore, the generation current has a temperature dependence given by

$$J_g(T) \propto \frac{n_i}{\tau_g} \propto T^2 exp\left(-\frac{E_g}{2\kappa_B T}\right) \tag{3.33}$$

The leakage current measured may be corrected to a reference temperature using the following correction:

$$I(T) = \left(\frac{T}{T_{ref}}\right)^2 exp\left(-\frac{E_g}{2\kappa_B}\left[\frac{1}{T} - \frac{1}{T_{ref}}\right]\right) I(T_{ref}) \tag{3.34}$$

The total leakage current can then be reduced by decreasing the temperature of operation of the detector by means of a cooling circuit.

Besides the diffusion and the generation currents there are other contributions such as the currents through the surface and the edges of the detector. These currents can be eliminated by using an implant surrounding the junction region, known as the *guard ring* structure that will be explained later. The currents then flow through the guard ring rather than the sensor reducing the sensor leakage current to a negligible level. Therefore, the leakage current can be controlled to a certain extent by proper design and careful manufacturing process.

The electric field in the depletion region increases as the reverse bias voltage is raised. If the reverse bias is increased to very high values, the charge carriers are accelerated high enough to ionize atoms of the crystal lattice. The new electron-hole pairs created also gain kinetic energy and participate in the release of more carriers. An avalanche breakdown occurs and as a result a dramatic increase of the current. This avalanching process can lead to an electrical breakdown at the junction which is the region of the maximum electric field. The voltage at which the electrical breakdown occurs is called the *breakdown voltage*, V_{bd} and is given by [63]:

$$V_{bd} = \frac{\varepsilon E_{max}^2}{2qN_D} \tag{3.35}$$

where we assume, for instance, a n-type sensor where $N_A >> N_D$ and with E_{max} the maximum electric field before breakdown.

3.2 Silicon Detectors Technology

The radiation exposure has negative effects on the electrical performance of the silicon detectors:

- The leakage current and detector noise will increase due to the creation of new energy levels.
- Due to trapping effects, the colection times will increase and therefore the charge collection efficiency will decrease (for small and fixed integration times).
- The efective doping concentration will change requiring a much higher voltage to fully deplete the silicon.

All these effects, that will be explained at section 3.3, must be taken into account during the sensor's design and development. We must ensure that the silicon sensors are going to be able to maintain their good performance after radiation exposure.

3.2.1 Sensor types

As explained in the previous section, a silicon detector consists basically on an asymmetric pn structure. This structure would have a large doping concentration on one side of the juntion, for instance a heavily doped n-type material (n^+). The other side will be lightly doped, for example, a p-type region (p^-, shortened simply to p). In this case the depth of the depleted region on the n^+-side is small compared to the depth on the weakly doped p-side. The electric field always grows from the n^+ implant. Increasing the reverse bias the electric field can be extended far into the p bulk. Hence the $+$ implant may be made only microns wide and the depletion region in the p bulk silicon can be a few hundred microns wide.
High Energy Physics (HEP) experiments require high segmentation in the tracking systems for accurate position and momentum measurements. This is the reason for using *silicon microstrip detectors* in this kind of experiments. The segmentation of the sensor is achieved by dividing the diode into small parallel regions called $strips$. Each *strip-bulk* junction acts as an individual silicon detector. A schematic cross-section of such type of detectors is shown in figure 3.8.

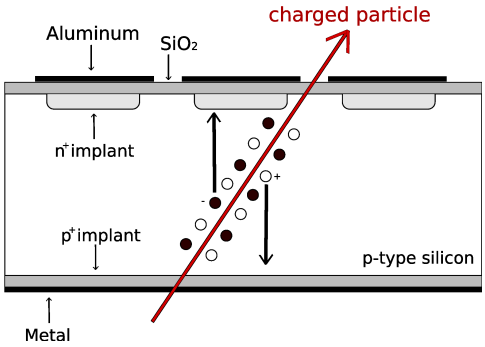

Figure 3.8: Schematic view of a silicon microstrip detector. The bulk is p-type silicon and the electrodes are n^+ implants. Holes drift towards the p^+ back-plane, while electrons towards the n^+ implants. An insulator (SiO_2) is used to protect the silicon of the wafer. The strips are connected to the readout electronics through an aluminum layer. With this configuration electrons are registered by the readout.

Depending on the type of the implants and the silicon bulk, the microstrip sensors can constitute different structures:

- *p-on-n*

  The silicon bulk in $p-on-n$ sensors is n-type with p^+ strip implants on the sensor surface. The back implant is n^+ so the abrupt junctions are between the strips and the bulk silicon. An oxide layer (SiO_2) is used as passivation layer to protect the silicon bulk. The connection of the implants to the readout electronics can be made following two configurations: a direct connection between the aluminium traces and the implants (DC) or distributing a second SiO_2 layer on top of the implants (AC). In the DC case, the leakage current flows directly into the readout electronics. On the other hand, with an AC configuration the implants and the aluminium strips are separated by the oxide layer. This layer acts as a capacitor, therefore, a polysilicon resistor is needed to provide a voltage reference to the strips. Figure 3.9 shows two $p-on-n$ sensor sketches with both configurations.

  In these devices the depletion region grows from the strips to the backplane allowing the sensor to operate partially depleted. The readout electrodes will collect holes. Under radiation exposure, due to the lower mobility of holes, the trapping effects will be more probable and for the short collection times at *HL-LHC* the charge collection efficiency will be negatively affected.

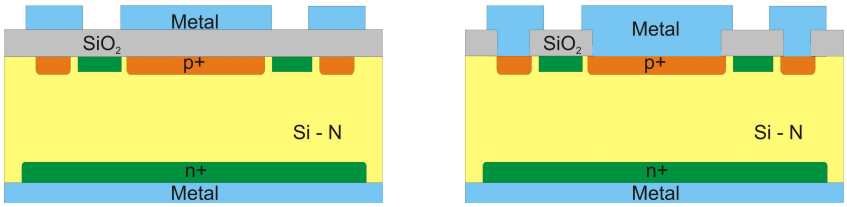

Figure 3.9: Drawings of two p-on-n silicon microstrip sensors. The bulk sensor is n-type while the strip implants are p^+ doped silicon. The AC configuration uses a SiO_2 layer as a capacitor between the aluminium traces and the implants (left) while the DC uses a direct connection between them (right).

They will also suffer from *type inversion* with the change of the effective doping concentration due to radiation damage. With radiation exposure the n material becomes less n-type and can be turn to p-type. Therefore, the junction will dissapear from the strips and the bulk and will migrate to the sensor backplane. These effects will be explained in detail in section 3.3.

- n-*on*-n

  These sensors have n-type doped silicon bulk and n^+ implants. The p-n juction is created at the backplane with a p^+ implant. In this case, the depletion region grows from the backplane to the front n^+ implants so the device must be fully depleted to achieve good charge collection efficiencies. Nevertheless, the electron collection by the n^+ implants provides higher signal collection efficiency under trapping effects than in p-on-n sensors. Radiation damage will also cause *type inversion* on these devices (see section 3.3), however this results in the bulk silicon becoming lightly p-doped and turning the sensor to n-on-p. They will be able to operate partly depleted.

  These sensors need isolation structures that will be explained after. This will be needed in both sides of the sensor and the fabrication requires aligned double sided processing (for the inclusion of guard ring structures near the junction before irradiation) which increases the complexity and cost of such devices.

  Figure 3.10 shows a drawing of an n-on-n sensor where its components can be distinguised.

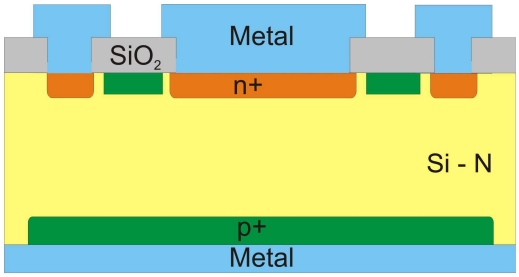

Figure 3.10: Sketch of an n-on-n silicon microstrip sensor. The bulk sensor is n-type while the strip implants are n^+ doped silicon. The pn junction is created at the backplane with a p^+ implant.

- *n-on-p*

  In this kind of sensor the detector bulk is p-type and the strip implants are n^+ placed above the p-type silicon surface. The n^+ strips readout electrodes will collect electrons that will suffer less charge trapping than holes allowing higher signal integration in the short collection times at *HL-LHC*. This results in a higher charge collection efficiency [64].

  In p-type sensors the depletion region grows from the implants to the backplane. This allows the sensor to operate partially depleted since the p–n junction is always on the signal collecting side, making the sensor highly radiation-tolerant. Furthermore p-type sensors do not suffer from *type inversion* with irradiation since an increase in acceptors only increases the depletion voltage as explained in section 3.3.3.2.

  A sketch of the sensor components can be seen in figure 3.11. P-type sensors need isolation methods that will be explained below.

3.2.2 Isolation methods

The isolation methods are only needed in sensors with n-type implants. The irradiation of the detectors at high fluences has different negative effects on the sensors (these effects will be explained in detail in section 3.3). One of these effects is the creation of a layer of electrons or holes (depending on the sensor type) at the surface. This can cause high electric field regions in sensors that use n implants and lead to a breakdown of the sensor. To avoid this, different isolation methods can be used. In this kind of silicon sensors *p-stop* and *p-spray* methods are the most commonly used.

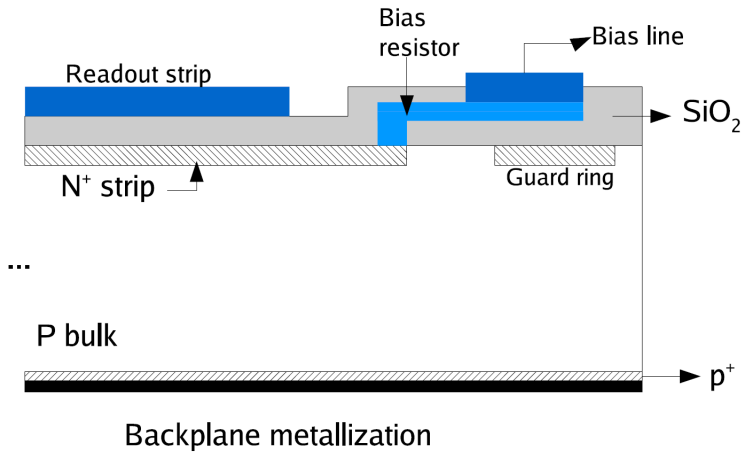

Figure 3.11: Schematic transversal view of a n^+p silicon sensor. The bulk is p-type silicon and the electrodes are n^+ implants. As in figure 3.8 SiO_2 is used to protect the silicon of the wafer and an aluminium layer is used to connect the strips to the readout electronics. With this configuration electrons are registered by the readout.

- ***P-stop* isolation:** This technique introduces a high dose of p^+ boron implant surrounding the strips [65]. Figure 3.12 shows an sketch of this method.

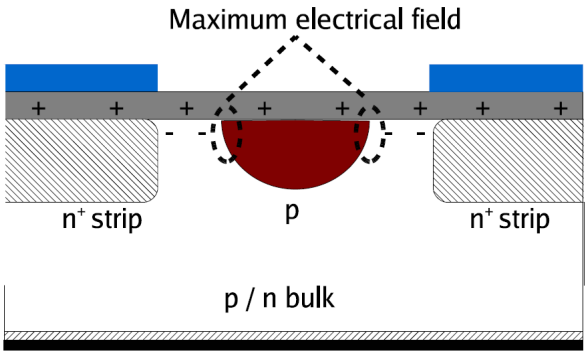

Figure 3.12: *P-stop* isolation technique for adjacent n^+ implants. The maximum field regions are located at the lateral pn-junctions. High dose of p^+ boron implant is used.

A typical dose of boron ions guarantee a good isolation (10^{14} boron ions/cm^2). The potential of the p-stop depends on the implant geometry, the backplane bias and the effective doping concentration of the substrate. The potential difference between n^+ strips and p-stops increases with the radiation fluence, leading to an increase in the electric field. Therefore, the breakdown voltage of sensors with p-stop isolation decreases with irradiation.

- ***P-spray* isolation:** This technique uses a low dose of p^+ boron implant that covers the whole surface [66]. The point of maximal electrical field is at the lateral pn-junction between the isolation boron implant and the n+ strips (as in the p-stop case). Figure 3.13 shows an sketch of this method.

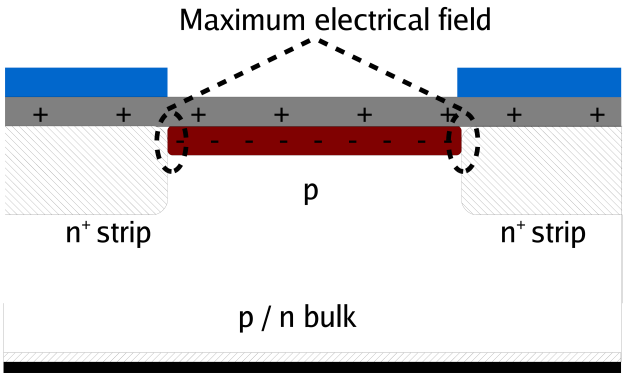

Figure 3.13: *P-spray* isolation technique for adjacent n^+ implants. The maximum field regions are located at the lateral pn-junctions. Low dose of p^+ boron implant is used.

  With the increase of the oxide charge to its saturation value the shallow *p-spray* layer moves into the depleted region and the electric field decreases. When the boron implant matches the saturation value of the oxide charge the lowest electric field is reached.

For *HL-LHC* strip sensors $n-on-p$ are selected as the best option considering different advantages above mentioned:

- Due to electrons collection in the readout electrodes less trapping of charge carriers are produced and the signal collection is higher for the short collection times at *HL-LHC*. This leads to a higher charge collection efficiency.

- The growth of the depletion region goes from the implants to the backplane allowing the detector to operate partially depleted. This is a benefit compared to the sensors that need full depletion to operate since with irradiation the full depletion voltage increases and can be higher than the breakdown voltage. The pn junction is always located between the implants and the silicon bulk and therefore there's no *type inversion*.

- $N-on-p$ sensors can be fabricated using a single-side lithography process, making them more cost-effective than $n-on-n$ sensors, which require a double-side process. For large strip detectors these costs have to be decreased significantly.

The microstrips which correspond to the implants on top of the silicon bulk surface are typically $10-20\ \mu m$ wide and $1-3\ \mu m$ deep (see figure 3.11). The bulk of the detector usually has a doping concentration of $10^{12}\ atoms/cm^3$. This should be compared to the intrinsic carrier concentration which is of the order of $10^{10}\ cm^{-3}$.

Each of the implanted strips is bonded to the front-end readout electronics, which amplifies the signal produced by ionizing radiation. In addition, other elements that can be also seen in figure 3.11 are necessary to form a proper silicon detector for the upgrade of ATLAS detector.

- An oxide layer (approximately $1-4\ \mu m$ thick) lies on top of the implanted strips, known as the AC oxide, which prevents the leakage current flowing directly to the readout electronics.

- The signal from each of the strips is AC coupled to a metal (aluminium) strip lying directly above the strip implants, and the charge is read out through this ohmic contact.

- A DC path is required between the back and front contacts to bias all the strips. This path is realized via a common bias line and placed on the strip side of the device. It is an implant running across all strips and connected to each strip via a polysilicon bias resistor and returned to the backplane. The DC path will carry the leakage current of the device, dominated by thermally generated carriers in the bulk.

- To maintain isolation between the implants p-stop technology is used.

- A low resistance ohmic contact to the back of the device is used to apply the high voltage to the sensor. It is obtained through a doped implant (of the same type of the bulk) with a layer of metal in direct contact covering the entire backside of the device. This doped implant is used to prevent the depletion region reaching the metallisation.

- In figure 3.11 one can also distinguish the guard ring structure which is independent of the type of sensor. This ring prevents the sensor from a possible electrical breakdown minimising the leakage current at the detector edges. Due to the complex mechanical cutting procedure of the sensor edges they will be conductive and at the backplane potential, which is the bias voltage. Due to the lateral extension of the depletion, when the space charge reaches the cutting edge the strong crystal damage which is present there acts as a very effective generation center and causes a dramatic increase of the leakage current. The purpose of the guard ring (or multiguard rings) is to stablish a smooth voltage drop toward the cutting edge and to assure that the outermost ring is on the backplane potential. No space charge region can then stablish outside the outermost ring.

Most of these features can be observed in the photograph of a n-on-p silicon microstrip detector which is represented in figure 3.14.

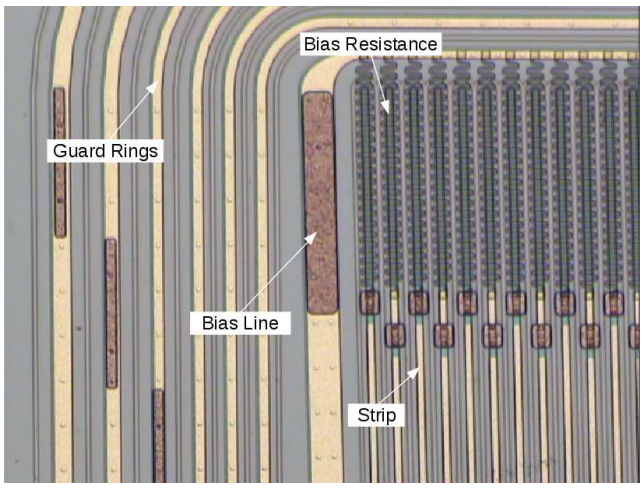

Figure 3.14: Microscope view of a silicon microstrip detector. There are pointed the strips, the bias resistance, the bias line and the guard rings.

3.2.3 Spatial resolution

The spatial resolution of microstrip detectors depends on different parameters:

- Statistical fluctuations of the energy loss and the diffusion of carriers: The drift movement of the charge carriers in the silicon sensor is, in average, along the electric field lines towards the electrodes. Due to the random multiple scattering with the material, the carriers can suffer from diffusion. This effect generates the

spread of the charge cloud mainly in the transversal direction to the drift path. The distribution of the charge carriers around the track may be described by a Gaussian function [67] and the standard deviation of the distribution is given by:

$$\sigma = \sqrt{2Dt} \tag{3.36}$$

with t the charge collection time. D is the diffusion coeficient (different for electrons and holes) described in equation 3.19 which is proportional to the mobility.

The drift time is inversely proportional to the mobility of the carriers, so that the standard deviation is equal for both carriers (see equation 3.12).

- External parameters such as geometrical factors and readout electronics noise: The strip pitch and the width of the electrodes can determine at first order the position resolution of a silicon detector. ATLAS uses binary readout (it is only distinguished if a particle hits a strip but not the deposited charge), the position resolution Δx would be:

$$(\Delta x)^2 = \frac{1}{p}\int_{-p/2}^{p/2} x^2 dx = \frac{p^2}{12} \tag{3.37}$$

According to the above equation, the resolution of the silicon sensor would correspond to its strip pitch divided by $\sqrt{12}$. For an ATLAS sensor with a strip pitch of $80\ \mu m$, the σ corresponds to $23\ \mu m$. Typical strip pitches are $20-200\ \mu m$, which results in resolutions of approximately $6-60\ \mu m$.

3.2.4 Sources of noise

Different noise sources can be identified for silicon detectors.

- Electrons are in constant motion colliding with each other and with the material. This motion represents a small current. The sum of all these currents taken over a long period of time is zero, but their random fluctuations over short intervals constitute a thermal noise. This thermal noise (also called *Johnson noise*) has a white spectral density, i.e. the noise power per bandwidth unit is constant. The thermal fluctuations are proportional to $\sqrt{\frac{4k_BT}{R_{bias}}}$. Hence, the sensor should have high values of the bias resistor.

- Fluctuations in the number of charge carriers occur in the current flow. There is a non-constant current due to these fluctuations. This is called *shot noise* (also know as *parallel noise*) and is measured as the variance of the fluctuations about the mean constant current. In this case, the noise is proportional to $\sqrt{2qI_{leakage}}$ and also has a white spectrum.

- The major contribution to the total noise probably comes from the read out electronics. The signal generated in silicon detectors is generally of small amplitude ($\sim$3.6 fC). The front-end electronics usually include a pre-amplifier and shaping stages. This process amplifies the signal as well as the noise that will affect the charge measurement. Therefore, the signal-to-noise ratio (SNR) gets degraded. Noise contributions can be determined from the analysis of the front-end circuit (figure 3.15). In this block diagram an AC detector is represented by a capacitance C_d, the bias voltage is supplied through a resistor R_b and the sensor is coupled to the preamplifier through a dc blocking capacitor C_c.

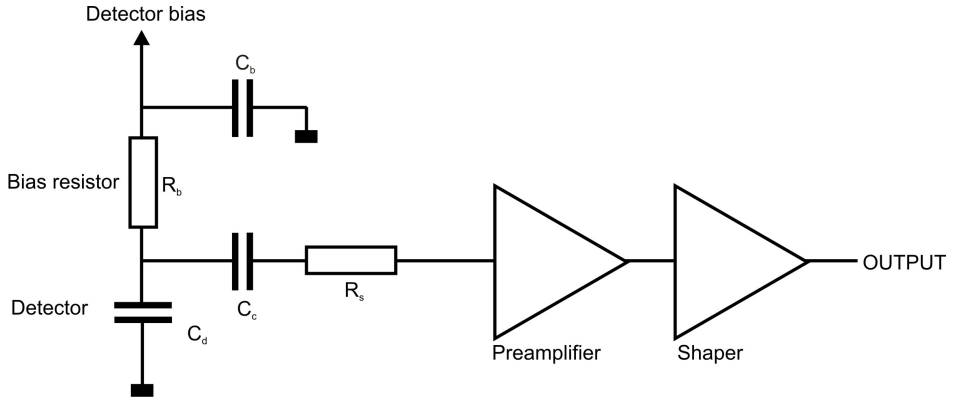

Figure 3.15: Block-diagram of a typical front-end circuit.

  The series resistance R_s is the sum of all resistances present in the input path (the electrode resistance, any protection networks and parasitic resistances in the preamplifier input transistor).

The electronic noise can be described in terms of either voltage or current noise sources. The thermal (i_{nb}) and shot noise (i_{nd}) of the detector are represented by current noise generators. On the other hand, the series resistor, R_s acts as a voltage generator (e_{ns}). The amplifier white noise is described by a combination of voltage (e_{na}) and current noise source (i_{na}) at its input.

The total noise is generally expressed in terms of the equivalent noise charge (ENC). It corresponds to a signal which would generate an output voltage of the same magnitude as the *root mean square* (*RMS*) of the noise distribution in the system (SNR = 1). The ENC is usually expressed in Coulombs or the corresponding number of electrons.

The total noise is given by the individual noise contributions added in quadrature, which can be expressed as [62]:

$$(ENC)^2 = a\left(2qI_{leakage} + \frac{4k_BT}{R_{bias}} + i_{na}^2\right)\tau_s + b\left(4k_BTR_s + e_{na}^2\right)\frac{C_d^2}{\tau_s} + c \qquad (3.38)$$

where a, b, and c depend on the shape of the pulse determined by the pulse shaper and τ_s is the shaping time. The voltage noise contributions increase with the capacitance. At short shaping times, the voltage noise dominates, whereas, the contribution of the current noise increases with the shaping time, i.e. with pulse duration. The total noise is minimum when the current and voltage noise sources are equal.

3.3 Radiation damage on Silicon Detectors

The silicon detectors employed in the ATLAS tracker system for the *HL-LHC* will have to deal with an extremely harsh radiation environment. To optimize their design in terms of radiation tolerance it is crucial to understand how radiation affects silicon detectors and electronics.

The radiation induced defects suppose microscopic damage to the silicon crystal structure. The consequences of these defects are shown through macroscopic effects. To ensure the proper operation of the experiment during its expected lifetime the radiation effects must be carefully evaluated.

The damage caused by radiation can be divided basically into bulk and surface damage.

3.3.1 Bulk Damage

The incident radiation causes the displacemet of the atoms from their lattice sites and deep levels in the band gap are formed as a consequence. The interaction of the radiation with the lattice may lead to permanent material changes. The silicon

atoms displaced from their original sites in the crystal structure are known as *Primary Knock-on Atoms* (PKA) and they produce the main defects in the silicon lattice. When a PKA obtain an excess momentum starts moving but it is slowed down by the neighbouring atoms. If the momentum transfer is enough, it may depart from its site over a distance of several lattice constants. To displace a silicon atom to an interstitial position an energy of 25 eV is required (on average) [68]. If this is the case, a *Frenkel pair* is created [69]. This pair corresponds to the displaced atom and the leaving vacancy at its original location.

With diffusion, a migration process of intersticials and vacancies starts, in which most of them recombine. However, some stable divacancies can be formed. They are a complex formation of two neighbouring vacancies [70]. Higher complex formations can also be built while the rest diffuses away. Those can react with other radiation induced defects, forming defect complexes, or react with impurity atoms such as carbon, oxygen and phosphorus (most common impurities in silicon bulk).

A representation of these interactions can be seen in figure 3.16.

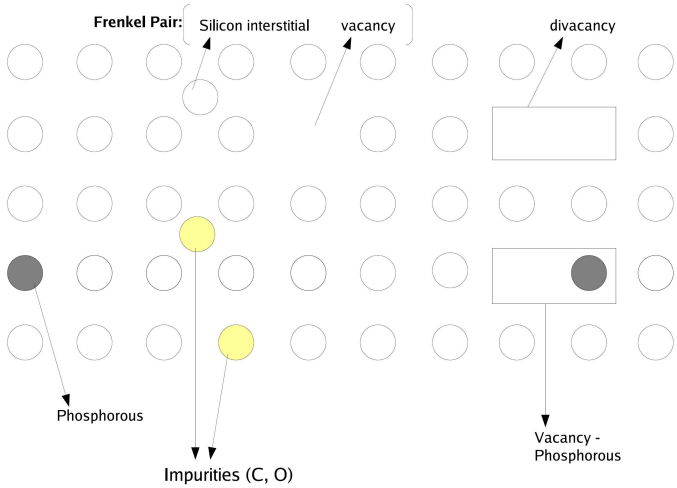

Figure 3.16: Schematic diagram of some defects in a silicon crystal lattice.

The complex formations of interstitials and vacancies defects can establish energy levels in the band gap which constitute traps. These traps are spatially well localised inside the semiconductor lattice and are also called “points defects”.

In the case of heavy incident particles, like neutrons or protons, a multiplicity of secondary displacements can occur due to the transference of high energy to the PKA. Isolated interstitial atoms and vacancies are then formed along the PKA

trajectory. During the collisions the kinetic energy of the individual atoms decreases so the distance between these collisions also decrease. This leads to the formation of clusters of point defects which are random and irregular. Due to thermal motion, point defects and clusters can interact during and after irradiation. The strongly temperature-dependence of the defects mobility will also cause a complex annealing behaviour. In addition, the defects may be electrically active and hence change the electric properties of the material.

Although for charged particles the main mechanism of energy loss is ionization, high energetic hadrons can also suffer scattering collisions with the silicon atoms of the lattice. In this case, the non-ionizing energy loss ($NIEL$) is at the origin of the damage for bulk silicon sensors. This quantity summarizes all energy deposited in the crystal which has not been used for the fully reversible process of ionization. It allows to compare the damage caused by the different types of particles with different energies. The displacement damage is proportional to the incident energy of the incoming particle ($NIEL$ hypothesis). It must be defined for a specific particle type and energy. It is typically given as the equivalent of 1 MeVneutron (set as a standard for normalisation). It is observed experimentally that the $NIEL$ scaling hypothesis does not provide a perfect theory to fit all measured data. The damage may also depend on the specific modes of energy transfer between the radiation and the silicon lattice, which are not included in the $NIEL$ scaling hypothesis [71]. Nevertheless, it manages to successfully account for most of the particle and energy dependences of the observed damage in silicon and it is widely used.

3.3.2 Surface Damage

Surface damage is primarily introduced by ionisation of the isolating silicon dioxide (SiO_2) layer by traversing particles. Electron-hole pairs generated by ionisation in the silicon bulk are generally collected by the read out electrodes and the backplane. Carriers in the oxide layers however can not necessarily escape the region and can be accumulated in the interface between the SiO_2 and the silicon bulk. Due to the higher mobility of the electrons they are swept out from the oxide faster than holes which are eventully captured at the oxide-silicon interface. This leads to a positive charge buildup in the oxide. This charge induces the creation of an electron layer placed at the silicon side of the interface and called the electron inversion layer. The electrical behaviour in this region will be affected by the presence of the electron

inversion layer. In a detector with n-type readout electrodes, the electron layer will short the n-type strips together and a not desirable signal sharing will be possible between them. The devices will need isolation between strips to avoid this signal sharing. The strip isolation techniques have been explained in section 3.2.2. In a detector with p-type read out electrodes, a higher field region will be created between the implants and the electron layer.

These two effects can have great influence on the properties of segmented silicon sensors by increasing the depletion voltage and leakage current. The effective doping concentration, interstrip resistance and capacitance can be also degraded.

3.3.3 Effect of Radiation Damage on Sensor Properties

The defects induced by radiation alters the silicon lattice symmetry. This leads to the appearance of new energy levels in the forbidden gap that may act as generation and recombination centers. Depending on the relative concentration of carriers and empty defect states generation or recombination will dominate. In the case of the reverse biased junction, the conduction band of the depletion region is underpopulated and generation prevails.

Defects affect three important aspects on the dectector properties such as:

- **Leakage current:** States close to the centre of the band gap tend to generate leakage current. Lattice defects are able to capture and emit electrons and holes in the depleted region leading to an increase in the leakage current and detector noise. As a consequence the signal to noise ratio will decrease and the power consumption will increase.

- **Charge collection efficiency:** Energy states between band gap centre and either band gap edge can generate both current and space charge, as well as trap charges. When signal charge is trapped in the depletion zone it may be released too late causing a signal loss. Therefore, a decreasing of the charge collection efficiency occurs.

- **Effective dopant concentration:** Radiation damage in the silicon changes the values of the doping concentrations. This leads to a change in the effective dopant concentration, N_{eff} requiring a much higher voltage to fully deplete the silicon.

Furthermore, annealing effects also have an influence on macroscopic sensor properties.

3.3.3.1 Leakage Current

The creation of traps with deep energy levels close to the middle of the forbidden band causes the arise of the generation current. This leads to an increase in the leakage current of the detector. The valence and conduction bands with a deep defect can be seen in figure 3.17.

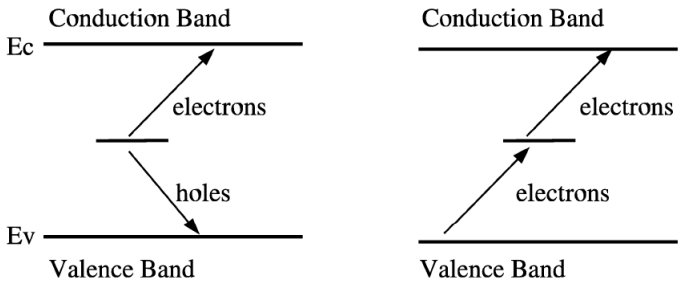

Figure 3.17: Deep defect levels acting as generation centres. On the left the defect level generates a electron-hole pair. On the right the electron in the valence band is promoted to the conduction band by a deep level.

The leakage current generated in the bulk volume greatly increases linearly with the equivalent fluence received by the silicon detector and can be parametrised [61] by:

$$\Delta I_{vol} = \alpha\Phi \tag{3.39}$$

ΔI_{vol} corresponds to the increase in leakage current measured after irradiation of the sensor with the equivalent fluence Φ. The constant α is the current related damage rate. It depends on the intrinsic charge carrier concentration and therefore on the temperature at which the measurement was performed. However, it has been measured [72] that α is independent of the detector fabrication process, the initial silicon resistivity and the concentration of other dopants (like oxygen or carbon).

In figure 3.18 the linear increase of the current with the equivalent fluence is shown.

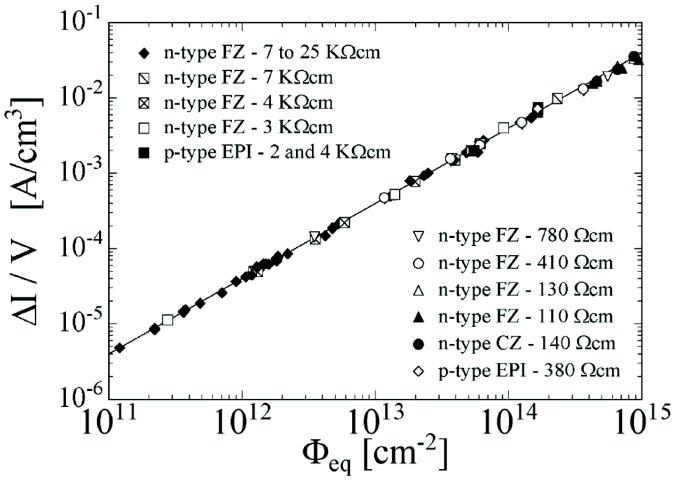

Figure 3.18: Scaling of the leakage current with the equivalent fluence. The leakage current presents a linear dependence with the fluence. The parametrization constant corresponds to the damage constant α. Image from [61].

3.3.3.2 Efective doping concentration and depletion voltage

As seen in section 3.1.4 the effective doping concentration of a silicon sensor is given by the amount of donors and acceptors in the silicon bulk ($N_{eff} = N_d - N_a$). The depletion voltage V_{fd} is proportional to the absolute value of N_{eff}, as described in equation 3.27. According to the expression given for N_{eff}, defects created by irradiation resulting in donor states increase the effective doping concentration and thus the depletion voltage. On the contrary, acceptor states will decrease N_{eff}. In p-bulk material, $N_a > N_d$ thus N_{eff} is initially less than zero, so an increase in acceptors only increases the depletion voltage. In n-bulk material, however $N_d > N_a$ having an N_{eff} value larger than zero. An increase in acceptor states will decrease V_{fd}. With increasing fluence, n-type silicon become less n-type until at a certain fluence where enough acceptors have been created to cancel out the initial donor concentration. With further increasing fluence the material behaves more and more as p-type.

Figure 3.19 shows the change in the effective doping concentration for n-type silicon and the depletion voltage as a function of the dose.

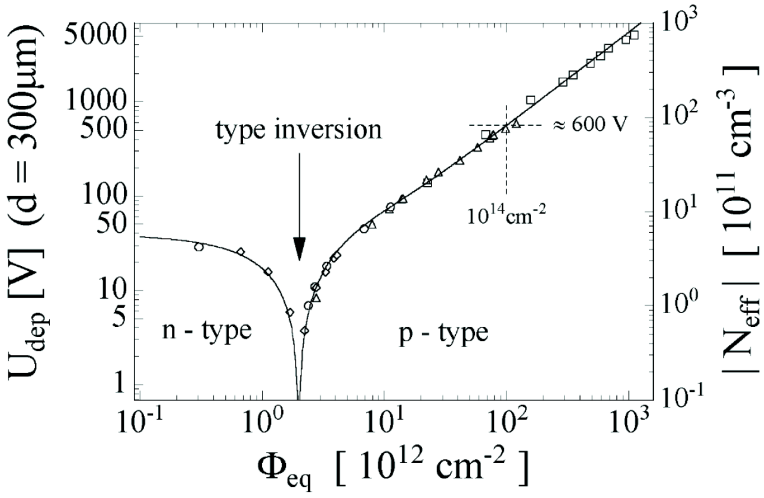

Figure 3.19: Variation of the depletion voltage with the absolute effective doping concentration versus the normalized fluence [73].

At the *type inversion* point the space charge region is neutral. With increasing radiation the space charge gains a net negative charge and above this value, the doping concentration increases dominated by acceptor-like defects with a negative space charge. The silicon bulk becomes effectively p-type and is said to be *type inverted*. The pn-junction will move from the p^+-side of the sensor to the n^+-side and the space charge region grows from there.

Even after inversion the sensor remains operational but will not be fully depleted. The collected signal under this situation will be directly affected since the charge carriers produced in the undepleted region suffer from diffusion and are collected late by the electrodes (after the colletion time). In the case of an initial p-type silicon, the material does not suffer *type inversion*.

3.3.3.3 Charge Collection Efficiency

A critical aspect of radiation damage is the trapping of charge carriers and thus, the reduction of the charge collection efficiency (CCE). As explained before, under the presence of an applied electric field the charge carriers created by the radiation drift to the electrodes. These carriers can be trapped by deep defect levels. Due to the lack of free charge carriers in the depletion region the traps are mostly unoccupied. If the charge is holded by the trap a time above the shaping time of the electronics the charge collection efficiency decreases. When extra free electrons are generated due

to an ionising radiation, they can lose energy and fall into the unoccupied traps, as illustrated in figure 3.20.

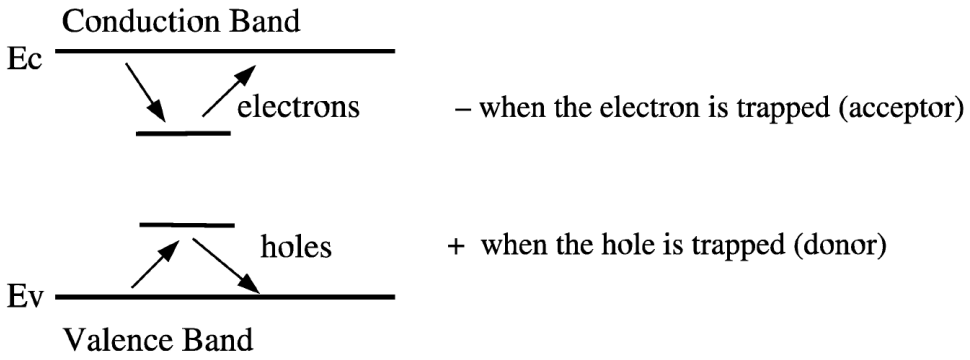

Figure 3.20: Deep defect levels acting as traps for charge carriers. When the charge carrier is held is not mobile and stayed trapped. At some later time the electron (hole) is released to the conduction (valence) band.

The number of traps icrease linearly with the radiation equivalent fluence according to:

$$N_{traps} = \eta \phi_{eq} \tag{3.40}$$

with η the trap introduction rate. Electrons have about three times the mobility of holes so they can travel much further in a given time and are less susceptible to trapping effects.

The loss of charge due to trapping is of the order 65% at the highest *HL-LHC* fluences [64].

3.3.3.4 Annealing

Radiation induced defects in silicon sensors are not static. They migrate through the silicon lattice due to thermal process. This thermal movement of the atoms over time will initially counteract the change of the doping concentration. After irradiation the doping concentration still changes so the detector properties can be subjected to change as well. The process of evolution in time of the detector characteristics is called *annealing*.

The annealing behaviour of the effective doping concentration N_{eff} and thus the depletion voltage is described by the *Hamburg Model*. The total change of the effective

doping concentration N_{eff} varies with fluence Φ, time t and temperature T according to the expression [74]:

$$\Delta N_{eff}(\Phi_{eq},t(T)) = N_a(\Phi_{eq},t(T)) + N_C(\Phi_{eq}) + N_Y(\Phi_{eq},t(T)) \tag{3.41}$$

where N_a is the *beneficial* annealing component, N_C is the *stable* annealing component and N_Y is the *reverse* annealing component. Each annealing component will be described below.

The *Hamburg model* was originally developed for n-type substrates. After several annealing studies (some of them presented in chapter 4) with p-type detectors it was determined that these kind of sensors do not follow the *Hamburg model* as accurately as n-type sensors and different parameters must be revisited for a correct description of the annealing behaviour for p-type substrates [75] [76]. This will be discused in chapter 4. Since all these new results are still under investigation the annealing components will be presented in this chapter in terms of the *Hamburg model* for historical reasons.

The time evolution of the effective doping concentration after several annealing steps at 60°C is shown in figure 3.21. N_{eff} decreases towards a minimum and then rises again beyond its initial value.

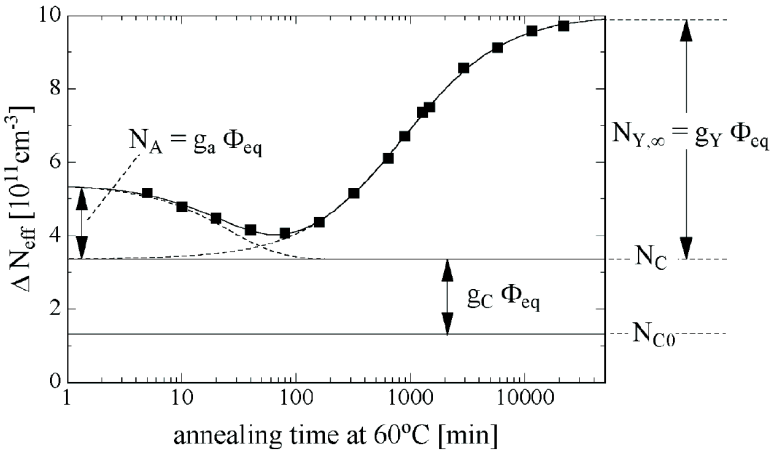

Figure 3.21: Annealing (for n-type substrates) of the irradiation-induced changes of ΔN_{eff} at 60°C after irradiation with a fluence of 1.4 $\times 10^{13}$ $n_{eq}cm^{-2}$ [77].

- **Beneficial annealing**

  The short term beneficial annealing component, N_a, is described by

$$N_a(\Phi,T,t) = \Phi_{eq} g_a exp\left(-\frac{t}{\tau_a(T)}\right) \tag{3.42}$$

  where g_a is the introduction rate and was determined experimentally to be $g_a = (1.81 \pm 0.14) \times 10^{-2} cm^{-1}$

  $\tau_a(T)$ is the temperature-dependent decay time that can be expressed by the Arrhenius relation

$$\frac{1}{\tau_a(T)} = \kappa_{a,0} e^{-E_a/k_B T} \tag{3.43}$$

  where $\kappa_{a,0} = 2.4^{+1.2}_{-0.8} \times 10^{13} s^{-1}$ and the activation energy of the beneficial annealing process, $E_a = (1.09 \pm 0.03)$ eV [61].

  The name beneficial comes from type inverted detectors where depletion voltage decreases. This beneficial annealing may be associated with the thermal suppression of the mobility of defects in the damaged silicon.

- **Stable annealing**

  The second term of the variation of N_{eff} with fluence and time corresponds to the stable annealing coefficient and does not depend on time. According to the *Hamburg model* the stable annealing can be parametrized as:

$$N_C(\Phi) = N_{C,0}(1 - e^{-c\Phi}) + g_c \Phi \tag{3.44}$$

  The first term of the equation characterizes the deactivation of the initial donor states and corresponds to the so-called *incomplete donor removal*. It depends exponentially on the fluence with a final value of $N_{C,0}$ wich is the initial concentration of removable donors. $N_{C,0}$ differs from N_{eff} before irradiation ($\Phi = 0$) due to a partial donor removal, while part of the initial donors stay electrically active even after very high fluences. c is the material dependent constant which relates fluence and donor removal. The removal rate is $dN/d\Phi$ = -$cN(\Phi)$, leading to an exponential reduction of active dopants with fluence.

The second term in 3.44 accounts for the creation of acceptor-like defects leading to a negative space charge. The constant rate of the acceptor states production is given by $dN/d\Phi = g_c$ where g_c is the introduction rate[1]. This coefficient (g_c) represents the probability to create an acceptor state by hadron per unit path length in silicon. Due to the creation of deep level acceptor states the original donor states are neutralized. This leads to a decrease in N_{eff}.

The stable annealing is the most important damage component with respect to the application and operability of silicon detectors in intense radiation fields. The beneficial component has a short time constant so it will occur during maintenance periods and the reverse annealing component is suppressed by low temperature operation. So that N_C is the most significant annealing component, which can not be controlled by temperature.

- **Reverse annealing**

The reverse annealing term is related to an increase in the N_{eff} for longer annealing times and therefore an increase in the full depletion voltage. The space charge becomes more negative due to the build-up of acceptor states. The long reverse annealing term depends strongly on the detector temperature and can be parametrized differently depending on the underlying model. There has been several studies to clarify whether the reverse annealing should be described as a first order [78] or a second order [79] process. It is stablished that the reaction kinetics underlying the reverse annealing is best described as a first order process. However, the best fit to the individual annealing curves was found to be the one with second order approach [61]. So a pragmatic compromise between both approaches is used for the parametrization of the data using:

$$N_Y(t) = N_{Y,\infty}\left(1 - \frac{1}{1+t/\tau_Y}\right) \tag{3.45}$$

N_{eff} increases up to a saturation value $N_{Y,\infty} = g_Y\Phi$ for very large times with a time constant (τ_Y) of about 350 days at room temperature. g_Y is the reverse annealing rate and was determined to be $g_Y = (5.16 \pm 0.09) \times 10^{-2} cm^{-1}$ [61].

[1] As an example the introduction rate for neutron irradiation is $g_c = 1.5 \times 10^{-2}\ cm^{-1}$ for standard silicon and $g_c = 2.0 \times 10^{-2}\ cm^{-1}$ for oxygenated silicon [77]

The temperature dependence of the reverse annealing process can be expressed by a standard Arrhenius relation of the time constant:

$$\frac{1}{\tau_Y} = \kappa_{Y,0} e^{-E_Y/k_B T} \tag{3.46}$$

with $\kappa_{Y,0} = 1.5^{+3.4}_{-1.1} \times 10^{15} s^{-1}$ and the activation energy of the reverse annealing process, $E_Y = (1.33 \pm 0.03)$eV [61].

Considering figures 3.19 and 3.21 it is clear that despite the high radiation fluences a beneficial annealing period results in less N_{eff} and therefore lower depletion voltages. However, for long annealing times this N_{eff} starts to increase. Taking into account the bias voltage value during operation (between 500 and 600 V) this means that after long periods of annealing the full depletion voltage is going to increase above 500 V and the sensors would operate not fully depleted. This will affect negatively to the charge collection efficiency of the sensors.

The reverse annealing contribution can be avoided by cooling the detectors below 0°C. This contribution must be taken into account during short maintenance shutdowns where the cooling system is disconnected and the detectors are therefore warmed up. The time range where the reverse annealing does not affect significantly the behaviour of the detectors will be analyze in chapter 4.

3.4 Experimental techniques for the characterization of Silicon Microstrip Detectors

Considering the expected total fluences of fast hadrons above $10^{16}\ cm^{-2}$ in the *HL-LHC*, the tracking detectors must be:

- radiation tolerant enough to survive the expected time of operation at such high fluences
- provide a fast and efficient charge collection

- be as thin as possible[1] to reduce the material in the total detector and the full depletion voltage value in the sensor. The energy lost per length unit is big due to the high density ($2.33\ g/cm^3$). Thus, sensors can be very thin and produce a clear signal.

As introduced in previous sections different electrical parameters of a silicon sensor are decisive to stablish the correct operation. This is for instance the case of the leakage current and the full depletion voltage. The characterization of a silicon detector implies the determination of these parameters using experimental techniques, as the Current-Voltage and Capacitance-Voltage curves, as well as its charge collection efficiency.

These kind of devices are easily influenced by environmental conditions. Therefore the electrical tests must be carried out under controlled areas. At *Instituto de Física Corpuscular* (*IFIC*) a clean room class 10000[2] with an area of $80\ m^2$ is used to that effect. A picture of the clean room can be seen at figure 3.22. The clean room system allows to control the temperature and the humidity. The work values were set to $(20 \pm 0.5)°C$ and $(45 \pm 5)\%$ respectively and they are within the fixed values by the ATLAS Collaboration $((21 \pm 2)°C$ and $(50 \pm 10)\%)$ for the characterization of detectors.

Figure 3.22: Panoramic view of the clean room facility at *IFIC*.

[1] To avoid problems for wafer deformation during high temperature processing the *Semiconductor Equipment and Material International* (SEMI) standards recommend thicknesses of 200 and 250 μm for 4 and 5 inches wafers respectively for high resistivity thin sensors [80].

[2] Particle count of a size $0.5\ \mu m$ and larger should not exceed a total of 10 000 particles per cubic foot.

3.4.1 Current-Voltage (IV) characterization

The leakage current contributes to the noise of the detector and degrades its performance. It is dominant compared to the other currents in the detector and determines its power consumption. Hence, it drives the design of the high voltage lines, the dimensions of the cables and the cooling systems in an experiment. Since the leakage current is one of the major contributions to the avalanche breakdown of the detector it will establish the maximum operation voltage. As seen in section 3.3, the current scales with radiation fluences, so for irradiated sensors the leakage current contribution to the noise is higher than for not irradiated sensors. Controlling the IV characteristics of the detectors is therefore mandatory. The measurement of the leakage current allows us also to detect sensor defects and problems in the wafer litography when the electric field is so high.

A probe station placed at the temperature/humidity controlled clean room is used to measure the dependence of the leakage current with the voltage. The sensors were held against a metal chuck of the probe through a vacuum suction system. Finely-tipped needles were used to make contact with the metal pads on the front face of the detector, consisting of the strip structure and the guard rings surrounding the device under test. A picture of the setup can be seen in figure 3.23 where a zoom to the needle and a microscope image are also depicted.

Figure 3.24 shows a sketch of the electrical connections during a standard IV measurement. The voltage is applied to the probe station chuck so the sensor is biased by its backplane. The probe needle is poking the bias ring stablishing ground contact. A Keithley K237 power supply is used as current meter to measure the variation in the current through each needle with the applied voltage.

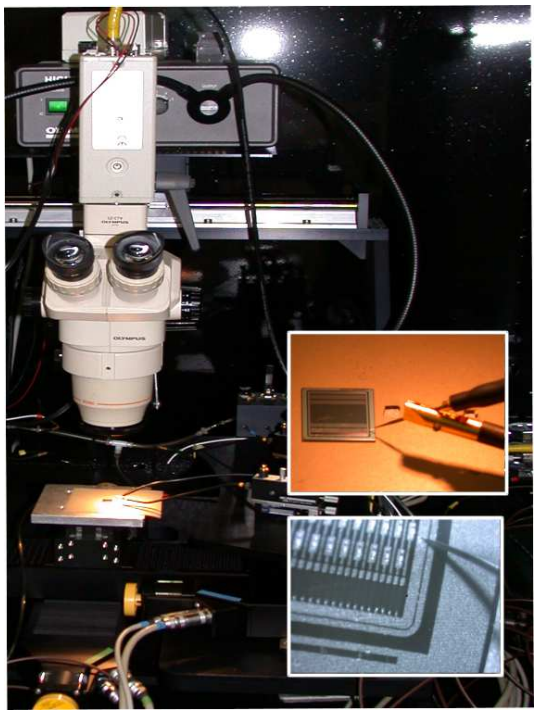

Figure 3.23: Probe station inside a Faraday cage used for IV and CV measurements in a clean room. A zoom to the needle and a microscope image can also be seen.

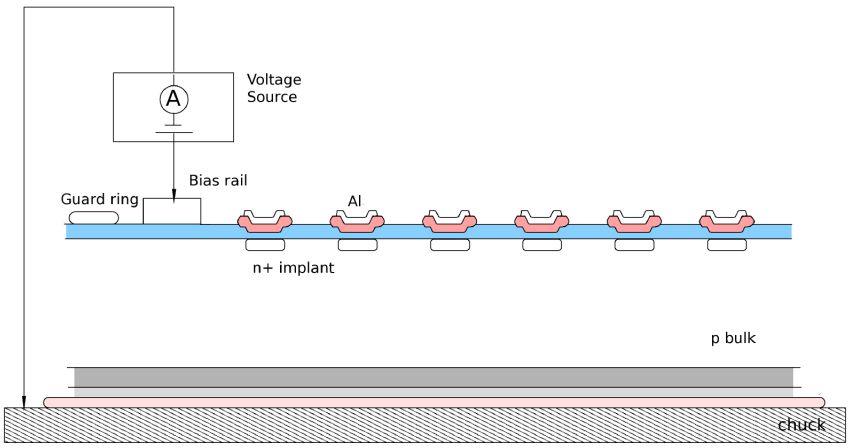

Figure 3.24: Sketch of the IV measurement system used on a $n^+ - p$ sensor. The power supply and the metal chuck can also be distinguised.

Figure 3.25 shows two typical IV curves for irradiated sensors. One of them (sensor $W639\text{-}EC\text{-}SP\text{-}E\text{-}P18$) has a normal behaviour where the leakage current is low and constant in the voltages range. However, the other one (sensor $W609\text{-}EC\text{-}SP\text{-}C\text{-}P17$)

presents increasing leakage current with the bias voltage and sensor breakdown around 900 V.

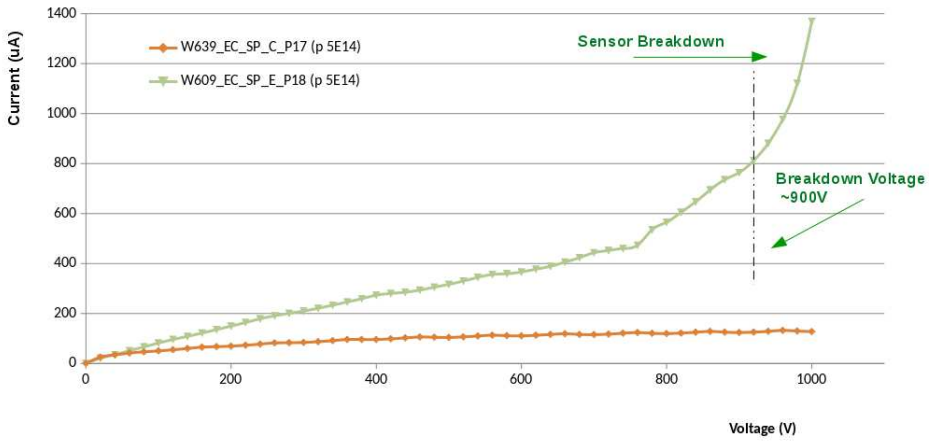

Figure 3.25: Typical IV curves obtained during irradiated sensor measurements. Sensor $W639\text{-}EC\text{-}SP\text{-}E\text{-}P18$ presents normal behaviour with low and constant leakage current. Sensor $W609\text{-}EC\text{-}SP\text{-}C\text{-}P17$ shows increasing leakage current with the bias voltage and breakdown around 900 V.

As explained in previous sections, in the case of irradiated sensors, the sensors must be cooled down to maintain the radiation effects unaltered during the study period. Furthermore, the dependence of the leakage current with the temperature is not negligible. Due to this, for measurements in irradiated sensors, the metal chuck is replaced by a thermal metal chuck made at IFIC to maintain the sensors cold enough during the measurements. A chiller machine is used as cooling system and dry air is blown on top of the the sensor's surface to avoid water condensation. The chiller temperature in these cases is set to $-5°C$. In figure 3.26 a detail of the thermal chuck is presented.

The voltage range used for the IV curve goes typically from zero to (600-1000) V in (10-20) V steps. Between each current measurement 10 seconds of delay is stablished to let the current stabilized. A maximum current level is also set to protect the sensor from breakdown.

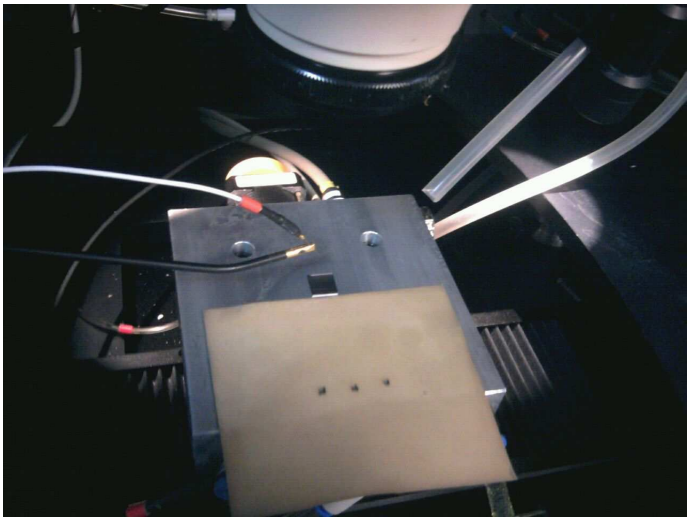

Figure 3.26: Detail of the thermal chuck used inside the Faraday cage in the case of irradiated sensors where dry air and chiller tubes can be distinguised.

This compliance level changes for each sensor type. Typically:

- 100 μA in not irradiated mini sensors.
- (100-150) μA in not irradiated full size sensors.
- (10-15) mA in irradiated mini sensors.

The devices are controlled by *GPIB* ports (*General Purpose Information Bus, IEEE488*). For the readout and control a home-made *C++* data adquisition software *Probe++* [81] was developed. This software allows to monitor and store the current obtained for each bias voltage applied. Figure 3.27 shows an example of a measurement window of the programme *Probe++*.

3.4.2 Capacitance-Voltage (CV) characterization

For the CV measurements inside the clean room a similar system was used. To measure the capacitance of a sensor as a function of the applied voltage the system incorporates a LCR meter (Wayne Kerr 6425B). The LCR meter is connected in parallel across the device with the Keithley voltage source as shown in figure 3.28.

The neddles configuration is the same as in the measurement of the current-voltage characteristics. The device is biased by its backplane and a needle is poking the bias ring of the sensor. The voltage range used for the CV curve is similar to the IV test.

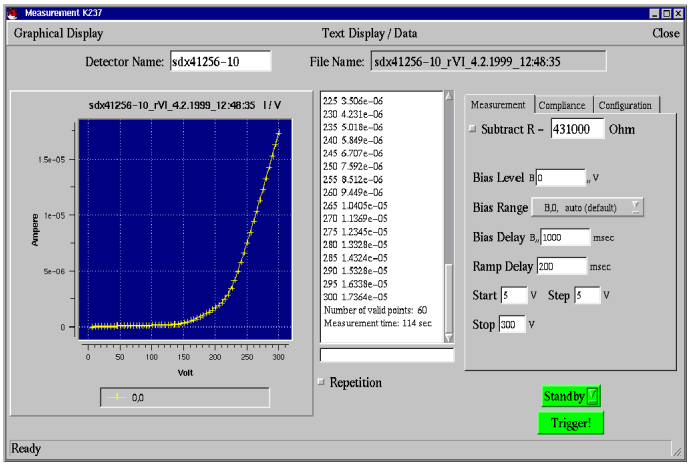

Figure 3.27: Example of the IV measurements with the data adquisition system used (*Probe++*) [81].

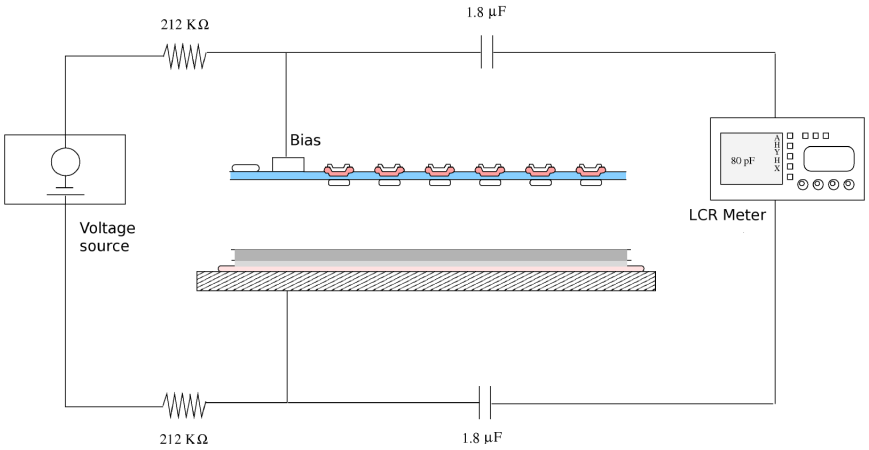

Figure 3.28: Sketch of the CV measurement system used.

This range goes from zero to (600-1000) V in (10-20) V steps. The capacitance is very sensitive to current variations so in this case between each measurement 20 seconds of delay is stablished to ensure the current stabilization. The current compliance level is the same as in the IV test.

The probe needle simultaneously works as the ground connection of the device and applies a small-amplitude AC voltage to the corresponding contacts at a frequency ω. The amplitude of the resulting small-signal AC current flow can be used to calculate

the capacitance between the two contacts, given that,

$$I_c = V_c / Z_c = V_c j\omega C \tag{3.47}$$

where V_c is the applied voltage and $Z_c = 1/j\omega C$ is the detector impedance seen by the AC signal.

The strip detector can be treated as an extended network of coupled distributed resistors and capacitors. The equivalent diagram of a n-on-p sensor is shown in figure 3.29. R_{bias} is the polysilicon bias resistor and it is situated between the bias line and the front-end electronics.

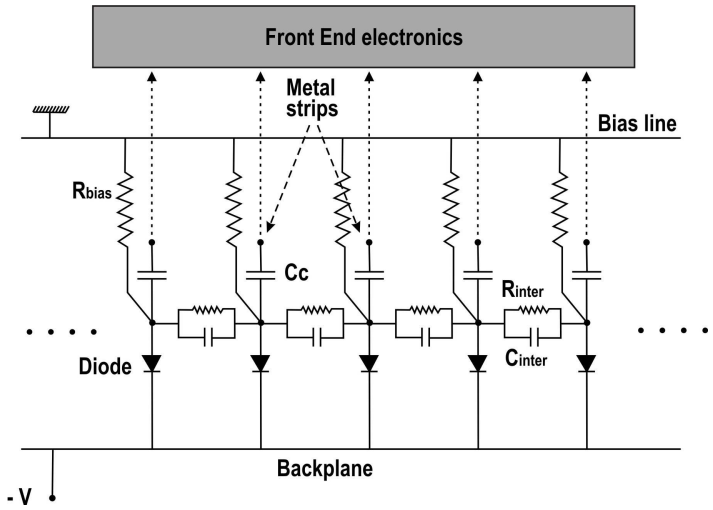

Figure 3.29: Equivalent diagram of a $p-type$ silicon microstrip sensor. The strip detector can be treated as an extended network of resistors and capacitors.

The implant strip and the metal strip can be represented as a series of finite but small resistors with distributed capacitors to the other electrode, the neighboring strips and the backplane. The coupling capacitor shown in figure 3.29 constitutes a low pass filter due to the high resistivity of the implant and leads to a frequency dependence in the measured capacitance [82].

Following RD50 recommendations [83] a study on the dependence of the capacitance respect to the frequency was carried out in different devices to stablish the proper value where the capacitance remains almost independent on the applied voltage. Figure 3.30 shows an example of the curves obtained in this study (top) and a zoom of the region of interest (bottom). Due to the achieved results a frequency of $30\ kHz$

will be used for the measurement of the capacitance in all these tests unless explicitly mentioned otherwise.

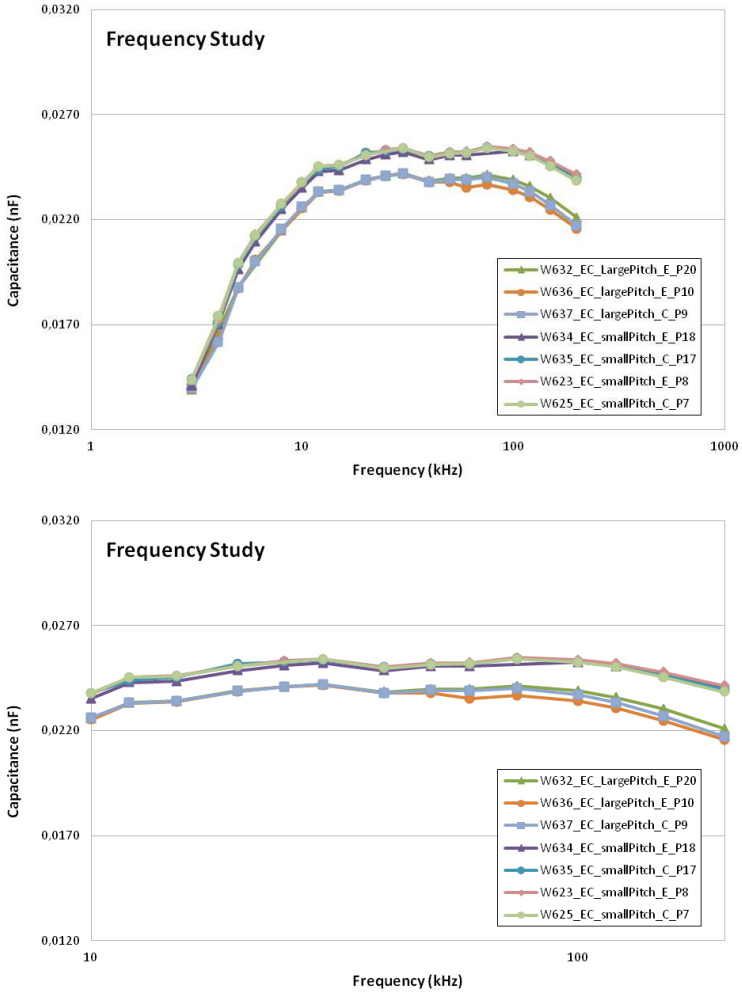

Figure 3.30: Frequency study to determine the proper value where the capacitance remains almost independent on the applied voltage (top). Zoom of the results obtained for the frequency analysis (bottom). A frequency value of $30\ KHz$ will be used in all the CV tests unless explicitly mentioned otherwise.

The DC supply was decoupled from the small-amplitude AC voltage of the LCR meter using capacitors. This extra capacitance is accounted for through a trimming calibration of the system capacitance.

As seen in section 3.1 the square of the capacitance of a diode is proportional to the inverse of the applied bias voltage (as given in equation 3.28), the measured capacitance dependence on the voltage of a device can be used to extract the width

of the space charge region. The capacitance of a diode is unchanged with applied bias after full depletion therefore the full depletion voltage, V_{fd}, may be determined from the CV method. An example of a CV curve can be seen in section 3.1. It is a good practice to make use of the $1/C^2 - V$ curve to determine the full depletion voltage that will also show the characteristic kink at V_{fd}. The value for the V_{fd} can be extracted fitting the data to two straight lines, one to the linearly increasing section before full depletion and one to constant capacitance section after full depletion. The point of interception of the two lines corresponds to the point at which the device is fully depleted and therefore the value of the full depletion voltage may be obtained. Figure 3.31 shows an example of a CV curve obtained for a no irradiated mini sensor.

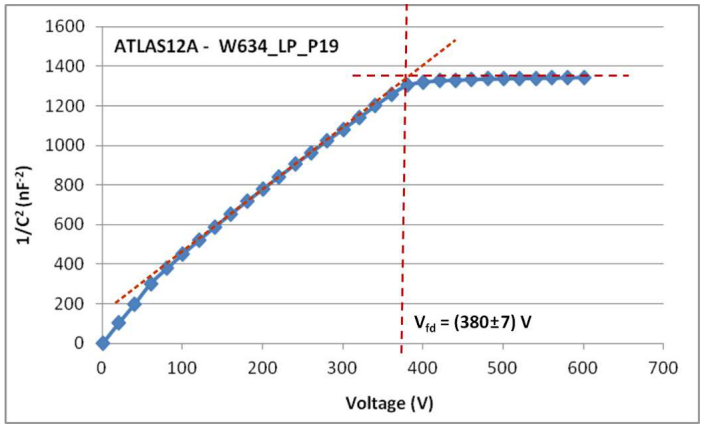

Figure 3.31: Full depletion voltage extracted from a typical Capacitance-Voltage curve in a silicon microstrip sensor. The inverse of the square of the capacitance is plotted versus the bias voltage of the sensor.

The extracted value for V_{fd} is the minimal voltage required to obtain maximal charge collection efficiency, which is ultimately the most significant parameter for detector operation. In the case of irradiated detectors, the obtained V_{fd} is not 100% correlated to the one obtained by the CV method in a simply way. This is due to the effect of trapping since a number of charge carriers is removed to the signal by trap defects affecting to N_{eff} and therefore to V_{fd}.

3.4.3 Charge Collection measurement system

The charge collection efficiency (*CCE*) of a detector gives us important information about the performance of the device. By measuring the total collected charge versus the bias voltage one can evaluate the depletion behaviour of the detector, since only

the carriers generated in the depletion region will be collected. Moreover with the charge collection efficiency one can quantify the radiation damage on the detectors for different fluences and verify if sensors with high radiation dose are still functional.

A ^{90}Sr β source is used to measure the charge collection in the setup (Activity: $0.2723\ \mu Ci$, $10.08\ kBq$, Ref. date: 15 December 2013). This source emits electrons with a spectrum of energies up to $2.28\ \mathrm{MeV}$ that will pass through the silicon detector. As the energy loss of electrons of this energy is close to minimum ionising particle (*mip*), these electrons generate around 80 electron-hole pairs (most probable value (*mpv*), see section 3.1.1) per micron along their path. In that way, these electrons can be referred to as mips. The source will also emit low-energy electrons which will be stopped by the detector and generate a larger, and variable quantity of charge carriers. In the radiactive source (RS) setup shown in figure 3.32 (left), a microstrip silicon detector is placed below the β source. Under the detector, there is a scintillator ($0.5 \times 0.5\ cm^2$), connected to a photomultiplier tube as well (figure 3.32 (right)).

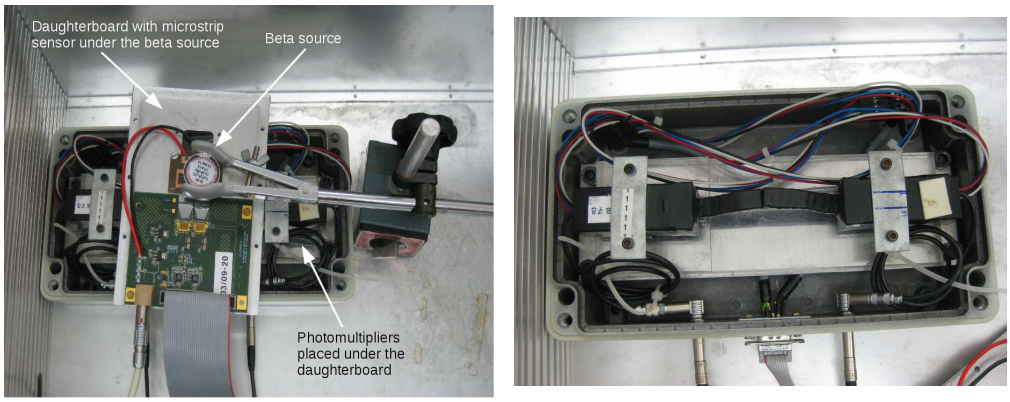

Figure 3.32: β source setup used for charge collection measurements (left). The source is placed above the silicon microstrip sensor. Below the detector two photomultipliers (right) are placed to provide external trigger.

All the system is mounted into a Faraday's cage to avoid external light and isolate the system from radiated noise. The reverse bias voltage applied to the detector is supplied by an external power supply (Keithley 2410 1100V Source Meter).
When the radioactive source emits a high-energy electron, it passes through the detector. Then, it is absorbed by the scintillator and the light pulse generated is detected by the photomultiplier. The photomultiplier produces a fast electrical negative analogue pulse which is amplified and discriminated, obtaining a digital pulse used as trigger for the system. The trigger signal is also used to exclude the lower-energy

β that may be stopped by the silicon sensor and will not reach the scintillator. The setup includes two photomultipliers taking as trigger the coincidence signal between them. Nevertheless, it is recommended to use an unique calibrated photomultiplier since many electrons will be absorbed by the scintillator plastic and will not reach the photomultiplier below [84]. A sketch of the complete system can be seen at figure 3.33.

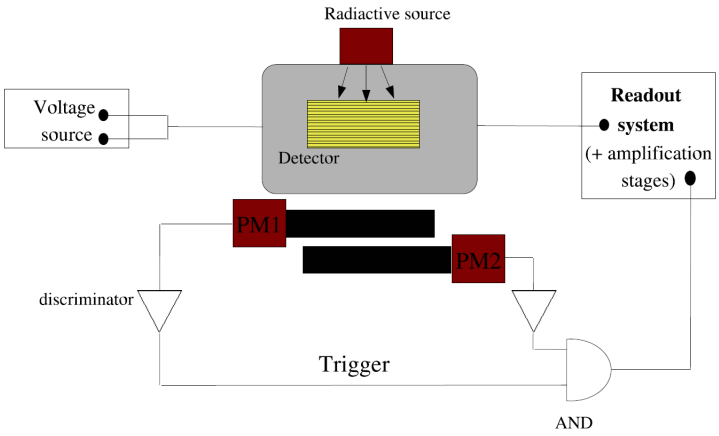

Figure 3.33: Scheme of the complete radioactive source setup.

Figure 3.34 shows a typical charge-voltage curve obtained with a not irradiated barrel sensor.

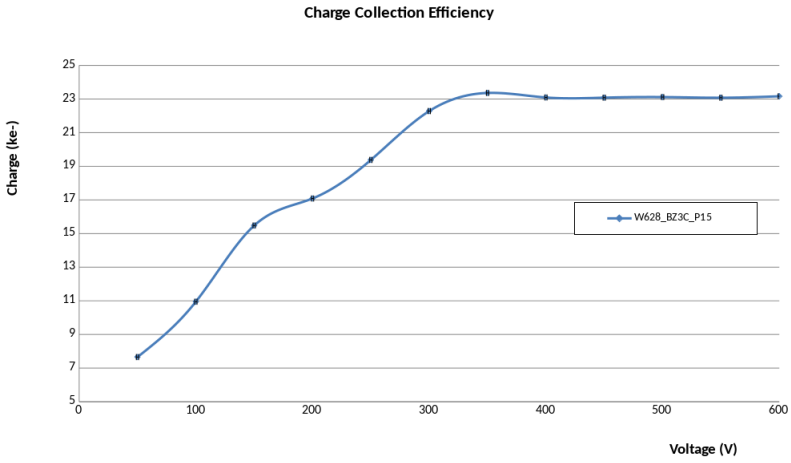

Figure 3.34: Typical charge-voltage curve obtained with a not irradiated barrel sensor using the beta setup.

When working with irradiated sensors all the setup is placed inside a vertical freezer and maintained at $-35°C$, as shown in figure 3.35.

Figure 3.35: Charge collection measurement system placed inside a vertical freezer for measuring irradiated sensors. The temperature is maintained to $-35°C$.

The output signal of the detector goes directly to the data acquisition system to process and store the data (the data acquisition system will be explained in section 3.4.5).

3.4.4 Strip Integrity: Laser measurements

For completeness during the characterization of the microstrip sensors, a laser setup was used. With this system one can test different sensor details, for instance:

- Verify electrical connections and properties such as the quality of the bonding process or the channel response (looking for bad channels).
- The performance of each individual strip can be analize looking at the uniformity of the signal per channel.
- The radiation influence on the collected charge and the signal deformation can be also studied.

- The charge sharing evolution between strips after radiation exposure.

The setup is placed inside a Faraday's cage that shields the setup from electrical and magnetic fields. Outside the Faraday's cage the same high voltage source used in the β source setup biases the sensors up to $1000\ V$ typically during testing purposes. As in the case of the charge collection setup the output signal of the detector goes directly to the data acquisition system (see 3.4.5).

The setup includes three high-precision stages that move the laser in the perpendicular direction to the strips (X), along the strip (Y) and near/far from the strips (Z). They are controlled by a motion controller (Newport MM4005) (figure 3.36). This controller has a GPIB interface and can, thus, be controlled from the PC or manually. Position control accuracy is $1\ \mu m$ in each channel. This alternative offers a good spatial resolution when the laser is properly focused.

Figure 3.36: Motion controller (Newport MM4005) included in the laser setup. It controls three high-precision stages that move the laser in the perpendicular direction to the strips (X), along the strip (Y) and near/far from the strips (Z). This motion controller includes a GPIB interface and can be controlled from the PC or manually.

The system is ready to test also irradiated sensors due to a thermal base made of aluminium (figure 3.37). The coolant liquid from a chiller machine circulates by means of a cooling coil built inside the aluminium base as can be seen in figure 3.38. Dry air is also blown on top of the the sensor's surface to avoid condensation.

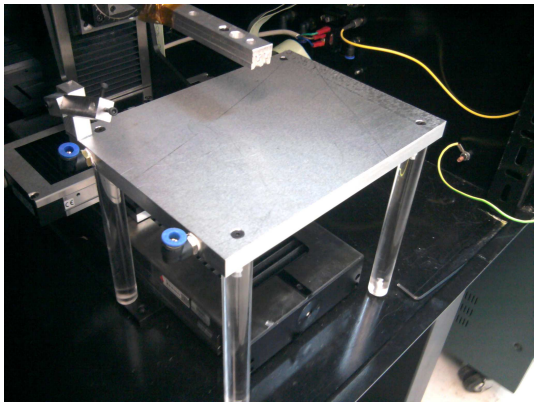

Figure 3.37: Thermal base made of aluminium to be used during laser measurements on irradiated sensors. Coolant liquid from a chiller machine circulates inside the base. A support for a dry air tube is included to avoid condensation over the sensor.

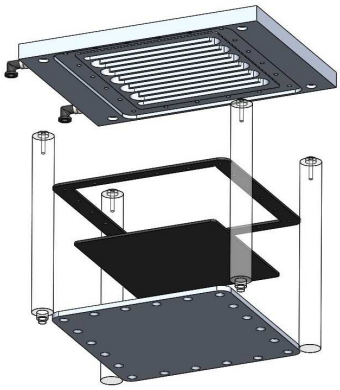

Figure 3.38: Sketch of the thermal base shown in figure 3.37. The coolant liquid circulates through a cooling coil. The aluminium parts are depicted in grey color. To contain the liquid two viton gaskets are used (pieces in black color).

The laser light is led through an optical fibre with a focusing lens to the sensor and emits in the close infrared with a wavelength of of 980 nm, therefore with an energy[1] of 1.26 eV per photon. The laser beam is a beam of photons instead of charged particles (as in the case of the β source setup explained in section 3.4.3).

The amount of light that penetrates a certain depth (x) decreases exponentially with $(-x/d_0)$ where d_0 is the attenuation length coefficient. For a wavelenght of 980 nm the attenuation lenght value is around 100 μm [85]. Figure 3.39 shows the variation of the attenuation legth with the wavelenght [86].

For a wavelength of 980 nm and silicon sensors of about 300 μm the laser signal will be totally absorbed. Since the laser beam energy $(1.26$ eV$)$ is lower than the energy required for the generation of an electron-hole pair in silicon $(3.6$ eV$)$, the ionization is generated by exciting the electrons of the bands ($E_{laser} > E_{GAP} = 1.1$ eV in silicon).

[1] The photon energy is directly related to the wavelength of the light. The relation is given by: $E_{ph} = \frac{hc}{\lambda}$ where h is the Planck's constant ($6.626 \times 10^{-34} Js$), c is the speed of light in vacuum and λ is the wavelenght.

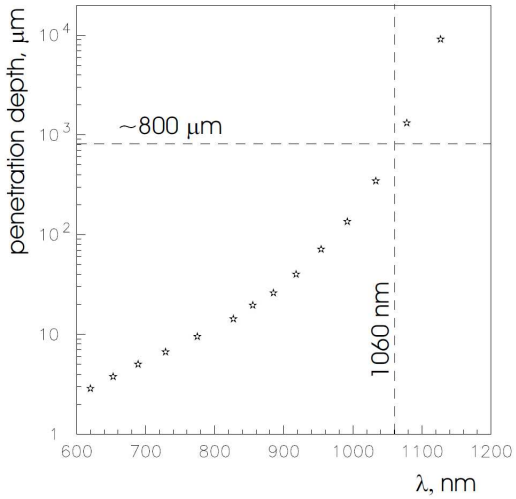

Figure 3.39: Dependence of the light penetration depth in silicon as a function of the wavelength. Picture taken from [86].

Laser general features	
Class	1
Diode peak power	0.5 mW
Wavelength	980 nm
Power supply	5 V
Pulses width	5 ns
Rise time	1 ns

Table 3.3: General features of the laser used in the setup.

A summary of the principal characteristics of the laser used are shown in table 3.3.

Accurate focusing of the laser over the detector is crutial when laser measurements are being done. This is carried out varying the distance from laser to sensor (Z direction) in small steps and measuring the width of the laser signal pulse in number of channels as shown in figure 3.40. The best Z value will correspond to the minimum width achieved.

To get a more precise focus the laser is then moved perpendicularly to the strips (X direction). The signal of the near neighbours (left and right) is measured to calculate the center of the strip. In this X position the variation in Z will be repeated and the new minimum width of the laser will be taken.

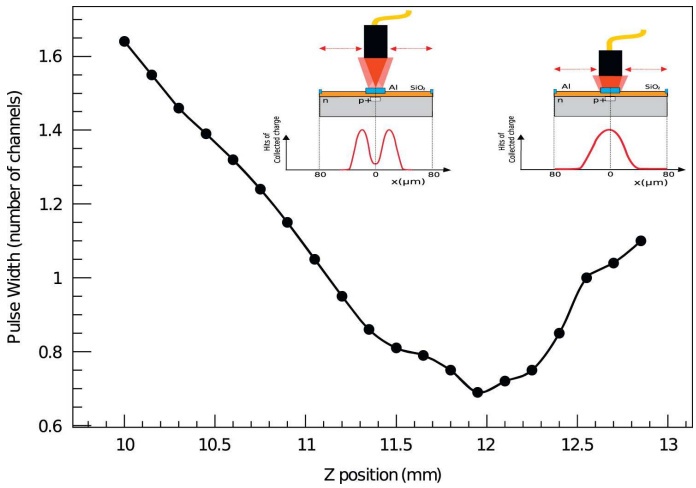

Figure 3.40: Laser cluster width as a function of the distance between laser and sensor surface. The distance at the minimum width is considered to be the proper focus.

Once a proper focus is achieved, a laser scan is carried out in X direction. The signal on each channel is readout on each step, which is usually of the order of $2\ \mu m$. A signal like in figure 3.41 is produced for each channel. The dip in the middle of the strip width corresponds to light losses due to the reflection of the laser by the aluminium on top of the implant.

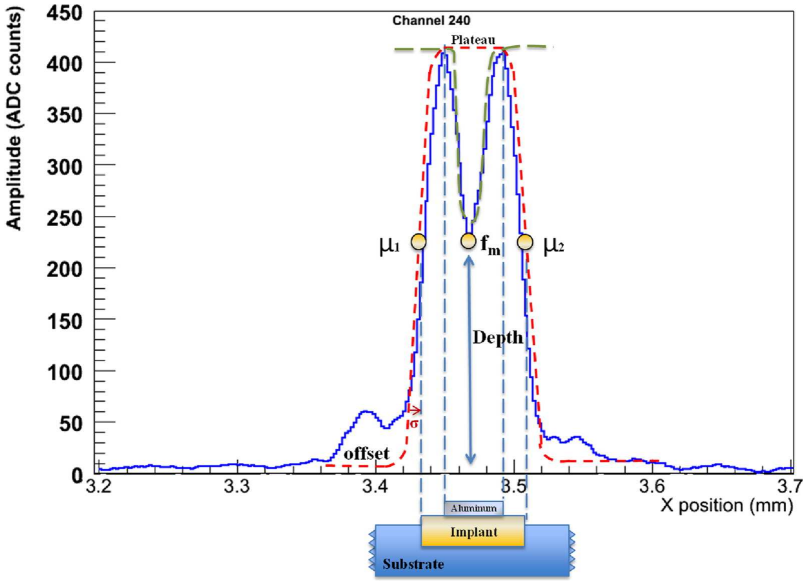

Figure 3.41: Sketch of the signal as seen in a given channel during a laser scan. The picture also shows the parameters of the function fit.

The channel signal can be fit to a function of the form:

$$f = P\left[\frac{1}{2}\left(Erf\left(\frac{x-\mu_1}{\sigma}\right) - Erf\left(\frac{x-\mu_2}{\sigma}\right)\right) - \beta Gaus\left(\frac{x-\frac{1}{2}(\mu_1+\mu_2)}{\sigma}\right)\right] \quad (3.48)$$

The result of the fit shows that the laser beam spot (the σ parameter on the fit) we managed to obtain with this setup was $(7 \pm 2)\ \mu m$.

Figures 3.42 and 3.43 depict an example of the results obtained using this laser system in a real test with silicon microstrip sensors.

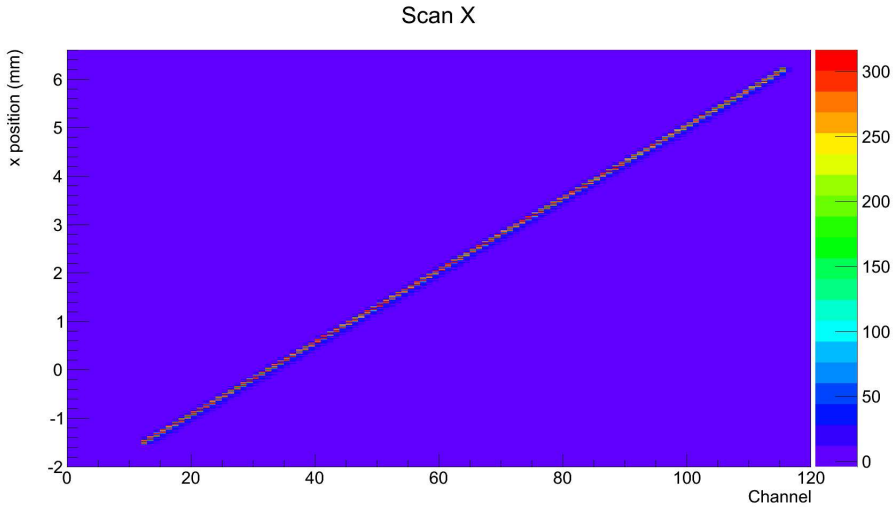

Figure 3.42: Signal per channel obtained in a laser scan with a selected sensor region (around $8\ mm$). The color bar on the right represents the amount of charge in ADC counts.

3.4.5 Data analysis with ALiBaVa

ALiBaVa (*A Liverpool Barcelona Valencia*) is an analogue signal readout system for microstrip silicon sensors. It is compact and portable and was developed as a result of a collaboration among the University of Liverpool, the CNM (*Centro Nacional de Microelectrónica*) of Barcelona and the IFIC of Valencia [87].

The system uses two front-end readout chips (2×128 channels) and is able to measure the collected charge of microstrip sensors reading out all the channels of the detector simultaneously. It can operate either with non-irradiated and irradiated sensors as well as with *n-type* and *p-type* sensors.

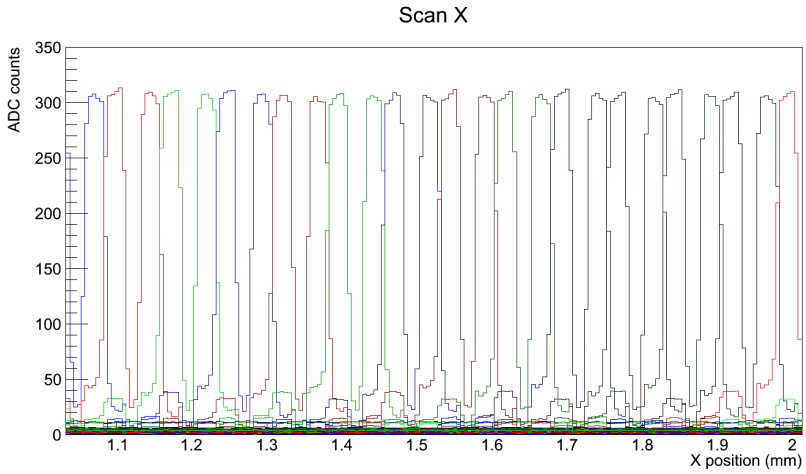

Figure 3.43: Projection of the data obtained in 3.42 in the direction of the laser movement (X direction). All the strips show similar distribution and amount of charge achieved (around 300 ADC counts)

ALiBaVa consists of two main parts:

- **Hardware:** The hardware part is a dual board based system composed by a mother and a daugther board. The mother board is intended to process the analogue data that comes from the readout chips, manage the trigger signals, control the whole system and communicate with a host computer via USB. The daughter board is a small board designed to contain two $Beetle$ readout chips [88], pitch-adaptors and to provide mechanical support to the sensors. In case of using the radiactive source setup (RS), the hardware (see figure 3.44) will use an external trigger input to acquire the sensor signals. On the contrary, in the laser setup, no external trigger is needed since the laser is fired from the ALiBaVa. For this purpose a pulse is sent by the mother board to the laser periodically. The signal produced in the sensor is acquired after an auto-trigger signal generated by AliBaVa, which is synchronized with this pulse but delayed. This delay is chosen by the user by means of the program. The acquired data will be roughly processed and sent by the hardware in order to be stored in a computer for a more detailed processing.

- **Software:** The software part (figure 3.45) is the interface between the equipment and the user by means of a *Graphical User Interface* (GUI).

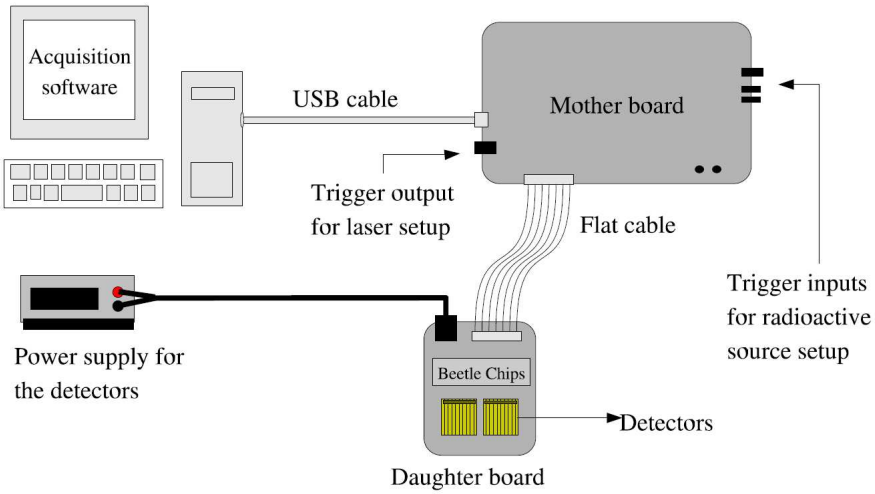

Figure 3.44: Block diagram of the ALiBaVa system with its different components.

It controls the ALiBaVa card and is able to configure the device, receive the data that the card sends via the USB and store it in a file for further analysis. The GUI also monitors the data during the acquisition so that the user can detect problems or just find the proper parameters to run the system in an optimal way.

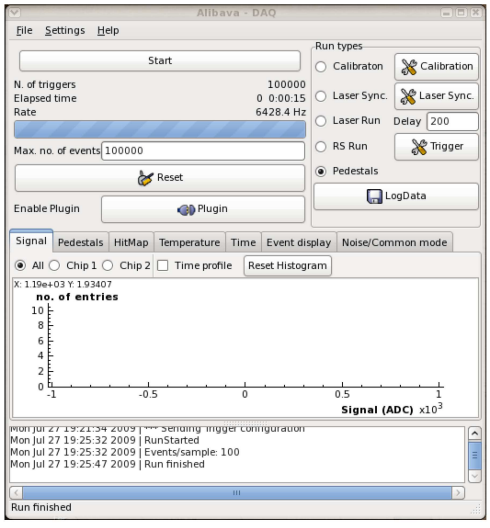

Figure 3.45: ALiBaVa software main window.

A more detailed description of the software can be found on [89].

3.4.5.1 Understanding the ALiBaVa output: from data to physics

As explained in section 3.1.4 a high-energy particle passing through a detector deposits energy through a series of collisions with atoms in the material. The amount of energy deposited in the detector and hence the signal generated will vary from particle to particle due to the statistical nature of the process. Over a large number of hits, the quantity of energy deposited will follow a predictable distribution:

- In a thick detector, the number of collisions will be large, and so this distribution will be a $Gaussian$ about the mean value.
- For a typical silicon detector, which is relatively thin (about $300\ \mu m$), the number of collisions will be smaller. The energy loss will follow a $Landau$ distribution convoluted with a $Gaussian$ distribution to compensate for any broadening of the espectrum due to noise, and non uniformity of the incident particle momentum. Figure 3.46 shows the Landau distribution (a) and the convolution with a Gaussian (b).

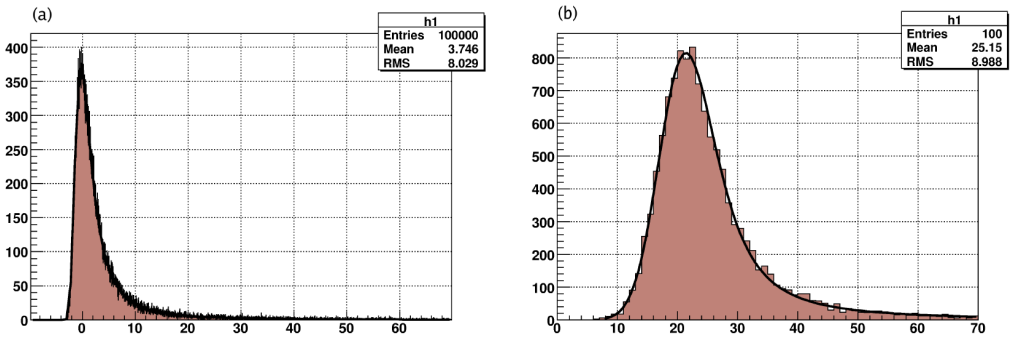

Figure 3.46: Examples of a Landau distribution (a), and a Landau convoluted with a Gaussian distribution (b).

By integrating the current signal induced by the charge motion the system can obtain the deposited energy. The height of the pulse obtained is proportional to the original current induced on the strip and can be measured through an analog-to-digital converter (or ADC).

Figure 3.47 shows the reconstruction of the signal sent by the $Beetle$ using an electron as incident particle. The averaged collected charge in electrons versus the TDC measurement is plotted. Since with a p-type detector electrons are collected the resulting pulse is negative.

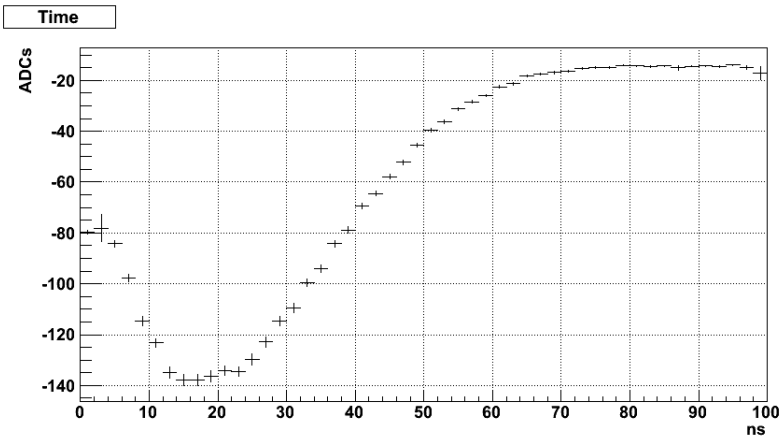

Figure 3.47: Time profile obtained for a $p-type$ microstrip silicon sensor biased to 1000V. The average of the collected charge (in ADC counts) as a function of the TDC measurement (in ns) is plotted.

Previoulsy to the measurement of the charge with the ALiBaVa, the standard procedure starts with a calibration of the system and the measurement of pedestals data. Common mode noise corrections are also applied.

During the calibration measurements each $Beetle$ chip inject a specific amount of charge which is programmed via an integrated circuit bus ($I2C$) [90]. In particular, charges from 0 electrons to 102500 electrons are injected in 1025 electrons steps (with 100 samples acquired typically). From these data a calibration curve can be generated (figure 3.48) and the gain for each channel can be derived.

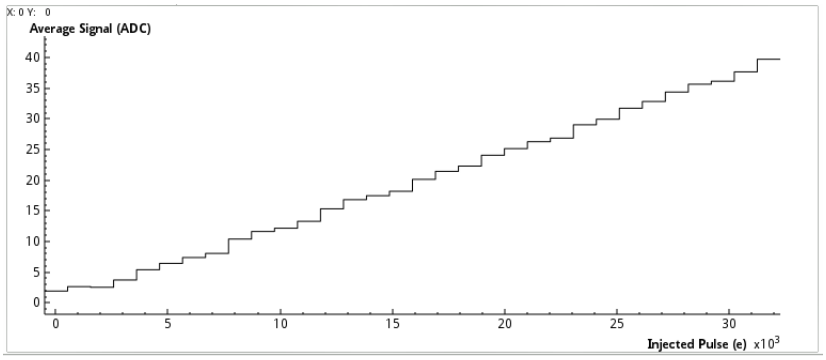

Figure 3.48: Charge calibration scan to get gain and offset.

The pedestals can be computed on-line either by making a pedestal run at the very beginning or can be estimated while taking data. Pedestals are calculated without external signal presence.

The resulting file of a pedestals run contains the average of the data for each channel (pedestal level in ADC counts) and the RMS (*Root Mean Square*) of the data for each channel (noise in ADC counts). Typical values of pedestals and noise are depicted in figure 3.49.

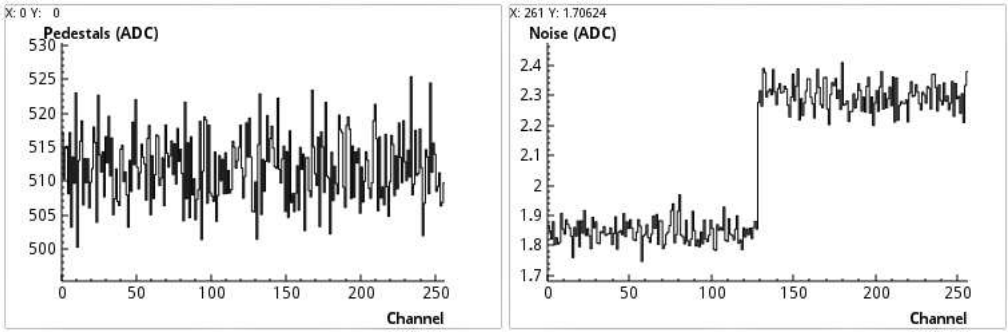

Figure 3.49: Pedestals level (ADC counts) versus the channel number (left) and noise level (ADC counts) versus the channel number (right). The noise value showed is computed as the RMS (Root Mean Square) of the pedestal distribution.

A detailed description of the format of the output files can be found on [89].
After the calibration of the system and the pedestals adquisition, the user can start with the laser or the RS run. In this stage different parameters of the run can be specified such as the total number of events or the sample size. Each run generates a data file in a raw format, i.e ADC counts versus input channel for each event. These raw data are corrected by subtracting the pedestal value and by performing a common mode correction. ALiBaVa provides a collection of macros developed for the ROOT framework [91] to read the data files and produce histograms. From the corrected data, the signal is computed as the sum of strips in a cluster. Clusters are built around strips with a SNR (signal to noise ratio) higher than 6. This strips are called *seeds* and are not already in the cluster. The adjacent channels to the seed will be added while their SNR is higher than 2.5. Depending on the acquisition type (laser, RS, calibration, etc ...) different representations will be available. For the analysis of the charge collection efficiency of a microstrip sensor, one of the most important plot would be the spectrum of the signal obtained for a selected timecut. This time cut includes events with TDC measurements between a peak of typically 10 ns. This spectrum plot corresponds to a histogram of the amplitude of recorded events. The resulting spectrum fits a $Landau$ distribution convoluted with a $Gaussian$ (as mentioned before)

as seen in figure 3.50. The peak value will correspond to the most probable value (MPV) of the charge generated for a mip in the silicon detector.

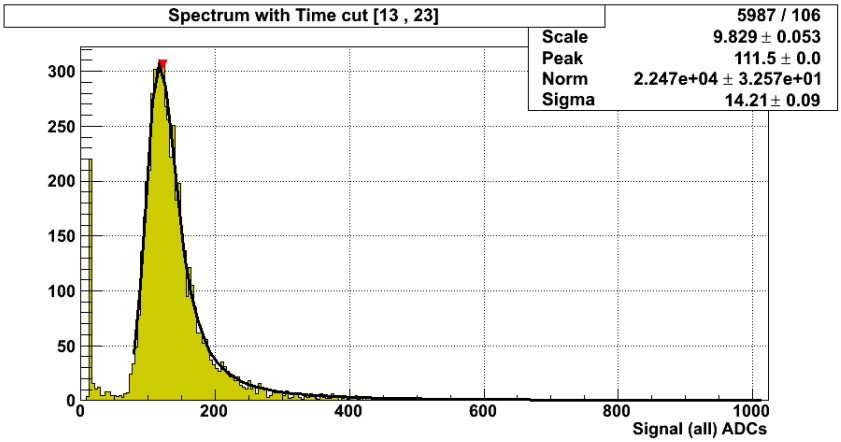

Figure 3.50: Spectrum of the signal acquired with a time cut between 13 ns and 23 ns. The number of events as a function of the absolute value of the collected charge (in ADC counts) is represented.

As seen in section 3.1.1 the Bethe-Bloch equation predicts an average energy loss of 388 $\mathrm{eV}/\mu m$. This means that for a 300 μm thick silicon sensor the most probable energy loss for a mip is 81 keV [92]. Hence the mean charge deposited by a mip amounts to 23000 electrons; which is equal to 3.6 fC. It is the most probable energy that is used for calculations of collected charge from a silicon detector. The spectrum plot is obtained for different bias voltage values (typically from 0 to 1000 V). The different peak values are represented versus the bias voltage to extract the charge collection efficiency for every silicon detector. An example of the obtained curve can be seen in figure 3.51.

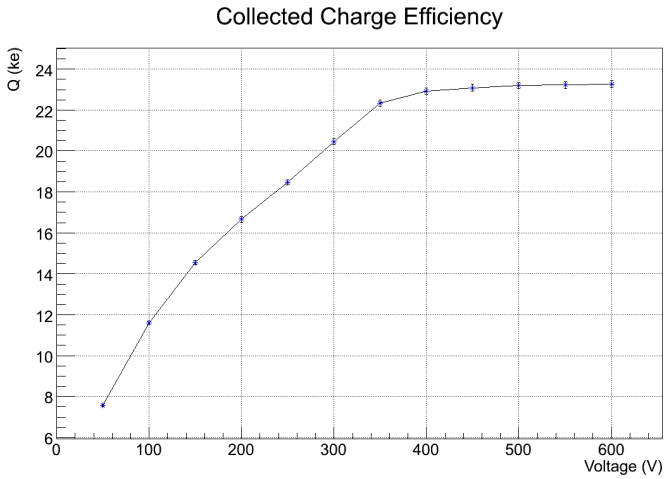

Figure 3.51: Collected charge usig the ALiBaVa system versus the bias voltage for a microstrip $p-type$ sensor.

Chapter 4

Strip Petals for HL-LHC

As introduced in chapter 2 the future End-cap disks in the *HL-LHC* will be populated with Petals. The Petal is a modular mechanical unit and is designed to give support and cooling to the End-cap sensors. Several Petal prototypes were built to validate the production steps and verify the good electrical behaviour of the complete system. For that purpose different thermo-mechanical studies with the Petal carbon core and the electrical characterization of the silicon sensors were carried out.

4.1 Petal core assembly

The procedure described here is based on the experience gained during the construction of a number of Petal prototypes in Berkeley in 2009.
The basic components of the Petal core can be summarized in: a pipe made of stainless steel for the Petal cooling, carbon foam surrounding the pipe and providing good thermal path from the pipes to the carbon facings, honeycomb filling the empty space to provide robustness and two carbon facings. To build these components and assemble the complete structure different complex tools and machines are required.

- **Preparing the POCO foam:** Since the pipe is surrounded by closed-cell foam (POCO) the first step consists in machining the POCO foam so that it can house the pipe (Figure 4.1).

- **Bend and cut the pipe:** Pipes are cut to the desired length using a small handsaw and bent up to the indicated angle with two guide discs (one disc to check the length and diameter and the other one to correct the opening angle

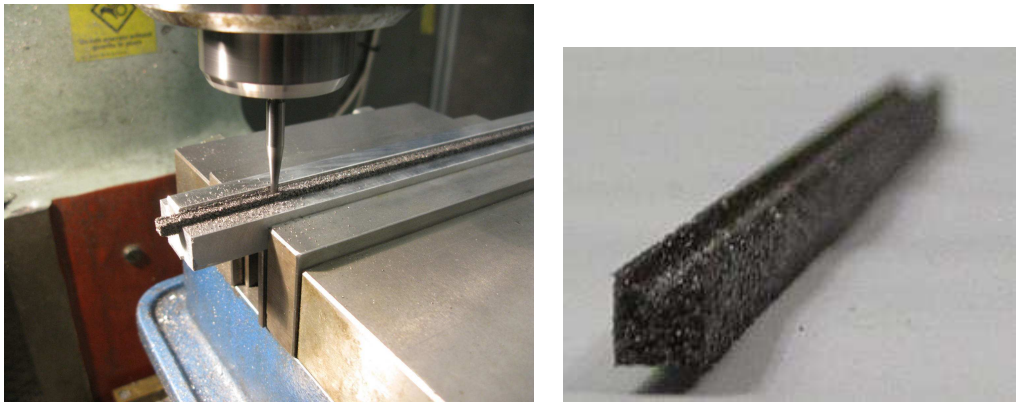

Figure 4.1: Machining of the POCO foam (left) and the resulting piece (right). The modelling of the base material piece goes first with a roughing down using a handsaw and then with a milling process. A custom-made milling cutter of circular cut is needed to mechanize the internal radius of contact with the pipes.

to the final measurement). Figure 4.2 shows a picture of the tool used to bend the pipe.

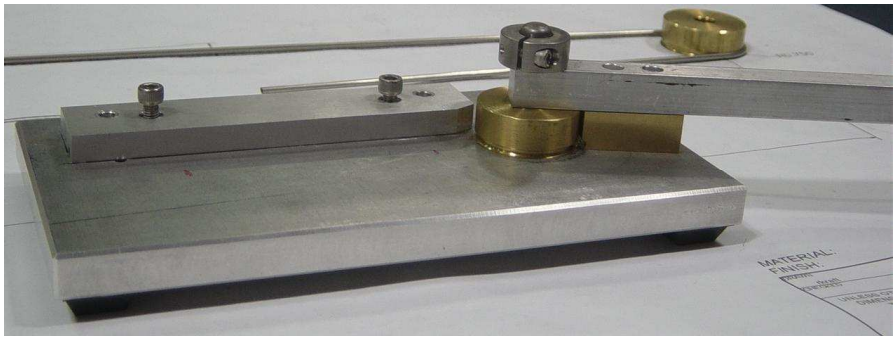

Figure 4.2: Tool used to bend the pipe using two guide discs, one to check the length and the final diameter and the other to correct the opening angle to the final measurement.

- **Glueing the POCO foam and pipe:** An aluminum platform with different holes for the positioning pins is used to house the pipes (Figure 4.3).

  A gel-like adhesive (*CGL* 7018) is used to assemble the pieces. All the foam parts are then put close to the aluminum bars and the pipes are inserted between the bars and the foam. When all the pieces have been placed the *CGL* is distributed onto all the joints. After 24 hours the subassembled foam can be extracted by taking out each aluminum bar carefully (Figure 4.4).

Figure 4.3: Aluminum platform used to glue the POCO foam and the pipes.

Figure 4.4: POCO foam and stainless steel pipes glued with CGL adhesive.

- **Preparing the Honeycomb:** Aluminum machined sheets are used to cut the honeycomb and place it in the honeycomb plate (Figure 4.5).

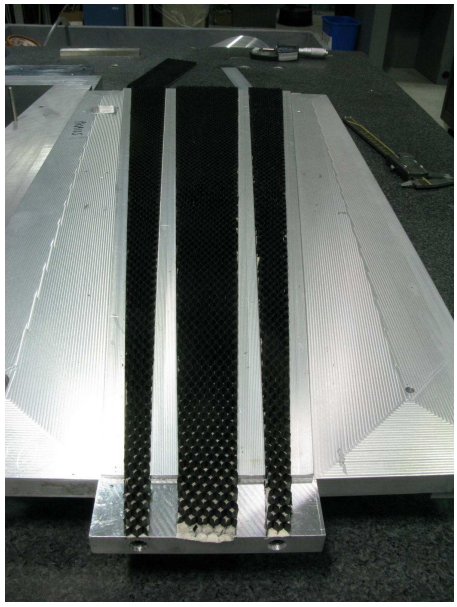

Figure 4.5: Honeycomb with final dimensions placed over honeycomb plate.

For the subassembly of the honeycomb an aluminium block is grinded and the side to place the honeycomb is machined using a CNC milling machine. Two handles have been placed onto the base in order to manage it more easily (Figure 4.6).

- **Assembly of the carbon facings:** The glue is spread out on the top of the foam using a machined tool wich controls the desired height of the glue layer (Figure 4.7).

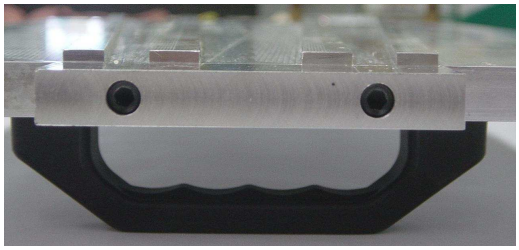

Figure 4.6: Handle attached to the aluminum base in order to manage the honeycomb structure easily.

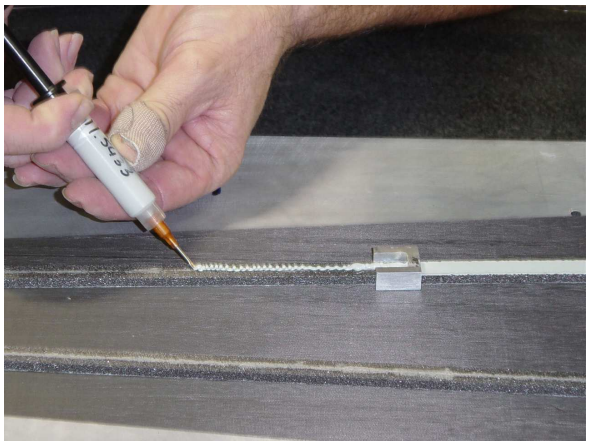

Figure 4.7: Tool used to control the height of the glue deposited on the POCO foam in the process of gluing to the carbon facing.

The foam is positioned on the facing contained in a vacuum base using two aluminium sheets as guide. Finally a central aluminium sheet is also placed (Figure 4.8).

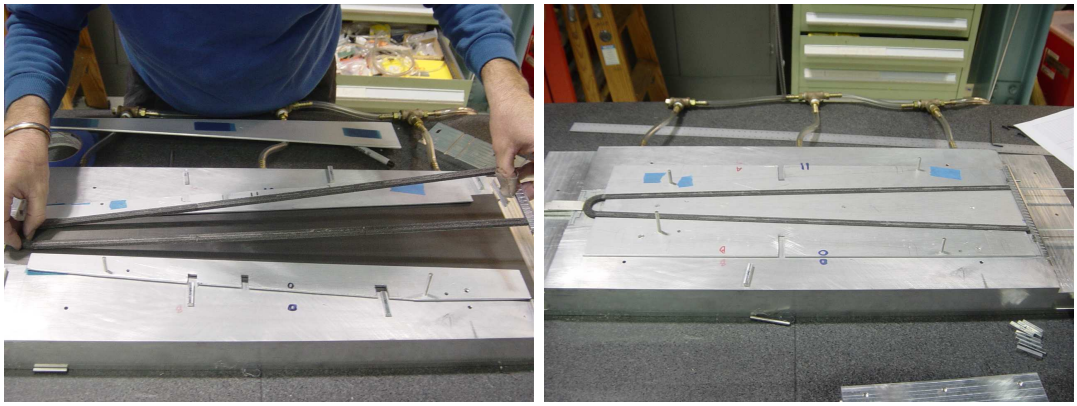

Figure 4.8: The foam is positioned on the facing using the aluminum sheets as guide (left) and then the central aluminum sheet is also placed (right).

After 24 hours CGL is distributed onto all the joints in the other face of the POCO foam in the same way as it was described in previous steps.

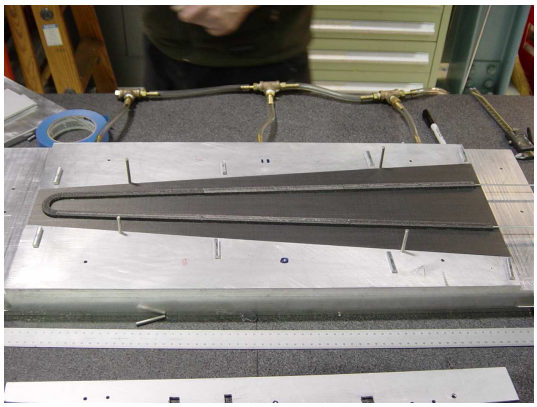

Figure 4.9: First carbon facing finally glued to the POCO foam and pipes.

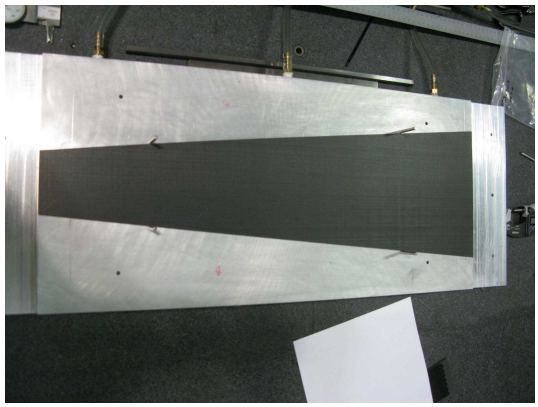

Figure 4.10: Second carbon facing placed on the vacuum base.

On the other hand the second carbon facing is attached to the honeycomb. The facing is fixed on the vacuum base using positioning pins and the compressor is then switched on (Figure 4.10).

To spread out the glue a polythene sheet is prepared and two sheets with an isolating tape are placed at the boundaries of a facing profile drawn in the polythene. All these pieces act as a facing mould and allow to adjust the epoxy to the desired height (0.584 mm).

Later on the honeycomb secured to the plate is immersed into the epoxy for 1 minute. The plate with the honeycomb is set on the vacuum base where the second carbon facing is. The structure has to cured during 72 hours.

- **Assembly of the closeouts:** The setup of foam and pipes is placed on the vacuum base. Then the closeouts are positioned on the ends of the vacuum base using their tooling base and covered with an epoxy. Then they are placed on the facings (figure 4.12).

- **Final assembly:** In order to avoid any curvature in the piece composed by the honeycomb and the facing, this piece is placed on an aluminum plate with the vacuum switched on and heated with a thermal blanket (Figure 4.13).

Figure 4.11: Polythene sheet with isolating tape which create a facing mould. This structure is used to contain the glue where the honeycomb will be immersed.

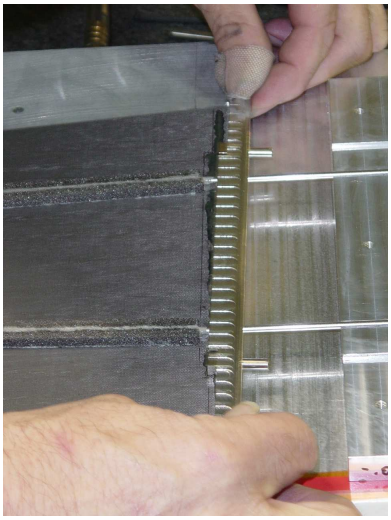

Figure 4.12: Once the closeouts are covered with epoxy they are placed on the facings of the Petal.

An epoxy glue[1] is applied over the POCO foam (which was previously glued to the facing) using the same tools and method described in earlier steps.

In the same way the honeycomb is submerged into epoxy[2] contained on a polythene sheet as described above and positioned close to the vacuum base.

[1]This epoxy is a mixture of HYSOL EA 9396 (52.63%), HYSOL EA 9396 accelerator (15.79%) and boron nitride (31.58%) which improves the thermal conductivity of the mixture.

[2]This epoxy is a mixture of HYSOL EA 9396 (76.9%) and HYSOL EA 9396 accelerator (23.19%).

Figure 4.13: A thermal blanket is used to avoid any curvature in the honeycomb. A heat-resistant and anti-adhesive plastic is put between the honeycomb and the thermal blanket.

With the help of the positioning pins both setups are fit properly (Figures 4.14 and 4.15).

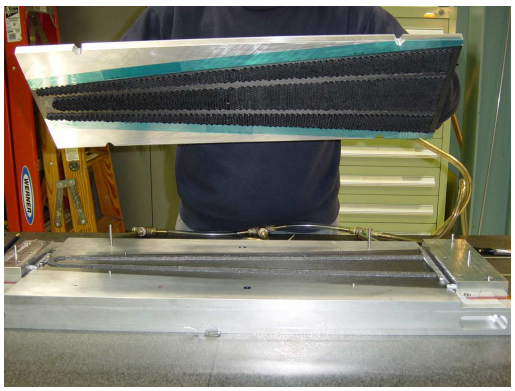

Figure 4.14: The honeycomb is positioned close to the vacuum base.

Figure 4.15: Honeycomb plate assembled to the vacuum base.

Once the epoxy is cured, the protective adhesive tape of the honeycomb system is carefully removed. After that a complete Petal core is finished and ready to proceed to mechanical tests (Figure 4.16).

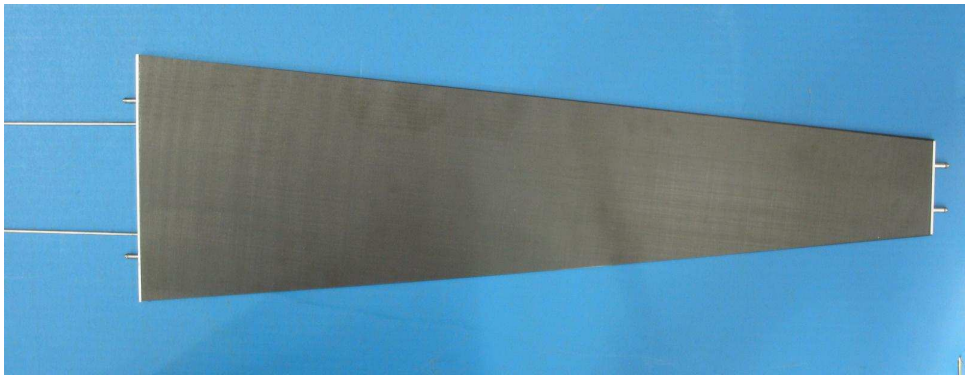

Figure 4.16: Petal core finished and ready for mechanical tests.

Two different Petal cores were built in total (figure 4.17). Although they are very similar, the second one includes some upgrades regarding the gluing steps and tooling modifications. Nevertheless in terms of thermo-mechanical aspects both prototypes are compatible. The major differences are summarize in table 4.1.

Prototype 1	**Prototype 2**
Carbon Facings K13D2U X/90X/X 0.21 mm	Carbon Facings K13D2U 90/0/90 0.21 mm
No Grinded Hcomb sandwich core	Grinded Hcomb sandwich core
	Hcomb gap reduction to any close element
9396; Honeycomb to Carbon Facing	
SS - CO_2 cooling pipe	
CGL between pipe & POCOFoam	
POCOFoam around SS pipe	
CGL; POCOFoam to Carbon Facing	9396 BN; POCOFoam to Carbon Facing
Top-bottom Al closeouts	
Positioning Pins	
CF tubes along sides	

Table 4.1: Major differences between the Petal prototypes built at Berkley.

Figure 4.17: Myself holding the two Petal cores at *IFIC*.

4.2 Thermo-mechanical Tests: Simulation and Experimental results

The tests described in this section have been done in order to check if the Petal specifications are preserved after fabrication, assembly and thermal cycles. The Petal prototype used in all these models and laboratory tests does not have silicon modules mounted on it.

4.2.0.2 Petal temperature profile

The *Finite Elements Analysis* (*FEA*) is a commonly used numerical method to perform solid mechanics simulations. A solid structure is built and boundary conditions are applied to recreate different scenarios.

The *FEA* simulations were carried out by the mechanics department of the institute using the *ANSYS* framework [93]. The first study simulated a steady state for a bare Petal with convection film coefficients as loads in the model. Different analysis were done modifying the bulk temperature on the pipes and environment conditions building a temperature profile on the Petal as can be seen in figure 4.18. The minimum

and maximum temperature achieved with the model are around -30 °C and -24 °C respectively.

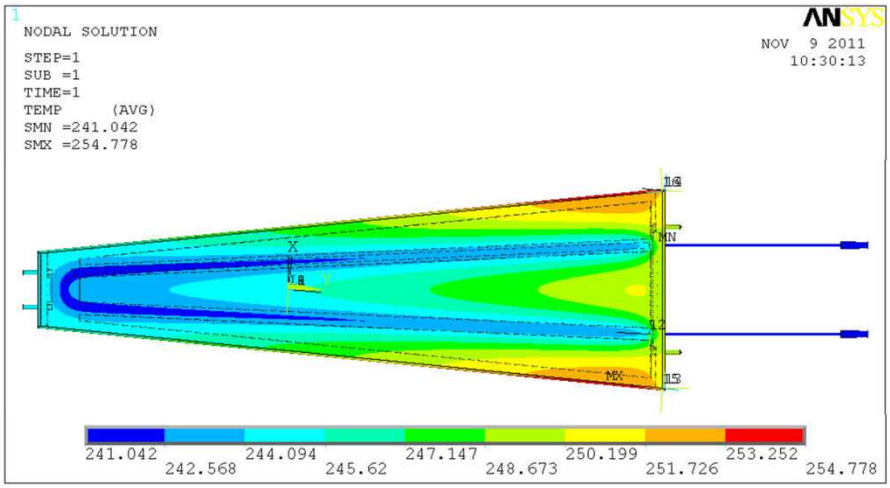

Figure 4.18: Petal core thermal *FEA* model. The temperature distribution on the Petal surface for a nominal temperature of the coolant (-30°C) is shown. For this simulation the air temperature was set to $T^{air} = 20°$C and the heat transfer coefficient to $h = 5\ W/(m^2K)$.

Figure 4.19: Petal CO_2 cooling system based on the open system developed by *NIKHEF* [94].

For the thermal tests in the laboratory the Petal prototype and an infrared camera (*ThermaCAM SC500*) were placed inside a large methacrylate box made at *IFIC*.

The CO_2 cooling system (figure 4.19) was based on the open system developed by *NIKHEF* [94].

The distance between the camera and the Petal prototype is approximately 90 cm. The Petal is fixed to the box using the metal support shown in figure 4.20 and the final setup can be seen in figure 4.21.

Figure 4.20: Metal support used to fix the Petal to the methacrylate box.

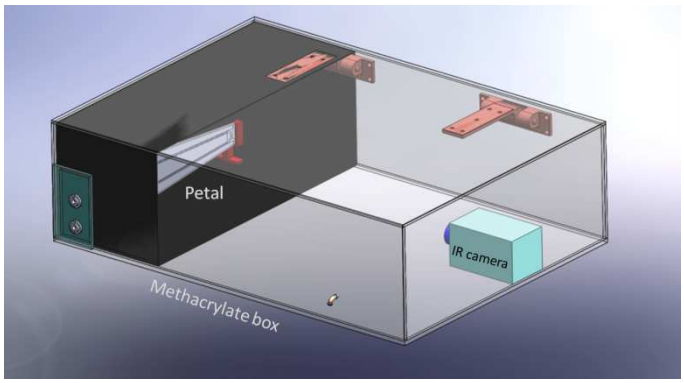

Figure 4.21: Setup used for the thermo-mechanical tests.

PT100 sensors where placed on the Petal surface to measure the temperature variation in different regions. These measurements can be compared also with the ones registered by the infrared camera.

The diagram of the different sensors locations along the Petal surface is shown in figure 4.22.

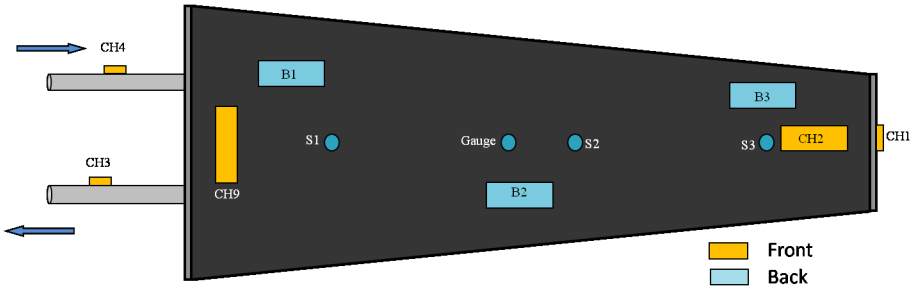

Figure 4.22: Diagram of the different sensor locations along the Petal surface. The *PT100*'s are labeled as CH_i and B_i. The capacitive sensors are labeled as S_i.

We can get the CO_2 temperature from the pressure using the *Mollier chart* which is a pressure-enthalpy diagram where the two phases (liquid-vapor) of the CO_2 are depicted. This diagram is shown in figure 4.23.

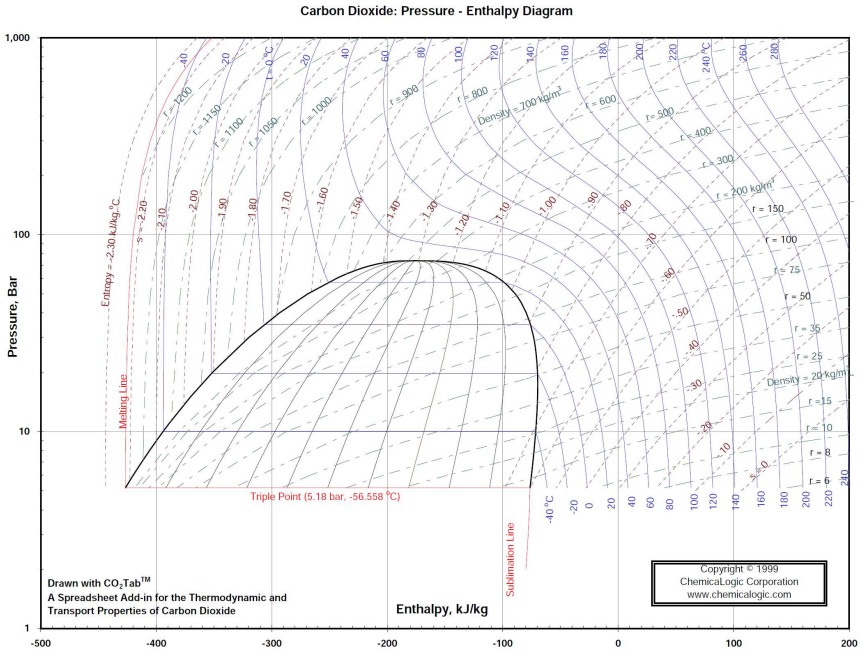

Figure 4.23: Mollier diagram for CO_2. Isothermal lines are shown as a function of the pressure and the enthalpy.

In this diagram isotherm lines are drawn as a function of the pressure and the enthalpy. The central region corresponds to the CO_2 change from liquid to vapor. For a given pressure we can obtain the temperature looking for the intersection with the corresponding isothermal line in that region. For instance, for a CO_2 pressure of

10 bar, looking at the diagram on figure 4.23, the corresponding isothermal line would be -40 °C.

The temperature variation in different positions of the Petal registered by the *PT100* sensors as a function of the input temperature (controlled with the CO_2 pressure) is depicted in figure 4.24.

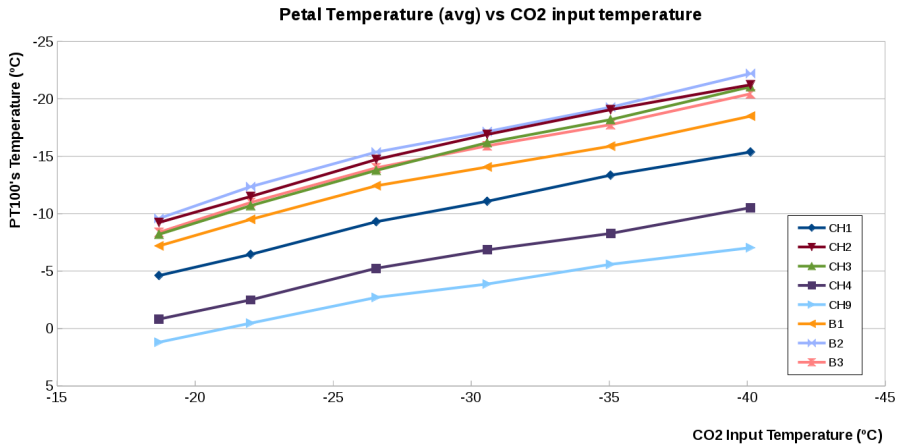

Figure 4.24: Variation of the temperature on the Petal surface registered by the *PT100* sensors as a function of the CO_2 input temperature.

Along the Petal all the *PT100* sensors have similar dependency with the temperature. The temperature measured at the end of the path (*PT100* B2) is lower than the temperature at the beginning (*PT100* B1) due the change of phase (gas to liquid) of the CO_2 inside the Petal. Along the pipes, the maximum temperature difference between the temperature sensors (B1, B2 and B3) is around 3 °C.

Using the *IR* camera we can monitor the temperature profile on the Petal surface. Figure 4.25 shows the temperature distribution for a 10 bar of CO_2 pressure. Note that the *IR* image has not been corrected by the emissivity of the different components.

From figure 4.25 the cooling pipes can be distinguished with uniform temperature along them. This allows us to verify if the Petal materials are glued properly. Otherwise, the thermal path from the pipes to the facings would be different and this could be detected on the *IR* image with a different temperature color scale.

The minimum measured temperature on the Petal surface all along the cooling pipe is depicted in figure 4.26.

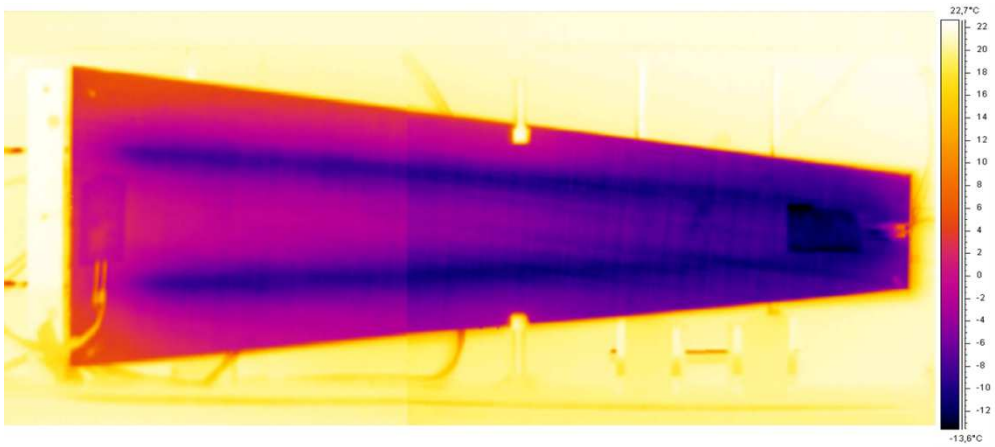

Figure 4.25: Temperature distribution on the Petal surface at 10 bar of CO_2 pressure as seen with the IR camera. Thermal uniformity is achieved along the cooling pipes. Note that the values are not corrected for emissivity.

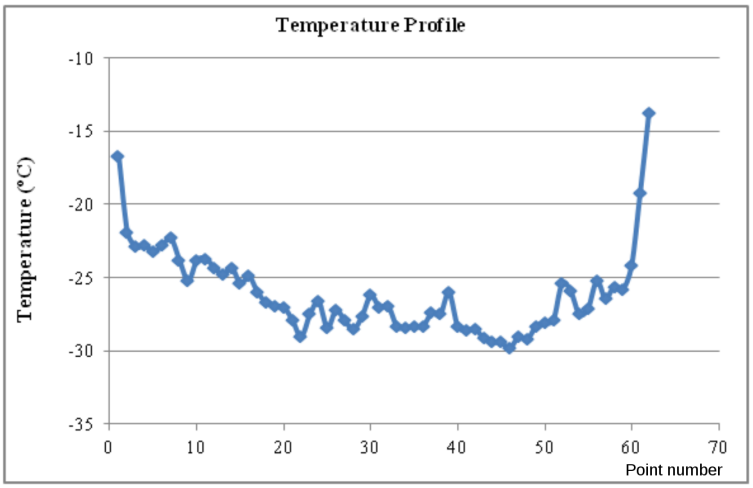

Figure 4.26: Minimum temperature along the pipe at 10 bar of CO_2 pressure registered by the *IR* image. Values corresponding to figure 4.25 and corrected using carbon fibre emissivity.

In this case the values have been corrected with the *IR* camera software using the carbon fibre emissivity (ε=0.8 at room temperature). Experimentally, to calibrate the *IR* camera, different materials with known emissivity (ε) and at a certain temperature (T) are used as reference. The emissivity and the temperature are correlated by the *Stefan-Boltzmann law*:

$$q = \varepsilon \sigma T^4 A \tag{4.1}$$

where *q* is the heat transfer, σ is the *Stefan-Boltzmann constant* and *A* is the area of the emitting object.

The obtained results (on average) for different CO_2 pressures are summarized in table 4.2.

	PT100 T (°C)								Camera T (°C)	
CO_2 P (bar)	CH1	CH2	CH3	CH4	CH9	B1	B2	B3	B1 location	B2 location
16	-9.3	-14.7	-13.8	-5.2	-2.7	-12.4	-15.3	-13.9	-12.1	-14,9
14	-11.1	-16.9	-16.2	-6.8	-3.9	-14.1	-17.2	-15.9	-15.1	-18.1
12	-13.4	-19.1	-18.2	-8.3	-5.6	-15.9	-19.3	-17.8	-16.3	-19.8
10	-15.4	-21.2	-21.1	-10.5	-7.0	-18.5	-22.2	-20.4	-19.4	-23.2

Table 4.2: Average obtained values of temperature along the Petal measured with the *PT100* sensors and the *IR* camera for different CO_2 pressures.

From table 4.2 the results present a very small difference (about 1 °C) between the temperature measured by the *PT100* sensors and the one registered by the *IR* camera. Therefore the *IR* camera is properly calibrated. Minimum temperatures of about -30°C can be reached at the Petal surface. With these tests we want to ensure that there are no risk of *thermal runaway*. The *thermal runaway* is a process in which the temperature of the silicon increases rapidly due to self-heating, leading to a temperature breakdown in the silicon. A high current flowing in the detector produces an increase of the temperature leading to higher current consumption which causes more heat in a closed loop that can destroy the sensor. Figure 4.27 shows a simulation of the highest temperature on a sensor as a function of its power.

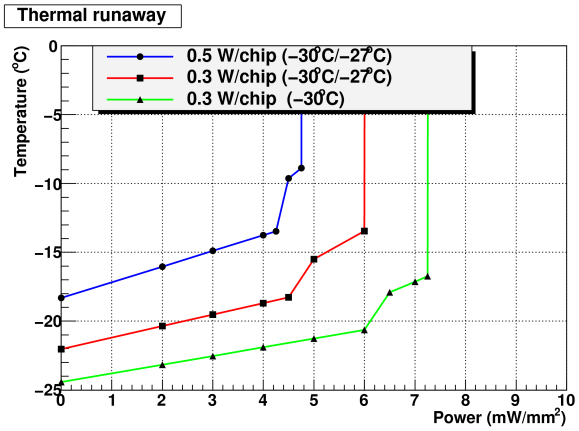

Figure 4.27: Highest temperature on silicon sensor as a function of its power. Coolant temperature of -30 °C (-27 °C in the return pipe). Considering a chip power around 0.3 $W/chip$, below -20 °C no thermal runaway is present [95].

Three different scenarios are simulated varying the power per chip and coolant temperatures (inlet and outlet). The total power in the silicon increases with the temperature leading to a critical point where a temperature breakdown occurs. From figure 4.27 the critical temperature values are between -15° C and -20° C.

We can make an estimation of the expected temperature at the silicon surface on a Petal using basic *heat transfer formula*. Considering a system composed by different materials, as the one presented in figure 4.28, the total heat transfer can be calculated with [96]:

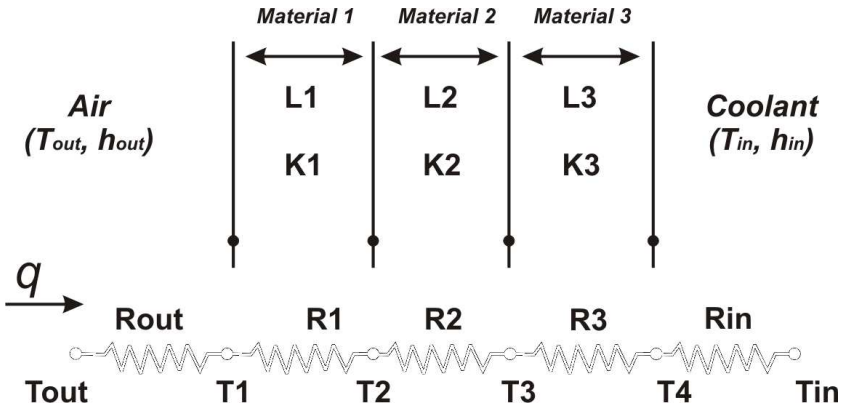

Figure 4.28: Heat transfer of a system composed by different materials.

$$q = \frac{T_{out} - T_{in}}{\sum R_i} \tag{4.2}$$

with R_i the thermal resistivity of each interface in the heat transfer path. For this basic calculation we only consider convection and conduction and the same area in all the materials (A). Therefore, each thermal resistivity is given by:

$$R_{convection,i} = \frac{1}{h_i \cdot A} \tag{4.3}$$

$$R_{conduction,i} = \frac{L_i}{\kappa_i \cdot A} \tag{4.4}$$

where h_i are the *convection heat transfer cofficients* between the silicon surface and the air, and between the CO_2 and the pipe, L_i are the different materials thicknesses and κ_i the *conduction coefficient* between them. The heat transfer (q) can be also writen as:

$$q = \frac{T_{out} - T_1}{R_{out}} = \frac{T_1 - T_2}{R_1} = \frac{T_2 - T_3}{R_2} = ... \tag{4.5}$$

with T_i the temperature of each interface. Figure 4.29 shows an sketch of the different Petal materials we have below the silicon sensors.

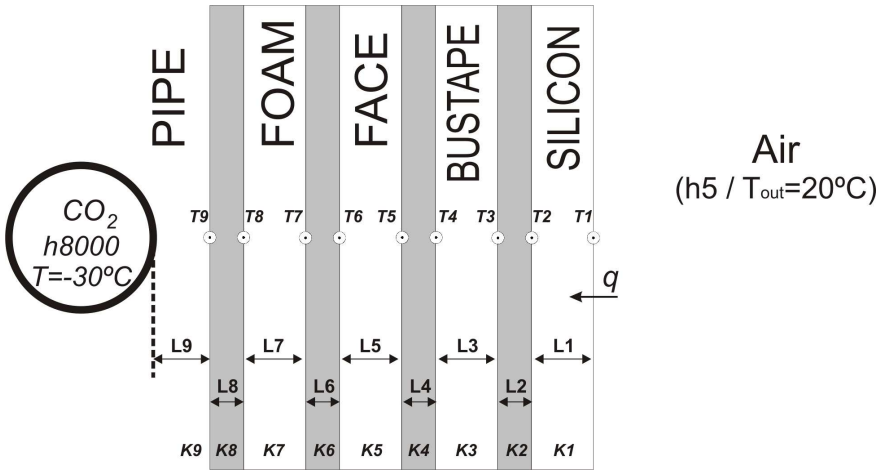

Figure 4.29: Petal materials considered to obtain the silicon temperature.

Using the material properties that are listed in table 4.3 the heat transfer is:

$$q = \frac{T_{out} - T_{in}}{\sum R_i} = \frac{293.15 - 243.15}{0.2} = 249.8\ Wm \tag{4.6}$$

Material Properties				
Part	**Material**	**L (mm)**	**κ (W/mK)**	**h (W/mK^2)**
Coolant (T_{in}=-30°C)	CO_2	—	—	8000
Pipe	Titanium	0.15	16.4	—
Pipe to Foam	Hysol Glue	0.1	1	—
Foam	Allcomp	5	30	—
Foam to Face	Hysol Glue	0.1	1	—
Face	K13C2U 0-90-0 CFRP	0.15	90/1/180	—
Face to Bustape	Hysol Glue	0.1	1	—
Bustape	Polyl/Cu/Al	0.2	0.17/0.24/0.17	—
Bustape to Sensor	DC SE4445 Glue	0.2	2	—
Sensor	Silicon	0.32	191	—
External Air (T_{out}=20°C)	—	—	—	5

Table 4.3: Properties of Petal materials from coolant to CO_2. Values taken from [97].

Therefore, using 4.5 we can extract the temperature at the silicon surface:

$$T_{Silicon} = T_{out} - q \cdot R_{out} \tag{4.7}$$

With these basic calculations (that do not consider the electronics above the sensors), the expected silicon temperature is around -29° C. With this temperature we are within enough safety margin to avoid the *thermal runnaway*.

In general, the minimum temperature achieved at the Petal surface with the thermal tests at the laboratory is also compatible with the results obtained by the *FEA* simulation presented above. The comparison between the results will be discussed in section 4.2.0.4.

4.2.0.3 Petal deflections and strains

From the results obtained in the previous *FEA* simulation a second study was carried out including a thermo-mechanical analysis with two more inputs as the reference temperature and the constraints used in the tests. The parameters of interest would be the deflections and strains on the Petal (longitudinal and out of the plane). These parameters were measured also on laboratory tests and are obtained at defined points along the Petal. An example of the thermo-mechanical solutions with *ANSYS* is shown in figure 4.30.

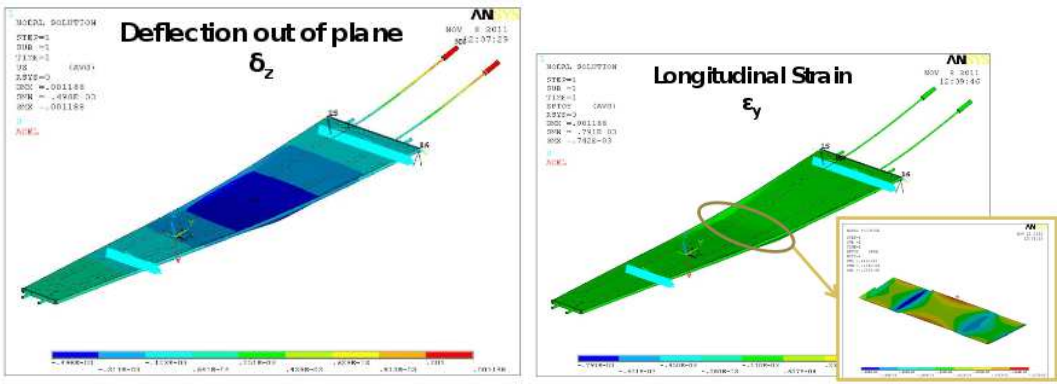

Figure 4.30: Deflections and strains obtained with the *FEA* model for the Petal structure.

The values obtained with the *ANSYS* model are summarized in table 4.4.

	Mechanical FEA		**Thermal FEA**	
	Span (mm)	**Load (g)**	**Air T^{re} (°C)**	**Cooling T^{re} (°C)**
	450	1250	20	-32
Deflection out of plane (μm)	147		36	
Longitudinal Strain ($\mu\varepsilon$)	24.1		53.7	

Table 4.4: Results acquired with thermo-mechanical *FEA* simulations on Petal prototype.

Mechanical Deformations on Petal

For the mechanical deformations test at the laboratory a *three point bending test* varying loads and spans is carried out. The Petal is placed in an aluminium base rested in two points and a load is applied in the centre of mass. Using a vision machine the arrow that appears is measured. The loads and the distance between points are varied to measure the deflections and at the same time a gauge is used to measure the longitudinal strain as shown in figure 4.31.

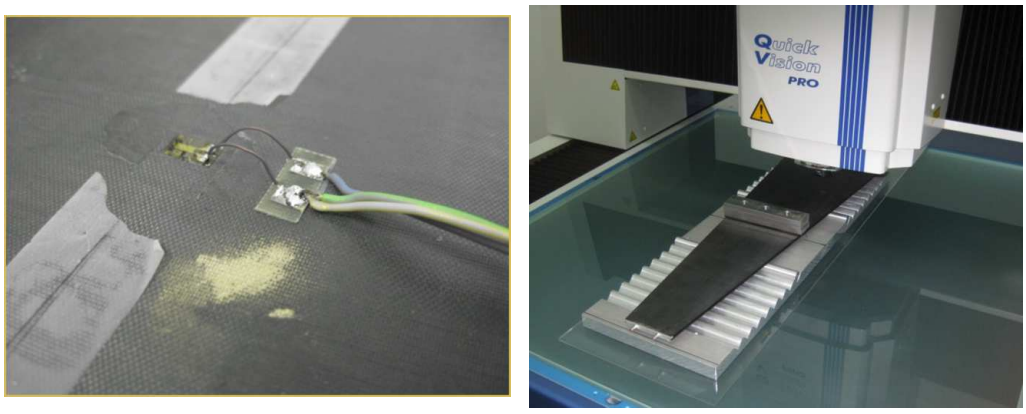

Figure 4.31: Strain gauge detail for measuring longitudinal strain on the bottom face of the Petal (left) and measuring process of the deflection on the top face of the Petal with a vision machine

Figure 4.32 shows the deflections and longitudinal strains as a function of the different spans for the Petal prototype. The results for a constant value of the span and for the different applied loads are summarized in table 4.5.

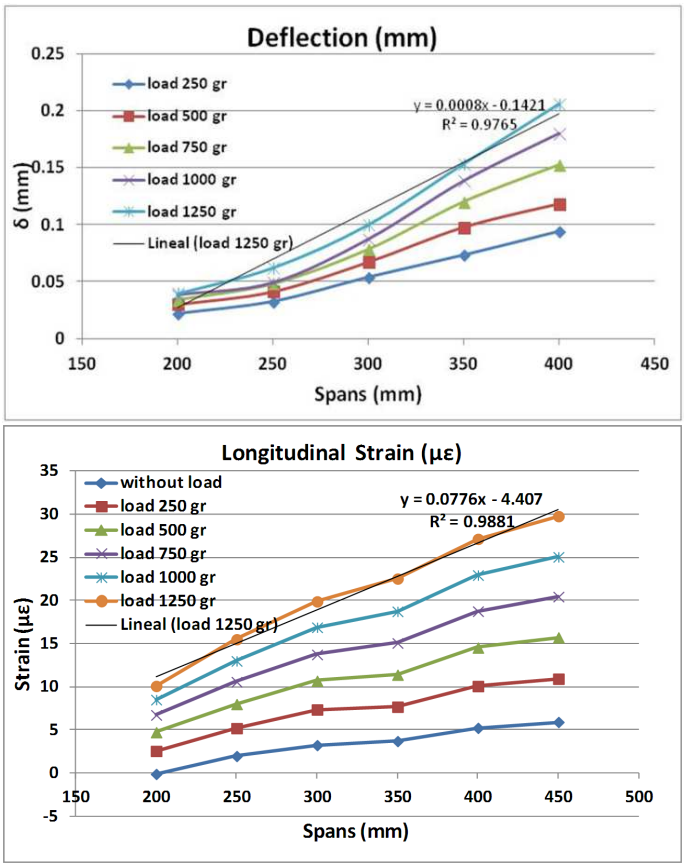

Figure 4.32: Plots of deflections (top) and strains (bottom) for the Petal prototype.

Span (mm)	Load (g)	Deflection (μm)	Longitudinal Strain ($\mu\varepsilon$)
450	500	81.2	15.72
450	750	118.2	20.43
450	1000	159.6	25.04
450	1250	196.6	29.75

Table 4.5: Deflections and strains obtained for different applied loads on the Petal prototype.

From the deflections presented above, the *Young's modulus* of the Petal facings can be calculated using the *ASTM* standard formulii [98]. Considering a simple sandwich structure, the deflections are a function of the applied loads:

$$\delta = \frac{PL^3}{48D} + \frac{PL}{4U} \tag{4.8}$$

where P is the applied load and L is the length or span of the supports. (D, U) are

parameters that depend on the geometry and mechanical modulus and are given by:

$$D = \frac{E_f b(d^3 - c^3)}{12(1 - v_f)} \tag{4.9}$$

$$U = G_c b \frac{(d + c)^2}{4c} \tag{4.10}$$

where v_f is the *Poisson's ratio*, *b* is the sandwich width in the middle section (b = 139.46 mm), *c* is the sandwich core thickness (c = 5.01 mm) and *d* is the total Petal thickness (d = 5.51 mm). E_f and G_c are the *Young's modulus* at the facings and the core respectively. From 4.8, representing the maximum deflections (normalized to maximum load and distance) (δ/PL) as a function of the square of the distance (L^2) we obtain a linear distribution (figure 4.33) which equation is given by:

$$\frac{\delta}{PL} = \left(\frac{1}{48D}\right) L^2 + \frac{1}{4U} \tag{4.11}$$

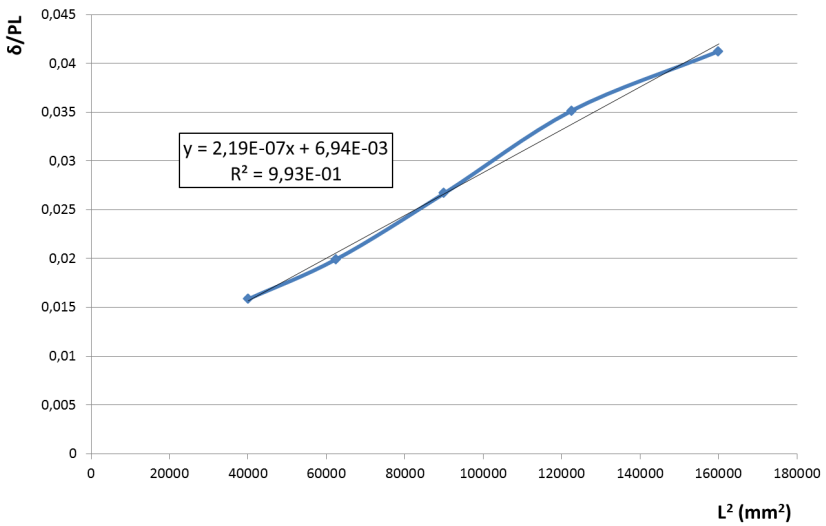

Figure 4.33: Maximum deflections (normalized to maximum load and distance) (δ/PL) as a function of the square of the distance (L^2).

The trend of the linear fit and the ordinate at the origin will provide the (*D*, *U*) parameters respectively. With them, and using 4.9 and 4.10, we obtain:

E_f = 215 GPa and G_c = 47 Mpa.

However the standard formulii used to derive these properties are for rectangular shapes so these parameters could only be used as an estimation.

Thermal Deformations on Petal

Three capacitive sensors have been used to measure the transversal deflections on the Petal, caused by low temperature and holding influences. A gauge[1] is also included in the setup for the longitudinal strains measurements. The diagram of the different sensors locations along the Petal surface was shown in figure 4.22.

Figures 4.34 and 4.35 show the strains and deflections results on the Petal (longitudinal and out of the plane), as a function of the input temperature, obtained at defined points.

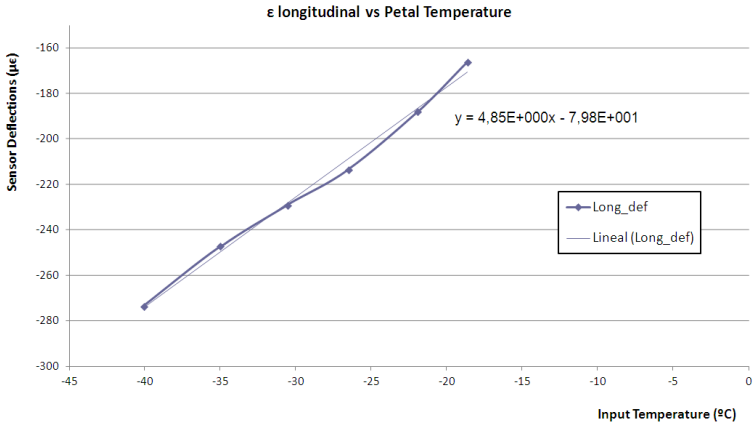

Figure 4.34: Longitudinal strains on the Petal measured with the gauge.

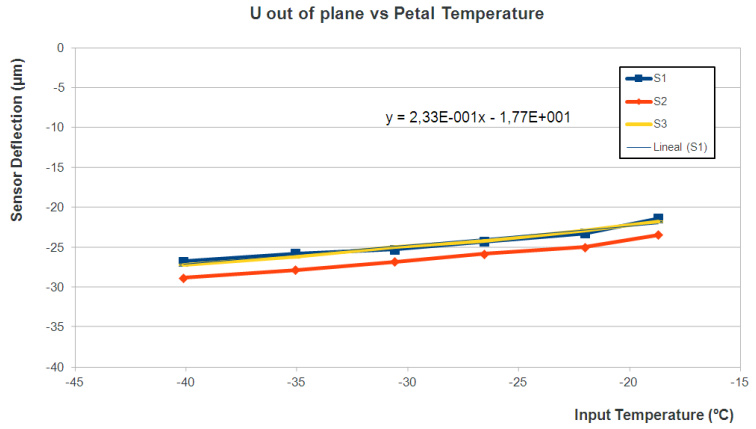

Figure 4.35: Transversal deflections measured by the capacitive sensors.

[1] The gauge measures small deflections per length and the unit $[\mu\varepsilon]$ will correspond to $[\mu m/m]$

Table 4.6 includes the results on average measured by the capacitive and gauge sensors.

CO_2 pressure	S1 avg. def. (μm)	S2 avg. def. (μm)	S3 avg. def. (μm)	Gauge strain ($\mu\varepsilon$)
20.5	-21,35	-23,4	-21,75	-166,1
18.5	-23,25	-24,95	-22,9	-188
16	-24,25	-25,8	-24,2	-213,5
14	-25,25	-26,8	-24,95	-229
12	-25,75	-27,8	-26,2	-247,2
10	-26,75	-28,8	-27,2	-273,5

Table 4.6: Results for the deflections and longitudinal strains on the Petal.

The response of the capacitive sensors is linear with the temperature, with a slope of 0.24 $\mu m/^{\circ}C$ (average of the three sensors). Regarding the longitudinal deflection measured with the gauge, a linear response is also obtained with a slope of 4.8 $\mu\varepsilon/^{\circ}C$. This means a total Petal deflection of about (4-5) $\mu m/(m^{\circ}C)$ in the longitudinal direction. Despite these values are not very high they should be taken into account during the decision of the final Petal fabrication materials. This is the case of the glues, for example, which should be flexible to deal with these deformations. Therefore the Petal temperature must be also well controled to guarantee that the deformations are within the specifications.

4.2.0.4 Simulation and Laboratory comparison

Tables 4.7 and 4.8 present a summary of the results for the mechanical and thermal *FEA* model calculations compared to the experimental tests results in the laboratory.

	Mechanical Test Span = 450 mm / Load = 1250 g		
	FEA simulation	**Lab. Test**	**Difference**(%)
Deflection out of plane (μm)	147	196.6	25
Longitudinal Strain ($\mu\varepsilon$)	24.1	29.75	19

Table 4.7: Comparison of the mechanical results obtained for the *FEA* simulation and the laboratory tests.

The experimental results obtained for the mechanical deformations are consistent with the expected values provided by the *FEA* analysis. We have to take into account that the simulated model can not reproduce the real setup conditions in detail due

to their complexity. The external conditions, such as the Petal holding or the room temperature distribution, have huge influence on the measurements and having discrepancies between simulation and laboratory results is frequent.

The mechanical deformations presented small differences. The Young's modulus of a Petal facing obtained from the laboratory results presented in table 4.7 is 215 GPa (from standard formulii for rectangular shape). From the FEA, the same Young's modulus is around 376 GPa. This modulus is highly dependent on the material properties used in the simulation and this difference gives us an idea of how much we need to improve our model.

	Thermal Test $Air\ T^{re}$ **= 20°C /** $CO_2\ T^{re}$ **= -32°C /** CO_2 **P = 12 bar**		
	FEA simulation	**Lab. Test**	**Difference**(%)
Deflection out of plane (μm)	36	27.8	23
Longitudinal Strain ($\mu\varepsilon$)	53.7	247.2	78
Minimum Temperature (°C)	-30	-29.8	0.7
Maximum Temperature (°C)	-24	-13.8	42

Table 4.8: Comparison of the thermal results obtained for the *FEA* simulation and the laboratory tests.

Regarding the results from the thermal stress (table 4.8), the minimum temperature achieved in the Petal surface is coherent with the simulations. The deflections out of plane are of the same order of magnitud but the maximum temperature and the deviations in the longitudinal strain have huge difference between laboratory and *FEA* results. With the *FEA* model the calculated deviations between the maximum and minimum temperatures are of about 6°C. However, in the laboratory we measured a higher deviation of about 16°C. Some Petal properties could not be properly simulated and the effective values used were not the appropiate ones. During the first Petal simulations the properties of the final materials used during the fabrication process were not well known and aproximate values were used to estimate different Petal parameters. The conductivity of the materials, for instance, would have huge influence in the final results. More restrictive values of the conductivity would lead to higer temperature variation. The temperature and the longitudinal deformations are linearly correlated and this could explain the difference between the *FEA* simulations and the laboratory results. Using the temperature difference of 16°C obtained at the

laboratory, we would have a longitudinal strain of about 144 $\mu\varepsilon$ which is more consistent with the obtained experimental values. Moreover the external conditions during the measurements, such as the room temperature and the humidity inside the metacrilate box, can not be perfectly controlled and this also makes an important difference with the *FEA* model. As we have mentioned before, these were the first *FEA* studies made with the Petal structure and the complete object was not perfectly modellated. Each Petal component has huge number of parameters to be controlled and it is really challenging to obtain a real scenario. These first tests give us an idea of how precise is our *FEA* model and which range of values should we expect in a real experiment. Despite the *FEA* and laboratory setup limitations the Petal deformations are under acceptable values and the achieved temperatures are within a safety range to avoid the *thermal runaway* in the silicon sensors.

4.3 Metrology of Petal prototypes

To measure the planarity of the Petal prototype two different configurations have been used: Petal held in a horizontal plane and in a *flag-like* configuration. An optical system and a coordinate measurement machine are employed respectively.

- **Horizontal configuration measurements**

  In this case the Petal is lying on a horizontal plane as shown in figure 4.36. The Petal is fixed with to pieces that keep the Petal support pins always at the same height with respect to the machine plane.

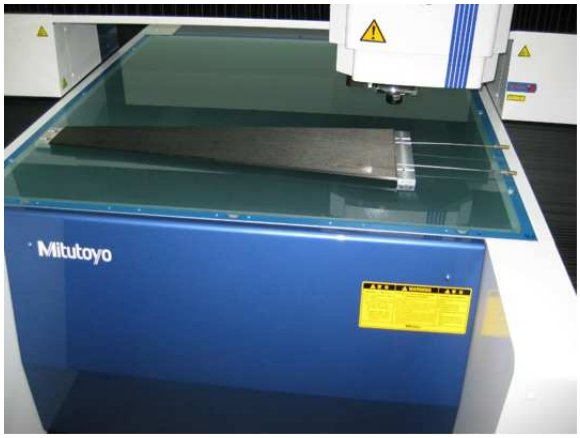

Figure 4.36: Optical system used to measure the surface of the Petal

With the camera we measured a grid of points in the Petal surface. All the points are converted to the coordinate system in which the dispersion in *Z* (normal to the surface) is minimal. This is in fact the reference defined by the eigenvectors of the covariance matrix built with all the data points.

The results are depicted in figure 4.37. The *3D* representation of the Petal surface and the projection into the *Z-X* plane (height-length) are shown.

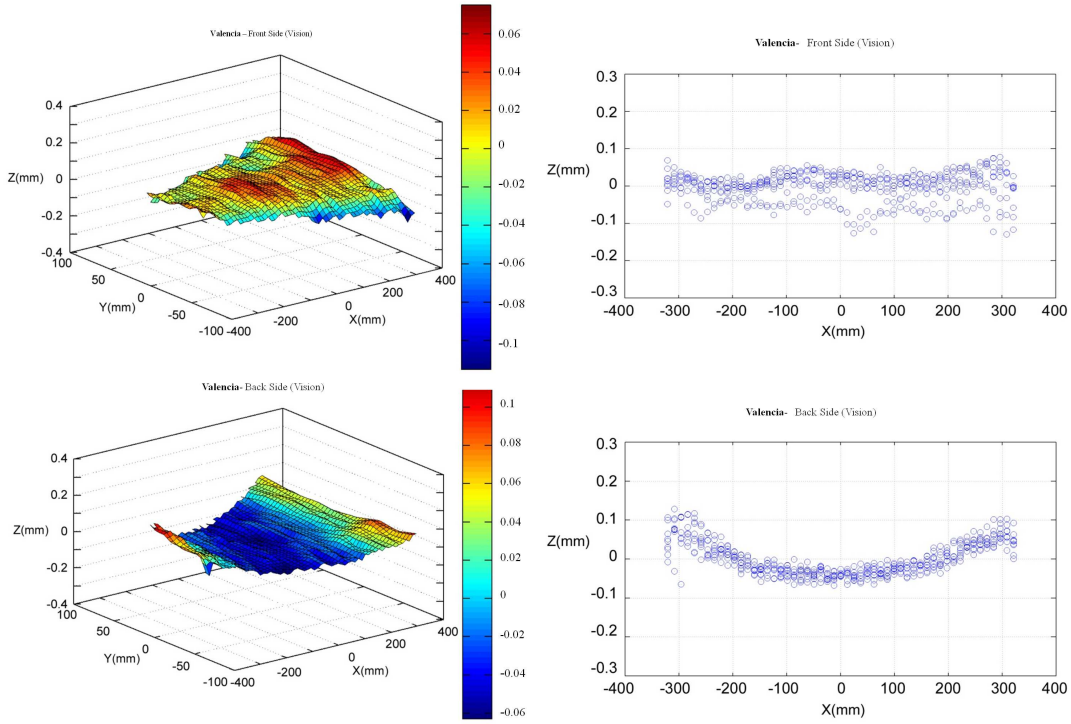

Figure 4.37: Petal surfaces as measured by the optical system. Left column shows the *3D* representation and the right column the projection on the *Z-X* plane.

A bow along the Petal length can be clearly appreciated in the back side. This is very likely due to gravitational sag but it is not seen in the front side. Different aspects of the fabrication process can also affect the planarity of the Petal such as the amount of glue deposited along the facing. Despite this is the less restrictive way of holding the structure it can also affect to the measurements introducing forces at the Petal extremes. Nevertheless, the specifications stablish an average planarity within $\pm$ 100 μm and all the points meet the specifications from the average along *Z*.

- ***Flag-like configuration measurements***

  In the second configuration a coordinate measurement machine (CMM) is used. This machine has a motorized automated probe head with electronic touch trigger probe shown in figure 4.38. As in the case of the optical system all the points are converted to the coordinate system in which the dispersion in Z (normal to the surface) is minimal.

Figure 4.38: Coordinate measuring machine with a touch trigger probe where we measured the Petal in a "flag-like" configuration.

The Petal is held in two different ways. One with 4 high stiffness constrain points and the second with 2 high stiffness points on the wide (top) side of the Petal and 2 low stiffness points on the narrow side (bottom) of the Petal. The result of the first configuration (4 stiff points) is shown in figure 4.39.

In the back side plot a torsion in the Petal is clearly appreciated and the deviation in Z is wider. As commented before, the holding of the structure can really affect to the planarity results. This is the most restrictive method and this can cause the Petal torsion.

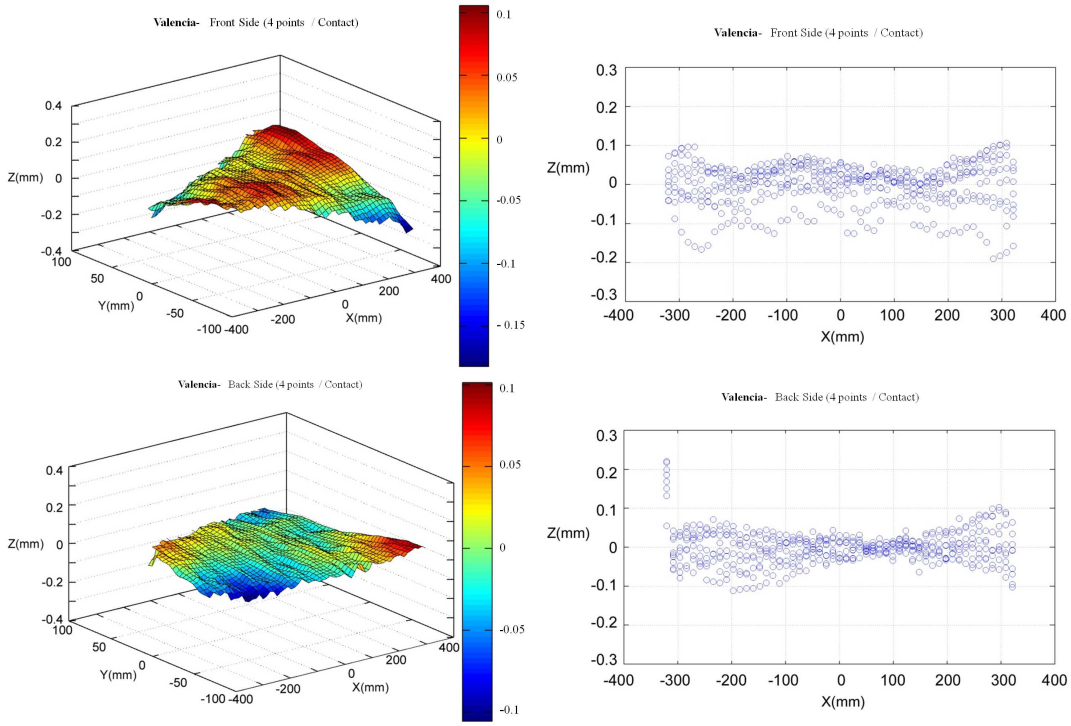

Figure 4.39: Petal measurements on the CMM with touch probe and 4 high stiffness constrains.

Leaving more freedom in the narrow part (2 low stiffness points) of the Petal, the data shown in figure 4.40 are obtained.

In this case a small bow is also seen in the back side but not in the front side. With this configuration the Petal torsion disappears and the deviation between the data points is lower. As for the optical system, all the results are within the specifications.

Despite the *flag-like* configuration is more restrictive than the optical system it allows us to obtain an estimation of the Petal thickness. It is calculated combining the data from the CMM relative to the two sides of the Petal (figure 4.41).

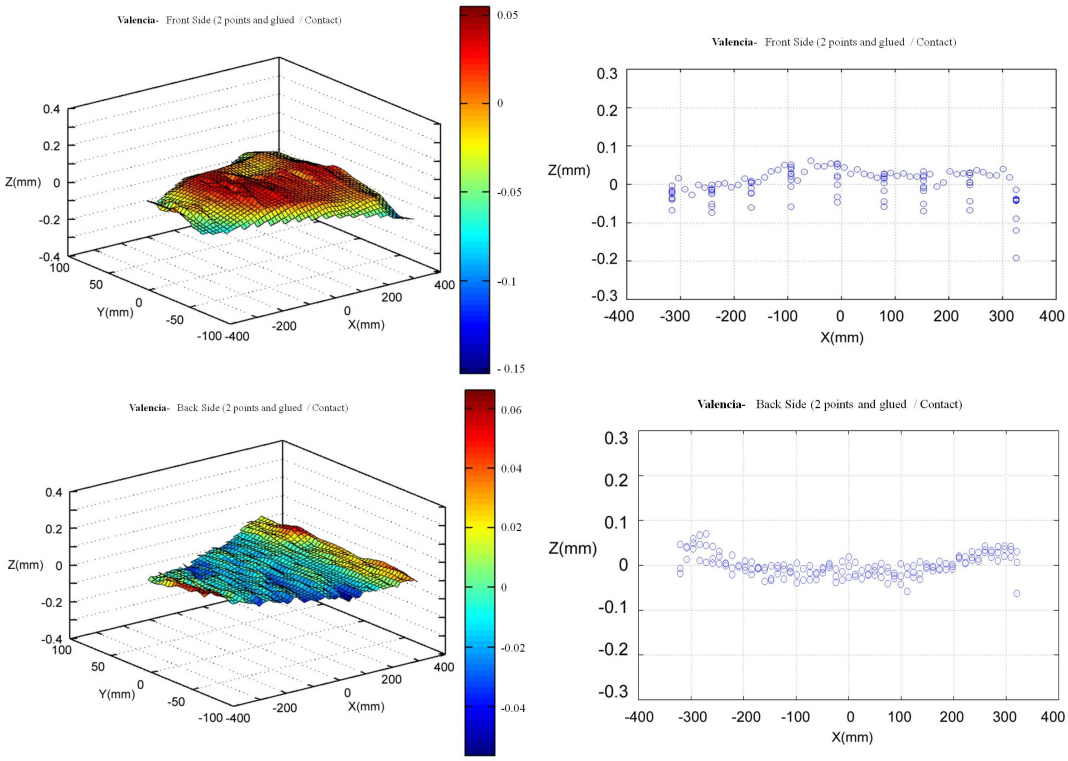

Figure 4.40: Results with 2 high stiffness constrains on the wide side and 2 low stiffness constrains in the narrow side of the Petal.

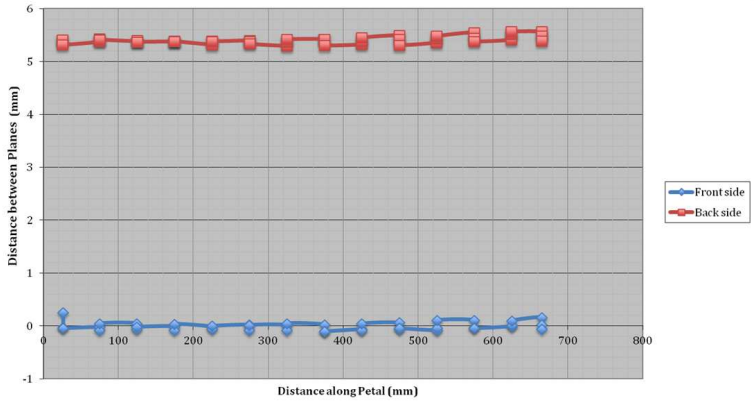

Figure 4.41: Plot combining the data points from the front and back sides of the Petal. The points come from the CMM and are all referred to the front side plane.

The measurements are quite linear in both sides. No deformations are appreciated and the Petal thickness is measured to be 5.4 mm.

4.4 Microstrip silicon detectors from Hamamatsu (ATLAS12A)

As introduced in chapter 2 the ATLAS ITk-Strips in the HL-LHC will have to deal with a fluence[1] of about 1.5×10^{15} 1MeV n_{eq}/cm^2 in the inner-most part and 5×10^{14} 1MeV n_{eq}/cm^2 in the outermost part. With these high dose of radiation expected over the sensors, their design must guarantee good operation during the whole lifetime of the experiment.

P-type sensors will be used for the ITk-Strips in the HL-LHC. Hamamatsu Photonics [99] has built different silicon sensor prototypes with specifications really close to the required by HL-LHC . The general specifications of the Hamamatsu wafers and sensors for the ITk-Strips system can be seen in table 4.9.

ATLAS12A General Specificacions	
Mask Requirements	
Silicon wafer diamenter	6 in. (150 mm)
Number of strip segments	4
Number strips per segment	1282
Orientation	<100>
Readout implant strip width	16 μm
Readout strips	22 μm
Readout	200×56 μm bond pads
Angle (θ) of stereo strips	40 mrad
Mechanical/Optical Properties	
Thickness	(310±25) μm
Uniformity of thickness within one sensor	10 μm (i.e. central value ±5 μm)
Flatness	within 200 μm
Electrical Properties	
Wafer bulk type	p-type, FZ
Initial Depletion voltage (V_{dep})	$V_{depletion} <$ 300 V
Resistivity	$>$ 3 kΩ cm (2.5 kΩ cm / $V_{dep} < 380\ V$ [100]
Maximum operating voltage	600 V
Total initial leakage (at 20°C)	$<$ 0.1 μA/cm^2 at 600 V
Resistance of n-implant strip	$<$ 20 kΩ/cm
Strip readout coupling	AC
Resistance of aluminium readout strips	$<$ 15 kΩ/cm
R_{bias} (Polysilicon)	1.5±0.5 MΩ resistor bias
$R_{interstrip}$	$>$10× R_{bias} at 300V
Strip isolation method	Narrow-common p-stop
Interstrip Capacitance (per side)	$<$ 0.9 pF/cm at 300 V, measured at 100 kHz
$C_{coupling}$	≥20 pF/cm, measured at 1 kHz

Table 4.9: Hamamatsu ATLAS12A large-area silicon microstrip sensor technical specifications. Values taken from [101] and [102].

[1] These fluences include a safety factor of two in the estimation.

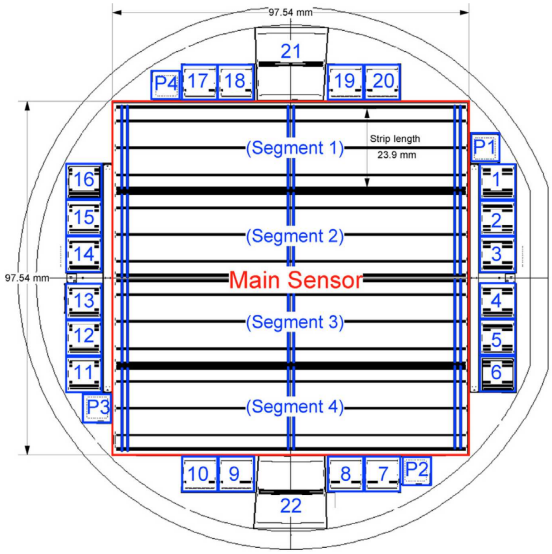

Figure 4.42: Mask layout of the ATLAS12A sensor in 6-in. wafer. The miniature sensors are labeled with the position numbers 1-24 and the $8 \times 8 mm^2$ diodes as P1-P4 [102].

Due to the high cost of the fabrication process and the sensitive handling of the sensors, fully-diced miniature sensors and test structures are built to carry out the first studies on the sensors performance (pre- and post-irradiation). These structures are included in the same wafer that the full size sensors. A view of the wafer layout is shown in figure 4.42.

The miniature sensors have rectangular shape which has a design similar to the main sensor. Each sensor has an outer dimension of (1×1) cm, with 104 readout strips, 8 mm long and a strip pitch of 74.5 μm.

In the start-up of the design process of the endcap sensors there were different options:

- **"Square" trapezoid:** A first alternative with a "square" trapezoid sensor shape to maintain symmetrical geometry with the Petal shape. To make the stereo angle the strips are inclined 20 mrad in a fan geometry. In this case the strips will not be parallel to the sensor edges so the latest strips do not reach the bonding pads and will not be connected to the readout electronics. These strips are called *orphan strips* and a drawing of the design can be seen in figure 4.43.

  To avoid "dead areas" in the sensor a solution was to gang the orphan to the neighbouring strips (that are connected to readout electronics). The connection

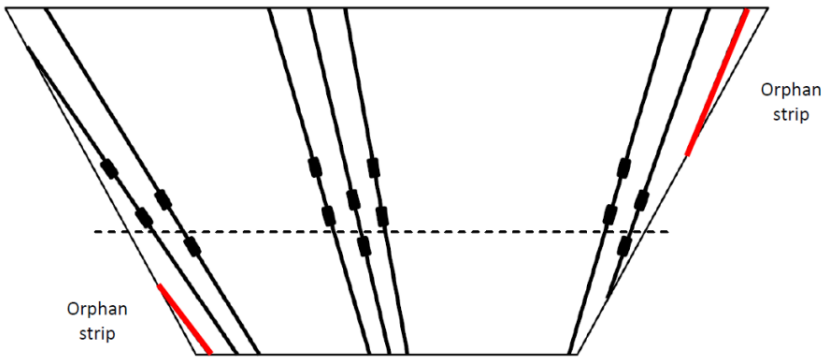

Figure 4.43: "Square" trapezoid sensor design with orphan strips (in red) near the sensor edges. These orphan strips do not reach the bonding pads. A proposed solution was to gang these *orphan strips* to the neighbouring ones.

can be made to the AC readout metals (*AC-ganging*) or between the strip implants (*DC-ganging*). In figure 4.44 both connections are depicted.

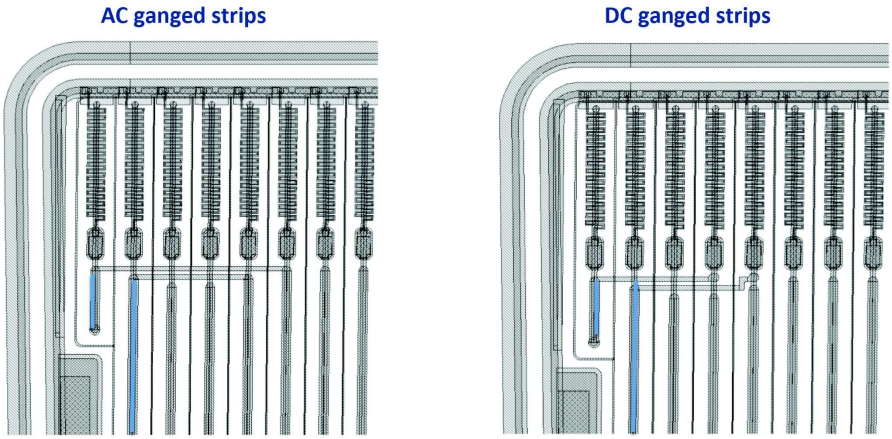

Figure 4.44: Possible solutions for connecting the *orphan strips*. *AC-ganging* connection (left) is made to the AC readout metals and *DC-ganging* (right) is made between the strip implants.

Figure 4.45 (left) shows a sensor with this "square" design.

Different strip pitches were also implemented in these sensors (small and large pitch). A summary of the principal parameters of the "square" trapezoid sensors can be seen in table 4.10.

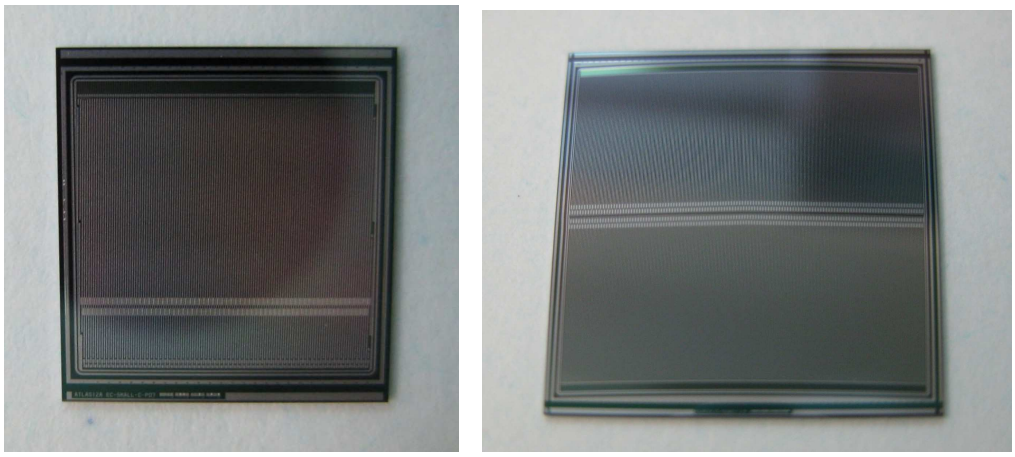

Figure 4.45: (Left) Picture of an ATLAS12A sensor with "square" design. In this sensor the strips are not parallel to the sensor edges and *orphan strips* appear. (Right) Picture of an ATLAS12A sensor with "skewed" design. In this case the strips are parallel to sensor edges and the perimeter has circular shape.

	Endcap "square" design (small pitch)	**Endcap "square" design (large pitch)**
Inner dimension of bias ring length × wide/narrow width (area)	8.14×8.52/8.33 mm^2 (0.686 cm^2)	8.14×8.58/8.37 mm^2 (0.690 cm^2)
Number of strips at wire-bonding pads	127	79
Strip Length (θ; stereo angle)	8.05/$cos\theta$ mm	
Strip Pitch wide/narrow	65.06/63.55 μm	104.69/102.05 μm
Angle (θ) of stereo strips	20 mrad	

Table 4.10: Principal parameters of the "square" trapezoid design for small and large pitch sensors [102].

- **"Skewed" trapezoid:** This second option avoids the *orphan strips* arranging the sensor edges parallel to the stereo strips. As in the first option the strips will be in a fan geometry. The trapezoid in this case turns to skewed trapezoid at the inclination angle of the stereo strips. For accomodating a smoth transition in the radial transformation region the sensor prototype has circular shape in the perimeter of the strip ends. However, the dicing lines of the miniature sensors are kept straight for this fabrication run for simplicity. The sensor dimension takes an area of (2×2) cm^2 in the ATLAS12A wafer layout.

In figure 4.45 (right) a photo of a sensor with this "skewed" design can be seen. The principal parameters of the "skewed" trapezoid sensors are summarized in table 4.11.

	Endcap "skewed" design
Inner dimension of bias ring length $\times$ wide/narrow width (area)	17.68$\times$18.38/16.73 mm^2 (3.10 cm^2)
Number of strips per segment	258
Top Segment	
Strip Length	8.77 mm
Strip Pitch wide/narrow	70.98/67.90 μm
Bottom Segment	
Strip Length	8.80 mm
Strip Pitch wide/narrow	67.67/64.6 μm
Skew angle	20 mrad

Table 4.11: Principal parameters of the "skewed" trapezoid design [102].

Despite having chosen the "skewed" sensors as the baseline for the ITk-Strips, the ganging of the *orphan strips* was such an interesting technology (for future developments) that a set of sensors was also built in order to test if their performance would be compromised by this method. This will be analyzed in section 4.4.3.

Together with endcap miniature sensors, also "barrel" sensors were built to be tested by the collaboration. These sensors include "axial" strips that run parallel to the sensor edges. All the devices must meet initially the pre-irradiation delivery specifications and the post-irradiation behaviour will be evaluated by the different institutes of the collaboration.

The general procedure to test the incoming devices (pre- and post-irraiation) starts with a visual inspection to determine possible physical defects and scratches on the sensor (due to fabrication process, packaging, trasportation or handling of the sensors). An electrical characterizarion will be carried out with a probe station following the steps explained in chapter 3 (IV and CV tests). The charge collection efficiency is then analized and all the tests are compared with the results obtained by other collaboration institutes.

Tables 4.12 and 4.13 list all the Hamamatsu sensors tested in this thesis (pre- and post-irradiation) with their identification number (from numbered wafer), the type of sensor (whether it is a barrel or an endcap sensor), the irradiadiation type and fluence, the ganging used (if necessary) and the different tests carried out.

ATLAS12A Measurements (pre-irradiation)					
Sensor Identification	**Type**	**Ganging**	**Tests carried out**		
			IV - CV	**CCE**	**Laser scan**
W634-LargePitch-C-P19	Endcap	DC	x	x	x
W632-LargePitch-E-P20	Endcap	DC	x		
W636-LargePitch-E-P10	Endcap	AC	x	x	
W637-LargePitch-C-P09	Endcap	AC	x		
W623-SmallPitch-E-P08	Endcap	AC	x		
W625-SmallPitch-C-P07	Endcap	AC	x		
W634-SmallPitch-E-P18	Endcap	DC	x		
W635-SmallPitch-C-P17	Endcap	DC	x		
W627-Skewed-E-P02	Endcap		x		
W631-Skewed-C-P01	Endcap		x		
W628-BZ3C-P15	Barrel		x	x	x

Table 4.12: Hamamatsu sensor inventory with the different not irradiated sensors tested in this thesis.

ATLAS12A Measurements (post-irradiation)								
Sensor Identification	**Type**	**Ganging**	**Irradiation type**	**Irradiation Site**	**Fluence** (n_{eq}/cm^2)	**Tests carried out**		
						IV - CV	**CCE**	**Laser scan**
W621-BZ3C-P12	Barrel	—	neutrons	Ljubljana	5×10^{14}	x	x	
W621-BZ3C-P02	Barrel	—	neutrons	Ljubljana	1×10^{15}	x	x	
W616-BZ3C-P02	Barrel	—	neutrons	Ljubljana	2×10^{15}		x	
W616-BZ3C-P04	Barrel	—	neutrons	Ljubljana	5×10^{15}	x	x	
W628-BZ3C-P02	Barrel	—	protons (70MeV)	CYRIC	1×10^{15}	x		
W626-BZ3C-P02	Barrel	—	protons (70MeV)	CYRIC	5×10^{14}		x	x
W627-P14	Barrel	—	Mixed Irrad.	Birminham	2.7×10^{14}		x	
W632-P14	Barrel	—	Mixed Irrad.	Birminham	5.5×10^{14}		x	
W609-smallPitch-E-P18	Endcap	DC	protons (23MeV)	Birminham	5×10^{14}	x	x	
W628-smallPitch-E-P10	Endcap	AC	protons (23MeV)	Birminham	5×10^{14}		x	x
W639-smallPitch-C-P17	Endcap	DC	protons (23MeV)	Birminham	5×10^{14}	x		x
W645-largePitch-E-P20	Endcap	DC	protons (23MeV)	Birminham	5×10^{14}		x	x
W644-largePitch-C-P09	Endcap	AC	protons (23MeV)	Birminham	5×10^{14}		x	
W642-smallPitch-E-P18	Endcap	DC	protons (23MeV)	Birminham	1×10^{15}	x		
W626-largePitch-E-P20	Endcap	DC	protons (23MeV)	Birminham	2×10^{15}	x		
W609-smallPitch-C-P07	Endcap	AC	protons (23MeV)	Birminham	2×10^{15}	x		
W605-largePiych-E-P10	Endcap	AC	protons (23MeV)	Birminham	2×10^{15}	x		
W604-largePitch-C-P19	Endcap	DC	protons (23MeV)	Birminham	2×10^{15}	x		
W631-smallPitch-C-P17	Endcap	DC	gamma	BNL	1 Mrad		x	
W631-smallPitch-E-P10	Endcap	AC	gamma	BNL	1 Mrad		x	
W627-smallPitch-C-P17	Endcap	DC	gamma	BNL	10 Mrad		x	
W625-smallPitch-E-P18	Endcap	DC	gamma	BNL	10 Mrad		x	
W609-smallPitch-E-P08	Endcap	AC	protons (23MeV)	Birminham	5×10^{14}	x	x	
W648-smallPitch-E-P18	Endcap	DC	protons (23MeV)	Birminham	5×10^{14}	x	x	

Table continues in next page

ATLAS12A Measurements (post-irradiation)								
Sensor Identification	Type	Ganging	Irradiation type	Irradiation Site	Fluence (n_{eq}/cm^2)	Tests carried out		
						IV - CV	CCE	Laser scan
W614-smallPitch-E-P18	Endcap	DC	protons (23MeV)	Birminham	1×10^{15}	x	x	
W638-smallPitch-C-P17	Endcap	DC	protons (23MeV)	Birminham	1×10^{15}	x	x	
W609-smallPitch-C-P07	Endcap	AC	protons (23MeV)	Birminham	2×10^{15}	x	x	
W782-smallPitch-C-P07	Endcap	AC	protons (70MeV)	CYRIC	1×10^{15}			x
W782-smallPitch-C-P17	Endcap	DC	protons (70MeV)	CYRIC	1×10^{15}			x

Table 4.13: Hamamatsu sensor inventory with the different irradiated sensors tested in this thesis.

4.4.1 Electrical tests: IV/CV measurements

The experimental techniques for measuring the $I-V$ and $C-V$ curves were introduced and described in chapter 3. The procedure is the same for not irradiated and irradiated sensors with slight differences in the setup.

Inside a probe station the sensors are held against a metal chuck and finely-tipped needles are used to make contact with the metal sensor pads. The bias voltage is applied through the backplane of the sensor and the ground contact lays on the bias ring. Therefore negative bias voltages will be used. The applied bias voltage is negative but the absolute value has been used in tables and plots for simplicity. As explained in section 3.4.1 the voltage range goes typically from zero to (600-1000) V in (10-20) V steps with 10 seconds of delay between measurements (to let the current stabilize).

Table 4.14 summarizes the stablished parameters in these tests for $I-V$ and $C-V$ characterization for not irradiated sensors.

Not Irradiated Sensors		
Set parameters	**I-V**	**C-V**
Max. bias Voltage (V)	600	600
Voltage Step (V)	20	20
Delay (s)	10	10
Current compliance (μA)	100	100

Table 4.14: Parameters used during $I-V$ and $C-V$ curves measurements with not irradiated sensors.

For the measurement of the capacitance the frequency employed in the component analizer was set to 30 kHz as explained in 3.4.2. Figures 4.46, and 4.47 show the leakage current and the capacitance (plotted as $1/C^2$) versus the bias voltage, respectively.

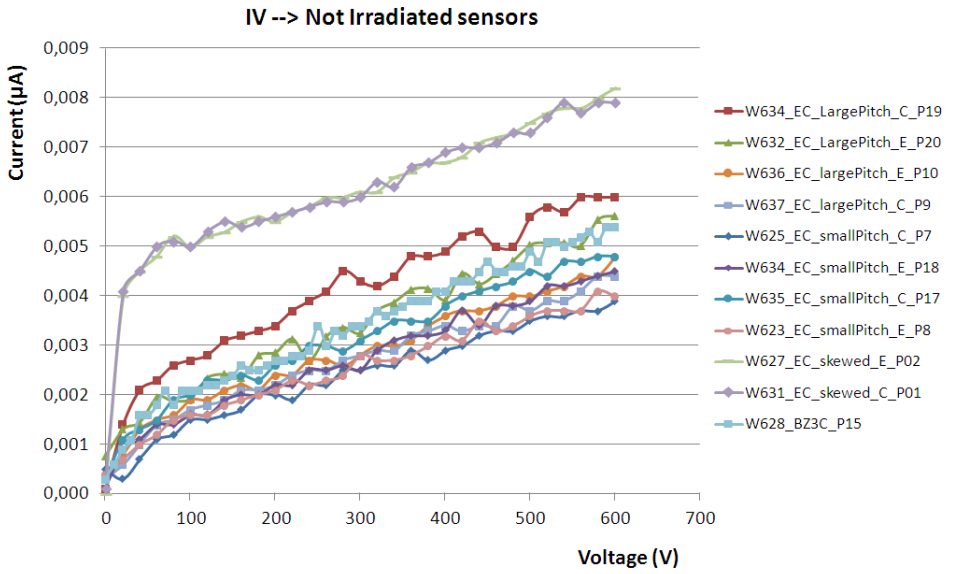

Figure 4.46: Leakage current as a function of the bias voltage measured with the probe station for the not irradiated sensors. No breakdown voltage was registered below 600 V.

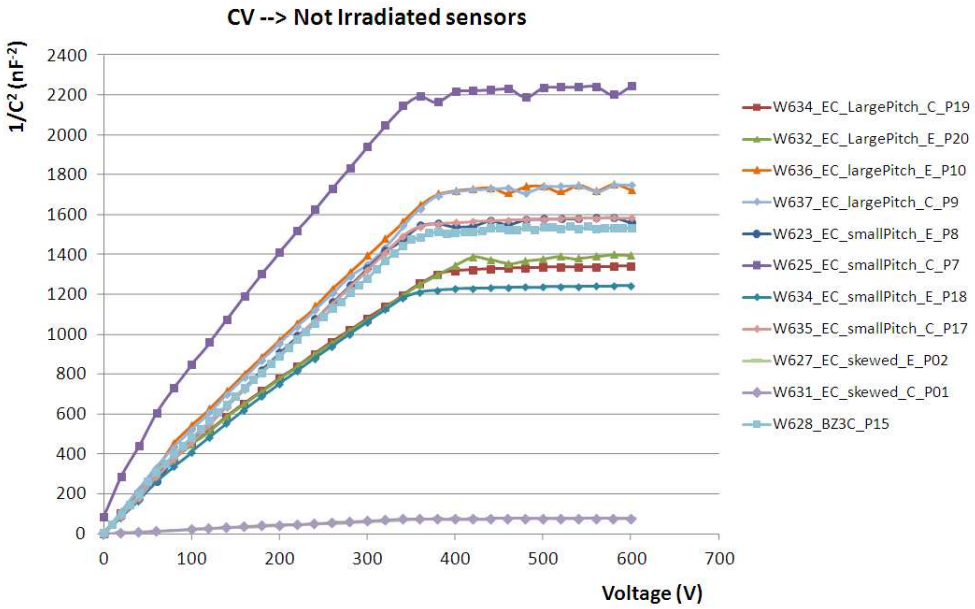

Figure 4.47: Capacitance as a function of the bias voltage measured with the probe station for the not irradiated sensors. Plotted as $1/C^2$. Full depletion voltage achieved around 350 V.

The jump in the leakage current and capacitance values between the skewed and the square sensors is due to their difference in size. The square sensors are (1×1) cm

while the skewed are (2×2) cm. The maximum leakage current registered is about 0.008 μA which is well below the technical specification's limit and no breakdown occured below 600 V. Concerning the full depletion voltage the average obtained is (363.2 $\pm$ 3.6) V. The specifications stablish a full depletion voltage below 300 V for a silicon resistivity $>$ 4 kΩ cm and accepting also a resistivity around 2.5 kΩ cm [100] with the corresponding depletion voltage ($\sim$380 V). Therefore the obtained average is within the specifications.

In the case of irradiated sensors the chuck is replaced by a thermal chuck connected to a chiller machine to maintain the sensors cold enough while taking data. Dry air is also blown inside the probe station to avoid water condensation.

The parameters set for each sensor measurement are summarize in table 4.15. The dry air blowing was improved in different iterations so the chiller temperature was reduced in the last measurements (from -1 °C to -7 °C).

Irradiated Sensors		
Set Parameters	**I-V**	**C-V**
Max. bias Voltage (V)	1000	1000
Voltage Step (V)	20	20
Delay (s)	15	20
Current compliance (mA)	5	5
Average Chiller Temperature (°C)	-5	-5

Table 4.15: Parameters used during $I-V$ and $C-V$ curves measurements with irradiated sensors.

The analized sensors were irradiated with neutrons or protons (see table 4.13) at different fluences (from 5×10^{14} to 5×10^{15} n_{eq}/cm^2). The $I-V$ curves obtained for neutron and proton irradiated sensors are shown in figure 4.48.

The maximum leakage current achieved (at 600 V) is about 850 μA corresponding to a neutron irradiated sensor at the highest dose. The current increase with fluence is consistent with bulk current increase. The majority of the sensors did not present breakdown below 1000 V despite some of them reached the breakdown voltage between (700-800) V. Nevertheless, these values are above the maximum operation voltage (600 V).

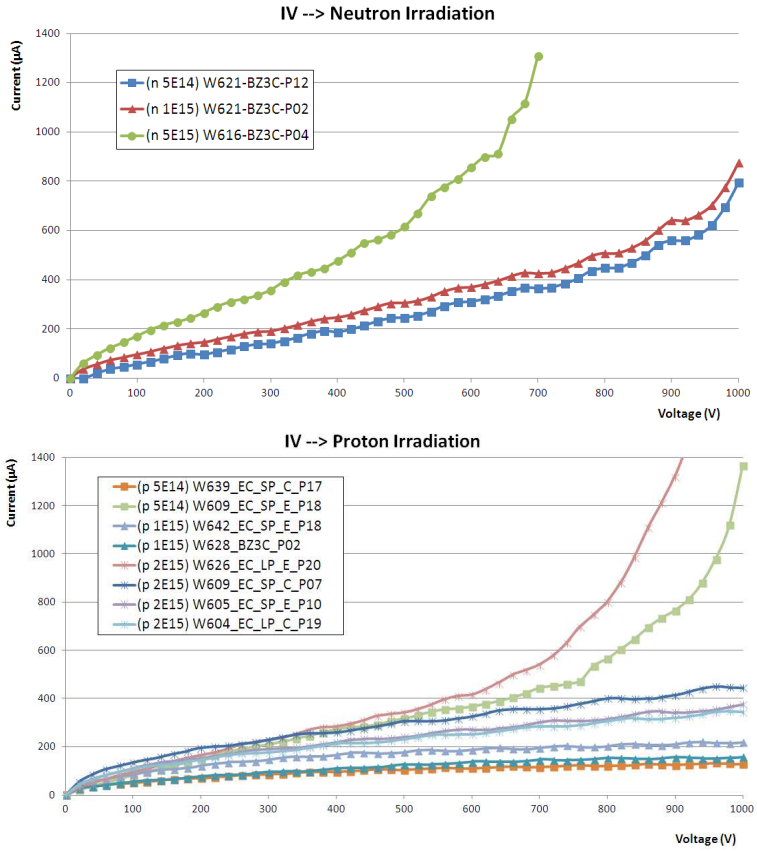

Figure 4.48: Leakage current as a function of the bias voltage measured with the probe station for the neutron (top) and proton (bottom) irradiated sensors. A thermal chuck was used to maintain the sensors cold enough during measurements. No breakdown voltage was registered below 600 V.

Figure 4.49 shows the $C-V$ curves measured for the neutron and proton irradiated sensors. Most of the sensors do not reach the *plateau* of the capacitance and below 1000 V the depletion voltage can not be determined with this method. We can only calculate the depletion voltage for three proton irradiated sensors with their $C-V$ curves. They are between 500 and 800 V.

From the results presented above it is clear that the effects of radiation damage in the case of neutrons are more evident than for protons. The radiation levels present at the Inner Detector were introduced in chapter 2. It was explained that close to the interaction point, charged hadrons dominate the bulk damage in silicon but further out neutrons are dominant. Therefore it is important to study the degradation introduced by each particle. In the case of neutrons both the radiation levels (see section 2.3.4) and the damage are higher.

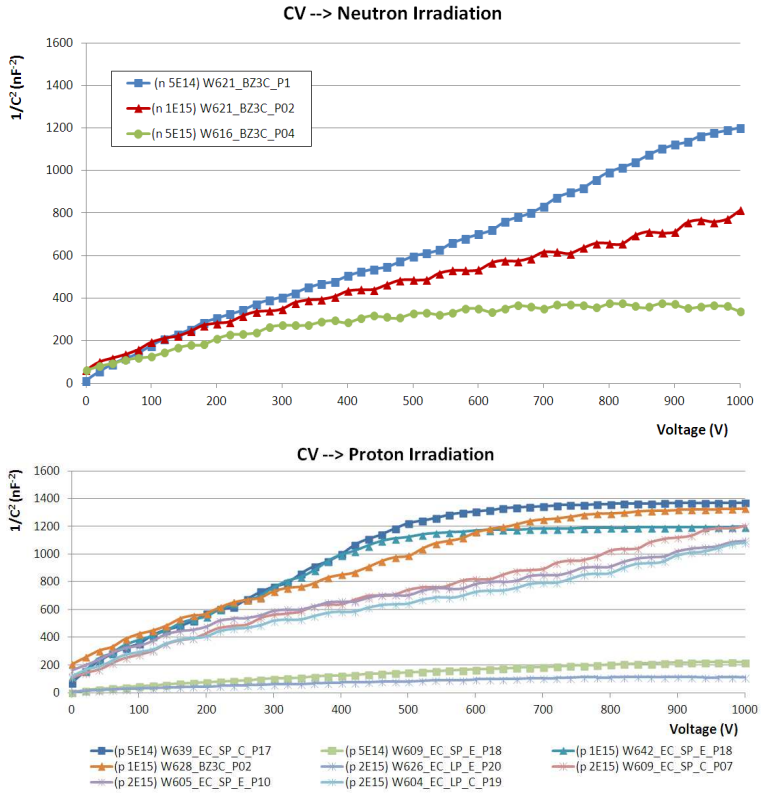

Figure 4.49: Capacitance as a function of the bias voltage measured with the probe station for the neutron (top) and proton (bottom) irradiated sensors. Plotted as $1/C^2$.

Figures 4.50 and 4.51 show the same $I-V$ and $C-V$ results selecting one sensor of each type of irradiation respectively.

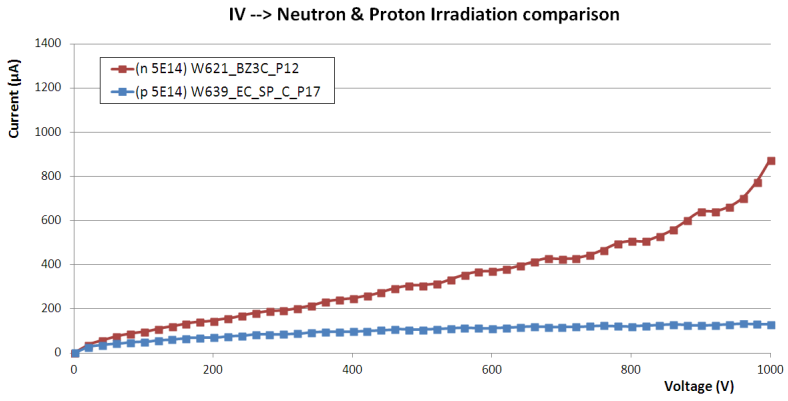

Figure 4.50: $I-V$ results for two different irradiated sensors (one with neutron irradiation an the other with proton irradiation).

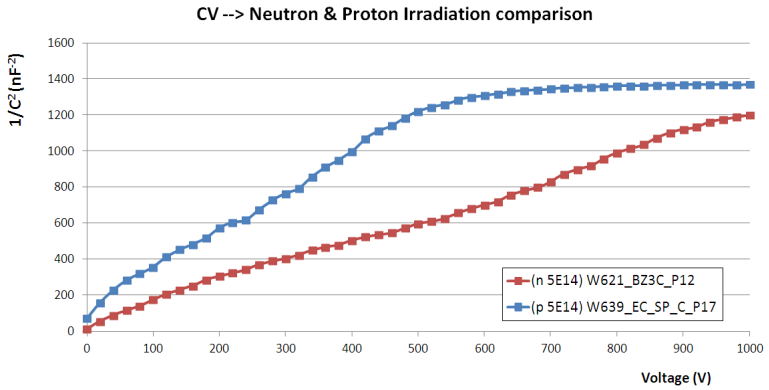

Figure 4.51: $C-V$ results for two different irradiated sensors (one with neutron irradiation an the other with proton irradiation).

The leakage current is one of the most affected parameters. Figures 4.52 and 4.53 show the increase of the current with the fluence for all sensors (neutrons and protons respectively).

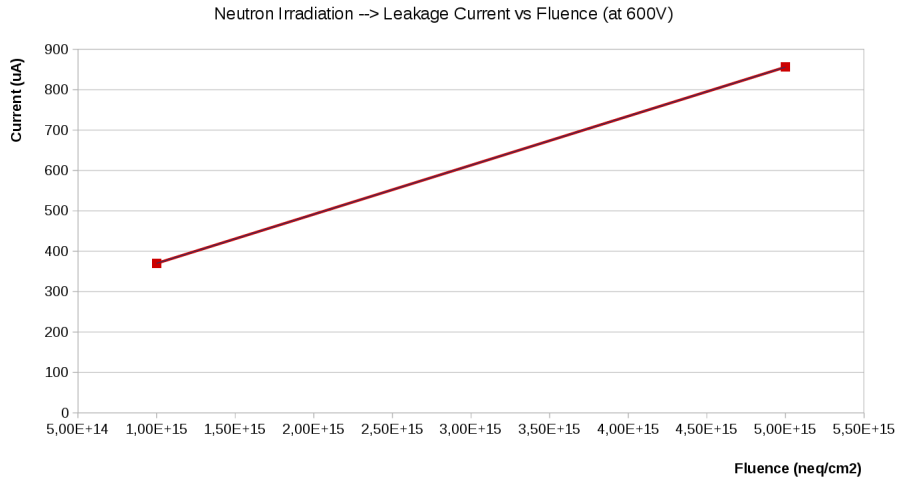

Figure 4.52: Leakage current as a function of the fluence for neutron irradiated sensors. An increase in the fluence affects directly to the leakage current of a sensor.

The effects of radiation on the electrical properties of the sensors were introduced in chapter 3. In particular, the leakage current would increase linearly with the fluence following:

$$\Delta I_{vol} = \alpha \cdot \Phi \tag{4.12}$$

where ΔI_{vol} would correspond to the difference in the leakage current before and

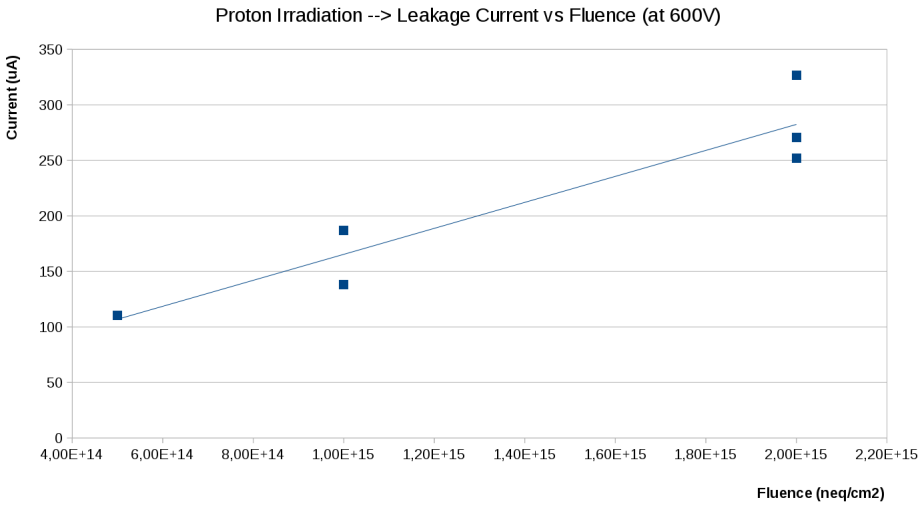

Figure 4.53: Leakage current as a function of the fluence for proton irradiated sensors. An increase in the fluence affects directly to the leakage current of a sensor.

after irradiation. The constant α was introduced in chapter 3 as the current related damage rate. In the literature its value is 6.4 $\times 10^{-17}$ (A/cm). From our measurements we can make an experimental estimation of α. Due to the fact that we don't have the $I-V$ curves of these sensors before irradiation the results of a not irradiated sensor would be used to calculate ΔI_{vol}. The function[1] to represent would be:

$$(I - I_{noirrad})/Volum = \alpha \cdot \Phi \tag{4.14}$$

and α corresponds to the derivative of the linear fit. Using our sensor results we obtained the values listed in table 4.16. The great concordance of the three α factors verify the good behaviour of the irradiated sensors measured.

Alpha Factor Calculation		
Theory	**Neutron Irrad. Sensors**	**Proton Irrad. Sensors**
6.40 $\times 10^{-17}$ (A/cm)	6.48 $\times 10^{-17}$ (A/cm)	6.24 $\times 10^{-17}$ (A/cm)

Table 4.16: Alpha factors calculated from neutron and proton iradiated sensors results. The theoretical value is also listed.

[1] For these calculations the leakage current was scaled to 21° C following:

$$I(T_2) = I(T_1) \cdot \left(\frac{T_2}{T_1}\right)^2 \cdot exp\left(-\frac{E_g}{2\kappa_B}\left(\frac{1}{T_2} - \frac{1}{T_1}\right)\right) \tag{4.13}$$

where E_g=1.21 eV is the *scaling parameter* [103].

In general, comparing the plots before and after irradiation it is clear that radiation has negative effects on the electrical properties of the sensors. The leakage current is five orders of magnitude higher after irradiation and due to the changes induced by radiation, in terms of the effective doping concentration, the capacitance behaviour also changes, increasing the full depletion voltage value.

A summary of the results obtained for not irradiated and irradiated sensors is presented in table 4.17. The specifications from the manufacturer are also included.

Specifications	Not Irradiated - Test results	Irradiated - Test results
I (600V) $< 0.1\ \mu A$	I_{max} (600V) = 0.0082 μA	I_{max} (600V) = 850 μA
$C_{coupling}$ (600 V) $\geq$ 20 pF	C_{min} (600 V) = 21.09 pF	C_{min} (600 V) = 27.63 pF
$V_{FD} \sim$ 360 V	V_{FD} (average) = (363.2 $\pm$ 3.6) V	—
$V_{Breakdown} >$ 600 V	$V_{Breakdown} >$ 600 V	$V_{Breakdown} >$ 600 V

Table 4.17: Summary of the results obtained from the $I-V$ and $C-V$ curves for not irradiated and irradiated sensors and the comparison with the sensor specifications. The values for not irradiated sensors meet the specifications while in the case of irradiated sensors the influence of radiation is clearly reflected on the electrical properties.

4.4.2 Charge Collection pre and post-irradiation

The charge collection efficiency is one of the most important parameters to analyze. After high irradiation fluences it is important to ensure that the sensors are going to measure a total charge above a noise threshold, stablished by the electronics. If not, due to the *ATLAS* binary system, some strips during the clusters formation would be lost. This could lead to a wrong position of the transversing particle hit that could compromise the tracking. Therefore, a comparison before and after irradiation of the collected charge is vital.

The collected charge is measured as a function of the bias voltage using the ALiBaVa system as explained in chapter 3. A β source (^{90}Sr) is placed above the sensor and a photomultiplier (below the sensor) will provide the trigger. The electrons registered at the readout electrodes form a signal which will be analized to extract the charge as a function of the applied voltage (see sections 3.4.3 and 3.4.5 for more details).

The active thickness of *ATLAS12A* sensors is (302$\pm$12) μm. From this thickness

(t) the expected charge can be estimated by [104]:

$$N = \frac{t}{3.7}\left[190 + 16.3ln(t)\right] \tag{4.15}$$

Therefore, for a not irradiated sensor the total collected charge above full depletion voltage will be $N = 23105$ electrons, commonly expressed as 23.105 ke^-. The ITk-Strips Collaboration agreed that normalizations will be used for all charge collection measurements. For that purpose all the institutes used the same type of not irradiated miniature barrel sensor as reference.

The collected charge registered at *IFIC* for this sensor can be seen in figure 4.54.

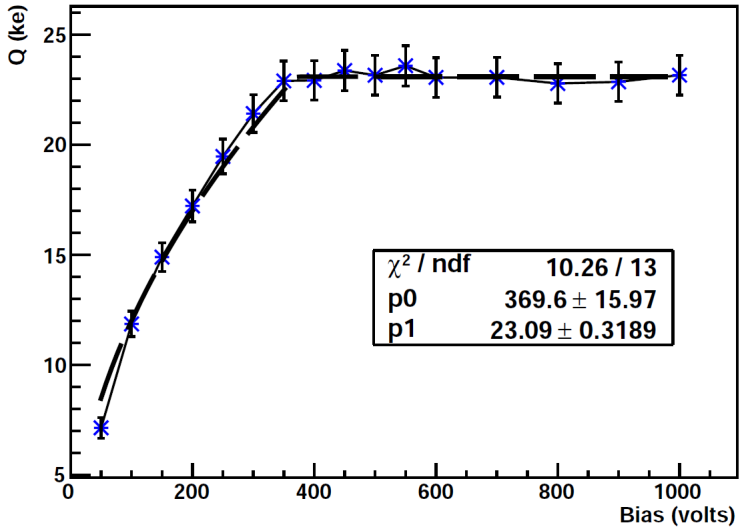

Figure 4.54: Charge Collection of a not irradiated barrel sensor. The curve is fitted to a function defined by 4.16. Parameters $p0$ and $p1$ indicate the full depletion voltage and the collected charge on average respectively.

The function used to fit the charge is defined as:

$$Q(V) = \begin{cases} Q_0 \cdot \sqrt{\dfrac{V}{V_{fd}}} & V < V_{fd} \\ Q_0 & V \geq V_{fd} \end{cases} \tag{4.16}$$

From 4.16 the collected charge above the *plateau* (above 400 V) is $(23.09 \pm 0.32)\ ke^-$. The theoretical value ($23.105\ ke^-$) is compatible with the measurement error. With this sensor a normalization factor is stablished to convert the ADC counts registered by $ALiBaVa$ to ke^- in the rest of the sensors. This factor is given by 4.17 and corresponds

to the relation between the average of the collected charge in ADC counts and the corresponding ke^- scaled to 23.105 ke^-.

$$f_{norm} = \frac{Calculated\ Charge\ (23.105\ ke^-)}{Average\ of\ ADC\ counts\ (above\ the\ plateau)} = 158.6\ (ke^-/ADC) \quad (4.17)$$

The error in the charge (in electrons) is given by:

$$e(Q) = \sqrt{(0.4)^2 + (0.035 \cdot Q)^2} \quad (4.18)$$

The uncertainty on the measurements due to the sensor variation in the Landau fit is included in the errors calculation. This value corresponds to 400 ke^- and comes from the standard deviation of the measurements below the full collection. An error of 3.5% in charge collection is also added in quadrature. This is a relative error that comes from normalization.

Besides the barrel reference sensor two more not irradiated sensors (End-cap type, EC) were also measured. All the collected charge curves are depicted in figure 4.55.

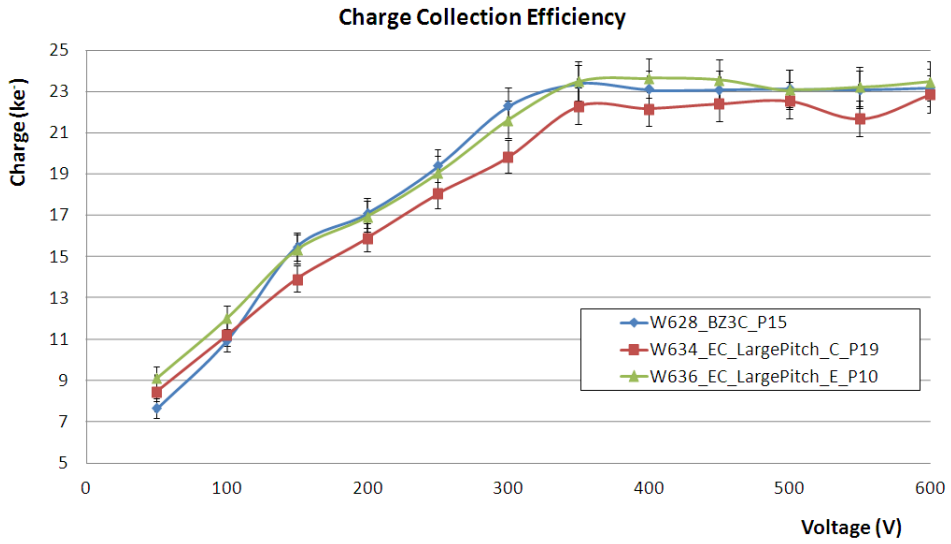

Figure 4.55: Collected charge resistered for the three not irradiated sensors. The full depletion voltage is around 370 V which is close to the value extracted from the $C-V$ curve. All the sensors collected a charge above 21 ke^- at full depletion.

All the sensors reach the full depletion voltage around 370 V which is equivalent to the value extracted from the $C-V$ curve. The total collected charge measured and the full depletion voltage for each sensor is summarized in table 4.18.

Charge Collection - Not Irradiated sensors		
Sensor	**Collected Charge (ke^-)**	**V_{fd} (V)**
W628-BZ3C-P15 (reference)	(23.1 $\pm$ 0.3)	(369.8 $\pm$ 15.6)
W634-EC-LargePitch-C-P19	(21.2 $\pm$ 0.5)	(376.9 $\pm$ 19.7)
W636-EC-LargePitch-E-P10	(23.4 $\pm$ 0.1)	(359.8 $\pm$ 18.1)

Table 4.18: Summary of the collected charge and full depletion voltage for the not irradiated sensors measured.

Sensor $W634\text{-}EC\text{-}LargePitch\text{-}C\text{-}P19$ had unexpected low charge collection (2 ke^- below the reference sensor). In the CCE curve it seems that its behaviour above full depletion was not very stable, having fluctuations of about 0,4 ke^- between measurements. Moreover, looking at the $I-V$ curve on figure 4.46 a small jump in the leakage current can be appreciated. The visual inspection on this sensor was repeated looking for scratches or dust deposition. However, no important issues were found. These sensors are extremely sensitive and handling or transportation can affect their behaviour.

In the case of the irradiated sensors the setup is placed inside a vertical freezer (at -35°C) as explained in 3. The difference in the charge collection with the reference sensor in these cases is more evident. Figure 4.56 shows the collected charge of all the measured sensors. Proton, neutron and gamma irradiated sensors are included.

For bias voltages above 450 V sensor $W626\text{-}BZ3C\text{-}P02$ presented microdischarges. These can be a consequence of high electric field regions around the implants. The microdischarges are identified by inestability in the leakage current with sudden increase and decrease in its amplitude. The measurements with this sensor were stopped to protect it from possible permanent damage.

From 4.56 it is clear that the higher the dose of radiation the less collected charge. The $I-V$ curves at 4.4.1 reflected that the damage induced by neutron irradiation is worse than the caused by proton irradiation. This effect is also revealed in the case of the charge collection. As explained in chapter 3 radiation causes the displacement of silicon atoms from its substitution site to an interstitial site to form a *Frenkel pair*. This radiation induced damage is mainly in the form of deep level single defects and defect clusters (extended damage region). For neutron radiation, the dominant damage is in the form of defect clusters while for gamma and electron radiations, it is mainly due to deep level single defects. For charge particles (protons, pions, etc.), it is the mixture of the two. For the same fluence the sensors irradiated with neutrons collected around

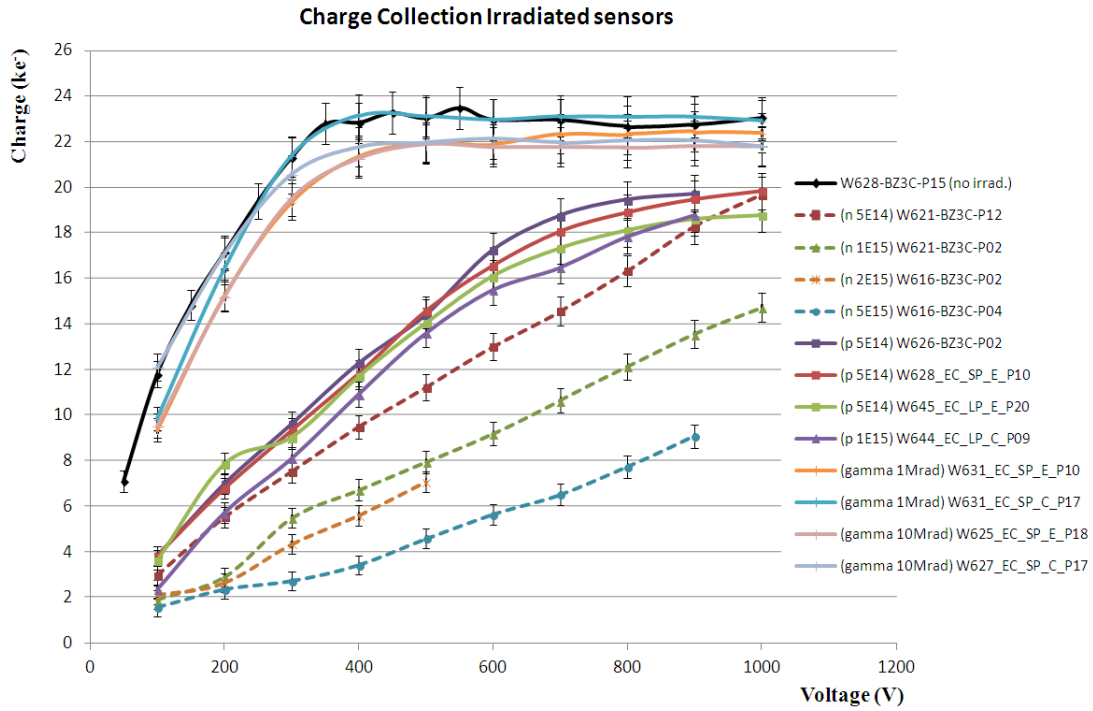

Figure 4.56: Collected charge measured for the irradiated sensors (irradiated with proton, neutron and gamma particles). The not irradiated sensor results are also included as reference.

30% less charge than the ones with proton irradiation. Moreover, for the sensors irradiated with protons a charge *plateau* is intuited around 800 V. This is compatible with the $C-V$ measurements where three proton irradiated sensors reached the full depletion voltage between 500 and 800 V. The *plateau* is not observed in sensors with neutron irradiation.

Regarding the sensors with gamma irradiation the behaviour of the charge colletion is similar to the not irradiated reference sensor presenting a *plateau* above 350 V. The total collected charge is quite close to 23 ke^- which is the expected value for a not irradiated sensor. Gamma particles do not damage the silicon bulk in excess. The major damage contribution is located at the sensor surface so the influence is not as strong as the caused by neutrons or protons.

Representing the average of the collected charge (for fixed bias voltage) as a function of the fluence the deterioration of the sensor performance is more evident. Figures 4.57 and 4.58 show this effect for neutron and proton irradiated sensors respectively.

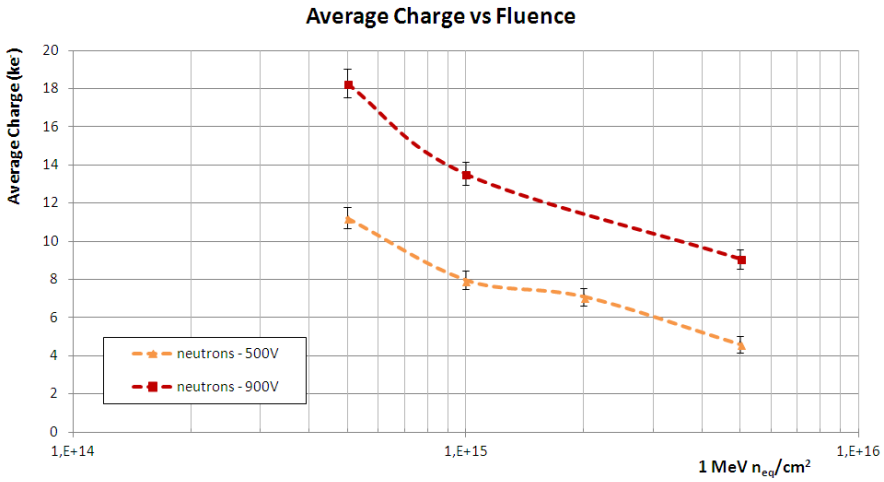

Figure 4.57: Charge collection as a function of the fluence for neutron irradiated sensors.

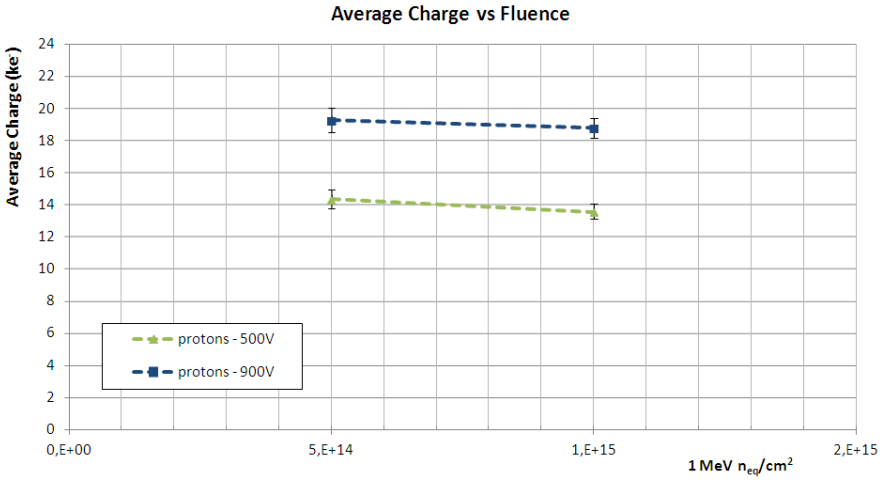

Figure 4.58: Charge collection as a function of the fluence for proton irradiated sensors.

Table 4.19 summarizes the results obtained for collected charge of the measured sensors selecting a bias voltage close to the HL-LHC voltage of operation (∼600 V). The not irradiated reference sensor result is also included for a directly comparison.

These tests were checked against the results from the other institutes involved. A summary of all the results of the collaboration is represented in figures 4.59 and 4.60 with the measurements obtained for neutron and proton irradiation respectively.

Charge Colection - Irradiated sensors (at 600V)		
Sensor	**Fluence**	**Collected Charge (ke^-)**
W628-BZ3C-P15 (reference)	no irrad.	(23.1 $\pm$ 0.3)
W621-BZ3C-P12	n; 5×10^{14} n_{eq}/cm^2	(13.0 $\pm$ 0.6)
W621-BZ3C-P02	n; 1×10^{15} n_{eq}/cm^2	(9.2 $\pm$ 0.5)
W616-BZ3C-P02	n; 2×10^{15} n_{eq}/cm^2	microdischarges
W616-BZ3C-P04	n; 5×10^{15} n_{eq}/cm^2	(5.6 $\pm$ 0.4)
W626-BZ3C-P02	p; 5×10^{14} n_{eq}/cm^2	(17.2 $\pm$ 0.7)
W628-EC-SP-E-P10	p; 5×10^{14} n_{eq}/cm^2	(16.6 $\pm$ 0.7)
W645-EC-LP-E-P20	p; 5×10^{14} n_{eq}/cm^2	(16.1 $\pm$ 0.7)
W644-EC-LP-C-P09	p; 1×10^{15} n_{eq}/cm^2	(15.5 $\pm$ 0.7)
W631-EC-SP-E-P10	γ; 1 Mrad	(22.4 $\pm$ 0.9)
W631-EC-SP-C-P17	γ; 1 Mrad	(20.0 $\pm$ 0.8)
W625-EC-SP-E-P18	γ; 10 Mrad	(21.2 $\pm$ 0.8)
W627-EC-SP-C-P17	γ; 10 Mrad	(20.6 $\pm$ 0.8)

Table 4.19: Summary of the collected charge measured for the irradiated sensors.

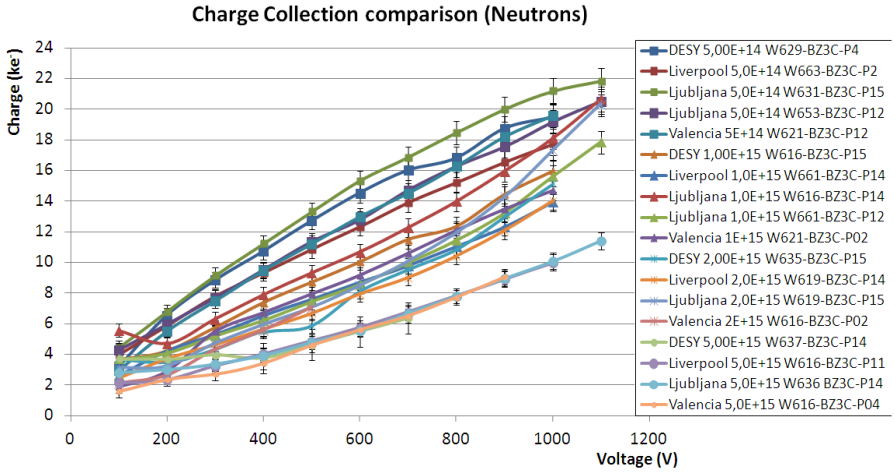

Figure 4.59: Summary of the collected charge measurements for the neutron irradiated ATLAS12A sensors by the seven groups involved. These results were published at [105].

The charge collection achieved by all the institutes for each radiation and dose is similar and proved to be consistent.

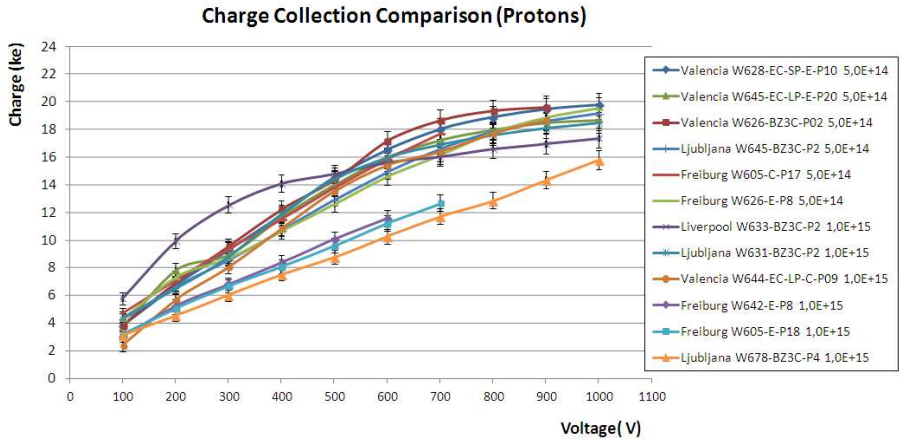

Figure 4.60: Summary of the collected charge measurements for the proton irradiated ATLAS12A sensors by the seven groups involved. These results were published at [105].

4.4.3 Laser measurements on ATLAS12A

For completeness during the electrical characterization of the sensors, several laser measurements were carried out. As explained in chapter 3.4.4 the laser techniques allow us to test the complete sensor and also strip by strip performance. We can verify the electrical connections and properties such as the quality of the bonding process or the channel response (looking for bad channels). The radiation influence on the collected charge, signal deformation and charge sharing can be also studied before and after irradiation. Each sensor strip must give a similar signal response for a similar traversing particle being detected. By using a laser one can recreate crossing particles in a specific sensor region and with the same amplitude.

The laser setup is placed inside a Faraday's cage and three high-precision stages move the laser in the direction perpendicular to the strips, along the strip and far/near the strip (up/down). The output of the signal is monitored with the ALiBaVa system. The data parameters, such as the laser focusing distance or the steps between the measurements during a scan, are controlled via a *python* script. The resulting output is then analized using the *ROOT* framework (for further details see section 3.4.4).

The sensors used with the laser setup are summarized in table 4.20.

4.4.3.1 Strip integrity pre and post-irradiation

As explained in chapter 3 the first step is to achieve a proper laser focus (for detailed description see section 3.4.4). Then a laser scan in the direction perpendicular

Laser Measurements	
Sensor	**Fluence (n_{eq}/cm^2)**
W628-BZ3C-P15	no irrad.
W634-EC-LP-C-P19	no irrad.
W616-BZ3C-P04	n; 5×10^{15}
W626-BZ3C-P02	p;5×10^{14}
W628-EC-SP-E-P10	p; 5×10^{14}
W645-EC-LP-E-P20	p; 5×10^{14}
W782-EC-SP-C-P07	p; 1×10^{15}
W782-EC-SP-C-P17	p; 1×10^{15}

Table 4.20: Sensors used with the laser setup. Not irradiated and irradiated sensors are included.

to the strips is done to see the signal registered by each individual strip.

Results with unirradiated sensors

Two not irradiated mini sensors (one barrel and one end-cap type) were analyzed in terms of their strip integrity. The results of the amount of signal measured (in ADC counts) as a function of the laser position (in the direction perpendicular to the strips) is depicted in figure 4.61 for both sensors.

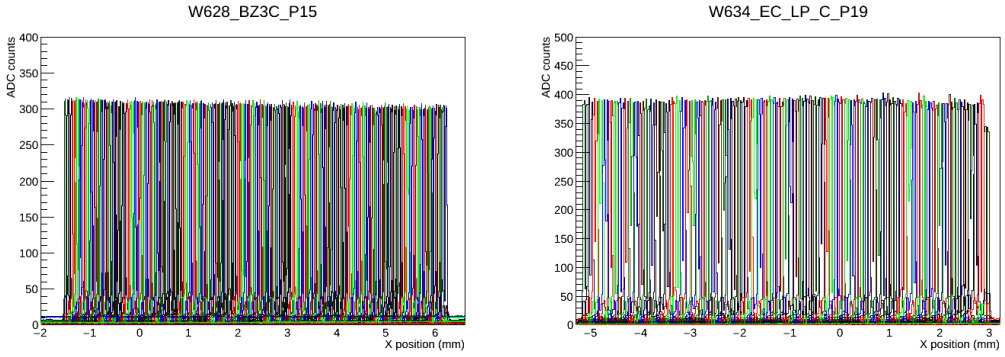

Figure 4.61: Signal amplitude (in ADC counts) as a function of the laser position (direction perpendicular to the strips) for two not irradiated microstrip sensors. Measurements taken at 200 V for sensor $W628\text{-}BZ3C\text{-}P15$ and 400 V for sensor $W634\text{-}EC\text{-}LP\text{-}C\text{-}P19$.

The typical relative charge collection profile of a single strip was introduced in chapter 3. It has two peaks (separated by a hole corresponding to the aluminium reflection) and decreases with the distance from the strip center (see figure 3.41). All

the strips achive approximately the same amount of signal per sensor. In the case of sensor $W628\text{-}BZ3C\text{-}P15$ (picture 4.61(left)) the signal is a bit lower as we move to the right side of the sensor. This is due to a laser focus degradation. The sensor is placed in an aluminium base but it is not perfectly perpendicular to the laser beam. A small inclination of the sensor surface causes a degradation in the laser focus in that region. Nevertheless, the difference in the amount of charge between the left and right sides of the sensor is small (around a 5%). The signal shape per strip is uniform as can be seen in figure 4.62.

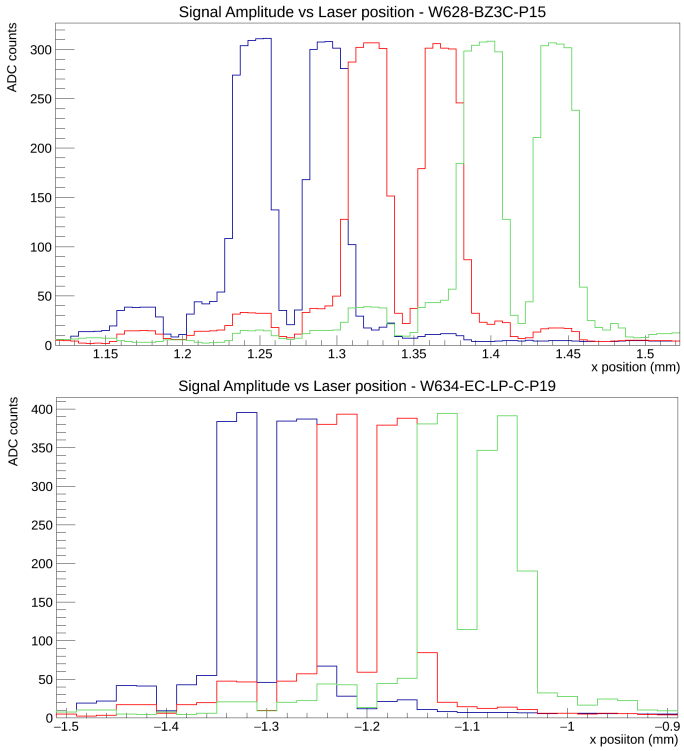

Figure 4.62: Signal amplitude (in ADC counts) as a function of the laser position (X direction) for three consecutive strips of two not irradiated microstrip sensors. Measurements taken at 200 V for sensor $W628\text{-}BZ3C\text{-}P15$ (top) and 400 V for sensor $W634\text{-}EC\text{-}LP\text{-}C\text{-}P19$ (bottom).

One important aspect to take into account is the behaviour of the signal at the border strips which are closer to the bias and guard rings.

Figure 4.63 shows the border strips (left and right) in the case of sensor $W628\text{-}BZ3C\text{-}P15$ where the signal is uniform.

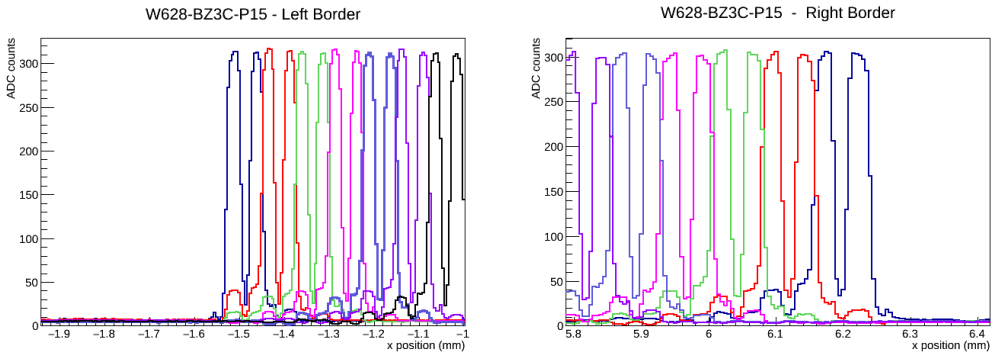

Figure 4.63: Signal amplitude (in ADC counts) as a function of the laser position (in the direction perpendicular to the strips) for the border strips of sensor $W628\text{-}BZ3C\text{-}P15$ (left and right respectively). Measurements taken at 200 V.

However, in the case of sensor $W634\text{-}EC\text{-}LP\text{-}C\text{-}P19$ the right border presents a strip with less signal collection. This strip appears in red color in figure 4.64 (right).

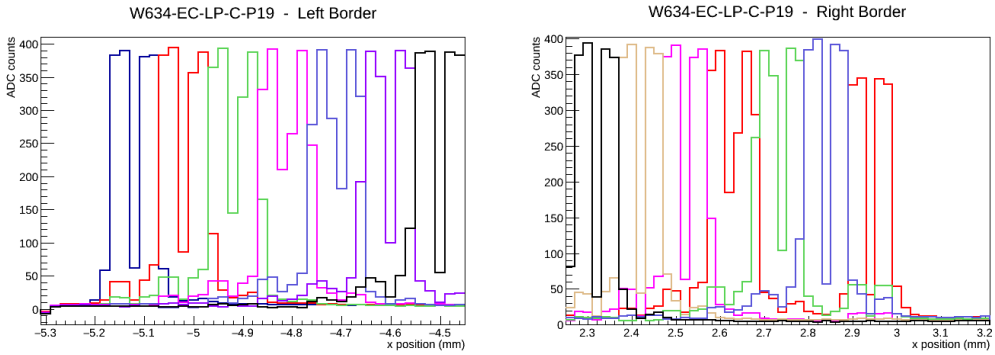

Figure 4.64: Signal amplitude (in ADC counts) as a function of the laser position (X direction) for the border strips of sensor $W634\text{-}EC\text{-}LP\text{-}C\text{-}P19$ (left and right respectively). The last strip of the right border (red strip) appears in two different X positions and with less collected charge. This is due to the DC ganging of the sensor (see section 4.4.3.2). Measurements taken at 400 V

Moreover this strip can be seen also duplicated in other position in the perpendicular direction. This effect is due to the DC ganging of the sensor and will be explained in section 4.4.3.2.

Representing the amount of collected charge and the laser position as a function of the channel number a quick inspection can been done looking for *holes* in the sensor (bad channels or not bonded strips). Figures 4.65 and 4.66 show these plots for the analized not irradiated sensors.

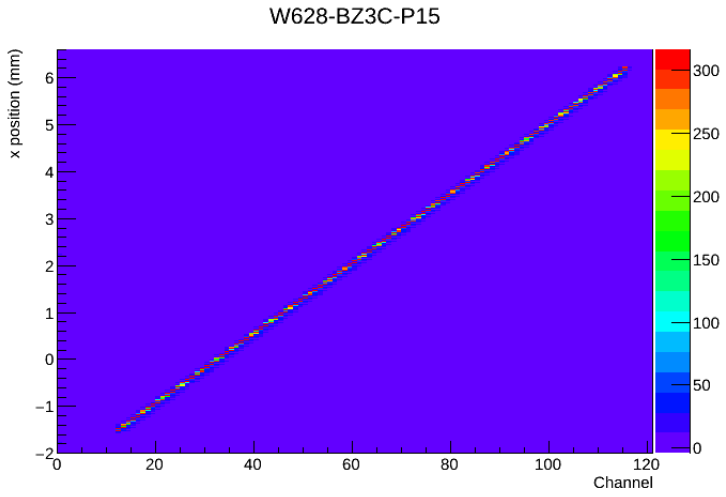

Figure 4.65: Signal amplitude (in ADC counts) and laser position as a function of the channel number for sensor $W628\text{-}BZ3C\text{-}P15$ (not irradiated). Measurements taken at 200 V.

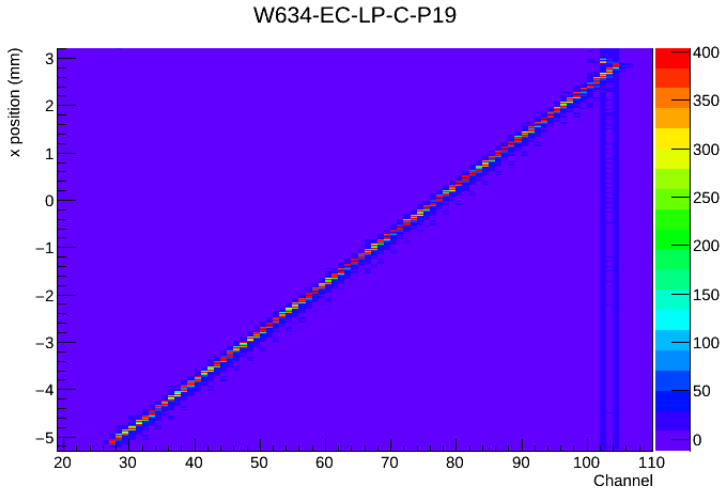

Figure 4.66: Signal amplitude (in ADC counts) and laser position as a function of the channel number for sensor $W634\text{-}EC\text{-}LP\text{-}C\text{-}P19$ (not irradiated). Measurements taken at 400 V

When the laser passes through the interstrip region the charge is shared between the two neighbouring strips. This maintains the total collected charge uniform. In the middle of this interstrip space the charge sharing should be the 50%. Figure 4.67 shows the shared charge between two selected strips in sensor $W628\text{-}BZ3C\text{-}P15$

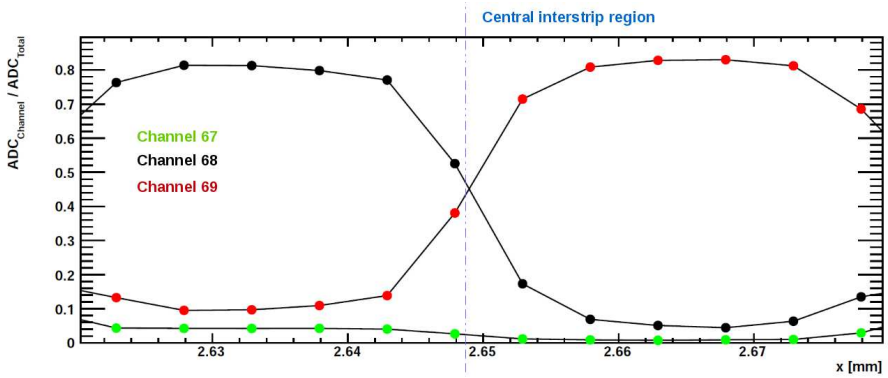

Figure 4.67: Charge sharing between channels 67, 68 and 69 of barrel mini sensor $W628$-$BZ3C$-$P15$. Measurements taken at 200 V. *Root* macro taken from [106].

The maximum collected charge for channel 68 is located around $x = 2.63\ mm$. Ideally, it shoud be the 100% of the total collected charge but in this case it only corresponds to the 81%. At that position a 10% goes to channel 69 (red) and a 4% to channel 67 (green). The remaining 5% corresponds to the rest of the neighbouring strips contribution and system uncertainties. We are not able to measure the total charge at the strip centre due to the aluminium reflection and therefore this intoduce an uncertainty to the system. One should keep also in mind that the laser beam is not a point light source.

The laser beam spot width is around 8 μm (with the laser properly focused) so it generates a charge cloud. It is usual to have charge dispersion so that not all the charge is read by only one channel at the strip center but also by neighbouring channels. As introduced above, in the middle of the interstrip region between channels 68 and 69 (x 2.65 mm) the shared charge should be the 50% per strip but the real case is that channel 68 collects a 47% and channel 69 a 43%. Appart from the charge cloud dispersion this could be also due to a small inclination in the aluminium base.

In general, both barrel and end-cap mini sensors presented good performance in terms of signal uniformity. No holes appeared in the results discarding possible damaged strips or defective electrical connections.

Results with irradiated sensors

The analized irradiated sensors are summarized in table 4.20. For the measurements with irradiated samples the metal base is replaced by a thermal base which was introduced in section 3.4.4. Cooling liquid from a chiller machine circulates inside

the thermal base maintaining the sensors cold enough during measurements and avoiding *thermal runaway*. Appart from this, the measurement procedure is similar to the used with not irradiated sensors.

Before the thermal base building some attempts to measure irradiated sensors at room temperature (21-22°C) were carried out. However, the huge leakage current made the procedure so sensitive. Low bias voltage had to be applied and the laser focusing was very dificult to refine. The different voltages used with these sensors and the corresponding leakage current measured are summarized in table 4.21.

Laser Measurements - Irradiated sensors				
Sensor	**Fluence (n_{eq}/cm^2)**	**Voltage (V)**	**$I_{leakage}$ (mA)**	**T (°C)**
W616-BZ3C-P04	n; 5×10^{15}	150	9.1	22
W626-BZ3C-P02	p; 5×10^{14}	150	8.2	22
W628-EC-SP-E-P10	p; 5×10^{14}	200	0.69	-8
W645-EC-LP-E-P20	p; 5×10^{14}	300	0.56	-8
W782-EC-SP-C-P07	p; 1×10^{15}	150	14.3	-10
W782-EC-SP-C-P17	p; 1×10^{15}	100	9.28	-10

Table 4.21: Summary of used paremeters during laser measurements with irradiated sensors.

To minimize the data taking time for sensors at room temperature the scan was reduced covering only few strips. The results obtained for sensors $W616\text{-}BZ3C\text{-}P04$ and $W626\text{-}BZ3C\text{-}P02$ are depicted in figures 4.68 and 4.69 respectively.

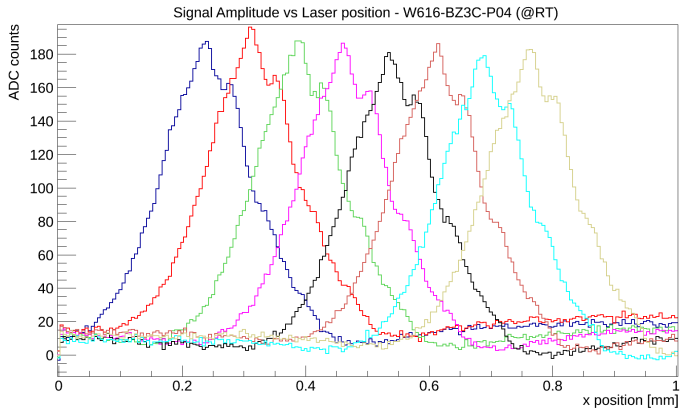

Figure 4.68: Amplitude signal as a function of the laser position for sensor $W616\text{-}BZ3C\text{-}P04$. Measurements taken at 150 V and 22 °C.

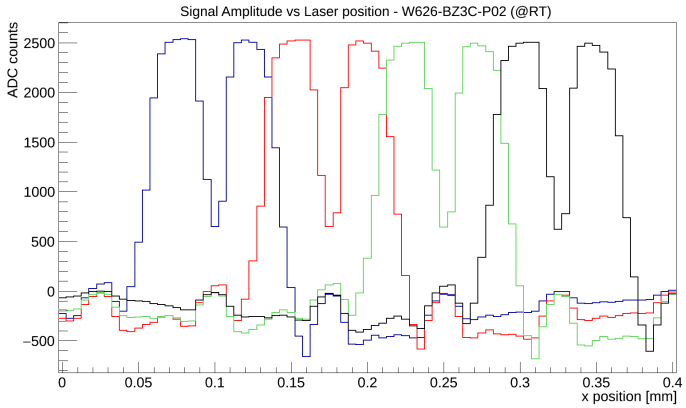

Figure 4.69: Amplitude signal as a function of the laser position for sensor $W626\text{-}BZ3C\text{-}P02$. Measurements taken at 150 V and 22 °C.

In particular for sensor $W616\text{-}BZ3C\text{-}P04$ measurements were really difficult to take. The signal amplitude was very low and the leakage current so high so the focusing process did not result very successful. For 150 V the typical signal amplitud is around 300-400 ADC counts and we were able to achieve only a maximum of aproximately 180 ADC counts. Moreover, the hole in the middle of the strips due to aluminium reflection can not be properly distinguised and this is usually caused by a poor focusing with the laser. Nevertheless, all the analyzed strips presented similar amount of collected charge and uniformity in the signal shape so the sensor is functioning properly. In the case of sensor $W626\text{-}BZ3C\text{-}P02$ the focusing step was better carried out and despite the huge leakage current the signal shape is the expected. The aluminium reflection can also be distinguished. The maximum collected charge is around 250 ADC counts which is closer to the expected value for the selected voltage.

Before the aluminium thermal base building these sensors were unbonded. During the bonding and unbonding processes the sensors suffer from mechanical stress so exposing them to a second bonding could compromise the repeatability of the results. So we decided not to repeat the tests with these sensors using the thermal base.

The results obtained for the irradiated sensors measured with the thermal base are presented in figures 4.70, 4.71, 4.72 and 4.73. Only few strips are depicted for simplicity.

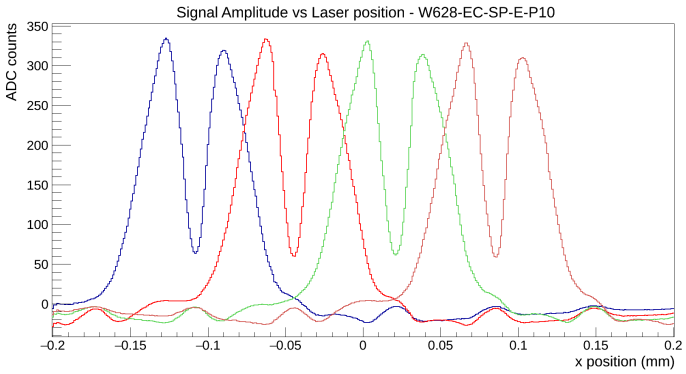

Figure 4.70: Signal amplitud versus laser position for sensor $W628\text{-}EC\text{-}SP\text{-}E\text{-}P10$. Sensor irradiated with protons at 5×10^{14} n_{eq}/cm^2. Measurements taken at 200 V and -8°C. Good laser signal uniformity and strip integrity. The laser focusing was properly set and the aluminium reflection can be seen clearly.

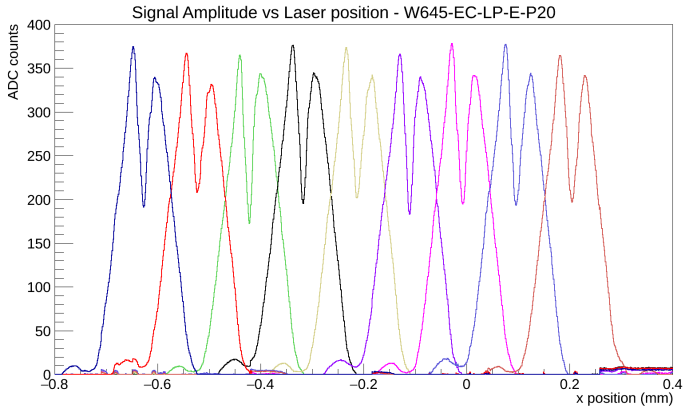

Figure 4.71: Signal amplitud versus laser position for sensor $W645\text{-}EC\text{-}LP\text{-}E\text{-}P20$. Sensor irradiated with protons at 5×10^{14} n_{eq}/cm^2. Measurements taken at 300 V and -8°C. Low aluminium reflection due to poor laser focusing. Nevertheless, good laser signal uniformity and strip integrity.

In figures 4.70 and 4.71 a small difference in the signal amplitude per strip can be appreciated. Each strip presents two signal peaks (left and right of the aluminium where the laser is reflected) and they are slightly different (about a 11%). This is caused by a not well focused laser scan. This effect is more evident in figure 4.71.

In general the irradiated sensors measured with the thermal base presented good laser signal uniformity. Moreover, the above results bring to light the importance of the laser focusing. For sensors of wafer $W782$ the doubled signal corresponding to the ganged strips can also be appreciated. These ganging options will be explained and analyzed in detail in section 4.4.3.2.

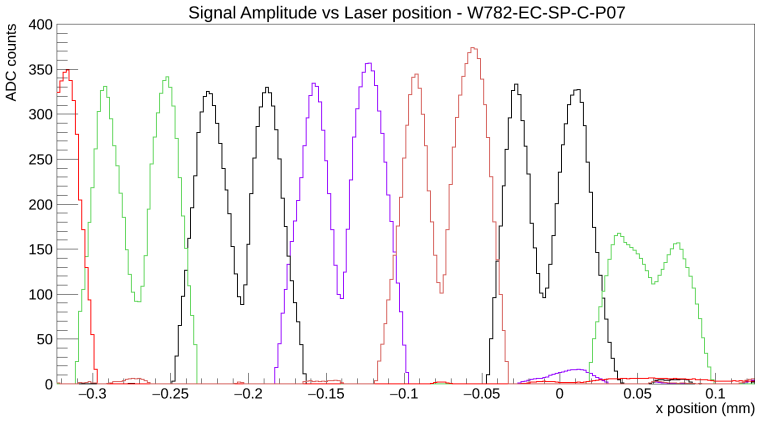

Figure 4.72: Signal amplitud versus laser position for sensor $W782\text{-}EC\text{-}SP\text{-}C\text{-}P07$. Sensor irradiated with protons at 1×10^{15} n_{eq}/cm^2. Measurements taken at 150 V and -10°C. Good laser signal uniformity and strip integrity. Last strip appeared doubled (green) and with lower amplitude due to AC ganging (see 4.4.3.2).

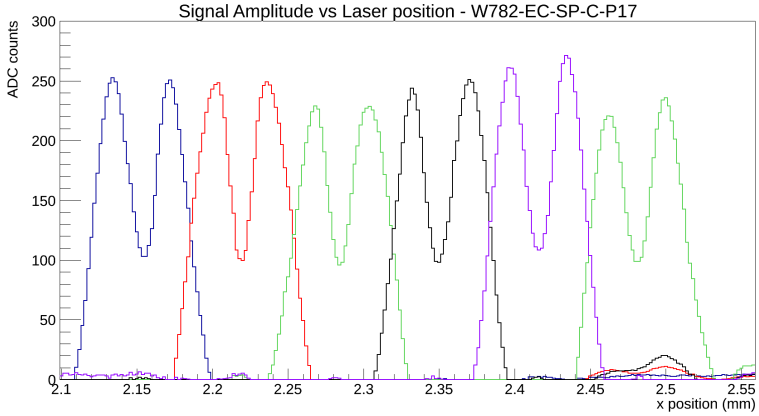

Figure 4.73: Signal amplitud versus laser position for sensor $W782\text{-}EC\text{-}SP\text{-}C\text{-}P17$. Sensor irradiated with protons at 1×10^{15} n_{eq}/cm^2. Measurements taken at 100 V and -8°C. Good laser signal uniformity and strip integrity. Last strip appeared doubled (green) and with lower amplitude due to DC ganging (see 4.4.3.2).

The charge sharing of an irradiated sensor ($W782$-EC-SP-C-$P07$) was also analyzed. The shared charge between two selected strips is depicted in figure 4.74.

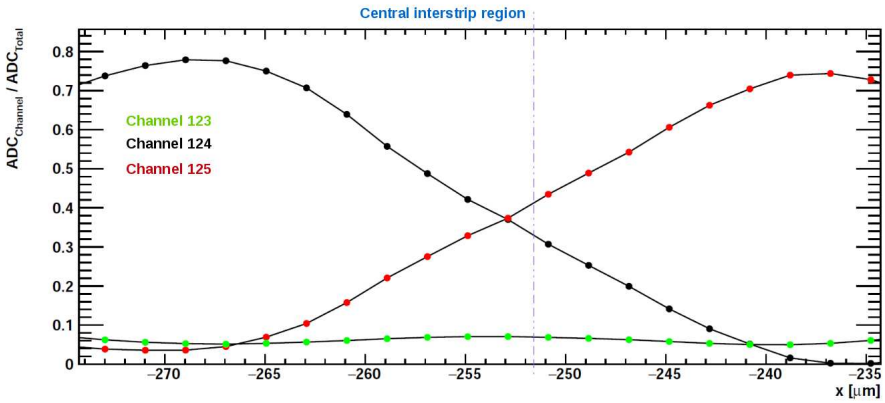

Figure 4.74: Charge sharing between channels 123, 124 and 125 of an end-cap irradiated mini sensor ($W782$-EC-SP-C-$P07$). Measurements taken at 100 V. *Root* macro taken from [106].

The maximum collected charge for channel 124 is located around $x = -269\ \mu m$ and corresponds to the 78% of the total collected charge. At that position a 3% goes to channel 125 (red) and a 5% to channel 123 (green). The remaining 14% will correspond to the rest of the neighbouring strips contribution and background noise. In the middle of the interstrip region between channels 124 and 125 (x$\sim$-252 μm) channel 124 collects a 34% and channel 125 a 40%.

Comparing the laser test results obtained with not irradiated and irradiated sensors, in both cases the laser signal was uniform along the sensors with no presence of holes or bad channels. In terms of charge sharing the irradiated sensor collected a lower maximum charge (respect to the total collected charge) and the charge sharing was higher due to the difference in the carriers diffusion in the silicon. The charge cloud is higher for irradiated sensors causing an increase in the charge sharing and degrading the charge efficiency. This is compatible with the noise and leakage current increase and charge trapping effects due to radiation damage in sensors.

4.4.3.2 Orphan strips solutions: DC versus AC ganging

The strip ganging was proposed as a solution to the *orphan strips* present at the “square” trapezoid sensors as introduced in section 4.4. Two possible ganging solutions were developed to avoid dead areas in the sensors. In the DC ganging the

connection of the orphan strip to the neighbours is made between the strip implants (DC connection). While in the AC ganging the connection is made through the readout metals (AC connection).

Two proton irradiated sensors were used to characterize both technologies in order to stablish which is the better option in terms of sensor performance. The sensors and the setup parameters used are summarized in table 4.22.

Laser Measurements - AC vs DC ganging					
Sensor	**Fluence (n_{eq}/cm^2)**	**Voltage (V)**	**$I_{leakage}$ (mA)**	**T (°C)**	**Ganging**
W782-EC-SP-C-P07	p; 1×10^{15}	150	14.3	-10	AC
W782-EC-SP-C-P17	p; 1×10^{15}	100	9.28	-10	DC

Table 4.22: Summary of used irradiated sensors for ganging studies and their setup parameters during laser measurements.

- ***DC* ganging characterization results**

  For the DC ganging characterization the laser scan was performed covering the ganging region. Figure 4.75 (left) shows a scheme of the laser movement over the sensor. The ganged strips appear marked with a red and green circle. The numbers of the last strips are also included.

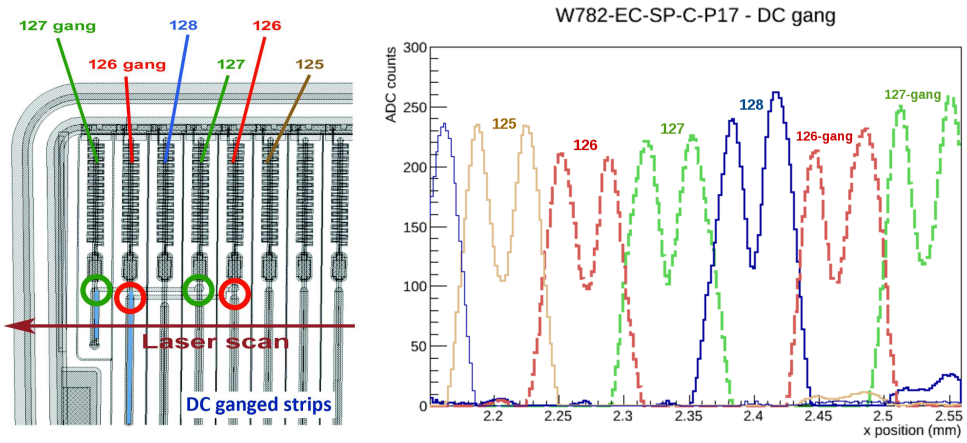

Figure 4.75: Laser movement over sensor $W782\text{-}EC\text{-}SP\text{-}C\text{-}P17$ (DC-gang) with channel numbers also drawn (left). Signal amplitude as function of the laser position (right).

When the laser passes through all the strips a double signal would appear for channels 126 (red) and 127 (green). These double signals can be seen in figure 4.75 (right) and are writen as 126-gang (red) and 127-gang (green). This is due to the fact that strips 126 and 126-gang (and the same for strips 127

and 127-gang) are connected together (by the ganging) and are readout by the same beetle channel. So they are plotted as the same *ASIC* channel in two different laser positions.

From figure 4.75 (right) a small signal coupling is detected around $x = 2.55$ mm. Isolating the 128 strip signal (figure 4.76) this double peak is clearer.

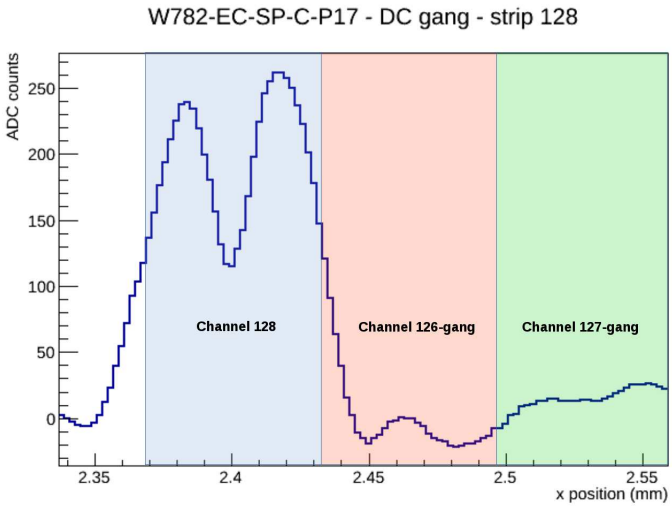

Figure 4.76: Signal coupling from channel 128. The strip signal appears also in channel position *127-gang*.

This coupling was at first considered as a result of the charge cloud dispersion. All the sensor strips should be affected by this effect but the coupling only appeared at channel 128 and therefore the cloud dispersion possibility was discarded. The *cross-talk* of channels (amplified by the ganging connection) may be another possible reason. This *cross-talk* effect can appear between the aluminium present at the ganging connection and the implant of a strip (see aluminium traces scheme at figure 4.75(left)). In this case, strip number 128 has both ganging connections above.

Another way to see clearly the effect of the ganging is representing the collected charge in terms of the laser position versus de channel as can be seen in figure 4.77

Channels 126 and 127 appear doubled out of the diagonal. The ganged strips presented also a drop of signal amplitude collecting an average of 12% less charge. Nevertheless, the signal shape is uniform and similar for all the analyzed strips.

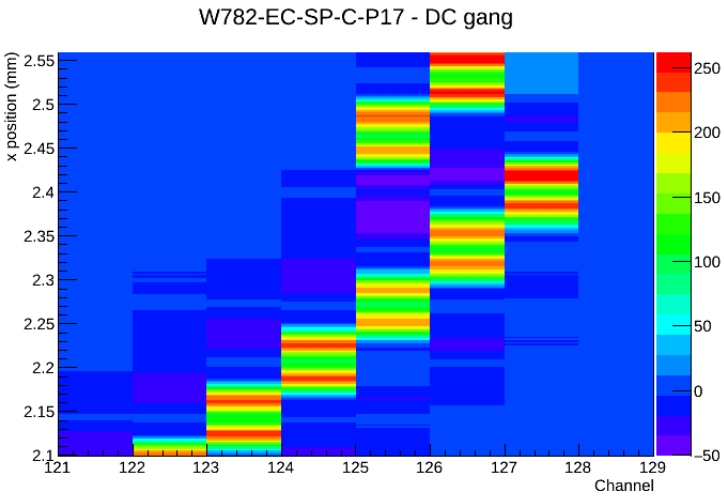

Figure 4.77: Laser position as a function of the channel number and the collected charge for sensor $W782\text{-}EC\text{-}SP\text{-}C\text{-}P17$ (DC-gang). Measurements taken at 100 V.

- ***AC* ganging characterization results**

  The AC ganging characterization is carried out similarly to the DC characterization. Figure 4.78 (left) shows the laser movement over the sensor and the results obtained in terms of signal amplitude (right).

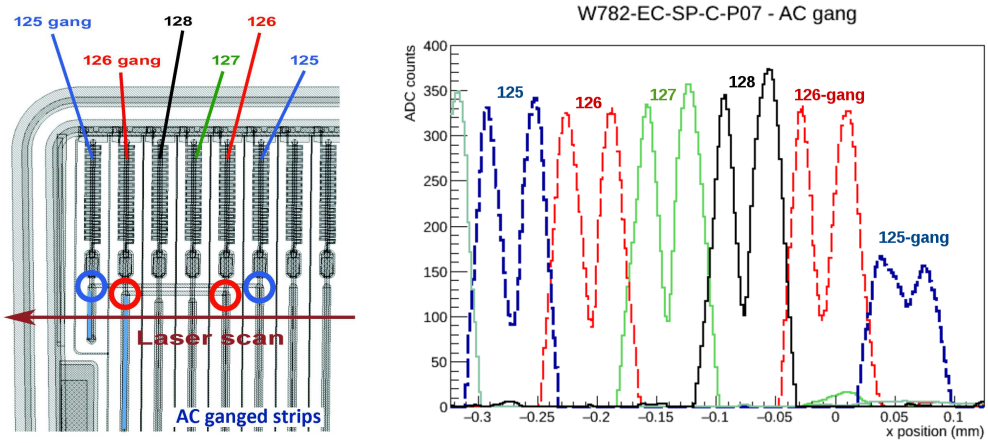

Figure 4.78: Laser movement over sensor $W782\text{-}EC\text{-}SP\text{-}C\text{-}P07$ (AC-gang) with channel numbers also drawn (left). Signal amplitude as function of the laser position (right).

In this case the ganged strips are marked with blue and red circles. A double signal appeared for strips 125 and 126 corresponding to the ganged strips 125-gang and 126-gang respectively. Representing the laser position as a

function of the channel number and the collected charge these double signals for ganged strips can clearly be seen (figure 4.79).

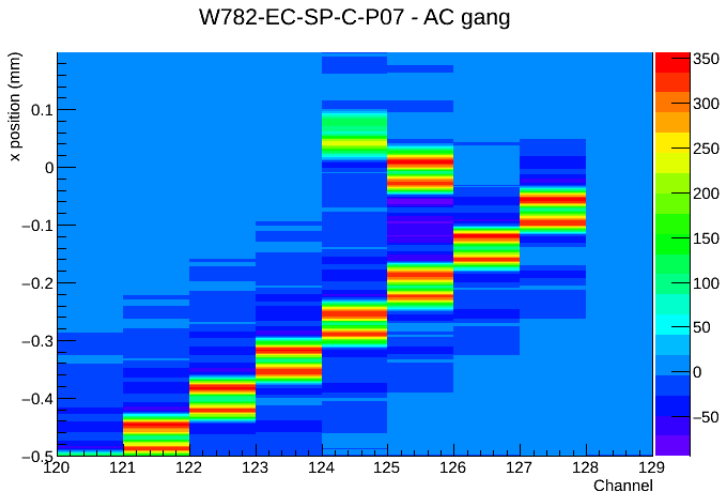

Figure 4.79: Laser position as a function of the channel number and the collected charge for sensor $W782\text{-}EC\text{-}SP\text{-}C\text{-}P07$ (AC-gang). Measurements taken at 150 V.

A drop in the charge collection can also be appreciated for the last strip (125-gang) collecting around 48% less signal than the neighbouring strips.

In general the AC ganging technology also allows to solve the *orphan strips* problem avoiding dead areas in the sensor as well as with the DC ganging. Despite one of the ganged strips presented a reduction in the charge collection it was still able to collect more than 50% of the charge. Besides this, the behaviour of all the strips in the ganging region was similar showing uniformity in the laser signal.

At the same time to *IFIC*, *Freiburg University* was also involved in these kind of studies and the tests were checked against to validate the results[1]. The experimental setup used by *Freiburg* is similar to the one used at *IFIC*. From all the sensors analyzed by *Freiburg University* we have selected the ones irradiated to similar doses to *IFIC* sensors to allow a direct comparison. Table 4.23 summarizes the used sensors for this purpose.

[1] These results were published in 2016 at *Nuclear Instruments and Methods in Physics Research* [107]

AC vs DC ganging - Comparison Results			
Sensor	**Fluence (neq/cm2)**	**Ganging**	**Site**
W645-EC-SP-C-P17	p; 2×10^{15}	DC	Freiburg
W604-EC-SP-C-P07	p; 2×10^{15}	AC	Freiburg
W782-EC-SP-C-P17	p; 1×10^{15}	DC	Valencia
W782-EC-SP-C-P07	p; 1×10^{15}	AC	Valencia

Table 4.23: Summary of the used sensors for AC and DC ganging laser measurements comparison.

Figure 4.80 shows equivalent laser scans for DC ganged sensors carried out by both institutes.

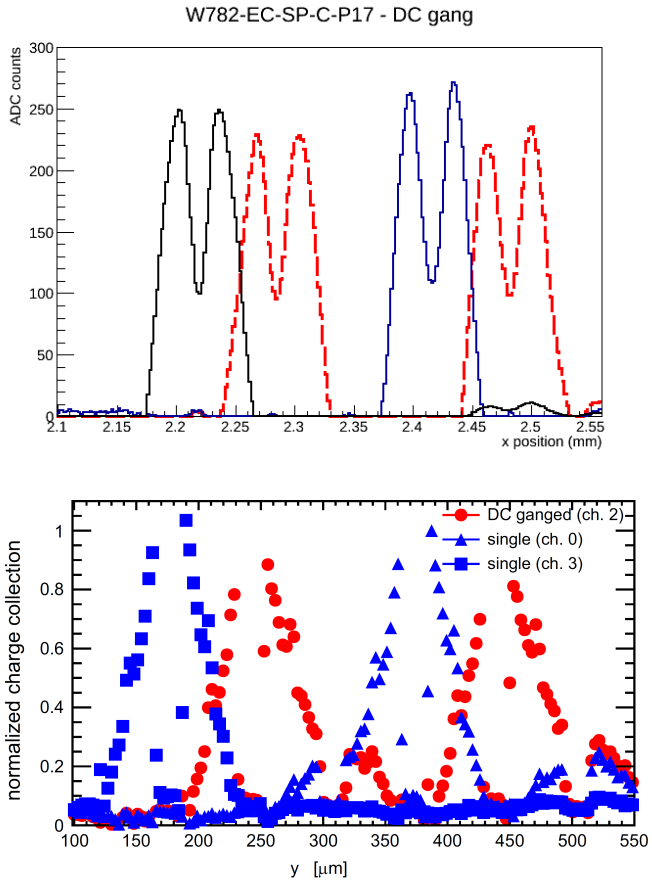

Figure 4.80: Comparison of signal amplitude as a function of the laser position results for DC-ganging sensors measured at *IFIC* (top) and *Freiburg* (bottom) institutes.

The laser signal registered in both cases is similar and reduced collected charge

in the ganging region is also confirmed by *Freiburg* results. They also observed some *cross-talk* in the last ganged strip region (around 500-500 μm in figure 4.80 (bottom)).

Regarding the AC ganging performance figure 4.81 shows the obtained results.

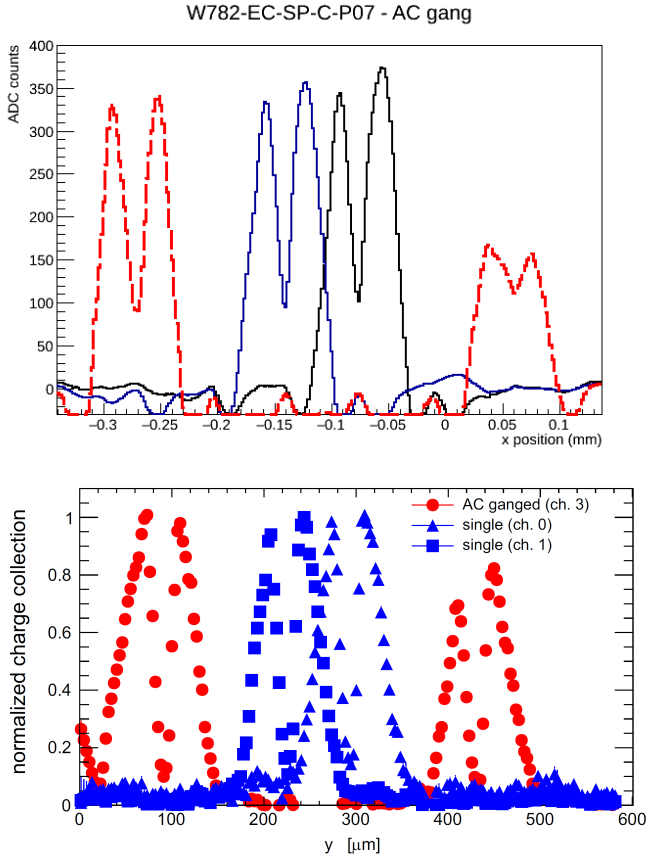

Figure 4.81: Comparison of signal amplitude as a function of the laser position results for AC-ganging sensors measured at *IFIC* (top) and *Freiburg* (bottom) institutes.

Both institutes registered less collected charge for the AC ganged strips and moreover less than for the DC ganged strips. Nevertheless, no *cross-talk* is present in these sensors and the laser signal is uniform in both cases. The above comparison confirm the consistency of the results carried out at *Freiburg University* as well as at *IFIC*.

Both AC and DC ganging showed good performance at different fluences. Each ganging technology presented small drawbacks. The most relevant are the higher drop in the collected charge of the AC *orphan strips* and the presence of small *cross-talk* on the DC ganging region. However, the signal uniformity and the amount of collected charge registered confirm the optimal performance of both technologies under high

radiation fluences. Despite both solutions are feasible for *HL-LHC* strip sensors, we would lean towards AC-ganging. The possible appearence of *cross-talk* effects with the DC-ganging can lead to tracking ambiguities and the tracking efficiency could be compromised.

4.4.4 Annealing studies

As introduced in chapter 3 the annealing of an irradiated sensor is the process of evolution in time of the detector characteristics, such as the doping concentration, the leakage current or the depletion voltage. These studies are important to determine the performance of the sensors especially during shutdown periods when the cooling of the detectors is not operating. The charge collection efficiency of a sensor is one of the most important parameters to analyze with the annealing process. As explained in section 3.3.3.3 the charge collected during the fixed integration time varies due to the trapping of charge carriers caused by radiation. With increasing annealing times a decrease in the trapping of electrons is observed. Therefore, this will lead to an increase of the collected charge with the annealing time in p-type sensors [108]. This effect can be seen in figure 4.82.

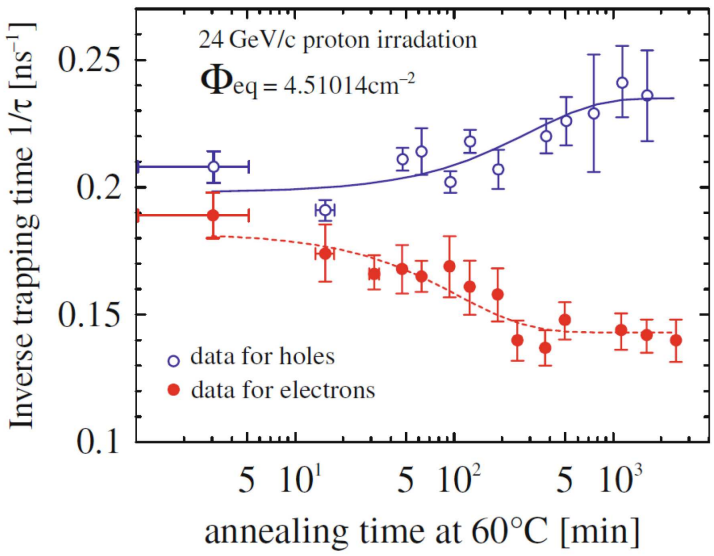

Figure 4.82: Behaviour of trapping for holes and electrons as a function of the annealing time. Picture extracted from [108].

The annealing of a sensor is a slow process. Each measurement can take days

or weeks at room temperature (RT) so in order to perform the studies in an affordable time, the sensors under study were exposed to a high temperature (60 °C). This process is known as *accelerated annealing*.

To scale the annealing from accelerated to RT a time scale factor is applied. The values used by the high energy physics detector community are 550 and 7400 for 60 °C and 80 °C respectively. These factors are multiplied to the times used at 60 an 80 °C and come from the calculation of the activation energies for beneficial and reverse annealing that was first performed by Moll [61]. However, some studies have shown different values and therefore the scaling factor calculation would need a revision [75].

Some recent experiments have been analyzing these factors [76]. However, no final conclusions have been yet stablished and this topic is still under study. Therefore, in this thesis the standard values accepted by the community will be used when necessary.

The annealed sensors and their properties are summarize in table 4.24.

Annealing Studies		
Sensor	**Fluence (n_{eq}/cm^2)**	**Irradiation Site**
W626-BZ3C-P02	p; 5×10^{14}	CYRIC Japan
W609-EC-SP-E-P08	p; 5×10^{14}	Birmingham
W648-EC-SP-E-P18	p; 5×10^{14}	Birmingham
W609-EC-SP-C-P17	p; 2×10^{15}	Birmingham

Table 4.24: List of analyzed irradiated sensors for annealing studies and their characteristics.

The annealing procedure is simple. To heat the sensors at a fixed temperature an climate chamber is used (figure 4.83). The temperature and the humidity can be set and controlled using a digital display with 0.1 °C of accuracy.

The selected annealing temperature is 60 °C and the annealing time is controled by an external chronometer. After heating the sensors they are introduced in the freezer and the collected charge is measured with the standard setup using the ALiBaVa system as explained in section 3.4.

Figure 4.83: Climate chamber used for annealing procedure. The temperature and the humidity can be selected.

Figure 4.84 shows the charge collection as a function of the bias voltage for each annealing time (top) and the collected charge (for a selected voltage) as a function of the annealing time (bottom) for sensor $W626\text{-}BZ3C\text{-}P02$. This sensor was irradiated at CYRIC (Japan) with protons at $5\times10^{14}\ n_{eq}/cm^2$.

As expected from figure 4.82 an increase in the collected charge is observed up to 300 min of annealing (for 500 V). This increase is about 3 ke^- and corresponds to the *beneficial annealing* period. Then a sudden decrease of about 3 ke^- occurs corresponding to the *reverse annealing* period. The *beneficial*, *reverse* and *stable annealing* periods were introduced in chapter 3. With the annealing of the sensor the leakage current was also increasing in each step and above 80 min of annealing it was very high ($> 400\ \mu A$) and unstable. Microdischarges also appeared so the measurements were only taken up to 500 V.

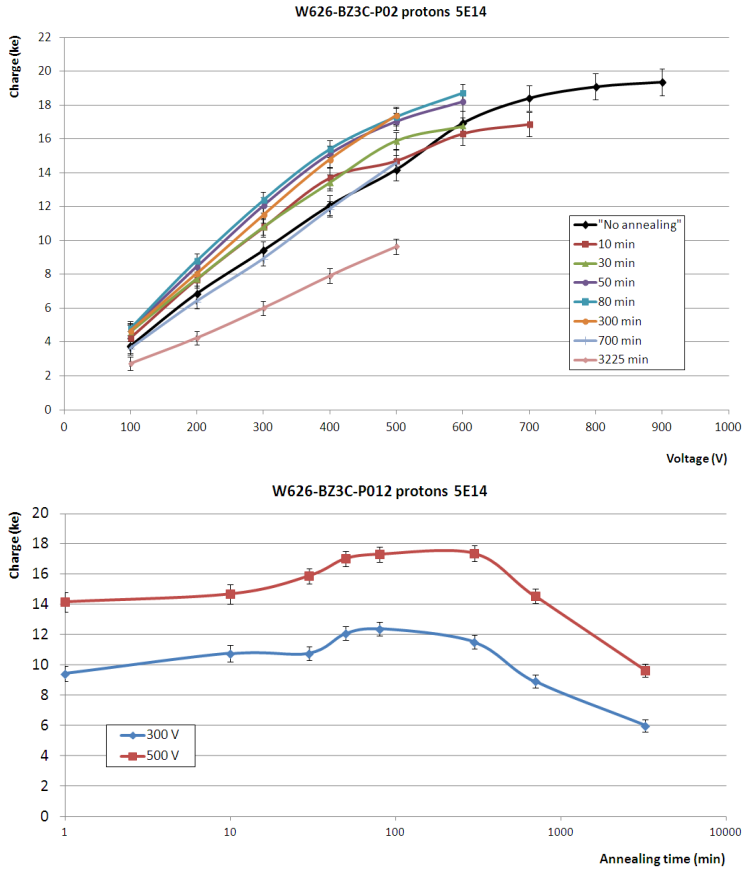

Figure 4.84: Charge collection as a function of the bias voltage at different annealing times (top). Charge collection for two selected bias voltages as a function of the annealing time (bottom).

Sensor $W609\text{-}EC\text{-}SP\text{-}C\text{-}P17$ irradiated at Birmingham with protons at a fluence of $2\times10^{15}\ n_{eq}/cm^2$ was also analyzed following the same procedure and the results are showed in figure 4.85

This sensor had a very stable behaviour and as in the case of the previous sensor an increase in the collected charge was observed up to 440 min corresponding to a *beneficial annealing* of about 4 ke^-. Above this a *reverse annealing* period starts up to 3340 min. Then a small increase in the charge collection have also been detected around 4270 min that could correspond to *charge multiplication* effects.

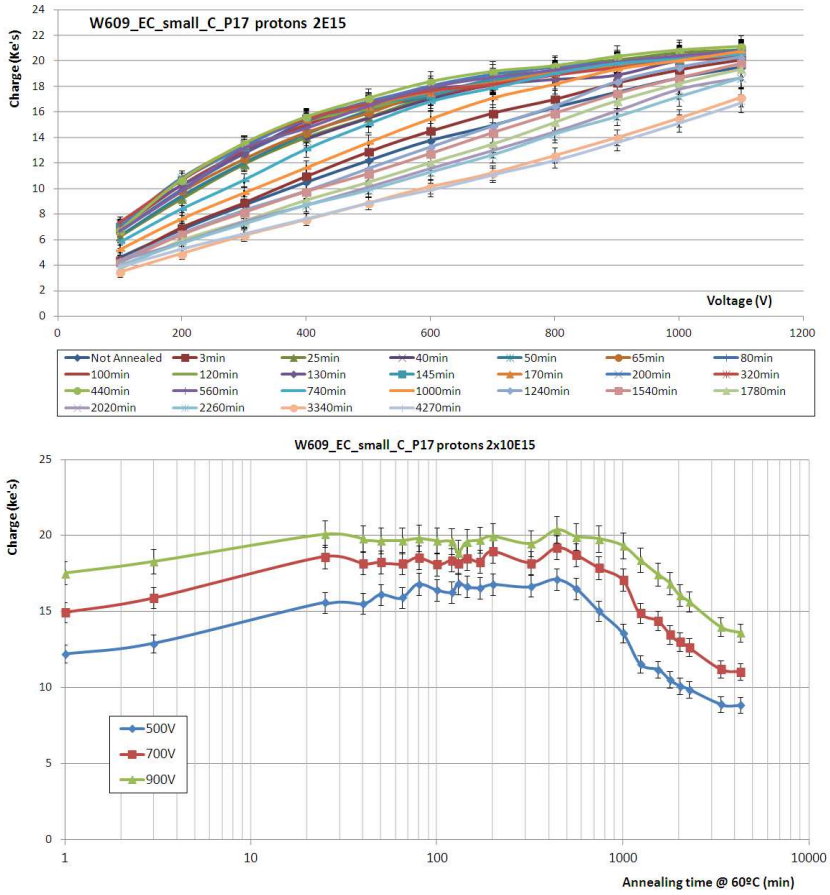

Figure 4.85: Charge collection as a function of the bias voltage at different annealing times (top). Charge collection for three selected bias voltages as a function of the annealing time (bottom).

The same studies for sensors $W609\text{-}EC\text{-}SP\text{-}E\text{-}P08$ and $W648\text{-}EC\text{-}SP\text{-}E\text{-}P18$ are depicted in figures 4.86 and 4.87 respectively. Both sensors have an irradiation dose of $5\times10^{14} n_{eq}/cm^2$ and were irradiated also with protons at Birmingham.

These sensors presented an odd behavior. They were bonded at the same time in the same ALiBaVa daughterboard and both had very noisy channels. The expected increase in the collected charge was not observed.

Sensor $W609\text{-}EC\text{-}SP\text{-}E\text{-}P08$ showed only decreasing charge with annealing time and in the case of sensor $W648\text{-}EC\text{-}SP\text{-}E\text{-}P18$ the charge was unstable showing also decreasing trend. The signal was almost covered by noise and data analysis was really difficult.

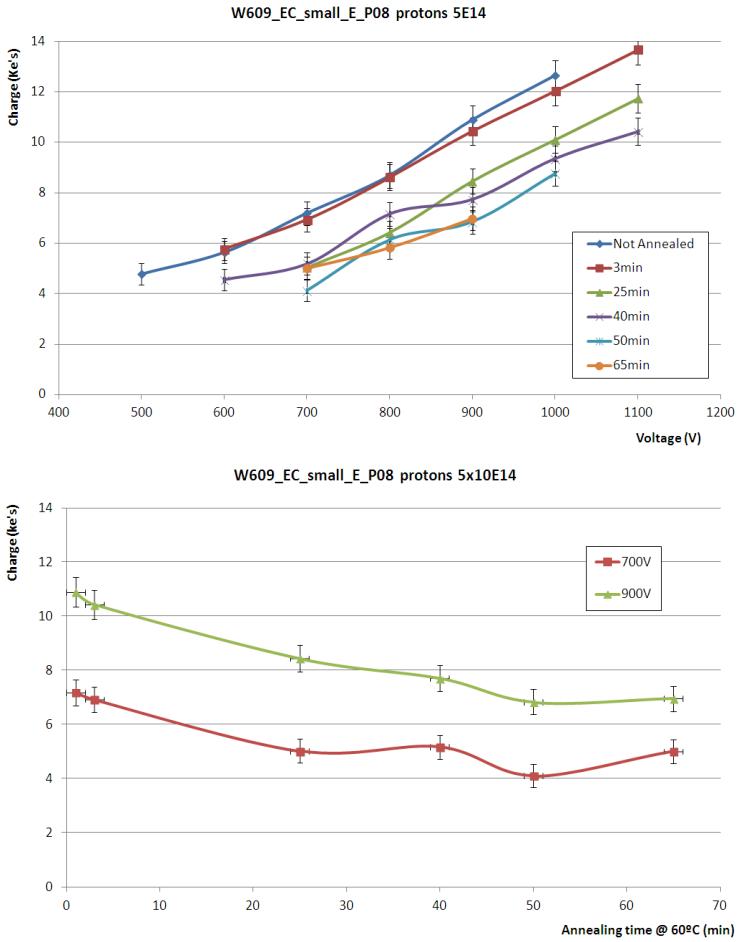

Figure 4.86: Charge collection as a function of the bias voltage at different annealing times (top). Charge collection for two selected bias voltages as a function of the annealing time (bottom).

Figure 4.88 shows the signal spectrum of each sensor at 700 V.

After 65 min of controlled annealing the leakage current started to increase dramatically ($I_{leakage}$ >20 mA) and the annealing was stopped.

Different institutes from the collaboration reported also problems during the analysis of sensors irradiated at Birmingham in similar dates. Some pulse shape reconstruction appeared with a double peak (figure 4.89) and therefore additional studies were carried out.

This double peak distribution could be causing the problems on the charge collection behaviour. Due to the difficulties fitting the data the resulting charge can not be extracted with precision.

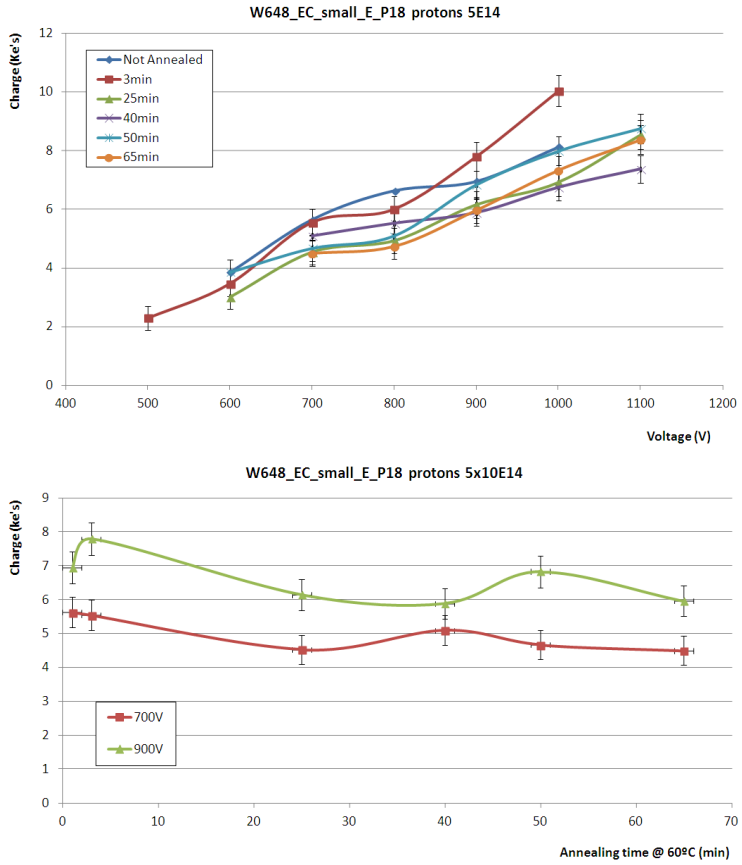

Figure 4.87: Charge collection as a function of the bias voltage at different annealing times (top). Charge collection for two selected bias voltages as a function of the annealing time (bottom).

Looking at the signal distribution per channel for sensor $W648\text{-}EC\text{-}SP\text{-}E\text{-}P18$ tested at *IFIC* non-uniformities in the collected charge are also observed (figure 4.90). Two channel regions showed significantly higher signal amplitude.

This effect was detected on different samples irradiated at Birmingham during 2015 and was also reported by *Freiburg University*. After several discussion it was concluded that the non-uniformity must be a result from an unsuccessful irradiation process. This hypothesis was then confirmed by the irradiation facility at Birmingham as well [109]. The irradiation procedure used threads to hold the sensors within a frame. It seems that these threads were protecting some regions of the sensors from the irradiation beam.

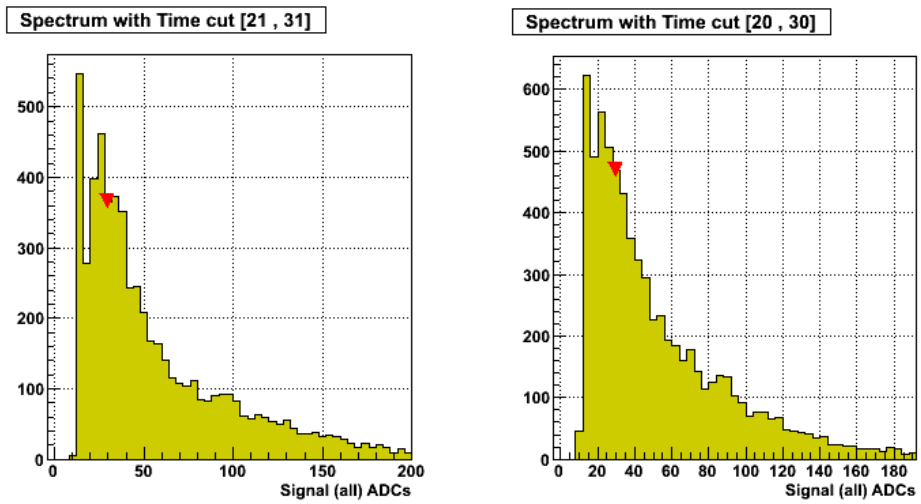

Figure 4.88: Signal spectrum at 700 V for sensors $W609$-EC-SP-E-$P08$ (left) and $W648$-EC-SP-E-$P18$ (right). In both cases the signal is almost covered by noise and it is difficult to distinguised.

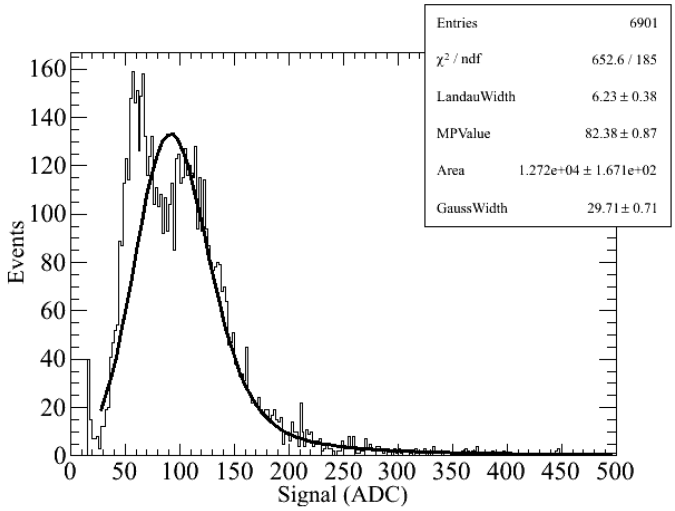

Figure 4.89: Reconstructed pulse shape of a Birmingham irradiated sensor with a fluence of $1\times10^{15}\ n_{eq}/cm^{-2}$ tested at *Freiburg University*. Picture taken from [76].

Different higher signal regions were found line up with the thread positions as can be seen in figure 4.91.

Table 4.25 presents a summary of the maximum collected charge and the corresponding annealing time for the analyzed *ATLAS12A* irradiated sensors.

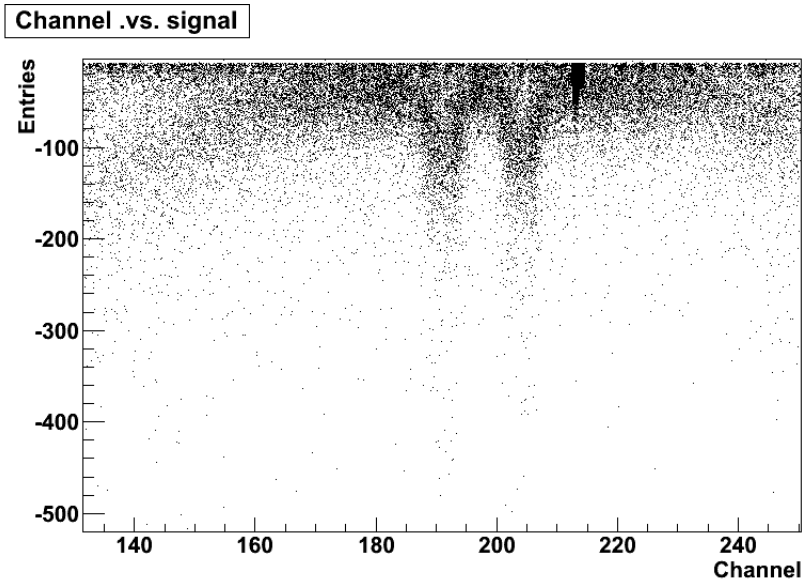

Figure 4.90: Signal distribution registered with ALiBaVa system at 1000 V for an irradiated sensor from Birmingham. Two channel regions are clearly detecting more signal.

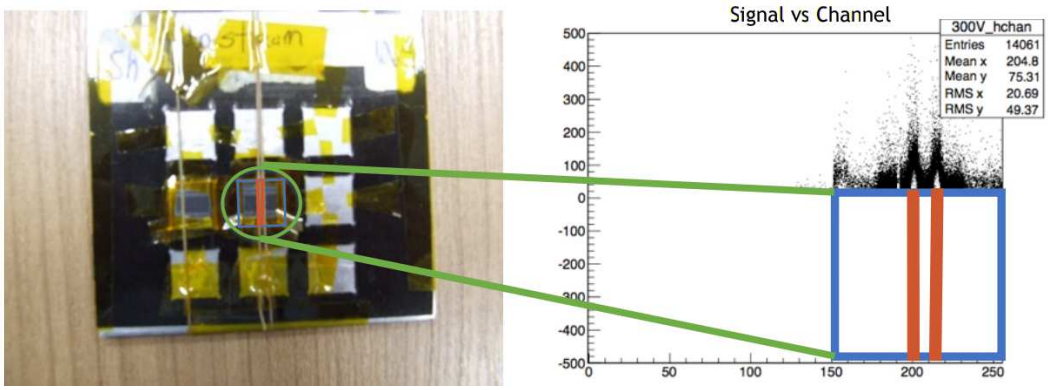

Figure 4.91: Sensors attached to frame with threads. They protected the sensors from irradiation and this caused non-uniformity of the applied dose during the procedure. This results in high charge collection on different sensor regions [109].

By taking results from sensor with more anealing data ($W609$-EC-SP-C-$P17$) one can directly compare them with the results published at [105] (figure 4.92, bottom). Despite the difference on irradiation fluence both sensors present similar behaviour.

Annealing Results			
Sensor	**Fluence (n_{eq}/cm^2)**	**Max. Collected Charge (ke^-) at 500 V**	**Annealing time (min)**
W626-BZ3C-P02 (CYRIC)	p; 5×10^{14}	17.35	300
W609-EC-SP-E-P08(B'ham)	p; 5×10^{14}	4.76	1
W648-EC-SP-E-P18(B'ham)	p; 5×10^{14}	2.28	1
W609-EC-SP-C-P17(B'ham)	p; 2×10^{15}	17.11	440

Table 4.25: Summary of obtained results for the annealing studies with *ATLAS12A* irradiated sensors.

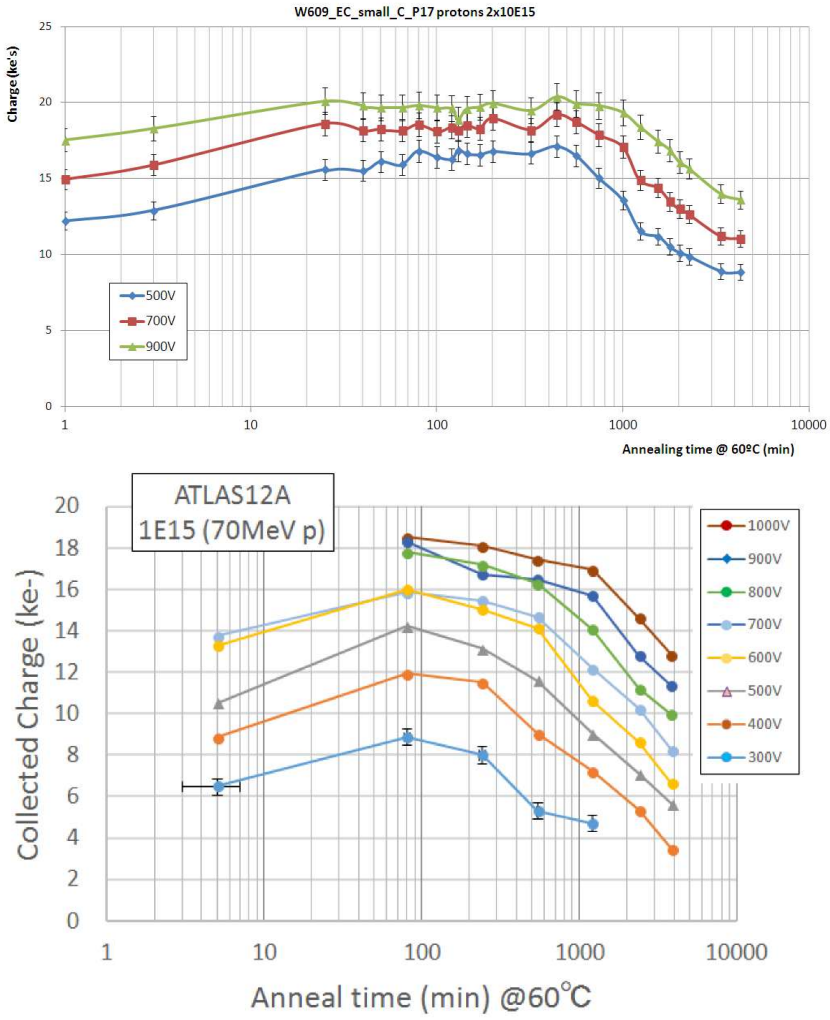

Figure 4.92: Comparison of obtained results in terms of charge collection as a function of the annealing time at *IFIC* (top) and the ones published at [105] (bottom).

From the results presented above we can conclude that the behaviour of the sensors will not be as strict as for the n-type sensors in terms of the annealing during

shutdown periods of the experiment. The reverse annealing period would start around 300-400 min of controlled annealing at 60 °C. This corresponds to 168 days (more than 5 months) at room temperature.

The present studies verify the good performance of the p-bulk strip sensors under high-radiation environments. They are still operational after high doses of radiation as the expected in the *HL-LHC* and their behaviour during shutdown periods will not be affected by external temperature of the experiment.

Chapter 5

First Petal prototype: The Petalet Project

As presented in chapter 4 the Petal is a complex object and its fabrication involves many production steps. Each Petal has six different module shapes and 13 different hybrids with a total of 18 sensors per Petal. The electronic part is composed by different elements, 7 different hybrids and a total of 113 chips, among other things (this part will be described in section 5.3). Figure 5.1 shows a scheme of the hybrids and chips distribution on a Petal.

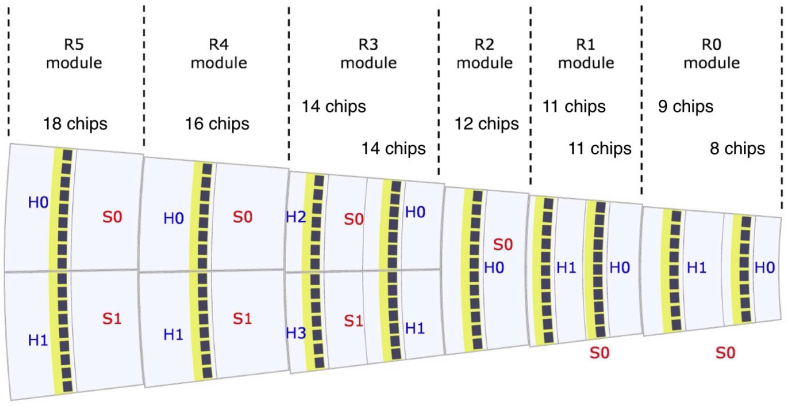

Figure 5.1: Each Petal face has 6 different module shapes (R_i). Each module can hold one or two sensors (S_0, S_1) and one or two of hybrids (H_0, H_1), with a total of 9 different sensors and 13 different hybrids per Petal face.

The production costs of building a complete Petal are high and an important contribution derive from the required silicon wafers masks. In order to minimize

the expense for testing purposes a small Petal prototype has been developed. An intermediate step that will allow us to study the special features of a Petal against a *stave*. The central region of the complete Petal design has been selected to be built. The prototype will include the three sensors on the region where the Petal splits into two sensor columns fabricated from 4 inch wafers[1]. This is the so-called *Petalet* (see figure 5.2).

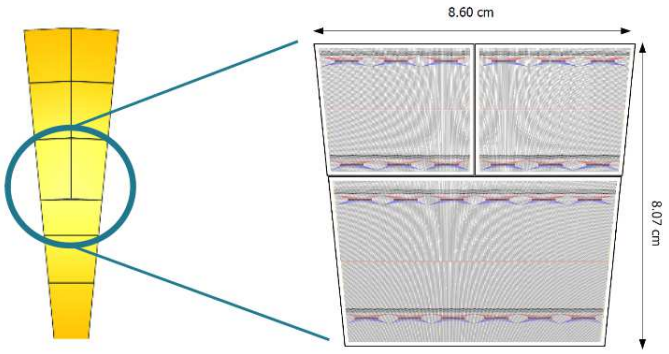

Figure 5.2: The central region of the Petal is selected to be built as Petalet.

The Petalet will help understanding the whole model and will allow to test different powering schemes and production methods. It consists of three sensors, two top sensors and one big sensor (see figure 5.3) mounted on a carbon core. The hybrids, housing the *ASIC*s, are glued on top of the sensors. Using a chiller machine a coolant will circulate inside the titanium pipes acting as coolant.

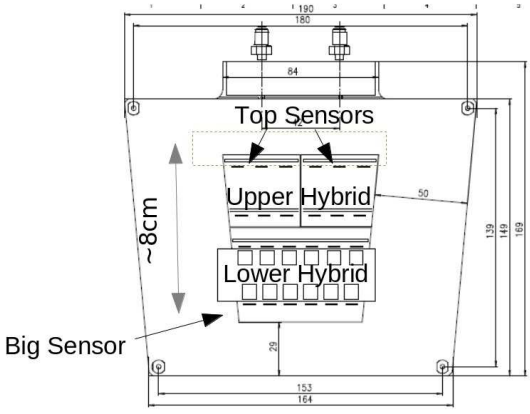

Figure 5.3: Schematic view of a Petalet with all its components and dimensions.

[1] This wafer size allows us to turn to different companies, such as *CNM* in Barcelona, which offer more affordable production costs.

5.1 Structure description

The Petalet core is based on the Petal core design introduced in chapter 4. It is built using similar materials and fabrication processes. Titanium pipes are used to provide cooling, with carbon foam surrounding them. The empty space is filled with honeycomb (made of carbon fibre) to provide stifness. Both sides are covered with carbon facings. Figure 5.4 shows the Petalet core components.

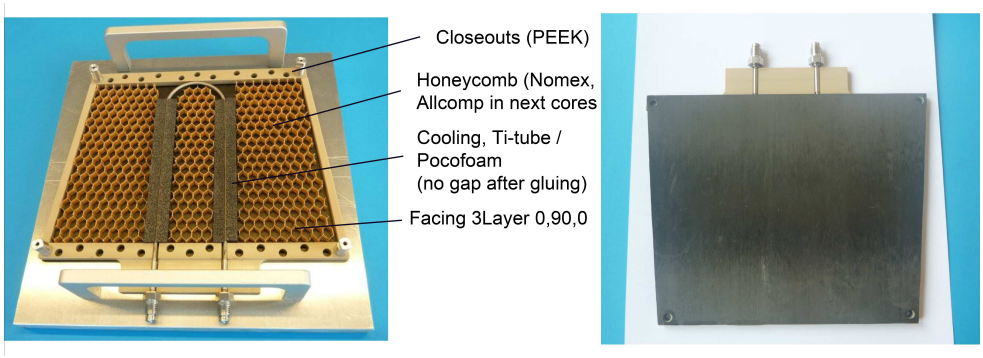

Figure 5.4: Petalet core based on the Petal core design. Titanium pipes surrounded by carbon foam are used to provide cooling. Stifness is achieved filling the empty space with honeycomb made of carbon fibre (left). The surface is covered by two carbon facings (right).

5.2 Petalet Sensors

As explained in chapter 4, 6 inches silicon wafers will be used to build the Petal sensors. Following the design which includes the stereo angle built in and the ganged *orphan strips* technology explained before, bonding problems could appear. Due to the strips distribution, large bonding angles are required to connect the strips to the *ASIC*s. However, the maximum bonding angle is limited by the size of the sensor bonding pad. This maximum angle is around 20 $^{\circ}$ to maintain the bonding yield. Figure 5.5 shows a sketch of the bonding angle problem. Increasing the sensor strip pitch will also increase the bonding angle.

Figure 5.6 shows a drawing of the maximum bonding angle calculation. Bonding pads on the sensor lie along a line of length L (128 channels times the strip pitch) at a distance d of a readout chip of width w. For instance, a strip pitch of about 100 μm would yield a maximum bonding angle of 40 $^{\circ}$. In order to reduce this bonding

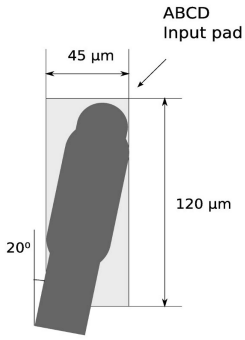

Figure 5.5: The maximum bonding angle possible is limited by the size of the smallest bonding pad size.

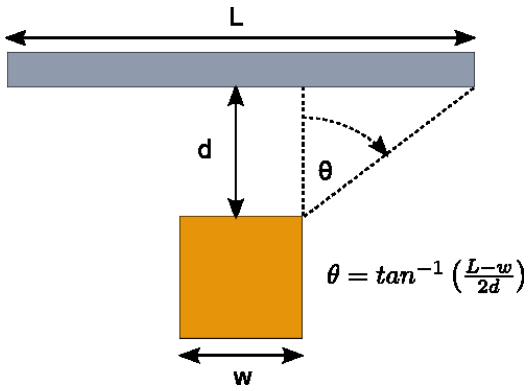

Figure 5.6: Maximum bonding angle calculation. A strip pitch of 100 μm leads to 40 $^{\circ}$ of bonding angle.

angle, maximizing the bonding yield and without compromising the strip pitch, several bonding pad schemes (built-in pitch adaptors) were developed and evaluated.

Real size and miniature n-in-p sensors with p-stop isolation were produced in *CNM* (Barcelona) using 4 inch wafers. The miniature sensors present different strip pitch which leads to different size. Two types of sensor bonding pads were analyzed: standard pads and embedded pitch adaptors (wich will be explained later). Figure 5.7 shows both types of sensors. The sensor fabrication properties are summarized in table 5.1.

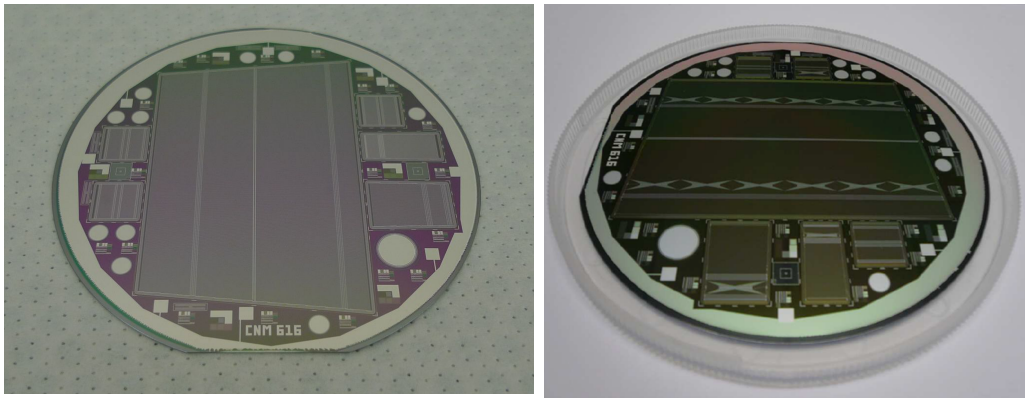

Figure 5.7: Petalet big sensor wafer with standard pads (left) and with embedded pitch adaptors in a second metal layer (right). Miniature sensors for testing purposes are also included in both wafers.

The electrical characterization of the mini and full-size sensors was carried out following the same procedure as for the *ATLAS12A* sensors. The objectives of these

CNM Petalet Sensors	
Substrate	P-type
Wafer Size	4 inch
Wafer technology	Float Zone
Isolation	p-stop
Thickness	(285$\pm$25) μm
Resistivity	(10,0$\pm$5,0) kΩcm
Pitch Size (miniature)	Large: 92 μm / Small: 58 μm / x-Small: 45 μm
Pitch Size (full-size)	Big: (max: 94 μm, min: 82 μm), Top (max: 101 μm, min: 92 μm)

Table 5.1: Fabrication properties of *CNM* sensors.

tests were to verify the fabrication process and then select the best full-size detectors to be used in the fabrication of the Petalet. Furthermore, the pitch adaptor technology will be evaluated.

5.2.1 Embedded pitch adaptors

As explained above, due to the large pitch dissimilarity betweeen detector pads and chip pads, large bonding angles appear. A possible solution is to integrate pitch adaptors in the detector adding an extra metal layer. This technique would reduce the risks and failures during the wire bonding. It also avoids extra pieces and assembly steps if we compare to the separated glass pitch adaptors used in the *ATLAS SCT* modules.

The second-metal traces of the embedded pitch adaptors are parallel to each other minimizing the crossing area to reduce the capacitive coupling between them. The traces keep the same angle (in each quadrant). This angle is the maximum that can be used for a minimum safety separation between traces of 20 μm[1]. Moreover, These requirements produce a butterfly shape in the second metal layer traces.

Figure 5.7 (right) shows a silicon wafer with different sensors where the embedded pitch adaptors (embedded *PA*s) with butterfly shape can be distinguished. A detailed view of its design and a microscope picture can be seen in figure 5.8. The wire bonds are also appreciated.

The addition of a second metal layer leads to two inherent challenges. One is the cross-talk between traces in the first and second metal layers, and the other is the

[1] This distance is chosen as a small but technologically safe distance between traces in order not to compromise the yield.

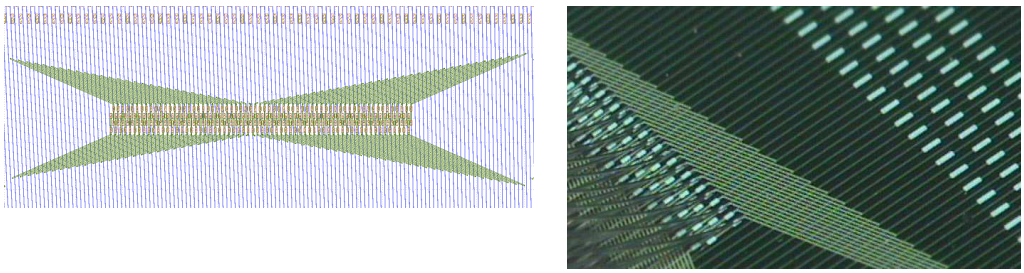

Figure 5.8: Detailed view of the embedded pitch adaptors design (left) and a microscope view where the wire bonds can also be appreciated (right).

possible signal pick-up from the bulk directly to the second metal layer traces. Figure 5.9 shows an scheme of this two possible effects.

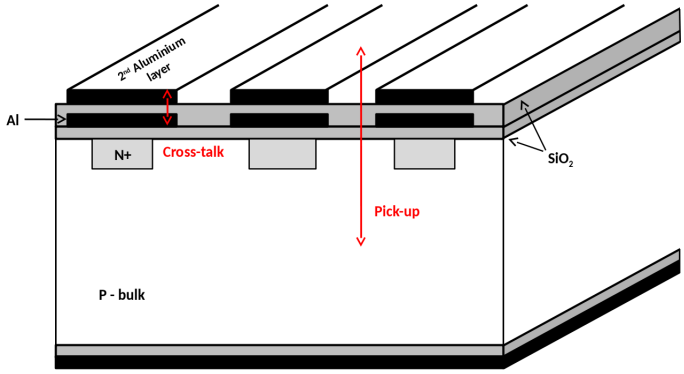

Figure 5.9: Scheme of cross-talk and pick-up effects. Cross-talk can appear between the first and the second metal layers. However, pick-up is a coupling effect between the second metal layer and the silicon bulk.

Due to these effects fake pulses could appear in the second metal channels. Cross-talk and pick-up will be analized with laser techniques in section 5.2.2.3.

In sensors with embedded *PA*s also standard pads are included for testing purposes. A scheme of the pads distribution can be seen in figure 5.10.

5.2.2 Tests with minis and full-size sensors

The tests carried out for the electrical characterization of Petalet sensors included:

- *IV*-*CV* curves: Determining the breakdown and full depletion voltages.
- Charge collection effiency studies: Obtaining the maximum charge collected above full depletion.

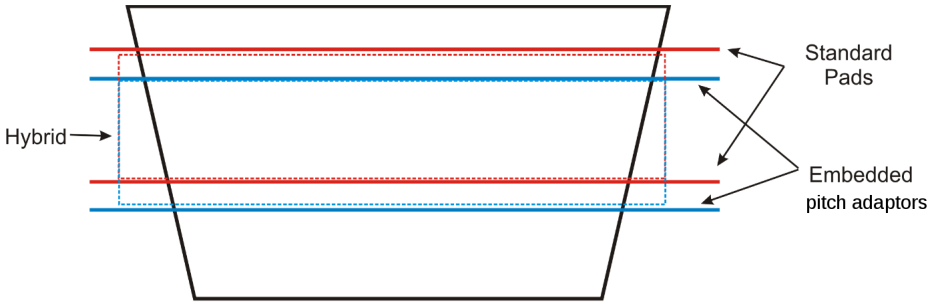

Figure 5.10: Standard and embedded pitch adaptors scheme distribution in a Petalet big sensor.

- Laser studies: analyzing the strip integrity and studying the possible cross-talk and pick-up effects in the sensors.

5.2.2.1 IV/CV characterization

After the silicon wafer fabrication different tests are carried out by the manufacters to ensure that the sensors accomplish the quality requirements before sending them to the collaboration institutes.

Table 5.2 summarizes the obtained values provided by *CNM* compared to the *ATLAS12* specifications.

Measurement	ATLAS12 specs	Petalet sensors
CV	$V_{FD} < 300$ V	$V_{FD} < 80$ V
IV	$I < 200\ \mu A/cm^2$ at 600 V	$I < 200\ \mu A/cm^2$ at 200 V
$I_{leakage}$ stability	< 3 % at 600 V / 24 h	< 2 % at 120 V / 12 h
$C_{coupling}$	$> 20\ pF/cm$	$> 40\ pF/cm$
C_{int}	$< 0.8\ pF/cm$ at 300 V	$< 0.7\ pF/cm$ at 300 V
R_{int}	$> R_{bias}$ at 300 V	$> 1\ G\Omega$ at 300 V
R_{bias}	$1.5\ M\Omega \pm 0.5\ M\Omega$	$1.7\ M\Omega \pm 0.3\ M\Omega$
$R_{implant}$	$< 20\ k\Omega/cm$	$17.3\ k\Omega/cm$
R_{metal}	$< 15\ k\Omega/cm$	$15\ \Omega/cm$ (std) / $30\ \Omega/cm$ (emb)

Table 5.2: Summary of *CNM* Petalet miniature sensors measured. Parameters extracted from [110].

The inventory of the measured sensors is presented in tables 5.3 and 5.4, for miniature and full-size sensors respectively. The type of pad is also included with *std* corresponding to stardard pads and *emb* to embedded *PA*s.

Miniature Sensor	Active Area (cm^2)	**Pitch Type**	**Pad type**
LP-6214-W01	$\sim$ 2.2	Large	std
LP-6214-W03	$\sim$ 2.2	Large	std
LP-6271-W06	$\sim$ 2.2	Large	emb
LP-6271-W12	$\sim$ 2.2	Large	emb
SP-6271-W06	$\sim$ 1.39	Small	emb
SP-6271-W12	$\sim$ 1.39	Small	emb
x-SP-6215-W04	$\sim$ 1	Super small	std
x-SP-6215-W05	$\sim$ 1	Super small	std
x-SP-6272-W10	$\sim$ 1	Super small	emb
x-SP-6272-W11	$\sim$ 1	Super small	emb

Table 5.3: Summary of *CNM* Petalet miniature sensors measured.

Sensor	**Pad**	**Sensor**	**Pad**	**Sensor**	**Pad**
BS-6214-W02	std	TR-6442-W13	std	TL-6215-W04	std
BS-6214-W03	std	TR-6215-W04	std	TL-6215-W05	std
BS-6441-W15	std	TR-6215-W05	std	TL-6442-W13	std
BS-6441-W14	std	TR-6442-W14	std	TL-6442-W14	std
BS-6901-W10	std	TR-6442-W16	std	TL-6902-W06	std
BS-6901-W05	std	TR-6904-W11	std	TL-6508-W06	emb
BS-6901-W03	std	TR-6902-W04	emb	TL-6508-W09	emb
BS-6271-W13	emb	TR-6272-W02	emb	TL-6904-W02	emb
BS-6507-W05	emb	TR-6508-W06	emb	TL-6904-W05	emb
BS-6903-W03	emb	TR-6508-W09	emb		
BS-6903-W09	emb				

Table 5.4: Summary of *CNM* Petalet full-size sensors measured. *BS*, *TR* and *TL* correspond to big sensor, top right sensor and top left sensor respectively.

Table 5.5 lists the tests parameters used during these studies. All the measurements were taken insid *IFIC*'s clean room facility at 20 °C. As in the case of *ATLAS12A* sensors, frequency studies were carried out to determine which was the correct value in each case for having capacitance uniformity (for more details see section 3.4.2).

Miniature sensors		
Set parameters	**I-V**	**C-V**
Max. bias Voltage (V)	200	200
Voltage Step (V)	10	10
Delay (s)	15	20
Current compliance (μA)	10	10
Frequency (kHz)	1	1
Full-size sensors		
Set parameters	**I-V**	**C-V**
Max. bias Voltage (V)	200 / 600	200 / 400
Voltage Step (V)	10	10
Delay (s)	15	20
Current compliance (μA)	120	120
Frequency (kHz)	10	10

Table 5.5: Parameters used during $I-V$ and $C-V$ curves measurements with miniature and full-size sensors.

Figures 5.11 and 5.12 present the results obtained for the I-V and C-V curves measured on the miniature sensors respectively.

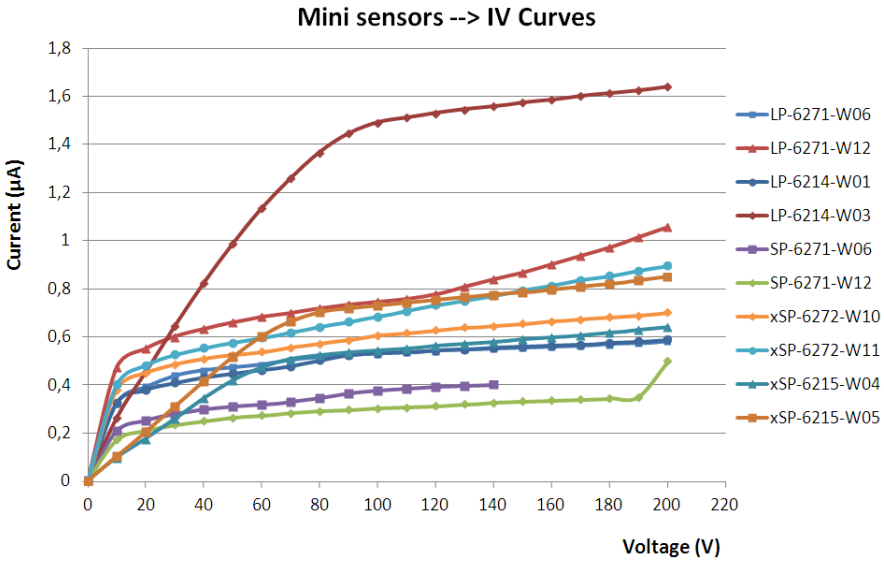

Figure 5.11: I-V curves obtained for the Petalet miniature sensors.

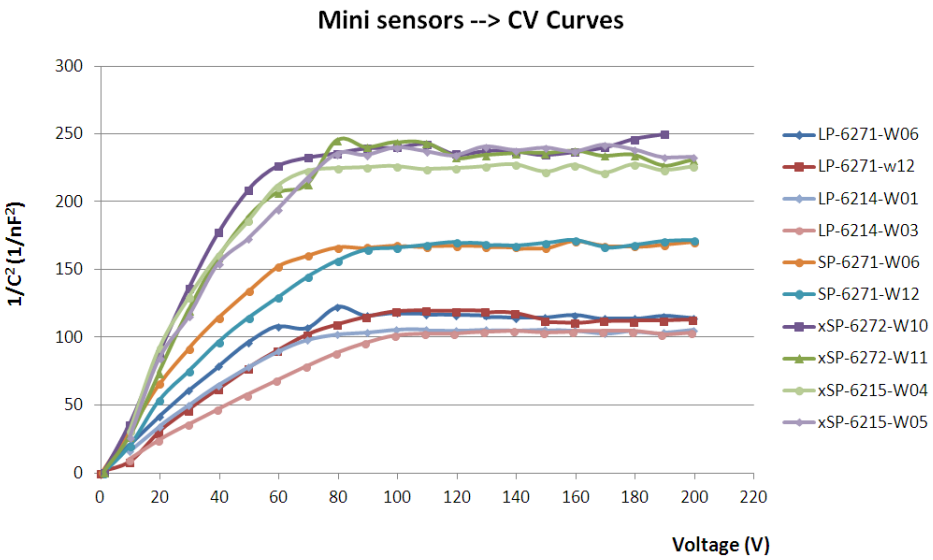

Figure 5.12: C-V curves obtained for the Petalet miniature sensors.

No breakdown was observed below the maximum bias voltage of the tests (200 V). A jump in the current of about 1 μA was measured in one of the 10 sensors. Nevertheless, all the leakage current values are below 2 μA which is far from the maximum value stablished by the specifications for mini sensors (200 $\mu A/cm^2$). Moreover the behaviour of the leakage current is quite constant with the bias voltages range used in the tests. Regarding the C-V curves the difference between the three types of sensors is clearly reflected. This is due to the equivalence between the capacitance and area ratio of the sensors. Comparing their difference in active area from table 5.3 and their difference in capacitance from figure 5.12 we obtain similar ratios: around a 30% between large and small pitch sensors and around a 50% between large an super small pitch sensors. All the full depletion voltages are below 100 V being the average of them (68.2 $\pm$ 3.2) V. This is far from the maximum value allowed by the specifications.

The depletion voltage values for each miniature sensor are presented in table 5.6.

Figure 5.13 shows an histogram of the depletion voltage values distribution. The average of the measurements is also included.

Regarding the full-size sensors the data have been separated on sensor type for simplicity. In these tests the high-voltage power supply was set to limit the output current to 120 μA in order to protect the sensors (see table 5.5). This makes that the maximum voltage applied for each sensor is different, depending on their behaviour.

Full Depletion Voltage - Miniature sensors	
Sensor	**V_{FD} (V)**
LP-6214-W01	(68.7 $\pm$ 2.2)
LP-6214-W03	(91.8 $\pm$ 0.9)
LP-6271-W06	(64.9 $\pm$ 4.8)
LP-6271-W12	(82.5 $\pm$ 5.5)
SP-6271-W06	(61.2 $\pm$ 1.8)
SP-6271-W12	(76.3 $\pm$ 1.6)
x-SP-6215-W04	(58.6 $\pm$ 2.1)
x-SP-6215-W05	(66.6 $\pm$ 1.8)
x-SP-6272-W10	(55.9 $\pm$ 1.2)
x-SP-6272-W11	(55.1 $\pm$ 5.6)

Table 5.6: Full depletion voltage values for miniature sensors extracted from their C-V curves.

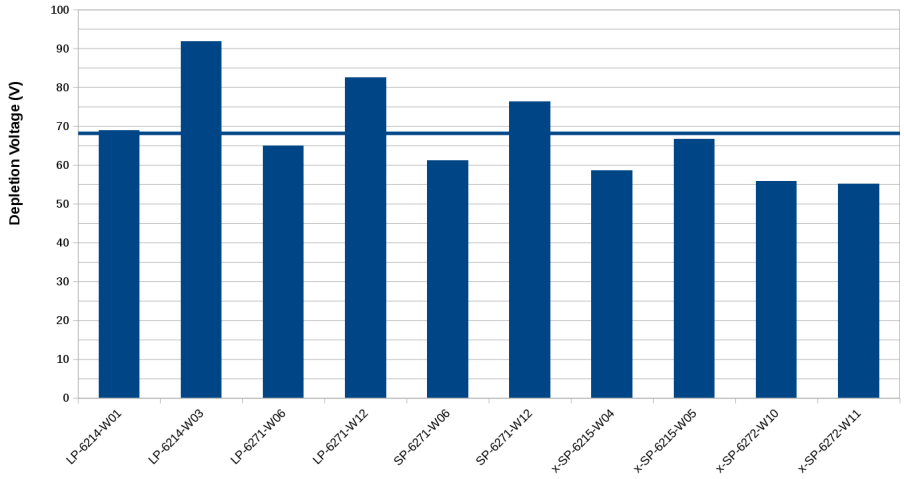

Figure 5.13: Histogram of the full depletion voltages obtained with the Petalet miniature sensors. The average value is also included.

Figures 5.14 and 5.15 present the results obtained for the I-V and C-V curves measured on the big sensors.

Looking at big sensors IV results (figure 5.14) only two sensors broke down below 200 V. Another group of three sensors maintained the leakage current below 80 μA and reached the breakdown around 300 V while the rest of them varied achieving breakdown voltages between 400 and 600 V. Appart from one sensor all the rest meet the specifications (see table 5.2).

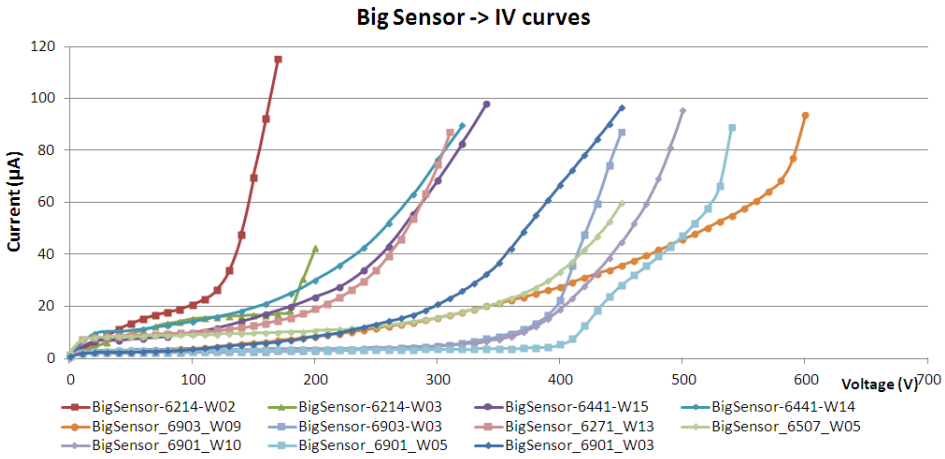

Figure 5.14: I-V curves obtained for the full-size big sensor manufactured by *CNM*.

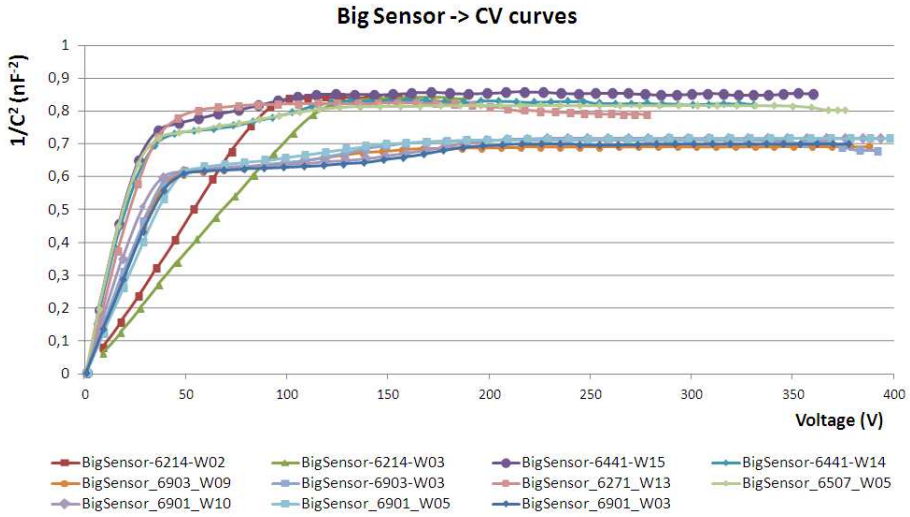

Figure 5.15: C-V curves obtained for the full-size big sensor manufactured by *CNM*.

Regarding the CV results the same sensors which presented higher leakage current also achieved a higher full depletion voltage (around 110-120 V). Nevertheless, they are still below the maximum value stablished by specifications (around 300 V). The rest of big sensors are fully depleted above 50 V. Moreover, in figure 5.15 three groups of sensors can be distinguised. The first group presents higher values of $1/C^2$ (which corresponds to lower capacitance values) and lower depletion voltages. The second group has lower values of $1/C^2$ (which corresponds to higher capacitance values) and also lower depletion voltages. And there is also a third group that presents higher values of $1/C^2$ (which corresponds to lower capacitance values) and higher

depletion voltages. Table 5.7 summarizes all the relevant results obtained with all the big sensors. There are no apparent geometrical differences between these sensors and with the experimental setup used. No defects were detected at the sensors surface neither. Therefore we do not have a direct explanation for these small differences.

Big Sensor	V_{FD} (V)	$I_{Leakage}$ (μA) **(at 200 V)**	**C** (nF) **(at 200 V)**	**Pad**	**Comment**
6441-W14	(38.2 ± 1.4)	29.95	1.09	std	Low C / Low V_{FD}
6271-W13	(39.7 ± 0.7)	19.06	1.10	emb	
6507-W05	(40.3 ± 1.6)	10.59	1.10	emb	
6441-W15	(41.8 ± 1.7)	23.44	1.08	std	
6901-W10	(43.1 ± 1.9)	3.74	1.18	std	High C / Low V_{FD}
6901-W03	(47.4 ± 3.5)	8.38	1.19	std	
6903-W03	(47.7 ± 4.2)	2.91	1.18	emb	
6903-W09	(51.3 ± 1.8)	8.51	1.20	emb	
6901-W05	(58.9 ± 2.4)	3.18	1.18	std	
6214-W02	(71.3 ± 1.1)	> 115	1.09	std	Low C / High V_{FD}
6214-W03	(83.9 ± 0.9)	21.62	1.09	std	

Table 5.7: Summary of results and comments for Petalet full-size big sensors.

Figures 5.16 and 5.17 show the I-V and C-V curves for top right sensors.

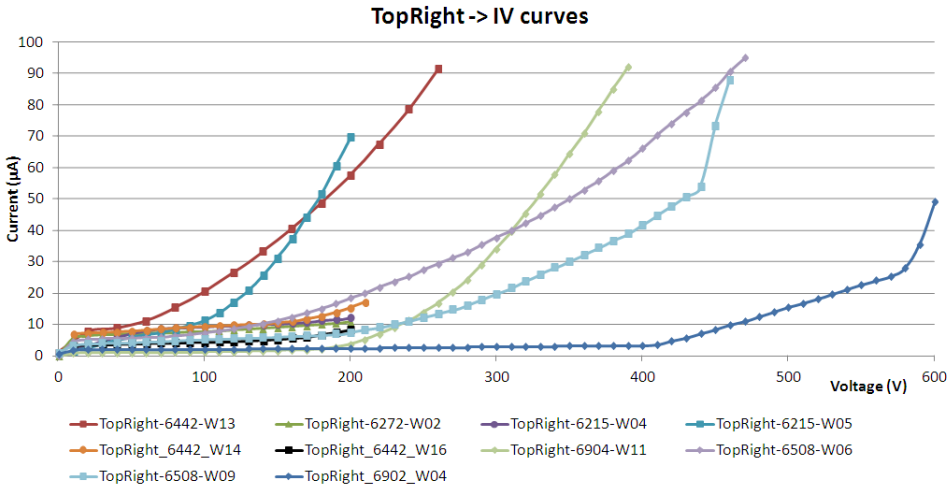

Figure 5.16: I-V curves obtained for the full-size top right sensor manufactured by *CNM*.

In the case of the top right IV curves there were two sets of measurements. The first batch of sensors was measured only up to 200 V with no breakdown presence.

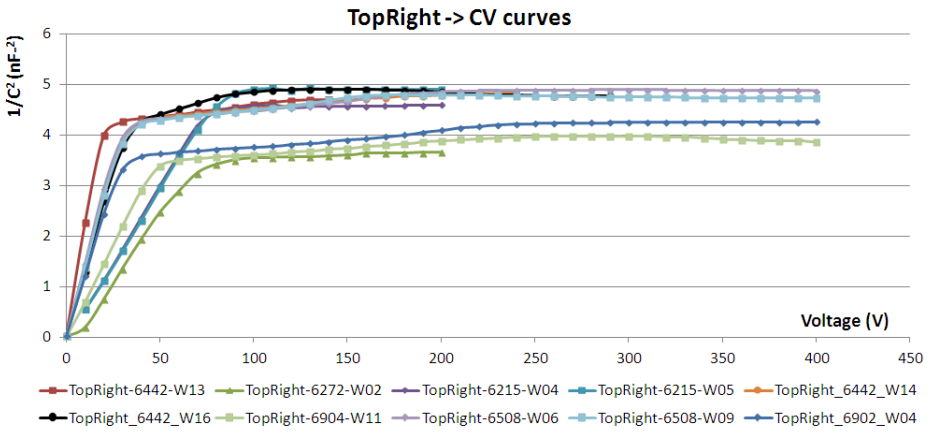

Figure 5.17: C-V curves obtained for the full-size top right sensor manufactured by *CNM*.

The second batch was intended to be measured up to 600 V. Below 200 V only two sensors presented high leakage current (above 80 μA) with breakdown voltages around 200 V and the rest of them meet the specifications. Regarding the CV curves the major part of the sensors achieved the full depletion around 50 V. As in the case of big sensors, three groups with different values of capacitance and depletion voltages can be distinguised. Table 5.8 presents all the relevant results for top right sensors.

Top Right	V_{FD} (V)	$I_{Leakage}$ (μA) **(at 200 V)**	**C** (nF) **(at 200 V)**	**Pad**	**Comment**
6442-W14	(30.5 $\pm$ 1.1)	15.38	0.46	std	Low C / Low V_{FD}
6508-W09	(35.4 $\pm$ 1.6)	7.42	0.46	emb	
6442-W16	(37.9 $\pm$ 2.7)	8.32	0.45	std	
6508-W06	(39.7 $\pm$ 2.9)	18.4	0.45	emb	
6442-W13	(41.1 $\pm$ 1.7)	55.23	0.50	std	
6902-W04	(35.0 $\pm$ 2.1)	2.36	0.49	emb	High C / Low V_{FD}
6904-W11	(58.4 $\pm$ 4.0)	3.75	0.50	std	
6215-W04	(72.5 $\pm$ 0.5)	12.17	0.46	std	Low C / High V_{FD}
6272-W02	(72.8 $\pm$ 1.2)	10.81	0.50	emb	
6215-W05	(79.7 $\pm$ 0.5)	69.78	0.45	std	

Table 5.8: Summary of results and comments for Petalet full-size top right sensors.

Top left sensors had similar behaviour to top right ones (see figures 5.18 and 5.19). In this case, no breakdown occured below 300 V and the full depletion voltage was 50 V on average approximately. And one more time we found three group of

sensors with different values of capacitance and depletion voltages.

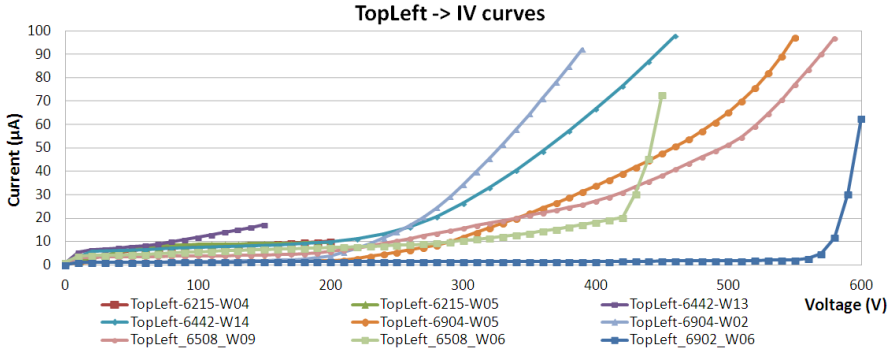

Figure 5.18: I-V curves obtained for the full-size top left sensor manufactured by *CNM*.

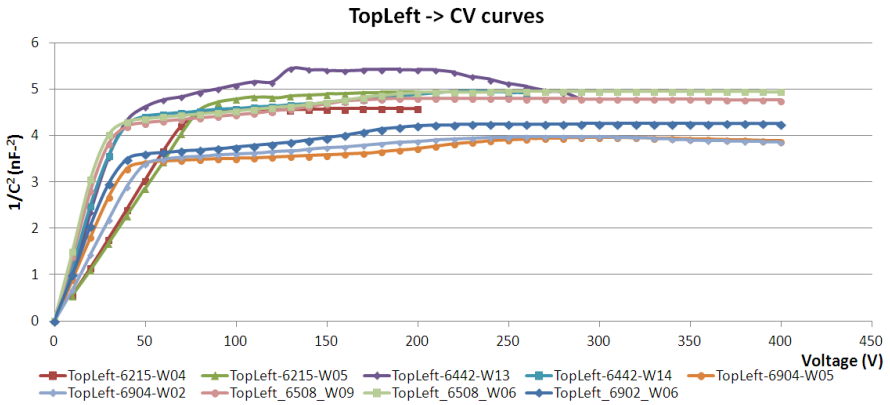

Figure 5.19: C-V curves obtained for the full-size top left sensor manufactured by *CNM*.

Table 5.9 presents all the relevant results for top left sensors.

In general, from the tables presented above, the relationship between the three groups of sensors could be in their run number. Table 5.10 lists all the sensors grouped by their capacitance and depletion voltage characteristics.

This effect affects the sensors independently of their pad technology having only in common a similar run number. Small changes in the resistivity or the effective doping concentration in these runs would affect directly to the capacitance of the sensors and this could be a possible reason. However, no difference during the sensors production was reported by the manufacturer. A detailed visual inspection was carried out on these sensors and they did not presented any defect in the surface. We did not find a convincing explanation to these dissimilarities. Nevertheless, despite this, all the sensors meet the specifications.

Top Left	V_{FD} (V)	$I_{Leakage}$ (μA) (at 200 V)	C (nF) (at 200 V)	Pad	Comment
6508-W06	(33.1 $\pm$ 1.6)	7.37	0.45	emb	Low C / Low V_{FD}
6442-W14	(34.9 $\pm$ 6.0)	9.79	0.45	std	
6508-W09	(35.5 $\pm$ 1.6)	5.56	0.45	emb	
6442-W13	(43.8 $\pm$ 3.3)	23.50	0.43	std	
6902-W06	(40.5 $\pm$ 5.1)	1.20	0.49	std	High C / Low V_{FD}
6904-W02	(50.9 $\pm$ 2.1)	3.05	0.50	emb	
6904-W05	(60.4 $\pm$ 3.8)	0.96	0.49	emb	
6215-W04	(72.1 $\pm$ 0.4)	10.02	0.47	std	Low C / High V_{FD}
6215-W05	(82.2 $\pm$ 1.0)	9.47	0.45	std	

Table 5.9: Summary of results and comments for Petalet full-size top left sensors.

Big Sensor	Top Right Sensor	Top Left Sensor	Capacitance / Voltage
6441-W14	6442-W14	6442-W13	Low C / Low V_{FD}
6441-W15	6442-W13	6442-W14	
6507-W05	6442-W16	6508-W09	
6271-W13	6508-W06	6508-W06	
	6508-W09		
6901-W10	6902-W04	6902-W06	High C / Low V_{FD}
6901-W03	6904-W11	6904-W02	
6901-W05		6904-W05	
6903-W03			
6903-W09			
6214-W02	6272-W02	6215-W04	Low C / High V_{FD}
6214-W03	6215-W04	6215-W05	
	6215-W05		

Table 5.10: Petalet sensors grouped by their capacitance and depletion voltage characteristics. These three groups correspond to similar run numbers.

Figures 5.20 and 5.21 show a histogram of the depletion voltage values obtained with all the full size sensors. The average value of the full depletion voltages is also included. Considering all the sensors, the average full depletion voltage was (50.68 $\pm$ 2.55) V which is far from the 300 V value stablished by specifications.

Since *CNM* sensors have low depletion voltages (around 50 V) a factor of 2 will be applied as margin to the Petalet bias voltage to ensure full depletion (100-150 V).

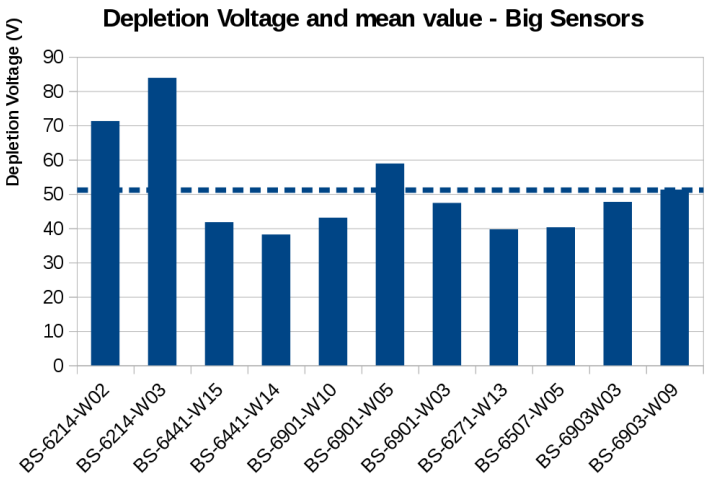

Figure 5.20: Histogram of the depletion voltage values obtained with the full size Big sensors. The depletion voltage average is also included.

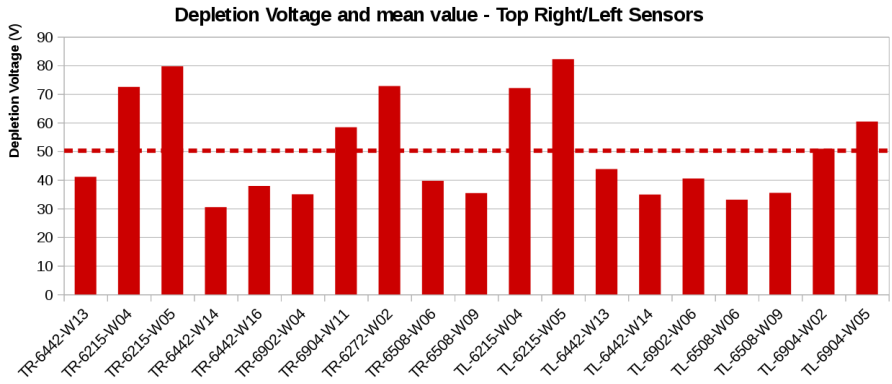

Figure 5.21: Histogram of the depletion voltage values obtained with the full size Top Right and Top Left sensors. The depletion voltage average is also included.

For the fabrication of two Petalets at *IFIC* we selected the sensors that presented low leakage current and low full depletion voltage below 100 V at the same time. They are summarized in table 5.11.

5.2.2.2 Charge collection characterization

The thickness of the Petalet sensors used for these studies is (285 $\pm$ 25) μm. Using equation 4.15 (see section 4.4.2) the expected collected charge above full depletion will correspond to 21.73 ke^{-}.

The collected charge on Petalet mini sensors have been measured using the *ALiBaVa* system similarly to the *ATLAS12A* charge collection measurements (see

Sensors for Petalet fabrication		
Sensor	$I_{leakage}$ **at 100 V** (μA)	V_{FD} **(V)**
BigSensor-6901-W10	3.40	(43.1 $\pm$ 1.9)
BigSensor-6901-W05	2.92	(58.9 $\pm$ 2.4)
TopRight-6442-W16	4.28	(37.9 $\pm$ 2.7)
TopRight-6902-W04	2.07	(35.0 $\pm$ 2.1)
TopLeft-6442-W14	7.30	(34.9 $\pm$ 6.0)
TopLeft-6902-W06	1.11	(40.5 $\pm$ 5.1)

Table 5.11: Sensors selected for Petalet fabrication with their electrical characteristics.

section 4.4.2).

The sensors used are listed in table 5.12. The type of strip pitch and pad are also included.

Miniature Sensor	Pitch Type	Pad type
LP-6214-W01	Large	std
LP-6271-W12	Large	std
SP-6214-W03	Small	emb
SP-6271-W06	Small	emb
x-SP-6215-W04	Super small	std

Table 5.12: Summary of *CNM* Petalet miniature sensors used for charge collection studies.

In figure 5.22 the collected charge as a function of the bias voltage is presented for each sensor.

The full depletion voltage is around 60 V for each sensor which is in good agreement with the values extracted from their CV curves (50 V approximately). All sensors presented similar behaviour regarding the total collected charge with an average value of (21.93 $\pm$ 0.87) ke^- at full depletion.

Table 5.13 summarizes the average values for the collected charge obtained at full depletion voltage and their particular value at 160 V for each measured sensor.

Regarding the full size sensors only one top right sensor was measured. The embedded *PA*'s were used for the wire bonding. Its charge collection as a function of the bias voltage is depicted in figure 5.23.

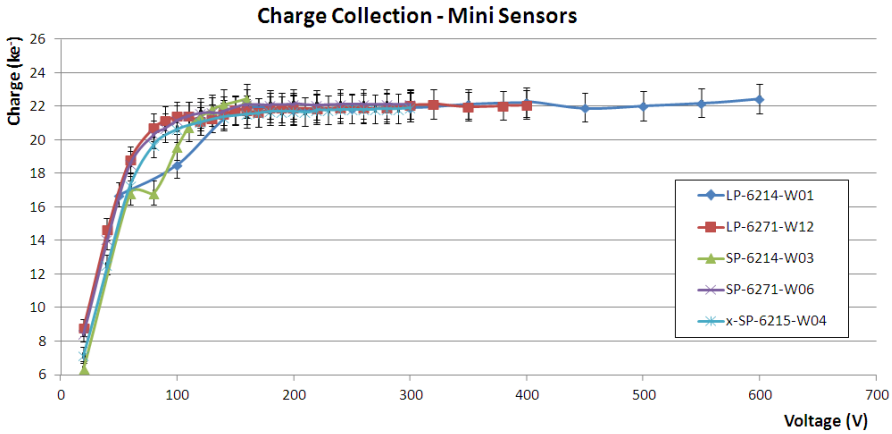

Figure 5.22: Collected charge as a function of the bias voltage for Petalet mini sensors.

Miniature Sensor	Collected Charge at 160 V (ke^-)	Average Charge at V_{FD} (ke^-)
LP-6214-W01	(21.78 $\pm$ 0.86)	(22.05 $\pm$ 0.87)
LP-6271-W12	(21.79 $\pm$ 0.86)	(21.93 $\pm$ 0.87)
SP-6214-W03	(22.48 $\pm$ 0.88)	(21.73 $\pm$ 0.86)
SP-6271-W06	(22.17 $\pm$ 0.87)	(22.10 $\pm$ 0.87)
x-SP-6215-W04	(21.57 $\pm$ 0.86)	(21.82 $\pm$ 0.86)

Table 5.13: Summary of *CNM* Petalet miniature sensors used for charge collection measurements.

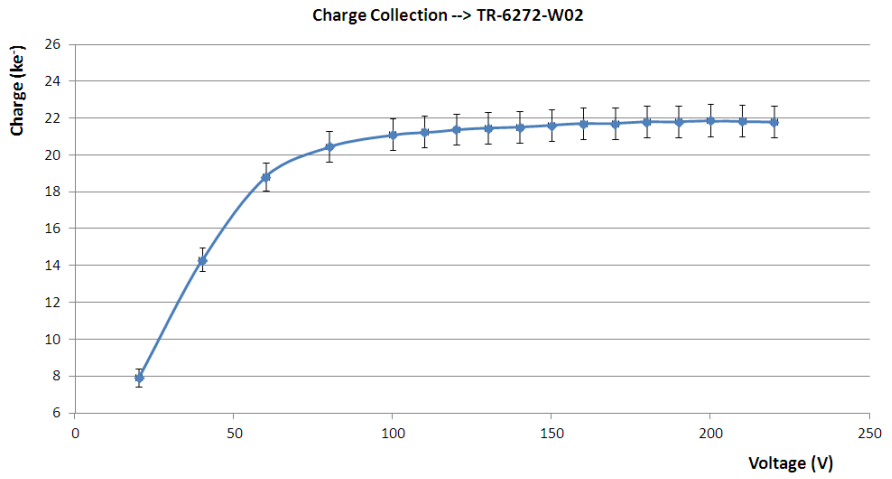

Figure 5.23: Collected charge as a function of the bias voltage for Petalet top right sensor. The wire bonding was stablished using the embedded pitch adaptors.

The charge collection distribution is quite uniform and the average of the total collected charge achieved at full depletion is (21.76 $\pm$ 0.86) ke^- which is compatible with the expected value. The full depletion voltage is around 70 V.

In general, all the measured *CNM* sensors presented good performance in terms of charge collection and the results are independent of the pads used for the wire bonding. The average of the total collected charge at full depletion for mini sensors is (21.93 $\pm$ 0.87) ke^-. For the top right full size sensor the total collected charge was (21.76 $\pm$ 0.86) ke^-. Both results are quite close to the expected value of 21.73 ke^- for a 285 μm silicon thickness.

5.2.2.3 Laser Measurements

All the results presented in this section were published at [111]. As explained in section 5.2.1 *cross-talk* and *pick-up* effects are the possible problems that can appear by using the embedded pitch adaptors technology (embedded *PA*s). With the laser system setup installed at *IFIC* we can scan different sensors looking for these effects. With the laser a perpendicular beam of particles crossing the detector can be recreated in a specific region of the sensor. The devices used for that purpose are summarized in table 5.14.

Miniature Sensor	Pitch Type	Pad type
SP-6214-W01	Small	std
SP-6271-W06	Small	emb

Table 5.14: Summary of *CNM* Petalet miniature sensors measured with the laser system for cross-talk and pick-up effects studies.

The test setup and procedure are similar to the ones used with *ATLAS12A* sensors. After doing the laser focusing (in Z direction) laser scans were carried out moving the laser in the transversal direction to the sensor strips (X direction) and registering the signal response of each channel at every position. Different laser scans are performed at different positions along the strips (Y direction) (for more details see section 4.4.3).

No problems were found for sensor $SP\text{-}6214\text{-}W01$ which has only standard pads. Figure 5.24 shows an example of the laser movement (left) over X direction and the amount of signal (in ADC counts) per channel (right) where each color corresponds to the signal registered by each individual channel.

All the strips have similar behaviour with signal uniformity across the sensor channels.

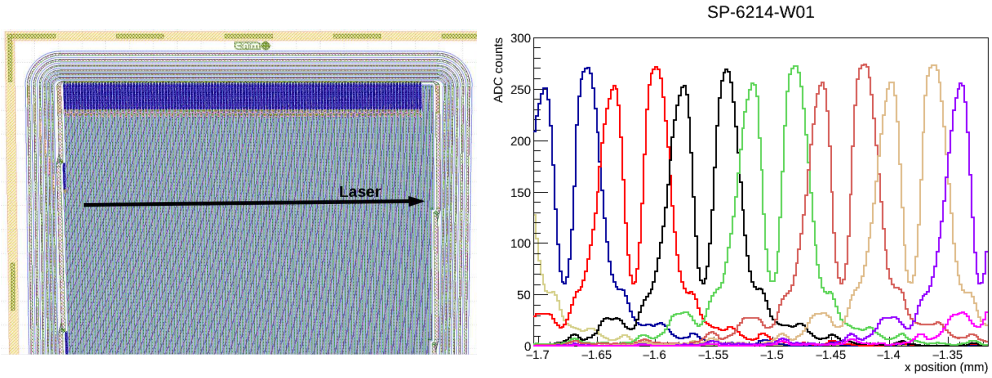

Figure 5.24: Scheme of laser movement (left) and example of obtained results (right) after a laser scan along X direction on sensor $SP\text{-}6214\text{-}W01$. Each color corresponds to the signal registered by each channel.

Regarding sensor $SP\text{-}6271\text{-}W06$ which has embedded *PA*s the same procedure was used. Different laser scans were carried out looking for possible *cross-talk* between strips. *Cross-talk* is an effect by which a signal transmitted on one channel can create an undesired effect in another channel. It can happen between traces in the first and second metal layers.

However, no sign of *cross-talk* was observed. The signal registered was uniform along the sensor as shown in the example depicted in figure 5.25.

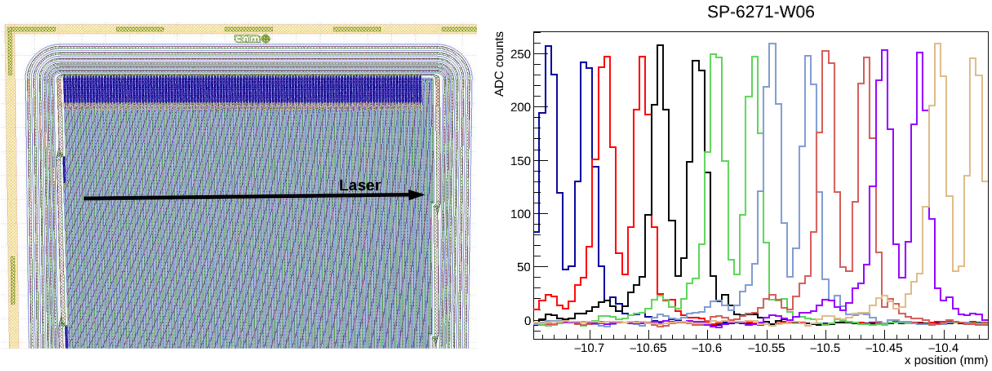

Figure 5.25: Scheme of laser movement (left) and example of obtained results (right) after a laser scan along X direction on sensor $SP\text{-}6271\text{-}W06$. All the strips presented signal uniformity and no presence of *cross-talk* was registered.

In order to study the *pick-up* effect the same procedure is carried out in the region of the embedded *PA*s. This effect creates fake signals when a particle hits the sensor under a second metal layer trace. A coupling between second metal strips and silicon

bulk could therefore appear. The major difficulty in this region is the high number of metal bands (due to the butterfly shape) where the laser will reflect. Figure 5.26 shows an scheme of the laser movement (left) and the resulting signal amplitude as a function of the laser position (right).

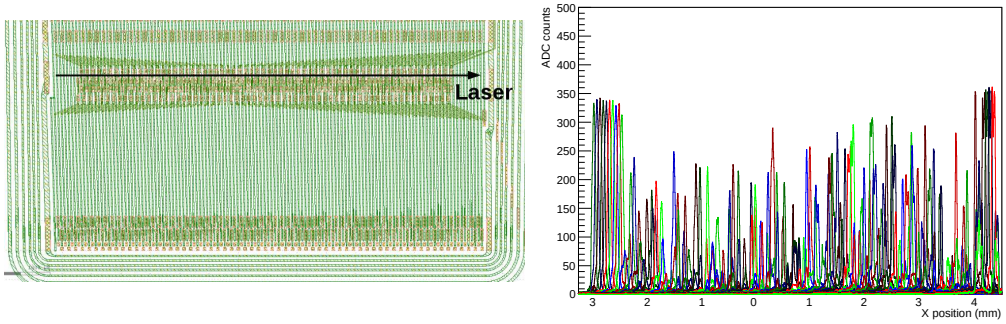

Figure 5.26: Scheme of sensor region under study and laser movement (left). Laser signal degradation due to high number of metal bands where the laser reflects (right).

Despite the laser reflection some channels have been detected coupled together which could correspond to *pick-up* effect. This is shown in figure 5.27 where channels 250, 251 and 256 are measured in the same laser position.

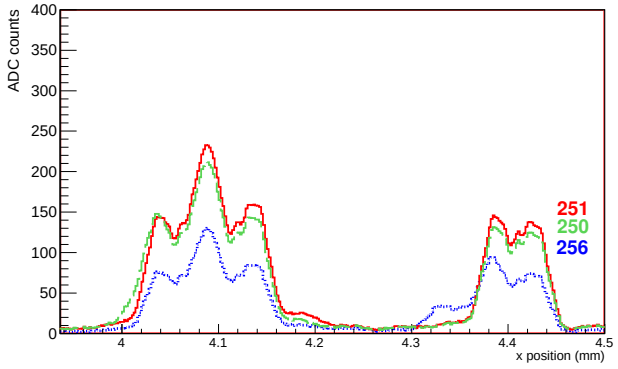

Figure 5.27: Signal amplitude as a function of the laser position. *Pick-up* effect is detected between channels 250, 251 and 256.

The connections between the strips and the *PA*s of channels 251 and 256 cross over channel 250 as it is seen in figure 5.28.

The result presented in figure 5.27 indicates that coupling of the bulk directly to the *PA*s can appear. Nevertheless, this effect has only been detected in a few number of channels and taking into account the small percentage of area occupied by the

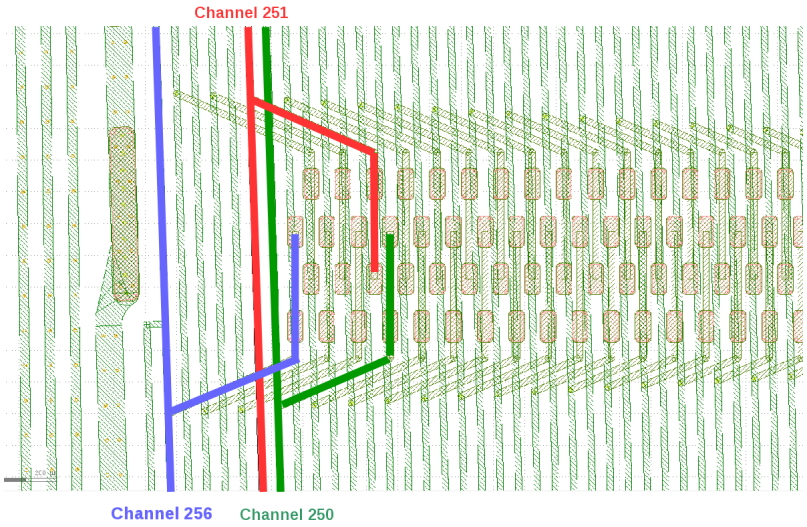

Figure 5.28: Connections sketch of the strips and the *PA*s of channels under study. *pick-up* effect is detected between channels 250, 251 and 256.

embedded *PA*s with respect to the total sensor area their influence in the whole system performance should be negligible. After these studies, more embedded *PA*s designs were developed to minimize the possible *pick-up* effects varying different parameters such as the metal trace width (10 and 20 μm) or the intermetal oxide layer (1, 2, 3 and 4 μm) [112]. However, the analysis of these new structures are out of the scope of this thesis work.

5.3 Electronics description

The main purpose of the Petalet programme is to develop the readout electronics for the silicon sensors. The design of the hybrids (composed by *PCB* and the *ASIC*s) and the buses for power, data and control signals must be developed. These buses are included in the so-called *Bustape*, consisting in a flexible piece of kapton and copper glued to the Petalet core. For this prototype it was proposed to avoid traces under the sensors. This would minimize the material in this region, enhancing the thermal disipation. This led to route the traces on both sides of the Petalet (right and left).

Two approaches were considered in order to solve some issues regarding the assembly of the modules (structure formed by the silicon sensor and its correspondent hybrid) and their powering and readout. The first problem is how to readout the outer

part of the Petalet where the sensors split in two columns (upper sensors) either with a single long hybrid or with two short hybrids. The second problem is how to route the power and data buses, considering the lack of space, and avoiding the coupling of the noise between power and data.

The two designs evaluated in the Petalet project were the so-called:

- *Split readout*
- *Common readout*

5.3.1 Split readout configuration

In the *Split readout* configuration the outer sensors are covered by a single hybrid as shown in figure 5.29.

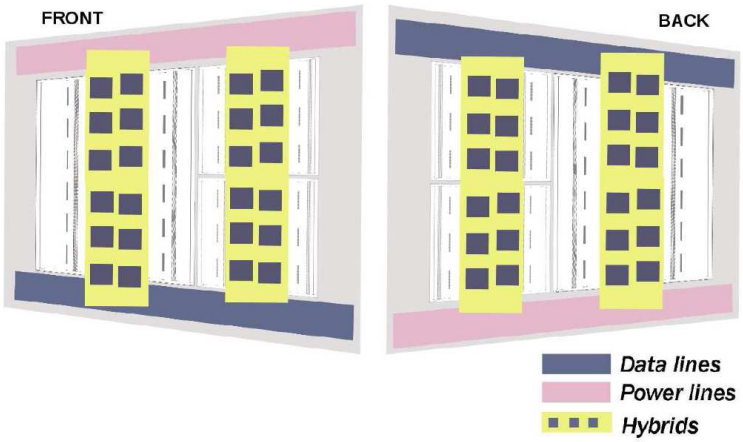

Figure 5.29: *Split readout* configuration scheme where two hybrids are used for sensors (one hybrid for the lower and one hybrid for the two upper sensors). Data and power lines are separated in two different sides (right and left) in this configuration.

This scheme offers the possibility of routing power and data buses to the left and right respectively, which is the safest approach regarding the noise coupling and results in two independent bustape pieces wich are more easily glued to the core. The assembly of this configuration is particularly challenging. The glue height between sensor and hybrid must be the same for both sensors to ensure coplanarity and to avoid mechanical stress between them.

DESY institute and *Freiburg University* were involved in the development and performance of the *Split readout* configuration.

5.3.2 Common readout configuration

The other option is the *Common readout* scheme (figure 5.30) where the outer sensors are covered by two short hybrids, resulting in two independent upper modules.

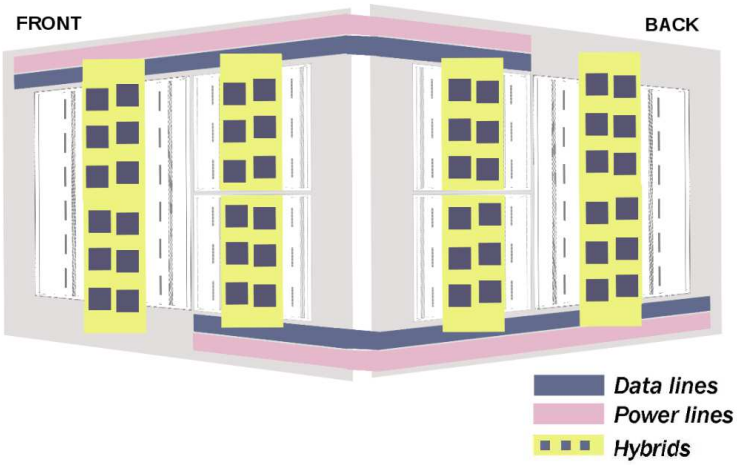

Figure 5.30: *Common readout* configuration scheme where three hybrids are used for sensors (one hybrid for the lower and two hybrids for the two upper sensors). With this configuration data and power lines are built in the same side of Petalet bus cable.

This configuration is simpler for the assembly than the *Split readout*. However, it forces to place the data and power lines in both sides (front and back side are fitted together). Due to the space restriction, power and data lines are routed close to each other, so care must be taken in order to avoid noise coupling.

In the case of the *Common readout* configuration *IFIC* (Valencia) was involved in its development, test and performance.

5.3.3 Electrical tests and results

The main goals of the electrical tests of the Petalet are to obtain the input noise and the gain for each Petalet channel and evaluate if the values are within specifications. These tests can be made due to the internal calibration circuitry of the *ASIC*s used to read out the detectors . The *ASIC*s are binary chips. This means that they provide a digital output, giving a logic '1' in every channel where a particle has been detected. To characterize the electronics the first step includes some configurations to adjust the delays coming from cabling, interface, and internal calibration capacitors. Then a three point gain (*3p gain*) scan is carried out. In this test threshold scans are performed at three different injected charges (0.5 fC, 1 fC, 1.5 fC) to determine the

V_{th50} parameter. The channel occupancy versus the threshold is represented. From the resulting distribution the V_{th50} parameter (for each charge) will be the threshold value where the occupancy is the 50 % (figure 5.31).

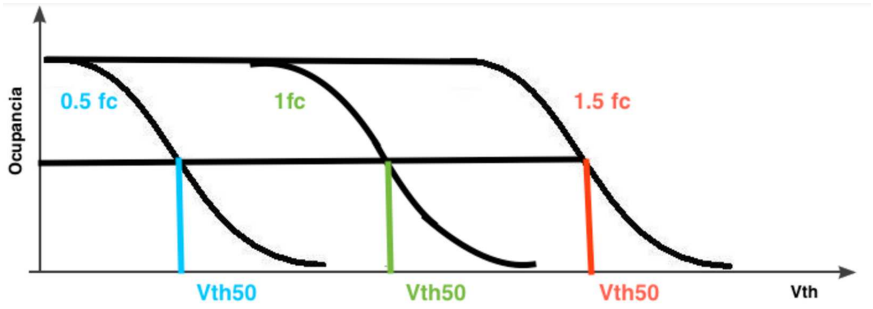

Figure 5.31: Channel occupancy as a function of the threshold for three different charge values. The threshold value where the occupancy is the 50 % is known as V_{th50} parameter.

The occupancy distribution is known as *S-curve* and corresponds to an error function where the sigma (σ) is the output noise of the system.

The three threshold scan points are linear with the injected charge and the gain will correspond to the derivative of the linear fit. An example of the linear fit is shown in figure 5.32.

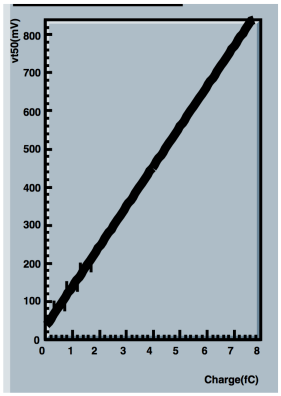

Figure 5.32: V_{th50} threshold values as a function of the injected charge.

With the gain value, the input noise can be calculated as:

$$Input\ noise = \frac{output\ noise}{gain} \tag{5.1}$$

All these tests are carried out in the different assembly steps. First only with the

hybrids in order to check if they work properly. Then with modules (hybrids glued to a sensor), where the sensor is biased. Finally, the best modules in terms of noise and gain will be glued on the Petalet and will be also tested. This will provide the final results.

Figure 5.33 shows an example of input noise (top) and the gain (bottom) versus channel number for a lower module of a *Common readout* Petalet. The noise magnitude is given in equivalent noise charge (ENC). The total input noise will be the average of the noise per channel (722 ENC for this module).

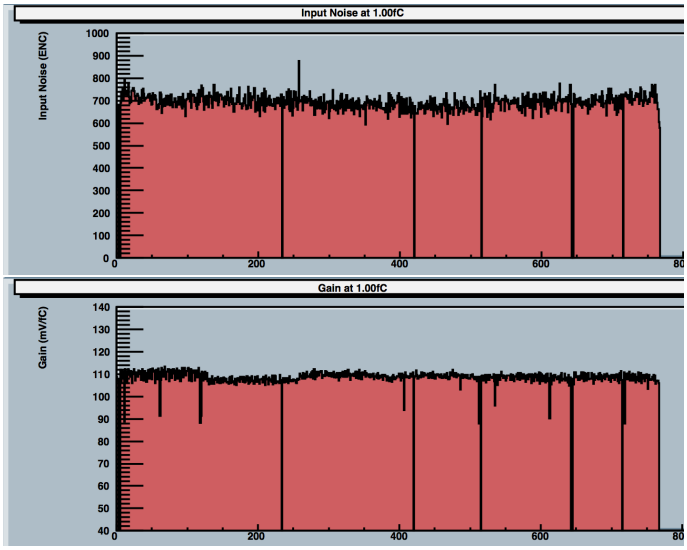

Figure 5.33: Input noise (top) and gain (bottom) as a function of the channel number for a lower module of a *Common readout* Petalet.

6 Petalets were tested in different collaboration institutes. Table 5.15 presents each structure characteristics and the testing site.

Site	Petalet Number	Type of sensor pads
DESY	Petalet-01; single sided	Standard
	Petalet-02; double sided	Standard
	Petalet-03; single sided	Embedded
Freiburg	Petalet-04; double sided	Embedded
	Petalet-05; double sided	Standard
Valencia	Petalet-07; double sided	Standard

Table 5.15: Petalets characteristics and testing sites.

All the setup conditions and obtained results for each different Petalet are summarized in table 5.16.

	DESY (standard) *double sided*	**DESY (standard)** *single sided*	**DESY (embedded)** *single sided*	**Freiburg (standard)** *double sided (only one side)*	**Freiburg (embedded)** *double sided*	**Valencia (standard)** *double sided*
T (°C)	0	15	5	- 20	- 20	- 15
V (V)	- 150	- 150	- 140	- 200	- 100	- 150
Input Noise (ENC)	601	674	728	597	727	618

Table 5.16: Summary of input noise results for the different Petalets tested by the collaboration institutes. Each setup conditions are also included.

Despite the differences between setup conditions all the values are around 600-700 ENC. The noisiest modules correspond to the embedded ones and they presented a different noise pattern than standard modules. This effect is shown in figure 5.34.

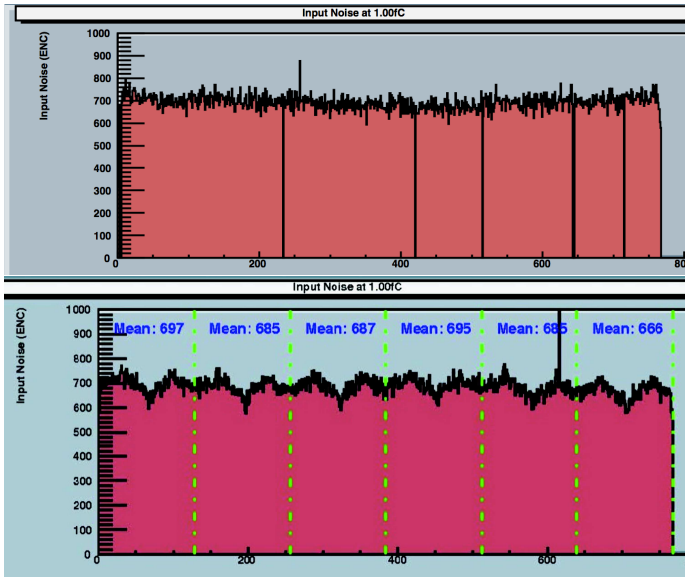

Figure 5.34: Input noise as a function of the channel number for standard (top) and embedded (bottom) modules.

After different additional tests it was determined that the effect was due to higher interstrip capacitance of the second metal layer of the embedded *PA*s. As explained in section 5.2 new embedded *PA*s designs were proposed and fabricated at *CNM* varying different parameters [112] but the analysis of these new structures were out of the scope of this thesis.

5.3.4 Petalet readout decision

After analyzing the design, development and results provided by the two potential readout topologies a commitee of experts was setup to make the recommendation on the baseline design to follow for the Petal readout electronics. Both solutions were conclude to be feasible, however due to limited time and lack of manpower only one design will be developed. The *Split configuration* allows for synergies in the development of hybrids and bus tapes with the barrel staves in a more direct manner. The congestion of the tracking on the connections between the bus tape and modules in the *Common readout* configuration also represented an additional complication. Nevertheless, the use of split hybrids in the *Common readout* scheme adds mechanical benefit during module mounting process. Therefore a combined solution was proposed. The Petal readout electronics will follow the *Split readout* configuration but using split hybrids in the outer modules as in the *Common readout* (connected together with wirebonds).

In the frame of this project many important aspects will be useful for Petal fabrication and test. New tools for module assembly, hybrids and modules design and development, mechanical and electrical tests, etc ... will suppose a clear advantage during future Petal final design and tests. The Petalet project has been definitely the first step in building full Petals for the ATLAS End-cap upgrade project.

Chapter 6

Conclusions

The work presented in this thesis is focused on the electrical characterization of silicon microstrip detectors that will be used in the phase II upgrade of the *ATLAS* Inner Tracker (in particular in the Endcaps region). Different silicon sensors technologies have been developed and analized in the last years and the chosen baseline for *HL-LHC* Inner Tracker was decided to be n-on-p technology.

In the first part of this work, the Petal structure was presented. Thermo-mechanical tests were carried out with the Petal core achieving compatible results with previous simulation studies and verifying the fabrication steps. At the Petal core surface the achieved temperatures along the pipe path were between -(20-30)°C. These values are low enough to disipate the heat generated by the electronic part of the Petal. Regarding the mechanical tests, the deformations of the Petal core were of about 200 μm for the deflections out of plane and about 30 $\mu\varepsilon$ for the longitudinal strains. The estimated *Young's modulus* at the Petal facings was 215 GPa being 376 GPa the obtained with the *FEA* model. The *FEA* simulation needs a proper implementation of the material properties, therefore these two values only would be used as an appoximation. In the case of the deformations due to temperature, the deflections out of plane were 0.24 $\mu m/^{\circ}C$ and about 4.8 $\mu\varepsilon/^{\circ}C$ for the longitudinal strains. These measurements were taken under a total input temperature variation of about 22 $^{\circ}C$ and they are compatible with the expected by simulations. These tests were carried out as first studies with the carbon core and they should change with all the Petal elements installed. Therefore that must be also evaluated with the complete structure. The planarity of the Petal core was also analyzed with a horizontal system obtaining an average deviation below 100 μm wich meets the specifications value. Combining

the obtained data relative to the two Petal sides (with a *flag-like* configuration system) the thickness was found to be 5.4 mm which also meets the specifications (about 5 mm).

Different p-type miniature sensors (ganged and not ganged) manufactured by *Hamamatsu* (*ATLAS12A*) were electrically characterized measuring their leakage current and capacitance for a voltage range. In the case of not irradiated sensors, no breakdown occured below 600 V. Regarding the full depletion voltage, the obtained average is (363.2 $\pm$ 3.6) V. This value is in coherence with the specifications.
Concerning the irradiated sensors measurements no breakdown was observed up to 600 V and the majority of the sensors did not achieved the full depletion region. The dependence of the leakage current with the fluence was confirmed with the determination of the alpha factor. In general, comparing the results before and after irradiation the negative effects of radiation on the electrical properties of the sensors are clearly reflected. Despite this, the sensors have good electrical behaviour at 600 V which would be the maximum voltage of operation.

They were also analyzed in terms of charge collection before and after irradiation using a beta source setup. The expected collected charge for these not irradiated sensors is about 23.1 ke^- and all the measured sensors (except by one) achieved this value. In the case of the irradiated ones the difference in the charge collection in terms of radiation fluence is more evident. The higher dose of radiation the less collected charge achieved. For the same fluence the sensors irradiated with neutrons collected around 30 % less charge than the ones with proton irradiation. Nevertheless, the sensors are still able to collect more than 5 ke^- at 500 V in the worst cases. The expected noise at *HL-LHC* would be below 1 ke^- [113]. This gives us a S/N above 5 in the worst case. Typically, the expected S/N for trackers is around 10. One should keep in mind that the irradiation studies apply a safety factor considering a total radiation fluence above the expected at the experiment. This shows us a more unfavourable scenario than the real situation. Therefore, considering that, our results highlight the good performance of p-type sensors even in the worst cases.

The signal registered by each strip independetly was also studied using laser techniques. In general, all the measured sensors showed uniformity per strip in the laser signal. Lower laser signal collection was observed in the case of irradiated sensors, as expected taking into account the previous studies. These laser techniques allowed us to analyze the effect of the ganged strips solutions (AC and DC ganging).

The ganged strips showed signal uniformity respect to the normal strips. Both solutions presented a drop in the collected charge. The amount of signal registered was smaller for the ganged strips (less few percent) being AC ganging the worst case. In addition, the DC solution also showed small cross-talk effect. Despite these small drawbacks both AC and DC solutions showed good performance for different radiation fluences. The total amount of charge registered confirmed the optimal performance of both technologies under high radiation fluences. The *ATLAS* collaboration decided that the future Petal sensors would point to the beam-line and the sensors would have a skewed wedge shape, therefore the ganging of the strips will not be needed.
Nevertheless, they maintained their interest in such a challenging technology.

Accelerated annealing was used with *ATLAS12A* sensors irradiated at different sites to investigate the evolution of the charge collection. Two of the four analyzed sensors showed decreasing and unstable trend of the charge up to 65 minutes of controlled annealing (at 60 $^{\circ}$C). They presented also high noise levels. The leakage current of the sensors increased dramatically ($I_{leakage} > 20mA$) and the annealing was stopped. The other two analyzed sensors showed normal annealing behaviour. An increase in the charge collection was measured in both cases corresponding to a beneficial annealing period. They achieved a charge increment between (3-4) ke^{-} after 300-400 minutes of accelerated annealing. Then a reverse annealing period starts where the collected charge decreases with the annealing time. In any case the reverse annealing period would start above 300 minutes of accelerated anneling which would correspond to 4-5 months at room temperature From these annealing studies we can conclude that the properties of the sensors will not be affected as much as for the n-type sensors, in terms of the annealing, during shutdown periods of the experiment.

All the studies presented in the first part of this work verify the good performance of the p-bulk strip sensors under high-radiation environments and confirm the good choice of these kind of sensors for *HL-LHC* scenario.

In the second part of this thesis the Petalet project was introduced. The Petalet p-type sensors were manufactured by *CNM*. In order to reduce the large bonding angle that appears in the full-size sensors, new embedded pitch adaptors (embedded *PA*s), integrated in an extra metal layer, were designed and produced. These embedded *PA*s were built in some sensors to be tested. Miniature and full-size Petalet sensors were electrically characterized. All the miniature devices showed good electrical

performance with no breakdown up to 200 V. The average of the full depletion voltages extracted from the C-V curves is around 68 V which is far from the maximum value set by specifications (300 V). Regarding the full-size sensors only one detector broke down below 200 V. The rest of them maintained the leakage current values within the specifications. All the sensors achieved a full depletion voltage around (50-60) V which is coherent with the value extracted in the case of the miniature devices. The total collected charge expected for these sensors is around 21.73 ke^{-} (sensor thickness of 285 μm). Using the same beta source setup than for the *Hamamatsu* sensors tests the total collected charge achieved by each sensor at full depletion is around 22 ke^{-} which is quite compatible with the expected value. All the obtained results for these sensors are very similar and therefore the second metal layer introduced by the embedded *PA*s does not affect negatively on the electrical sensor characteristics. The cross-talk and pick-up effects that can appear due to the embbeded *PA*'s were anlayzed using the same laser setup than for the *Hamamatsu* sensors. After several laser scans no presence of cross-talk was registered. All the strips presented good performance in terms of signal uniformity per strip and no coupling signals appeared. Some coupling signals were attribute to possible pick-up. Nevertheless, this effect was only detected in a few number of channels. The embedded *PA*s occupy a small percentage of area with respect to the total sensor dimensions therefore their influence in the whole system performance should be negligible. The Petalet sensors showed in general excellent electrical performance. The best full-size sensors in terms of leakage current and full depletion voltage were chosen to be mounted on a real Petalet and test the readout electronics with the complete structure.

The two approaches considered for the readout of the Petalet were the *Split* and *Common* configurations. In the *Split* readout configuration the outer sensors are covered by a single hybrid and the power and data buses are routed to the left and right respectively. In the case of the *Common* readout configuration the outer sensors are covered by two short hybrids, resulting in two independent upper modules. The data and power lines are routed in one side of the Petalet together. Different electrical tests were carried out to obtain the input noise and gain of both systems. Although the measurements in each institution were taken in slightly different setup conditions all the input noise results were between 600 and 700 ENC and the gain of the standard Petalets appeared flat. The agreement in the input noise and gain between all the Petalets bring to light the good performance of all the systems and the feasibility of the

two readout configurations. After some discussion it was decided by the collaboration to follow a combined readout solution. The decided bustape baseline for the Petal readout will separate data and power lines as in the case of the *Split* configuration but in addition the outer sensors will have split hybrids as for the *Common* readout. After having fabricated and tested Petalets with both standard and embedded *PA*s it was proven that the wire bonding of the electrical connections is possible in any case despite the large bonding angle. Therefore, the Inner Tracker collaboration decided to use standard pads as baseline for simplicity. The Petalet fabrication and analysis showed excellent performance. It stablished new fabrication steps and electrical tests to be carried out with the future Petals. Appart from the exceptional results obtained during the Petalet project it allowed to all the involved institutes to work together in a strengthen collaboration period, sharing knowledge, tools, designs and efforts.

Resumen en castellano

El CERN y el Gran Acelerador de Hadrones (LHC)

El *LHC* se ha convertido en el acelerador más potente de todos los tiempos. Su principal objetivo es dar respuesta a las limitaciones del Modelo Estándar y revelar la física más allá de él. El descubrimiento del bosón de Higgs en 2012 supuso el comienzo de una era en el campo de la física de partículas donde conseguir la mayor precisión posible en las medidas es vital.

En el *LHC* se aceleran y colisionan protones con una energía nominal de centro de masas de 14 TeV y una luminosidad instantánea nominal de 10^{34} cm^{-2} s^{-1}. Para la máxima luminosidad, los protones son acelerados en paquetes de 1.15×10^{11} protones cada uno, con una frecuencia de 40 MHz (esto supone una colisión cada 25 ns). Estas colisiones producen gran cantidad de partículas que son registradas por los experimentos del *LHC*.

El túnel del *LHC* (de 27 km situado a 100 m bajo tierra) alberga cuatro grandes detectores (ver figura 6.1). Cada uno se encuentra en un punto de colisión de los haces, que circulan en sentidos opuestos. Dos de estos experimentos son de propósito general, ATLAS [17] y CMS [18], los cuales pueden operar a la máxima luminosidad instantánea (10^{34} cm^{-2} s^{-1}). Ambos experimentos proporcionarán medidas de alta precisión en parámetros del modelo estándar y nuevos procesos físicos que pueden aparecen en la escala de energías del TeV. Existen otros dos experimentos de baja luminosidad: *LHCb* [24], que estudia física del quark *b* y TOTEM [26] para la medida de secciones eficaces totales y colisiones elásticas de bajo ángulo. Para las colisiones de iones pesados (plomo-plomo) el *LHC* cuenta con ALICE [25] que opera a una luminosidad de $10^{27}\ cm^{-2}s^{-1}$.

Dentro del programa físico desarrollado del *LHC* la luminosidad irá incrementando y los detectores pasarán por varias fases de mejora para adaptar todo su potencial a

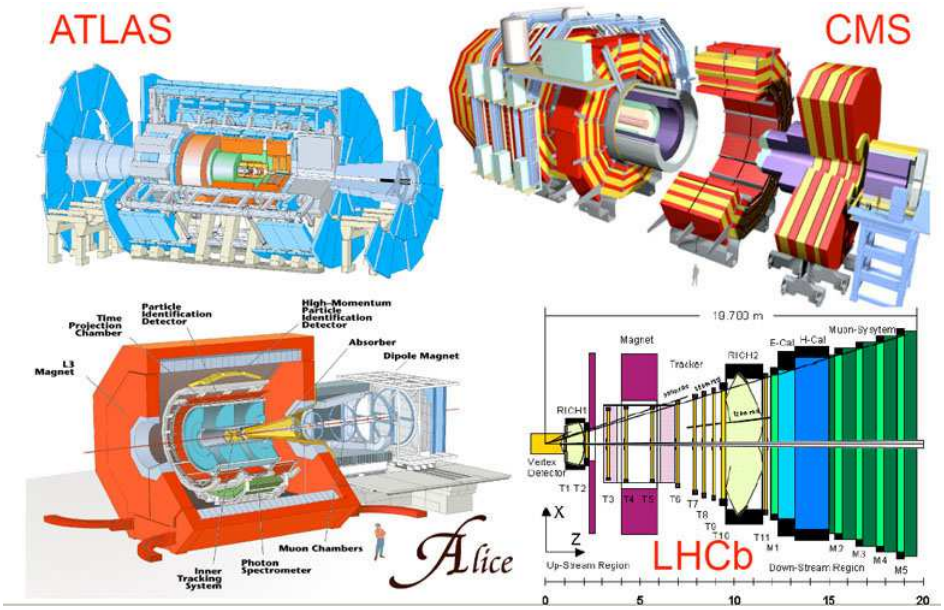

Figure 6.1: Detectores localizados en los cuatro puntos de colisión del *LHC* [23]

cada situación. Dado que este trabajo de tesis está centrado el la segunda fase de mejora del detector ATLAS y en concreto del sistema de *strips* del detector interno, ésta será la única parte que se explique en mayor detalle.

Mejoras en el detector interno de ATLAS para la fase 2

La segunda será la última fase de mejora, durante la cuál se preparará a los detectores para alcanzar la máxima luminosidad de 5×10^{34} cm^{-2} s^{-1}. Su comienzo está programado entre 2022 y 2023 y el detector interno se reemplazará por uno hecho completamente de silicio. El diseño de este nuevo sistema viene descrito en el documento oficial *Letter of Intent* [39] (*LOI*) y se puede ver en la figura 6.2.

El detector interno fue diseñado para operar durante 10 años a una luminosidad de 10^{34} cm^{-2} s^{-1}con un cruce de haces de 25 ns. La configuración actual del detector no podrá mantener las prestaciones requeridas. El nuevo diseño deberá utilizar sensores altamente resistentes a la radiación y con mayor granularidad. Todo esto, además, minimizando el material y ocupando un espacio similar al del actual detector interno.

El nuevo sistema de *strips* contará con:

- **Barril en la sección central:** El sistema Barril comprende la región entre

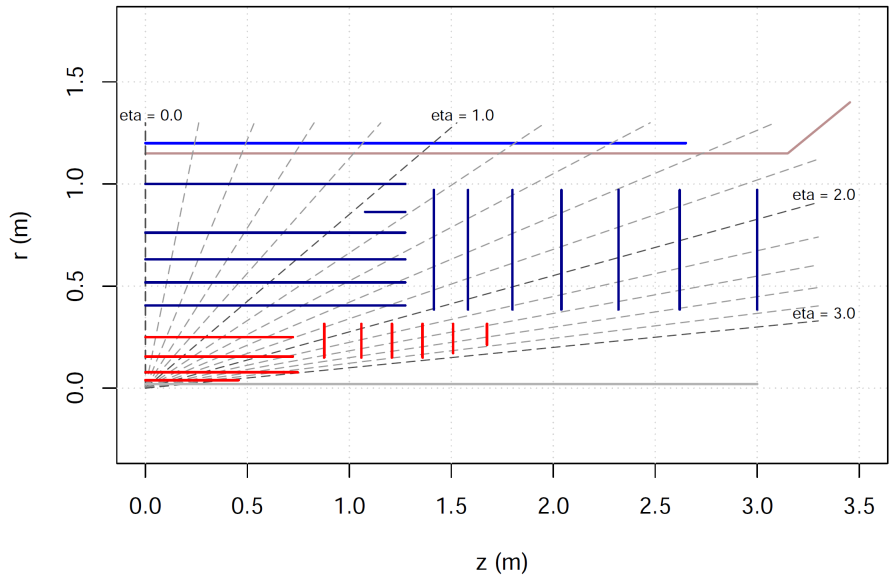

Figure 6.2: Diseño base del futuro sistema de trazas en el que se muestran las áreas activas de los sensores dispuestos en cilindros y discos.

$\pm$1.3 m y consiste en 5 largos cilindros que rodean la tubería del haz. El elemento mecánico básico del Barril es el *stave* y está formado por una parte central de baja masa (*core*) que le aporta rigidez mecánica y sirve de apoyo a los sensores. También aloja la parte eléctrica y el sistema de refrigeración. Cada *stave* tiene 26 módulos, 13 en cada cara, con los detectores girados para proporcionar medidas en la coordenada rZ. Los sensores de silicio son de tipo *microstrip* con implantes tipo n, substrato tipo p y tecnología *Float-Zone* (n-on-p *FZ*). Tienen un grosor de (320$\pm$15) μm y un tamaño de 97.54$\times$97.54 mm^2. Los principales componentes del *stave* se muestran en la figura 6.3(a).

- **End-caps:** Los End-caps constan de 6 discos en cada lado y cada disco contiene 32 Pétalos idénticos cuyos componentes se pueden observar en la figura 6.3(b). Un Pétalo es un módulo mecánico análogo al *stave* que sirve de apoyo para los sensores y contiene además su sistema de refrigeración. Cada Pétalo tiene sensores de 6 formas diferentes (9 sensores en total) formando 6 anillos a lo largo de la estructura. Los tres primeros anillos tienen un total de 32 sensores, mientras que los tres últimos anillos tienen el doble, 64 sensores. La figura 6.4 muestra un esquema de los componentes del Pétalo, de fuera a adentro: los sensores, el *Bustape* que provee de las conexiones eléctricas con

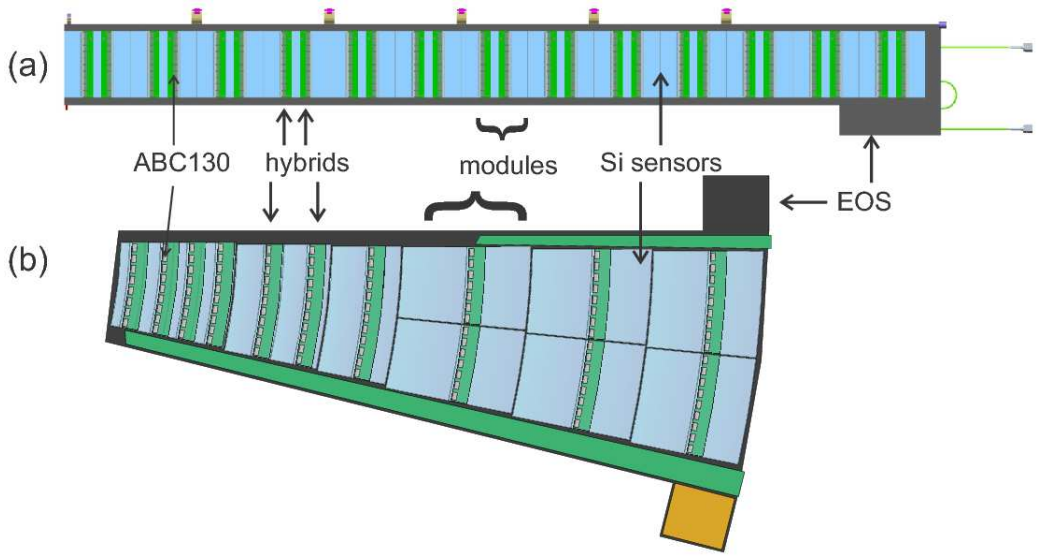

Figure 6.3: Componentes del *Stave* del barril (a) y los Pétalos (b).

el exterior, las tapas de fibra de carbono, las tuberías de refrigeración rodeando la espuma de carbono y por último carbono en forma de panal (*honeycomb*) rellenando los espacios vacíos.

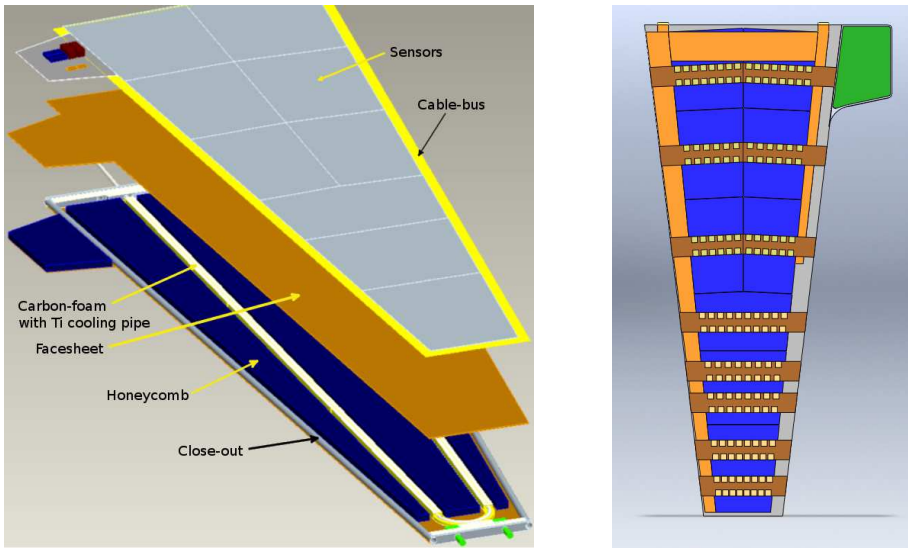

Figure 6.4: Esquema de los materiales que componen un Pétalo (izquierda) y dibujo de todos sus componenetes externos (sensores, cable *bus* e híbridos) (derecha).

Los sensores que se utilizan en los Pétalos son del mismo tipo que en el caso del Barril (n-on-p *FZ*) y del mismo grosor. En este caso los sensores necesitan

strips radiales para proporcionar medidas en la coordenada $r\phi$ para lo cuál los *strips* están rotados en el propio sensor.

Detectores de silicio resistentes a la radiación

En experimentos de aceleradores de partículas de alta energía, los detectores de silicio son muy utilizados debido entre otras cosas a la estructura de bandas energéticas de los materiales semiconductores. Un detector de silicio es básicamente una unión *pn* (que se consigue dopando el material con impurezas en pequeñas cantidades). La zona de desertización que existe en el sensor es la base para la detección de partículas en este tipo de detectores. Cuando una partícula atraviesa el diodo, ioniza el material y genera pares electrón-hueco, que se dirigen hacia los electrodos del detector.

En detectores de reconstrucción de trazas que requieren medidas de la posición con alta precisión se utilizan detectores de silicio de micro-bandas (o *microstrips*). En estos detectores las bandas (*strips*) actúan como uniones *pn* independientes.

Los detectores estudiados en este trabajo para la segunda fase de mejoras del detector interno de *ATLAS* son detectores de *microstrip* tipo *p*. En estos detectores el substrato es de tipo *p* y los implantes (*strips*) son de tipo *n* altamente dopado (n^+). Los *strips* n^+ recolectan electrones que, al tener una mobilidad mayor que la de los huecos, tienen menor probabilidad de quedar atrapados en la red cristalina. Este hecho es vital si tenemos en cuenta los tiempos de recolección de carga que se darán en el *HL-LHC* (25 ns). Sólo durante este tiempo se integra la carga recogida. En los detectores tipo *p* la zona de desertización crece[1] desde los implantes hacia la base del detector. Esto nos permite operar con el detector parcialmente desertizado ya que la unión *pn* siempre se encuentra en la región de recolección de señal, aunque deberemos tener en cuenta que sólo la carga depositada en el volumen activo del detector será recogida por los electrodos. Cuando una partícula atraviesa un detector de silicio ioniza el material y se crean pares electrón-hueco. El número de pares que se generan es proporcional a la energía perdida por la partícula incidente. La figura 6.5 muestra un esquema de un detector de *microstrips* tipo *p* y el proceso de generación de pares.

[1] En los detectores basados en uniones *pn* altamente dopadas, la zona de desertización crece desde la zona con mayor concentración de impurezas (zona más dopada) hacia la zona con menor número de impurezas.

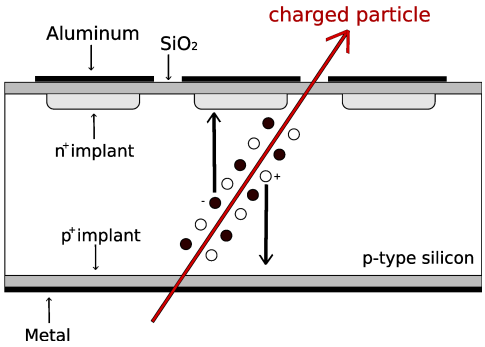

Figure 6.5: Esquema de un sensor de *microstrip*. El *bulk* es de tipo p y los electrodos son implantes n^+.

La señal generada por el movimiento de portadores de carga tiene forma de pulso de corriente, la cuál se integra para obtener la carga total depositada por la partícula. En un detector de unas 300 μm de grosor esperamos recolectar alrededor de 24000 electrones y el tiempo de recolección ronda los 10 ns. Si el tiempo de integración no es suficientemente largo no se estará midiendo toda la carga depositada.

Efectos de la radiación sobre detectores de silicio

La radiación induce defectos en la estructura cristalina del silicio los cuales suponen daños a nivel microscópico. Las consecuencias de estos daños microscópicos se reflejan posteriormente en efectos macroscópicos. Los daños causados por la radiación pueden dividirse en:

- **Daños en el sustrato:** La radiación incidente desplaza los átomos de silicio de sus posiciones en la red cristalina generándose pares (llamados pares de *Frenkel*) compuestos por el átomo desplazado y su posición vacante en la red. Además de pares sencillos se pueden formar también conjuntos complejos que dan como resultado la creación de niveles energéticos en la banda prohibida. Las nuevas bandas actúan como trampas que interaccionan con el material durante y después de la irradiación cambiando sus propiedades eléctricas.

- **Daños en la superficie:** El daño generado en la superficie está principalmente provocado por la ionización de la capa aislante de dióxido de silicio (SiO_2) que tienen los detectores. Los pares electrón-hueco generados en el sustrato por el paso de la radiación se desplazan hacia los electrodos y la base del detector

pero pueden quedar atrapados en el óxido e ir acumulándose en la interfaz entre el sustrato y el SiO_2. Los huecos son más propensos a quedar atrapados debido a su menor mobilidad, cargando positivamente esta región y generado una capa de electrones en el sustrato. A esta capa se la conoce como *capa de inversión* y altera el comportamiento eléctrico del sensor. En los detectores tipo *p* con implantes tipo *n* se producirá un intercambio de carga entre los implantes y la *capa de inversión* pudiendo establecer un cortocircuito.

Estos efectos pueden tener gran influencia en el comportamiento eléctrico del detector. Afectan principalmente a tres propiedades importantes del detector:

- **Corriente de fugas:** Los estados creados cerca del centro de la banda prohibida tienden a generar corriente. Los defectos de la red cristalina son capaces de capturar y emitir electrones y huecos en la zona de desertización incrementando así la corriente y el ruido en el detector. Cuanto mayor es la dosis de radiación recibida por el detector, mayor es la corriente de fugas total (ver figura 6.6).

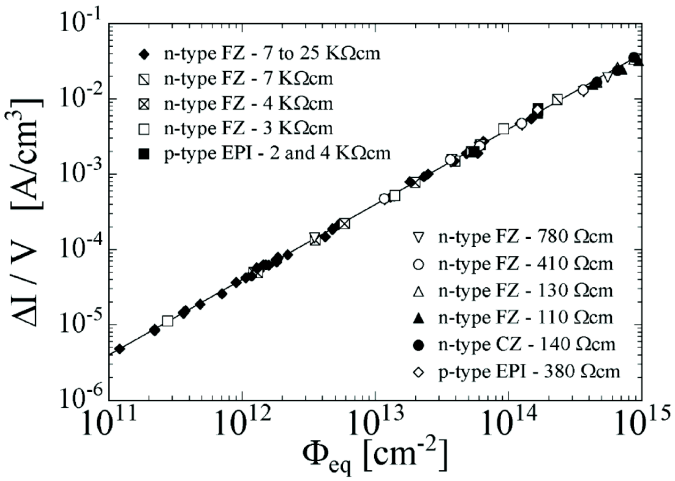

Figure 6.6: Dependencia de la corriente de fugas con la dosis de irradiación equivalente. Imagen extraída de [61].

Si la corriente en el detector es demasiado elevada el ruido en la electrónica aumenta y se enmascara la señal. Además se puede alcanzar la zona de ruptura del diodo y provocar una avalancha de corriente. El voltaje para el cuál

sucede la ruptura se conoce como *voltaje de ruptura* y viene dado por [63]:

$$V_{bd} = \frac{\varepsilon E_{max}^2}{2qN_D} \tag{6.1}$$

- **Eficiencia de la recolección de carga:** Los portadores de carga atrapados en los niveles de energía, generados por el efecto de la radiación, pueden permanecer en ese estado un tiempo superior al de lectura y no contribuyen a la carga total registrada. Esto supone una pérdida de señal, afectando negativamente en la eficiencia de recolección de carga. El número de trampas aumenta linealmente con la dosis de radiación según:

$$N_{traps} = \eta \phi_{eq} \tag{6.2}$$

donde η es el ratio de creación de trampas. Para las dosis esperadas en el *LHC*, la pérdida de señal debida al efecto de atrapamiento es del orden de un 15 % [114].

- **Concentración efectiva de dopantes:** Los defectos introducidos por la radiación cambian la concetración de dopantes en la unión conduciendo a un cambio de la concentración efectiva de dopantes y requiriendo un voltaje mucho mayor (en detectores tipo *p*) para desertizar completamente el detector. El votaje de desertización depende directamente de la concentración efectiva de dopantes (N_{eff}) según:

$$V_{fd} \approx \frac{q}{2\varepsilon_{Si}} \mid N_{eff} \mid d^2 \tag{6.3}$$

donde ε_{Si} es la resistividad del silicio, q la carga del electrón y d el grosor del detector.

En sustratos tipo *p*, N_{eff} va incrementando debido al aumento de aceptores y por tanto aumenta el *voltaje de desertización*. En cambio, en sustratos tipo *n* ocurre lo contrario. El aumento de estados aceptores provoca un descenso de N_{eff} y por consiguiente del *voltaje de desertización*. El material tipo *n* cada vez es menos *n* y puede cambiar de tipo. Este efecto se conoce como *inversión de tipo* (ver figura 6.7).

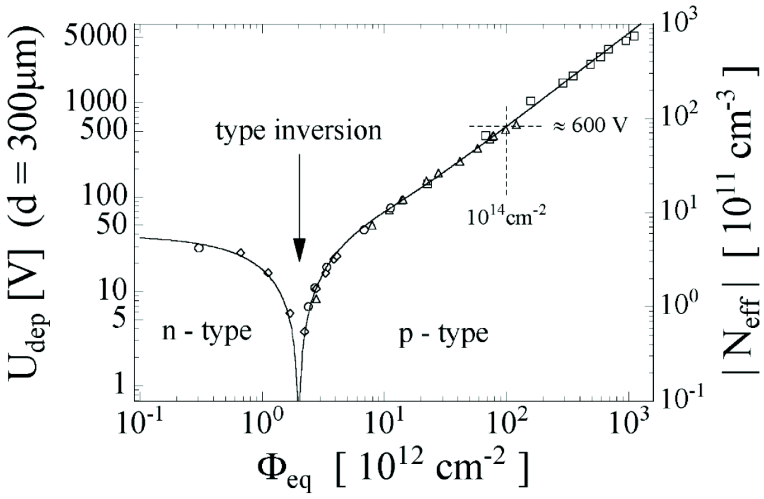

Figure 6.7: Variación del voltaje de desertización con la concentración efectiva de dopantes en función de la dosis normalizada [73].

Después de la *inversión de tipo* los detectores que acaban siendo de tipo n (como los que se utilizan actualmente en *ATLAS*), todavía son operativos pero sólo en desertización completa. Además, los defectos introducidos por la radiación no son estáticos. Migran a través de la red cristalina debido a procesos térmicos. Inicialmente, el movimiento térmico de los átomos contrarresta el cambio de la concentración de dopantes. Después de la exposición a la radiación esta concentración de dopantes sigue cambiando en el tiempo, de modo que las propiedades del detector también cambian. El proceso de evolución en el tiempo de las características del detector se conoce como recocido o *annealing* (por su traducción al inglés). El *modelo de Hamburgo* describe la variación de N_{eff} con la dosis de radiación, la temperatura y el tiempo según [74]:

$$\Delta N_{eff}(\Phi_{eq},t(T)) = N_a(\Phi_{eq},t(T)) + N_C(\Phi_{eq}) + N_Y(\Phi_{eq},t(T)) \qquad (6.4)$$

Cada componente corresponde a un periodo de evolución de N_{eff}: N_a es la componente de *annealing beneficioso*, N_C corresponde al *annealing estable* y N_Y es la componente de *annealing perjudicial*.

La evolución con el tiempo de N_{eff} puede observarse en la figura 6.8.

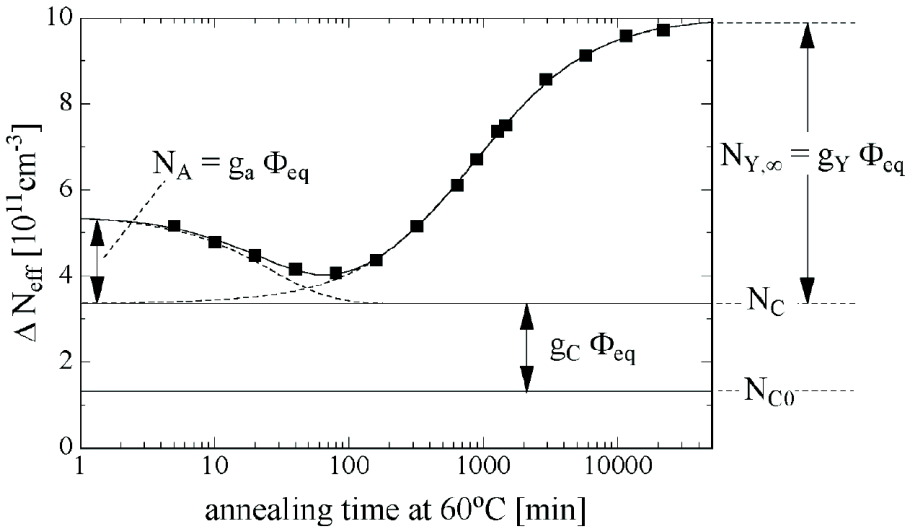

Figure 6.8: Comportamiento típico de *annealing* (en detectores tipo n) de cambios en la concentración efectiva de dopantes debido a los defectos introducidos por la radiación. Temperatura de 60°C después de irradiación a una dosis de 1.4 $\times 10^{13}\ n_{eq}cm^{-2}$ [77].

Pétalos de strips para los End-Caps del HL-LHC: medidas y resultados

Como se ha introducido anteriormente, para los *End-Caps* de *ATLAS* se usarán Pétalos. Éstos están compuestos básicamente por dos láminas de fibra de carbono (que dan apoyo a los sensores) en la parte externa e internamente por espuma de fibra de carbono (que sirve de camino térmico) y una tubería de acero como sistema de refrigeración. Los espacios vacíos se rellenan con fibra de carbono en forma de panal que aporta rigidez. Los sensores serán de *microstrips* tipo *p*.

Tests Termo-Mecánicos

Antes de pasar a la fabricación de los sensores se realizaron pruebas con la estructura de fibra de carbono para comprobar la efectividad del proceso de fabricación, la planaridad de la estructura, su rigidez, así como las deformaciones provocadas por su propio peso, la forma de sujeción y los cambios térmicos. Previo a las medidas en el laboratorio la unidad de mecánica del *IFIC* realizó diversas simulaciones (térmicas y mecánicas) mediante el análisis de elementos finitos (*FEA*) con las que poder

comparar. Para los tests en el laboratorio se utilizó una cámara infrarroja para observar el perfil de temperatura en la superficie y sensores *PT100* para la medida de temperatura en puntos locales. Las deformaciones transversales al plano del Pétalo y las elongaciones longitudinales se midieron utilizando sensores capacitivos y una galga extensiométrica, respectivamente. Los resultados obtenidos tanto para las simulaciones como para las medidas en laboratorio se presentan en las tablas 6.1 y 6.2.

	Tests Mecánicos **Distancia = 450 mm / Carga = 1250 g**	
	simulación *FEA*	**Laboratorio**
Deflexión fuera del plano (μm)	147	196.6
Estrés Longitudinal ($\mu\varepsilon$)	24.1	29.75

Table 6.1: Comparación de los resultados mecánicos obtenidos para las simulaciones *FEA* y en laboratorio.

En el laboratorio se obtuvieron deformaciones debidas a estrés mecánico de unas 200 μm en el caso de deflexiones fuera del plano y alrededor de 30 $\mu\varepsilon$ para las elongaciones longitudinales de la superficie (tabla 6.1). Estos resultados son del mismo orden que los obtenidos por las simulaciones.

	Test Térmico $T^{ra}\ Aire$ **= 20°C /** $T^{ra}\ CO_2$ **= -32°C /** CO_2 **P = 12 bar**	
	Simulación *FEA*	**laboratorio**
Deflexión fuera del plano (μm)	36	27.8
Estrés Longitudinal ($\mu\varepsilon$)	53.7	247.2
Temperatura mínima (°C)	-30	-29.8
Temperatura máxima (°C)	-24	-13.8

Table 6.2: Comparación de los resultados térmicos obtenidos para las simulaciones *FEA* y en laboratorio.

En el caso de deformaciones debidas a la temperatura (tabla 6.2), las deflexiones medidas en laboratorio son de 0.24 $\mu m/°C$ y son coherentes con lo obtenido por las simulaciones, mientras que las elongaciones presentan una variación del 78% con el análisis *FEA* obteniendo en laboratorio 4.8 $\mu\varepsilon/°C$. El modelo simulado es una primera aproximación de la estructura completa, por lo que muchas de las propiedades de los materiales pueden no estar bien implementadas. Además, las condiciones externas y el modo de sujeción del Pétalo durante tests reales influyen en gran medida sobre el sistema y reproducir estas condiciones mediante simulación es altamente complicado,

de modo que es habitual tener discrepancias en los resultados. Estos resultado son una primera aproximación y nos sirven para conocer cuán fiel es nuestro modelo y en qué rango de valores vamos a movernos durante el experimento.

La mínima temperatura alcanzada en la superficie del Pétalo, a lo largo de la tubería de acero, está alrededor de los -30 °C, valor que está en concordancia con lo previsto por las simulaciones.

Para medir la planaridad y el grosor de la estructura de fibra de carbono se utilizaron dos sistemas de medida: uno horizontal y otro vertical, respectivamente. En cada sistema se emplearon varios tipos de restricciones en cuanto a la sujeción del Pétalo. Mediante el sistema horizontal se establecieron desviaciones máximas de unas 100 μm que es el valor establecido por las especificaciones. Con el sistema vertical se midió la distancia entre las dos capas de fibra de carbono en varios puntos, obteniendo un grosor de 5.4 mm. El valor establecido por las especificaciones para el grosor es de unos 5 mm de modo que los resultados obtenidos son compatibles.

Tests sobre sensores de silicio

Los sensores de *microstrip* tipo *p* para los Pétalos del *HL-LHC* analizados en esta tesis fueron fabricados por *Hamamatsu Photonics* [99]. Debido al alto coste de fabricación y de lo delicados que son estos sensores se construyen miniaturas, de (1$\times$1) cm de tamaño, para los primeros estudios (pre y post-irradiación).

El diseño de los sensores estudiados en este trabajo mantiene la simetría con la forma del Pétalo. Los strips se inclinan 20 $mrad$ en cada cara para conseguir la coordenada $r\phi$ colocados en forma de abanico. Los *strips* no son paralelos a los bordes del sensor y no todos ellos llegan a alcanzar la línea donde se establecen las conexiones eléctricas, quedando por tanto huérfanos. Un esquema de este efecto puede verse en la figura 6.9.

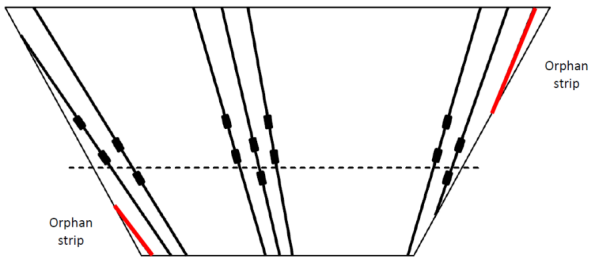

Figure 6.9: Diseño de un sensor con forma de trapezoide cuadrado con los *strips* huérfanos en los laterales.

Para evitar las zonas muertas del sensor se conectan los *strips* huérfanos a sus vecinos cercanos que sí están conectados a la electrónica de lectura. Se plantean dos opciones de conexión: directamente al pad de metal de los *strips* (conexión *AC*) o entre los implantes de los *strips* (conexión *DC*). Las dos opciones se pueden ver en la figura 6.10

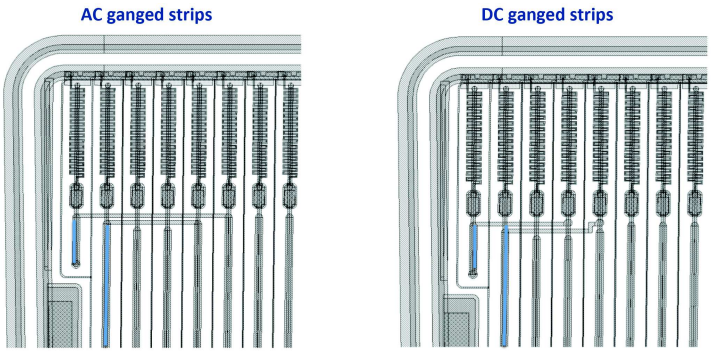

Figure 6.10: Soluciones posibles para conectar los *strips* huérfanos a sus vecinos. Conexión *AC* que se realiza entre los *strips* de aluminio del *readout* (izquierda) o conexión *DC* que se realiza entre los implantes.

Además de los sensores tipo End-Cap también se fabricaron miniaturas de sensores tipo Barril que incluye *strips* axiales dispuestos paralelos a los bordes del sensor.

Curvas I-V y C-V

Durante la caracterización eléctrica de los sensores (pre y post-irradiación) se mide la corriente en función del voltaje (curva IV) para observar si se produce ruptura del diodo y en ese caso determinar cuál es el valor del *voltaje de ruptura*. También se mide su capacidad en función del voltaje (curva CV) mediante la cuál se puede extraer el *voltaje de desertización completa* (V_{FD}). Las curvas obtenidas, tanto para detectores no irradiados como para los irradiados, se presentan en las figuras 6.11 y 6.12 respectivamente. Los detectores fueron irradiados con neutrones, protones y partículas gamma.

Los valores medios obtenidos para el *voltaje de ruptura* y *desertización completa*, así como para la corriente máxima y capacidad mínima registradas, se encuentran resumidos en la tabla 6.3. En esta tabla también se compara directamente con los valores establecidos por las especificaciones.

Los sensores no irradiados no presentan ruptura por debajo de los 600 V (valor de voltaje de operación de los sensores del *HL-LHC*). La media del *voltaje de desertización*

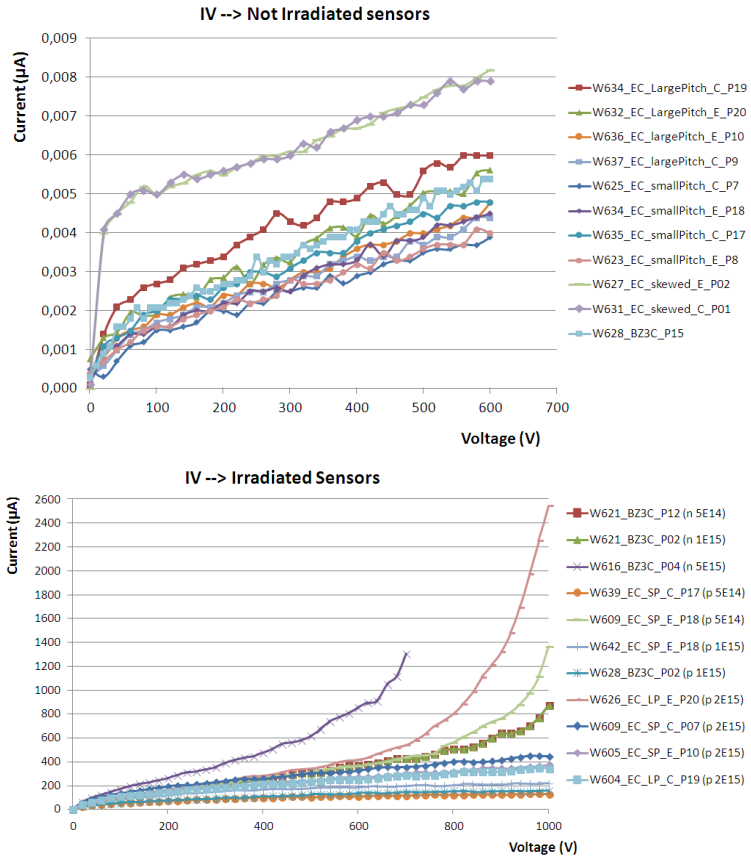

Figure 6.11: Corriente de fugas en función del voltaje aplicado medido con la caja de puntas para los detectores no irradiados. No existe ruptura por debajo de los 600 V.

Especificaciones	No Irradiados - Resultados	Irradiados - Resultados
I (600V) $< 0.1\ \mu A$	$I_{máx}$ (600V) = 0.0082 μA	$I_{máx}$ (600V) = 850 μA
C_{acoplo} (600 V) $\geq$ 20 pF	C_{min} (600 V) = 21.09 pF	C_{min} (600 V) = 27.63 pF
$V_{FD} \sim$ 360 V	V_{FD} (average) = (363.2 $\pm$ 3.6) V	—
$V_{ruptura} >$ 600 V	$V_{ruptura} >$ 600 V	$V_{ruptura} >$ 600 V

Table 6.3: Resumen de los resultados obtenidos para las curvas $I-V$ y $C-V$ de los detectores irradiados y no irradiados y su comparación con las especificaciones establecidas.

completa en no irradiados se sitúa en (362.2 $\pm$ 3.6) V valor que se encuentra en concordancia con el medido por otros institutos de la colaboración y dentro de las especificaciones.

La corriente de fugas en el caso de sensores irradiados resultó mucho mayor que en el caso de los no irradiados (como se esperaba) siendo la máxima la correspondiente

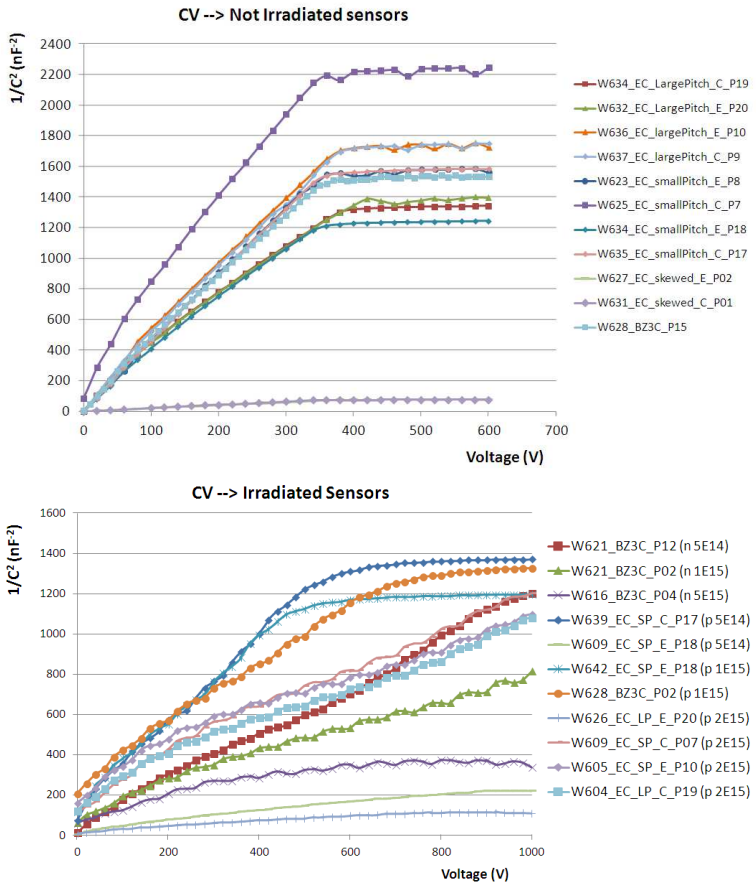

Figure 6.12: Capacidad en función del voltaje aplicado medido en la caja de puntas para los detectores no irradiados dibujado como $1/C^2$. El voltaje de desertización completa se alcanza sobre los 350 V.

a los detectores irradiados con neutrones a la máxima dosis. La irradiación con neutrones afecta mucho más a las propiedades eléctricas del sensor que la de protones o partículas gamma, por lo que los resultados obtenidos están dentro de lo esperado. A pesar del elevado valor de la corriente, no se observó ruptura por debajo de 600 V de modo que los sensores son todavía operativos incluso a las mayores dosis de irradiación. En cuanto a los estudios mediante curvas $C-V$, la mayoría de los detectores irradiados, no presentan una zona de capacidad constante, por lo que no es posible calcular el *voltaje de desertización completa* mediante este método.

En general, comparando los resultados antes y después de la irradiación, los efectos negativos de la radiación sobre las propiedades eléctricas de los sensores, son evidentes. La corriente de fugas aumenta cinco órdenes de magnitud después

de irradiar los sensores y el *voltaje de desertización completa* aumenta no pudiendo observar la región de capacidad constante en los rangos de voltaje utilizados. A pesar de esto, los detectores son capaces de seguir funcionando con buen comportamiento eléctrico para voltajes inferiores a 600 V.

Recolección de carga pre y post-irradiación

Para medir la recolección de carga se ha utilizado el sistema ALiBaVa [87] junto con una fuente radiactiva de emisión β^- (^{90}Sr). Midiendo la carga total recogida por el sensor en función del voltaje de alimentación podemos evaluar el comportamiento de la región desertizada del detector, ya que sólo los pares creados en esta región serán medidos. La carga total teórica [104] para un detector de este tipo es de 23.105 ke^-.

Se utilizaron sensores no irradiados e irradiados para estudiar los efectos de la radiaciíon en términos de recolección de carga. Se empleó además un sensor tipo barril, no irradiado, como sensor de referencia. La figura 6.13 muestra los resultados obtenidos para los sensores no irradiados medidos.

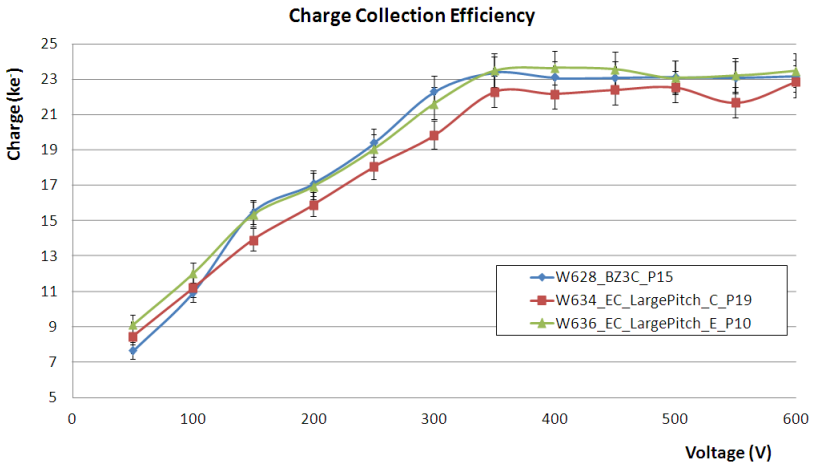

Figure 6.13: Carga recolectada medida para tres detectores no irradiados. El voltaje de desertización completa se encuentra en torno a los 370 V, valor próximo al extraído de las curvas $C-V$. Todos los detectores recolectan carga por encima de los 21 ke^-.

Todos los detectores alcanzan la región de desertización completa sobre los 370 V que es un valor cercano al obtenido mediante las curvas $C-V$. La carga recolectada y los voltajes de desertización completa para cada sensor se encuentran en la tabla 6.4.

Carga Recolectada - No Irradiados		
Sensor	**Carga Recolectada (ke^-)**	**V_{fd} (V)**
W628-BZ3C-P15 (referencia)	(23.1 $\pm$ 0.3)	(369.8 $\pm$ 15.6)
W634-EC-LargePitch-C-P19	(21.2 $\pm$ 0.5)	(376.9 $\pm$ 19.7)
W636-EC-LargePitch-E-P10	(23.4 $\pm$ 0.1)	(359.8 $\pm$ 18.1)

Table 6.4: Resumen de los resultados obtenidos para los detectores no irradiados en cuanto a carga recolectada y voltaje de desertización completa se refiere.

El sensor $W634\text{-}EC\text{-}LargePitch\text{-}C\text{-}P19$ es el único que muestra un comportamiento extraño con una carga total recogida menor que los demás (alrededor de 2 ke^- por debajo del sensor de referencia). La curva de carga por encima del *voltaje de desertización completa* es algo inestable, con fluctuaciones de unos 0,4 ke^- entre las medidas. Después de una inspección visual rigurosa y de repetir las medidas no se observó ningún elemento extraño ni cambio en los resultados, por lo que este efecto puede ser debido a un defecto de fabricación o a estrés mecánico durante la manipulación. Estos sensores son extremadamente sensibles y cualquier agente externo puede afectarles directamente.

En el caso de los detectores irradiados, la diferencia en cuanto a carga recogida, respecto al sensor de referencia, es más evidente. La figura 6.14 muestra los resultados obtenidos para los sensores medidos. Se incluyen los sensores irradiados con protones, neutrones y partículas gamma.

A partir de la figura 6.14 se deduce que la carga recogida es menor cuanto mayor es la dosis de irradiación recibida. Como se vió a partir de los resultados de las curvas $I-V$ y $C-V$, los daños producidos por la irradiación con neutrones es mucho mayor que con la de protones. La carga recogida en sensores irradiados con neutrones resulta un 30 % menor que la recogida por sensores irradiados con protones (para la misma dosis de irradiación). El *plateau* de carga para irradiación con protones se intuye por encima de los 800 V en algunos sensores, mientras que en el caso de la irradiación de neutrones este *plateau* no se observa en ningún caso.

En cuanto a los sensores irradiados con partículas gamma el efecto de la radiación a penas se refleja en la carga recogida. Las curvas resultantes se acercan mucho a lo esperado para detectores no irradiados. Esto es debido a que el daño provocado por las partículas gamma se localiza en la superficie del detector y es muy débil.

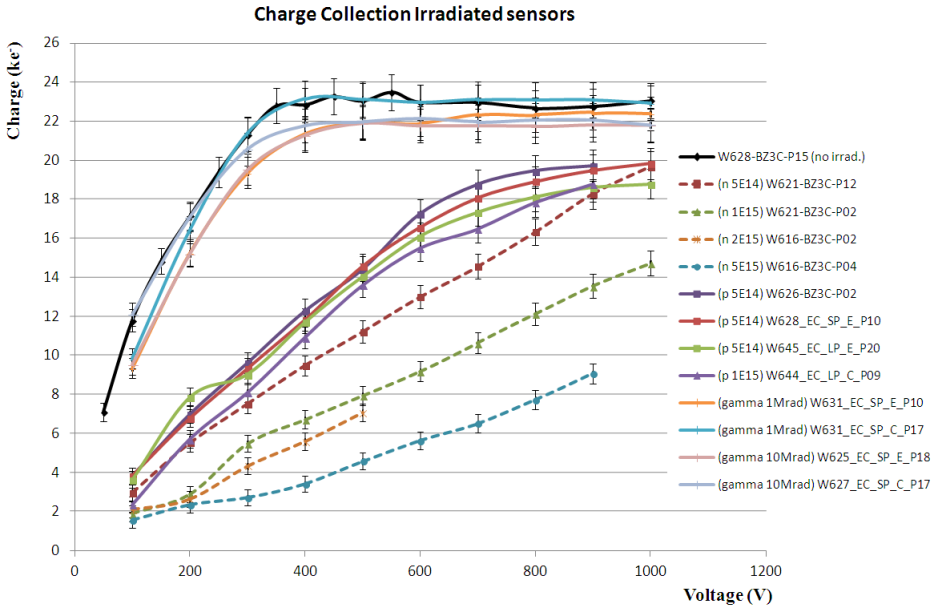

Figure 6.14: Carga recolectada para los sensores irradiados (con protones, neutrones y pratículas gamma). El resultado para el sensor no irradiado es también incluído como referencia.

En la tabla 6.5 se resumen los valores obtenidos para la carga total recolectada a 600 V.

Todos estas medidas fueron comparadas con las obtenidas por los demás institutos de la colaboración. La carga total recolectada es muy similar para cada dosis de irradiación, probando así la consistencia de los resultados obtenidos.

Medidas láser pre y post-irradiación

Como complemento a los estudios de caracterización eléctrica de los sensores, se realizaron medidas con un sistema láser cuyo movimiento se controla mediante unos ejes motorizados. Este sistema nos permite verificar el buen funcionamiento de los *strips* de forma individual, recreando el paso de una partícula por una región controlada del sensor. Además se puede observar si después de la irradiación la señal se degrada.

El perfil de carga recolectada por cada *strip* presenta dos picos separados por un agujero central. Esta falta de señal en el centro del *strip* corresponde con la región de la capa de aluminio donde el láser rebota. En la figura 6.15 se muestra un ejemplo de la carga recogida por tres strips en un sensor no irradiado en la cual se aprecia el

Carga Recolectada - Sensores Irradiados (a 600V)		
Sensor	**Dosis**	**Carga Recolectada (ke^-)**
W628-BZ3C-P15 (referencia)	no irrad.	(23.1 $\pm$ 0.3)
W621-BZ3C-P12	n; 5×10^{14} n_{eq}/cm^2	(13.0 $\pm$ 0.6)
W621-BZ3C-P02	n; 1×10^{15} n_{eq}/cm^2	(9.2 $\pm$ 0.5)
W616-BZ3C-P02	n; 2×10^{15} n_{eq}/cm^2	microdescargas
W616-BZ3C-P04	n; 5×10^{15} n_{eq}/cm^2	(5.6 $\pm$ 0.4)
W626-BZ3C-P02	p; 5×10^{14} n_{eq}/cm^2	(17.2 $\pm$ 0.7)
W628-EC-SP-E-P10	p; 5×10^{14} n_{eq}/cm^2	(16.6 $\pm$ 0.7)
W645-EC-LP-E-P20	p; 5×10^{14} n_{eq}/cm^2	(16.1 $\pm$ 0.7)
W644-EC-LP-C-P09	p; 1×10^{15} n_{eq}/cm^2	(15.5 $\pm$ 0.7)
W631-EC-SP-E-P10	γ; 1 Mrad	(22.4 $\pm$ 0.9)
W631-EC-SP-C-P17	γ; 1 Mrad	(20.0 $\pm$ 0.8)
W625-EC-SP-E-P18	γ; 10 Mrad	(21.2 $\pm$ 0.8)
W627-EC-SP-C-P17	γ; 10 Mrad	(20.6 $\pm$ 0.8)

Table 6.5: Resumen de las medidas de recoleción de carga en detectores irradiados.

rebote del láser en el aluminio.

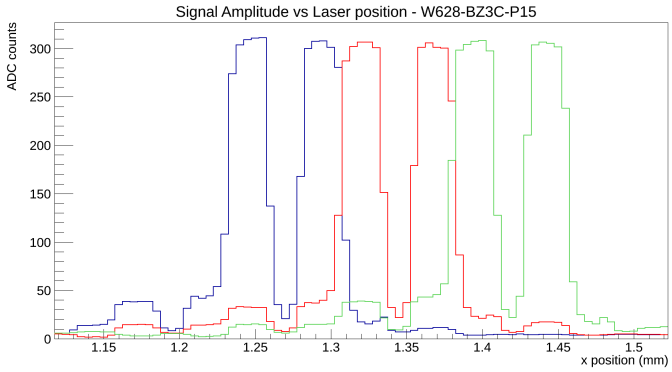

Figure 6.15: Amplitud de la señal (en cuentas de ADC) en función de la posición del láser para tres *strips* consecutivos de dos sensores no irradiados.

Se estudiaron dos detectores no irradiados haciendo un barrido con el láser en la dirección transversal a los strips, observando la cantidad de señal obtenida por *strip* (figura 6.16).

En general, ambos sensores presentan buen comportamiento en lo que a uniformidad de señal se refiere. Se obtuvieron valores máximos similares en los dos casos y ningún strip mostró falta de señal, descartando posibles daños en los strips o defectos

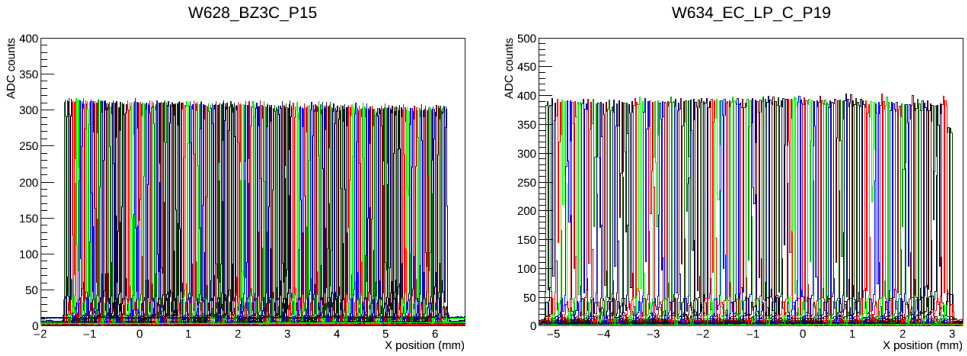

Figure 6.16: Amplitud de la señal (en cuentas de ADC) en función de la posición del láser para tres *strips* consecutivos de dos sensores no irradiados.

en las conexiones eléctricas.

En el caso de los sensores irradiados analizados se obtuvieron resultados similares sin falta de señal a lo largo de la superficie de cada sensor. Un ejemplo de estos resultados se muestra en la figura 6.17.

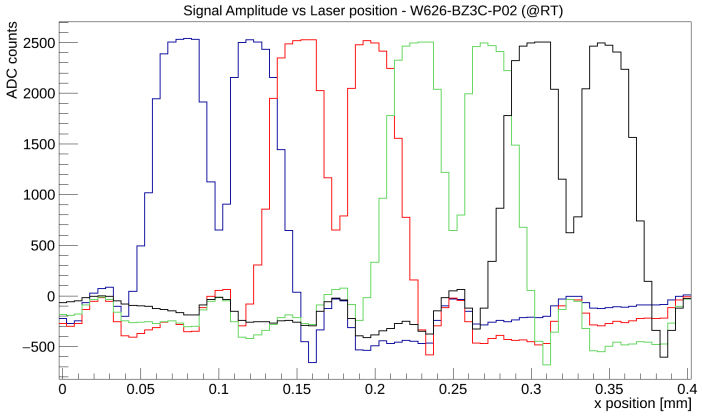

Figure 6.17: Amplitud de la señal (en cuentas de ADC) en función de la posición del láser para el sensor $W626\text{-}BZ3C\text{-}P02$.

- **Análisis de conexiones *AC* y *DC***

  Cuando el láser atraviesa la zona en la que existe una conexión entre *strips* aparece una doble señal en dos posiciones diferentes del láser, que parecen provenir del mismo *strip*. Esta doble señal es el producto de la conexión entre dos *strips* vecinos, los cuales se leen a través del mismo canal del chip. En la figura 6.18 se muestran los resultados obtenidos para dos detectores diferentes, uno con conexión *DC* (izquierda) y otro con conexión *AC* (derecha).

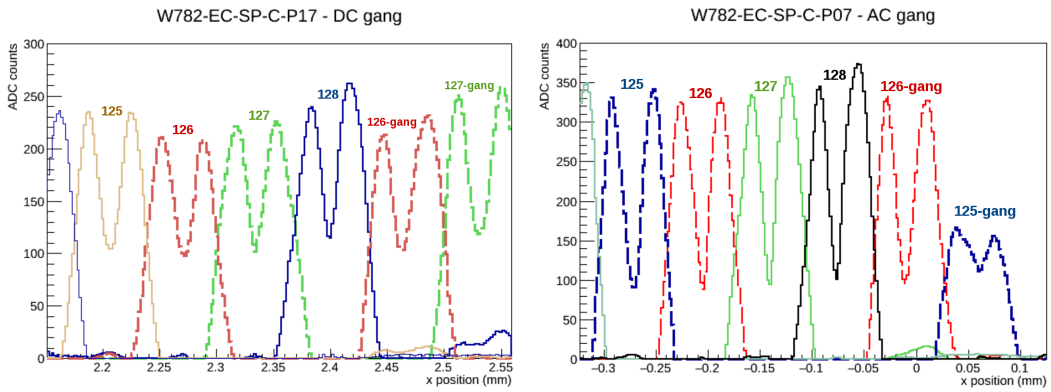

Figure 6.18: Amplitud de la señal en función de la posición del láser para dos detectores irradiados con *DC-ganging* (izquierda) y *AC-ganging* (derecha).

Como se puede comprobar, a partir de la figura 6.18, ambas soluciones presentan una pequeña bajada en la intensidad de la señal. Los strips que están conectados a sus vecinos recolectan menos carga que los demás. En el caso de la conexión *AC* este efecto es aún mayor. Estos resultados fueron validados con los obtenidos por otros institutos de la colaboración. Este efecto es común para todos. La máxima disminución de señal se sitúa entorno al 10-30%. Cabe destacar que los sensores analizados están irradiados con protones a una dosis elevada, por tanto, pese a la disminución de carga recolectada los sensores presentan un comportamiento óptimo. Ambas opciones serían válidas para hacer la conexión de los *strips* huérfanos.

Estudios de *Annealing*

Como se ha explicado anteriormente para ver cómo evolucionan los efectos de la radiación con el tiempo se realizan estudios de *annealing acelerado* utilizando para ello una cámara climática. En dicha cámara permanecen los sensores a 60° C, en un entorno de temperatura y humedad controlado, durante un tiempo determinado.

En detectores tipo *p* se leen electrones, los cuales tienen mayor movilidad que los huecos y por tanto tienen menor probabilidad de quedar atrapados en los niveles energéticos introducidos por la radiación. Al cabo del tiempo las trampas se reducen y por tanto durante el tiempo de integración de la señal la cantidad de electrones leídos aumenta. Debido a esto se produce un aumento de la carga recolectada conforme aumenta el tiempo. Un ejemplo de este efecto se observa en la figura 6.19.

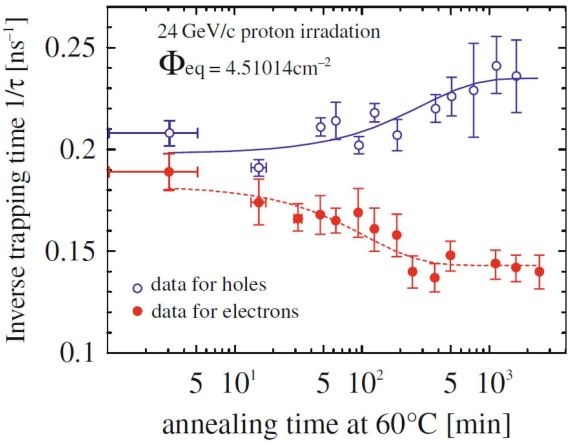

Figure 6.19: Comportamiento de las trampas en agujeros y electrones en función del tiempo de *annealing*. Figura extraída de [108].

En la figura 6.20 se muestra la carga recolectada, en función del voltaje de alimentación, para los distintos tiempos de *annealing* y para dos de los sensores medidos

El sensor $W626\text{-}BZ3C\text{-}P02$ muestra un incremento de carga recolectada a partir de 300 minutos de *annealing* (para 500 V), como esperábamos. Posteriormente se produce una repentina bajada en la carga que puede corresponder al periodo de *annealing perjudicial*. Durante las medidas con este sensor la corriente de fugas se hizo extremadamente alta ($> 400\ \mu A$) por encima de los 80 minutos de *annealing* y comenzaron a aparecer microdescargas por lo que las medidas se suspendieron. Fijándonos en los resulados para el sensor $W609\text{-}EC\text{-}SP\text{-}C\text{-}P17$ se observa también un incremento de la carga recolectada a partir de 440 minutos de *annealing* y más adelante un descenso, de nuevo, a partir de 3340 minutos de *annealing*.

A partir de la figura 6.19 uno esperaría no observar la región de *annealing perjudicial* en este tipo de detectores, pero sin embargo no es así. Estos resultados fueron contrastados con los obtenidos por otros institutos habiendo concordancia entre ellos. Recientemente se están llevando a cabo nuevas investigaciones, como la presentada en esta tesis, las cuales están mostrando que el comportamiento de los sensores tipo *p* en cuanto a *annealing* se refiere no se ajustan a la teoría. Todavía no se ha llegado a una clonclusión definitiva.

Los otros dos sensores analizados mostraron un comportamiento más extraño. La carga recogida por estos sensores para distintos voltajes y en función del tiempo

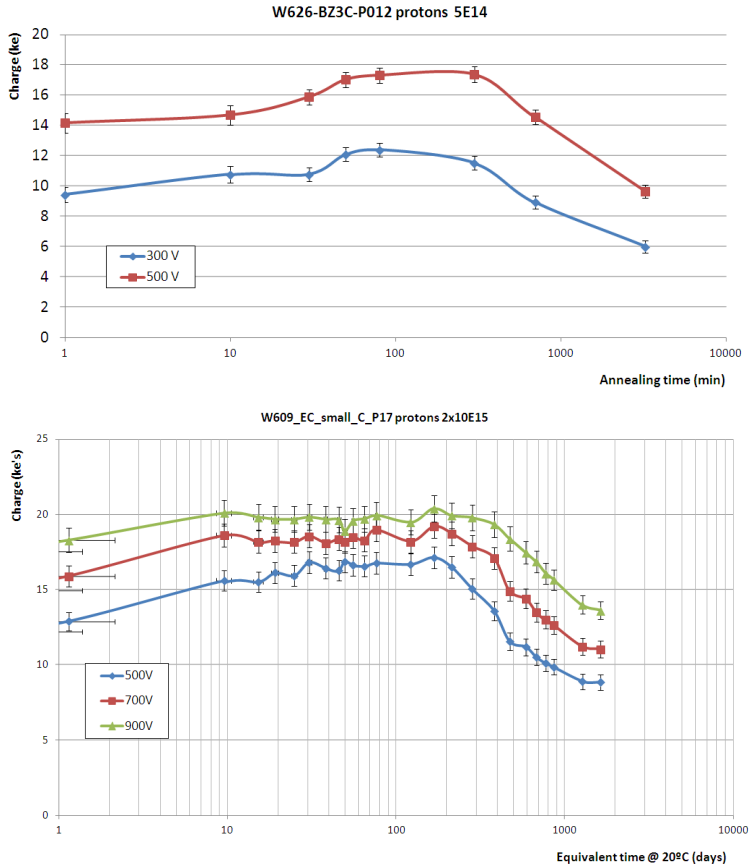

Figure 6.20: Carga recolectada en función del tiempo de *annealing*.

de *annealing* se muestra en la figura 6.21.

El aumento de carga recolectada a lo largo del tiempo no se observó. Además ambos tenían una corriente de fugas muy elevada lo cuál dificultaba las medidas. Su comportamiento no era estable y el alto ruido enmascaraba la señal obtenida haciendo el análisis muy complicado.

De los resultados obtenidos con los primeros sensores podemos concluir que durante los periodos de parada del detector, donde los sistemas de refrigeración permanecen desconectados, las propiedades de los sensores no se van a ver afectadas tan negativamente como ocurre en los detectores tipo n que hay actualmente funcionando en *ATLAS*. Pese a haber demostrado que este tipo de detectores sí puede sufrir *annealing perjudicial* sus efectos aparecen después de 4 meses, tiempo suficientemente alto como para comprometer el buen funcionamiento del detector completo.

Los estudios anteriormente mostrados prueban el excelente comportamiento de

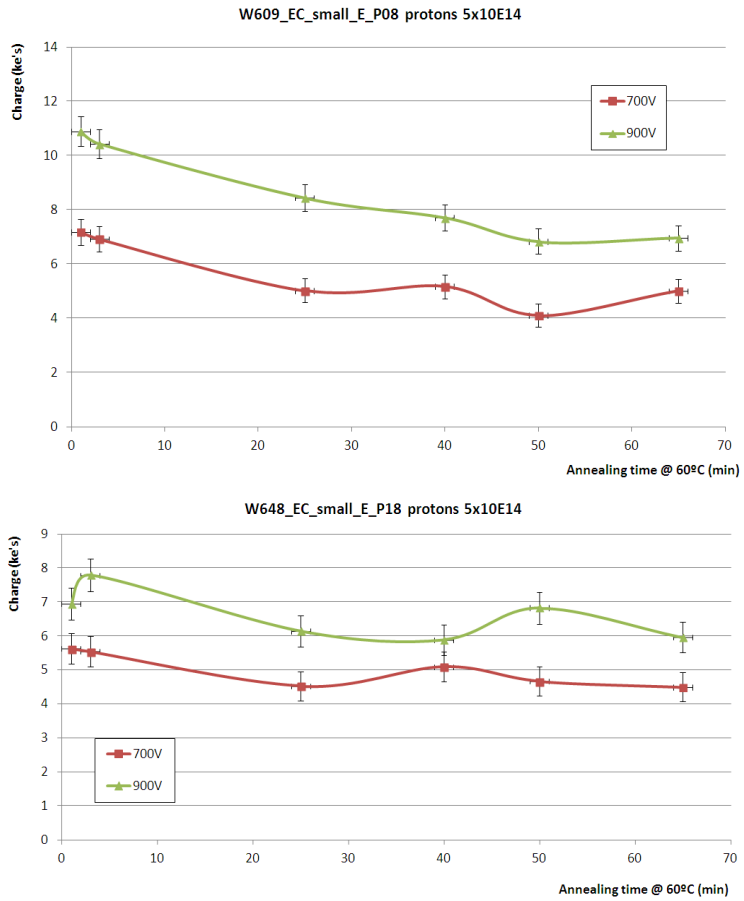

Figure 6.21: Carga recolectada en función del tiempo de *annealing*.

los detectores tipo *p*. Sus características eléctricas se mantienen en condiciones adecuadas incluso para las mayores dosis de irradiación, sin presencia de ruptura por debajo de 600 V y con una carga total recolectada por encima de los 5 ke^{-}, en los peores casos. Sin duda, este tipo de detectores cubrirán las necesidades de un experimento de estas características y bajo el tipo de escenarios esperados en *HL-LHC*.

Petalet: un concepto de diseño

Debido a la cantidad de pasos de producción y el alto coste de las máscaras de silicio que se necesitan para construir un Pétalo, su proceso de fabricación resulta elevadamente costoso. Por ello se decidió crear un prototipo a pequeña escala para poder estudiar diversos aspectos y minimizar costes. Así nace el proyecto *Petalet*. El

prototipo incluiría únicamente 3 detectores que corresponden a la región central del Pétalo en la que los sensores se dividen en dos columnas (ver figura 6.22).

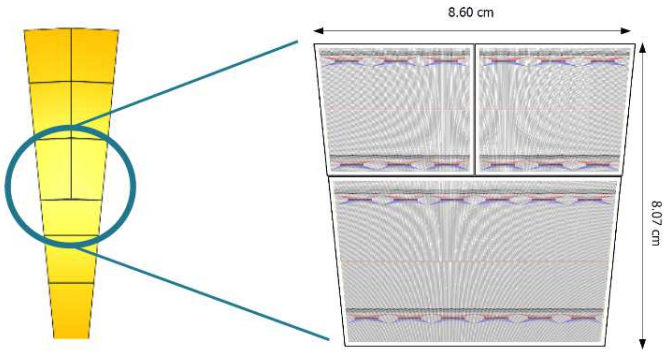

Figure 6.22: Región central del Pétalo seleccionada para construir el Petalet.

Los sensores del Petalet se construyeron a partir de obleas de silicio de 4 pulgadas y se fabricaron en el Centro Nacional de Microelectrónica (*CNM*) de Barcelona. Se fabricaron tanto sensores en miniatura, para realizar tests, como de tamaño real, para construir el Petalet.

Debido al tamaño de los sensores del Pétalo y a la distribución de *strips*, el ángulo de soldadura que se establece para los chips es muy alto. El *CNM* propuso como solución añadir una segunda capa de metal a los sensores que incluye unos adaptadores (*embedded PAs*) para poder soldar los *strips* a los chips más cómodamente.

Los procedimientos de medida fueron análogos a los empleados con los sensores de *Hamamatsu*.

Curvas IV y CV: resultados

Las curvas IV y CV obtenidas para los sensores en miniatura se presentan en la figura 6.23.

No se observó ruptura en el rango de voltajes aplicado y la corriente de fugas se mantuvo por debajo de 2 μA, que es el valor máximo fijado por las especificaciones. La *desertización completa* se alcanza en todos los sensores por debajo de los 100 V, siendo la media de (68.2 $\pm$ 3.2) V.

Los sensores de tamaño real se identifican como *big* (para el sensor más grande, el inferior), *top right* (el superior derecha) y *top left* (el superior izquierda). Los resultados obtenidos para estos sensores se muestran en las figuras 6.24, 6.25 y 6.26.

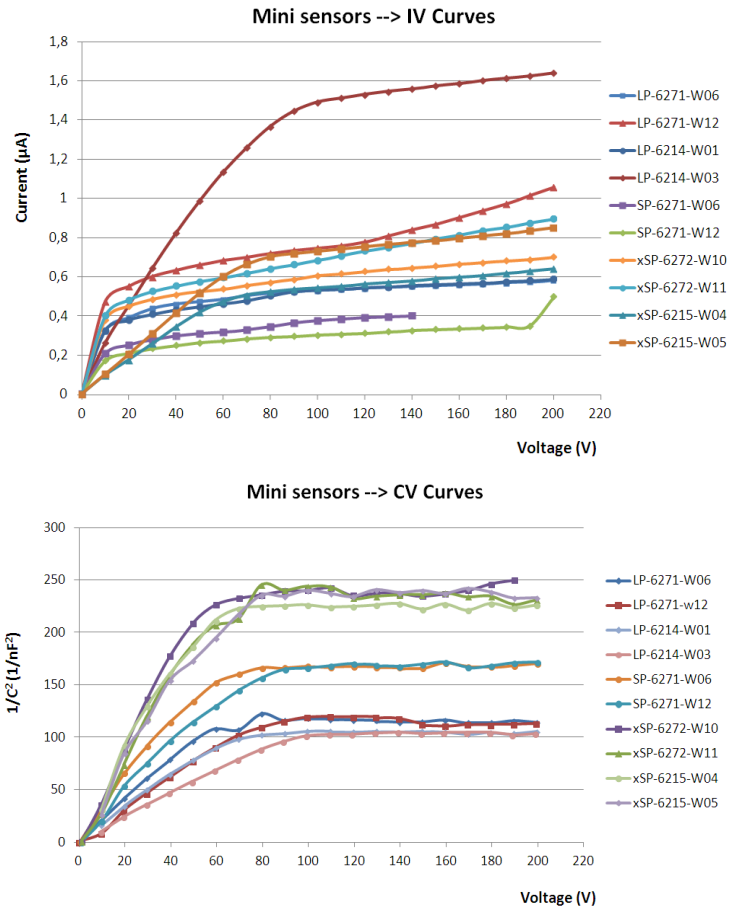

Figure 6.23: Curvas I-V (izquierda) y C-V (derecha) obtenidas para los sensores miniatura.

Excepto dos de los sensores, todos en general mostraron buen comportamiento eléctrico. El *voltaje de desertización completa* varía para cada detector pero se encuentra alrededor de los 50 V, siendo la media de (50.68 $\pm$ 2.55) V.

Para la fabricación del Petalet se escogieron los sensores que presentaban mejor comportamiento eléctrico, en cuanto a corriente de fugas y *voltaje de desertización completa* (ver tabla 6.6).

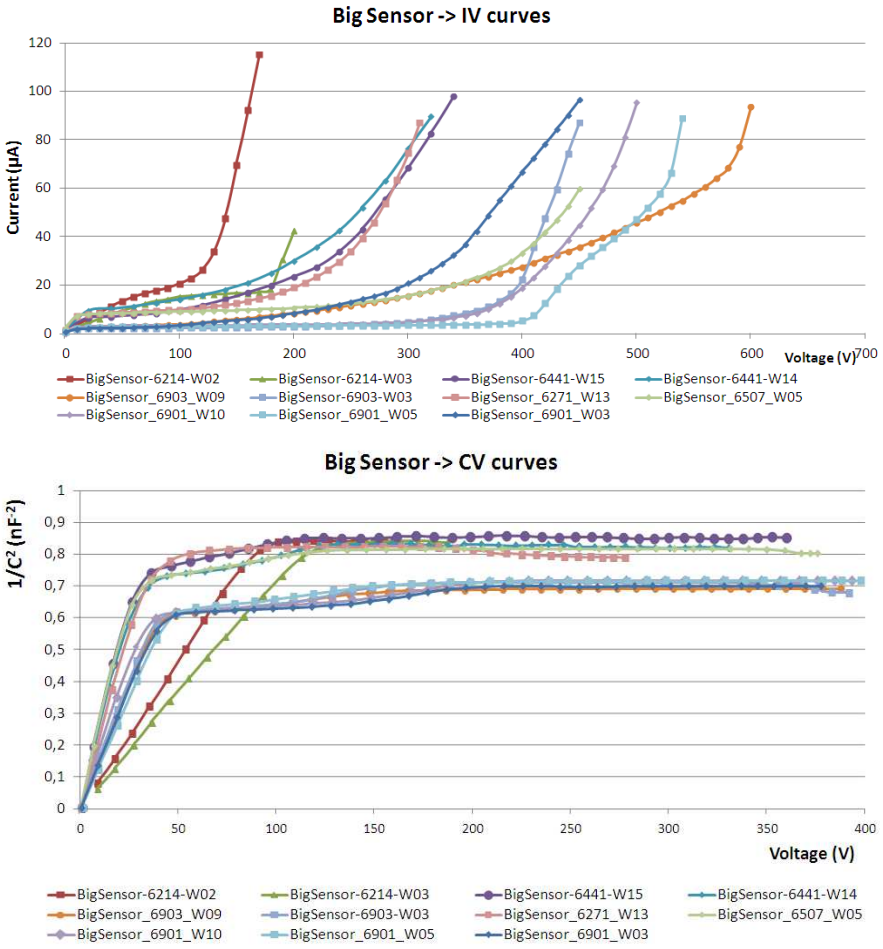

Figure 6.24: Curvas I-V (izquierda) y C-V (derecha) obtenidas para los detectores de tamaño real tipo *big*.

Sensores para Petalet		
Sensor	I_{fugas} **a 100 V** (μA)	V_{FD} **(V)**
BigSensor-6901-W10	3.40	(43.1 $\pm$ 1.9)
BigSensor-6901-W05	2.92	(58.9 $\pm$ 2.4)
TopRight-6442-W16	4.28	(37.9 $\pm$ 2.7)
TopRight-6902-W04	2.07	(35.0 $\pm$ 2.1)
TopLeft-6442-W14	7.30	(34.9 $\pm$ 6.0)
TopLeft-6902-W06	1.11	(40.5 $\pm$ 5.1)

Table 6.6: Sensores seleccionados para construir el Petalet y sus características eléctricas.

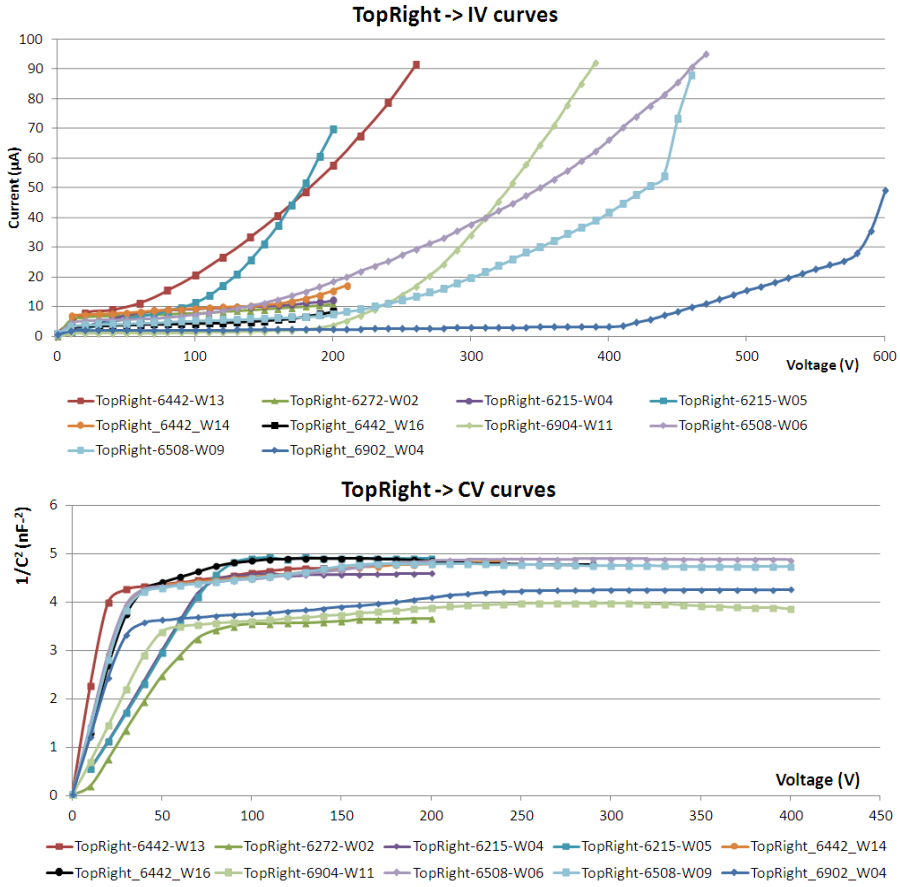

Figure 6.25: Curvas I-V (izquierda) y C-V (derecha) obtenidas para los detectores de tamaño real tipo *top-right*.

Eficiencia de recolección de carga: resultados

Los sensores del Petalet tienen un grosor de 285 μm por lo que les corresponde una carga total de 21.73 ke^- por encima del *voltaje de desertización completa*. La carga recogida en función del voltaje de alimentación para los sensores minis medidos se muestra en la figura 6.27.

Todos los sensores miniatura medidos presentan un comportamiento similar. La media de carga total recolectada se encuentra en (21.93 $\pm$ 0.87) ke^-, la cuaál está en concordancia con los esperado.

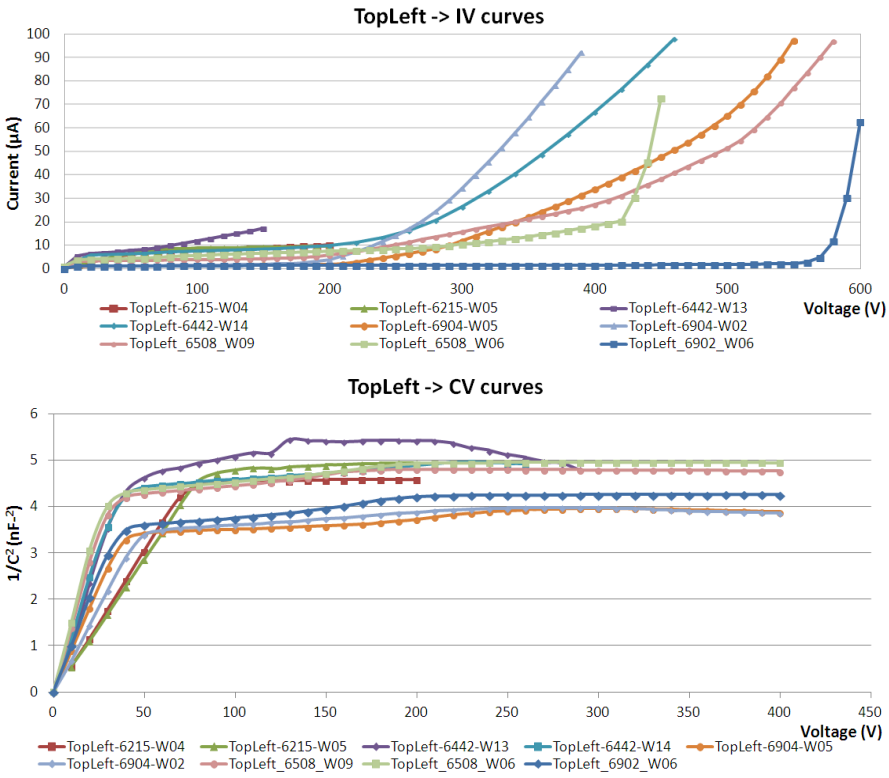

Figure 6.26: Curvas I-V (izquierda) y C-V (derecha) obtenidas para los detectores de tamaño real tipo *top-left*.

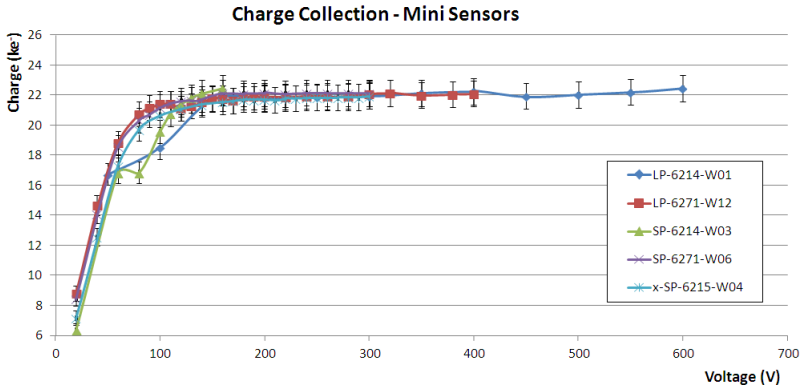

Figure 6.27: Carga recolecctada en función del voltaje aplicado en los sensores miniatura del Petalet.

Medidas Láser resultados

Con las medidas láser sobre los detectores del *CNM* se pretende analizar los efectos negativos que pueden provocar los *embedded PAs*. La segunda capa de

metal que se introduce en los sensores puede favorecer la aparición de dos tipos de acoplo:

- *cross-talk*: es el acoplo que se produce entre las dos capas de metal del sensor.
- *pick-up*: es el acoplo que se induce entre la segunda capa de metal y el sustrato del sensor.

Después de realizar varios barridos en distintas posiciones del láser se descartó la presencia de *cross-talk*. La señal registrada por *strip* resultó uniforme a lo largo del sensor medido.

Para estudiar el efecto de *pick-up* se situó el láser en la zona en la que se encuentran los *embedded PAs*. Debido a la alta densidad de líneas de metal las medidas resultaron complicadas de tomar ya que el láser se reflejaba en todas las zonas de aluminio. Pese a ello pudieron detectarse algunos canales acoplados. La intensidad de señal en función de la posición del láser, para dichos canales, se muestra en la figura 6.28.

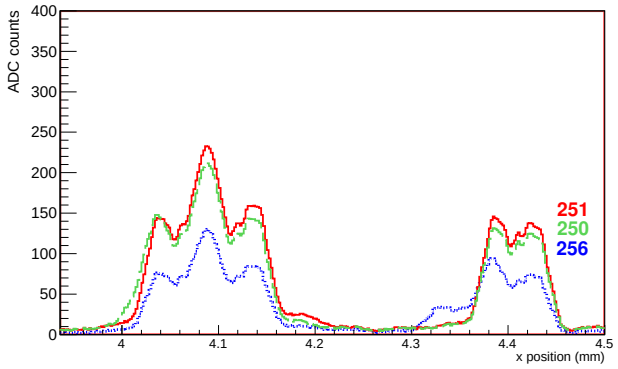

Figure 6.28: Amplitud de la señal en función de la posición del láser. El efecto de *pick-up* es detectado entre los canales 250, 251 y 256.

Por tanto, el acoplo entre la segunda capa de metal y el sustrato puede aparecer. Sin embargo, este efecto se detectó en muy pocos canales. Dado que los *embedded PAs* se encuentran tan sólo en una pequeña región del sensor (respecto al área total) la influencia que puede tener el efecto de *pick-up* en el sistema completo sería prácticamente despreciable. Todos estos resultados se publicaron recientemente en [111].

Electrónica de lectura

Uno de los objetivos principales del proyecto *Petalet* fue elegir el diseño de la electrónica de lectura asociada. Esto incluye el desarrollo del cable *bus* que contiene las pistas de datos y alimentación, llamado *Bustape*. Para el prototipo se propusieron dos diseños:

- ***Split Readout*:** donde los sensores superiores utilizan un único híbrido[1] lo cual posibilita dirigir las líneas de datos y alimentación a los lados del Petalet (izquierda y derecha respectivamente). Ésta es la forma más segura por lo que a acoplamiento de ruido se refiere pero el tener un único híbrido dificulta el ensamblado, ya que se debe garantizar la coplanaridad entre los dos sensores.

- ***Common Readout*:** En esta configuración los sensores superiores utilizan dos *híbridos* convirtiéndolos en módulos independientes facilitando así su montaje. Con este sistema se reciben líneas de datos y alimentación tanto por la izquierda como por la derecha del Petalet (delante y detrás). Debido a la restricción de espacio, las líneas deben ir muy juntas, por lo que hay que prestar especial atención en el diseño para evitar el acoplo de ruido entre ellas. El *IFIC* se encargó del diseño, desarrollo y verificación de esta opción.

Test eléctricos: resultados

En los tests eléctricos se evalúan el ruido y la ganancia por canal, inyectando en el sistema tres valores fijos de carga (0.5 fC, 1.0 fC y 1.5 fC) y realizando barridos variando el valor umbral (a partir del cual se detecta un evento). Para cada carga obtendremos un parámetro V_{th50}, el cual corresponde al umbral para el que la ocupancia en el canal es del 50%. La distribución de ocupancia por canal sigue una función error (ver figura 6.29) la sigma de la cual resulta ser el ruido de salida del sistema. Estos valores de V_{th50} son lineales con la carga y de su ajuste lineal obtenemos el valor de la ganancia (pendiente del ajuste). Con el ruido de salida y la ganacia podemos calcular el ruido de entrada mediante:

$$Input\ noise = \frac{output\ noise}{gain} \tag{6.5}$$

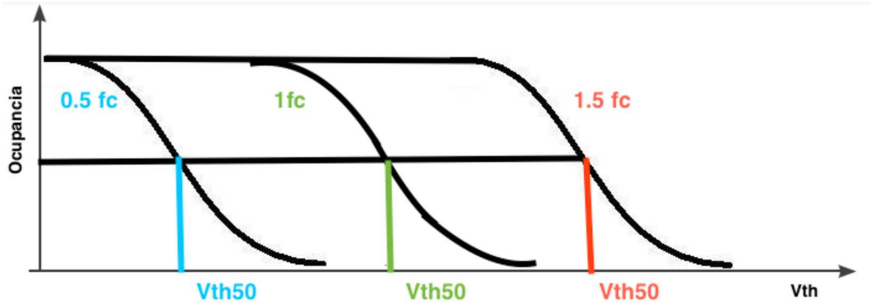

Figure 6.29: Ocupancia de canales en fución del umbral para tres valores de carga diferentes. El valor umbral en el que la ocupancia es del 50 % se conoce como paránetro V_{th50}.

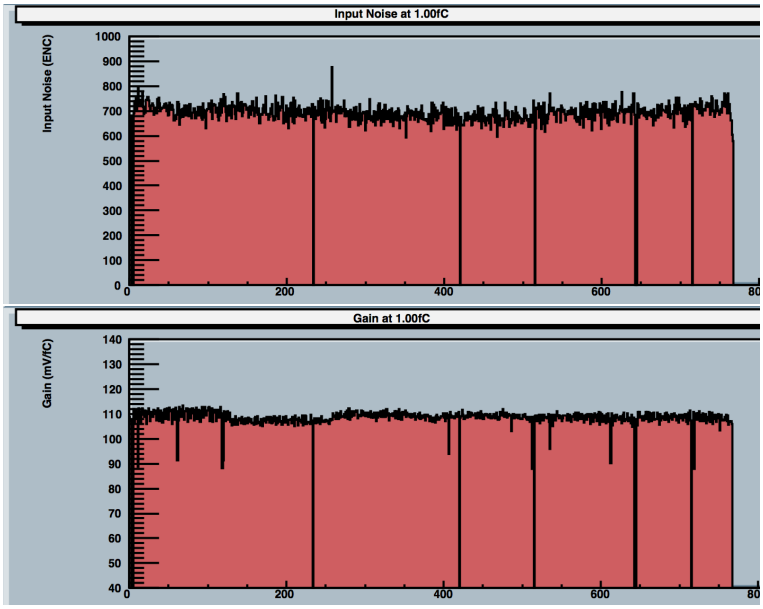

Figure 6.30: Ruido de entrada (arriba) y ganancia (abajo) en función del número de canal para un módulo *lower* en la configuración *Common readout*.

El ruido total vendrá dado por la media del ruido por canal. En la figura 6.30 se muestra un ejemplo de gráficas de ruido y ganancia obtenidos con estos tests.

Estas pruebas se realizan en cada paso del montaje y los mejores módulos en términos de ruido y ganancia son pegados en el Petalet y posteriormente testeados de nuevo. La colaboración testeó un total de 6 Petalets. Las condiciones de las pruebas, así como los resultados obtenidos para cada Petalet se encuentran resumidos en la tabla 6.7.

[1] Llamamos híbrido al sistema formado por la targeta *PCB* y los *chips*

	DESY standard double sided	**DESY standard** single sided	**DESY embedded** single sided	**Freiburg standard** double sided (only one side)	**Freiburg embedded** double sided	**Valencia standard** double sided
T ($^{\circ}$C)	0	15	5	- 20	- 20	- 15
V (V)	- 150	- 150	- 140	- 200	- 100	- 150
Input Noise (ENC)	601	674	728	597	727	618

Table 6.7: Resumen de los resultados de ruido de entrada para los diferentes Petalets construidos por la colaboración. Se incluyen además, las condiciones particulares de cada sistema.

A pesar de las diferencias de condiciones de trabajo, todos los valores de ruido obtenidos se encuentran entorno a los (600-700) ENC. Los módulos más ruidosos corresponden a los que incluyen sensores con *embedded PA*'s. Tests posteriores determinaron que los *embedded PA*'s introducían una mayor capacidad entre los *strips* de modo que aumentaba el ruido total de los módulos.

Electrónica de lectura: Elección final

Después de analizar en detalle los resultados obtenidos para cada tipo de electrónica de lectura, se convocó un comité de expertos que evaluase los resultados de ambas soluciones y extrajese unas recomendaciones para la elección de una de ellas. Ambas soluciones fueron valoradas como factibles. A pesar de la dificultad de montaje con la configuración *Split readout*, este sistema permite sinergias de una forma más directa con la parte Barril del detector, en el desarrollo de híbridos y fabricación del *Bustape*. En cuanto a la configuración *Common readout*, la congestión de líneas en las conexiones entre *Bustape* y módulos representa una complicación adicional. Sin embargo el uso de dos híbridos independientes hace que el proceso de montaje sea considerablemente más sencillo. De modo que se propuso adoptar una solución combinada aprovechando las ventajas de cada configuración. La electrónica de lectura que se desarrollará para los futuros Pétalos adoptará como base el sistema *Split readout* pero utilizando híbridos separados en los módulos externos como en el *Common readout*.

Conclusiones

El trabajo presentado en esta tesis está enfocado en la caracterización eléctrica de detectores de silicio de tipo *microstrip* que se utilizarán en la segunda mejora del detector *ATLAS* y en concreto en los *End-Caps* del detector interno. Esta fase de mejora está englobada dentro del proyecto llamado *HL-LHC* donde los detectores serán sometidos a altas dosis de radiación (niveles por encima de los $10^{15}\ n_{eq}/cm^2$ en la región interna). Los detectores deberán ser reemplazados por unos nuevos que sean capaces de mantener sus especificaciones de diseño en este tipo de escenarios. Diferentes tecnologías se han desarrollado y analizado ya en el pasado decantándose por utilizar detectores de *miscrostrip* tipo p-on-n.

En la primera parte de este trabajo, se presentó la estructura del Pétalo que contendrá los sensores de silicio. Las pruebas termo-mecánicas realizadas mostraron alta compatiblidad con las simulaciones previas realizadas.
Las deformaciones máximas debidas a estrés mecánico fueron de unas 200 μm y 30 $\mu\varepsilon$ para deflexiones y elongaciones, respectivamente. Con estos valores se obtuvo el módulo de Young de la fibra de carbono, siendo de 215 GPa. En el caso de deformaciones por estrés térmico se obtuvieron deflexiones de 0.24 $\mu m/^{\circ}C$ y de 4.8 $\mu\varepsilon/^{\circ}C$ para las elongaciones. La temperaturas medidas en la superficie están entre -14 y -30°C. Los resultados presentan algunas diferencias respecto a lo previsto por las simulaciones las cuales pueden estar debidas a la gran influencia de las condiciones externas en el sistema experimental y a la necesidad de implementar mejor las propiedades de los distintos materiales en el modelo simulado. La superficie del Pétalo además se encuentra dentro de las especificaciones de planaridad (por debajo de las 100 μm) y el grosor medido (5.4 mm) es cercano al establecido ($\sim 5\ mm$).

A su vez se caracterizaron eléctricamente sensores miniatura que sirven de base a los futuros sensores del Pétalo. La caracterización se realizó en términos de corriente de fugas, capacidad y recolección de carga pre y post irradiación. A partir de los resultados se puso de manifiesto el efecto negativo que produce la radiación sobre las propiedades eléctricas de los sensores. La corriente de fugas aumentó un factor cinco después de irradiar y la capacidad cambió, no siendo posible ver la región de capacidad constante e imposibilitando el cálculo del voltaje de desertización completa mediante este método. En cuanto a la carga recolectada, se observó una disminución con la dosis de radiación. Cuanto mayor es la dosis menor es la

carga total recolectada por los sensores. A pesar de ello, los sensores son capaces de mantener las especificaciones requeridas por el experimento en el voltaje de operación esperado (unos 600 V) aún para las mayores dosis de irradiación. Por tanto, estos estudios muestran resultados muy positivos. Como complemento a la caracterización eléctrica de los sensores, se realizaron estudios de integridad de la señal por *strip* (pre y post irradiación) mediante un sistema láser diferenciando además entre sensores que poseían *strips* huérfanos conectados mediante tecnología AC o DC. En general todos los sensores medidos presentaron uniformidad en la amplitud de la señal por canal. En el caso de detectores irradiados, se comprobó de nuevo cómo la exposición a la radiación afecta a las propiedades de los sensores obteniendo una disminución en la amplitud de la señal. En cuanto a la comparativa entre tecnología AC y DC se comprobó la eficacia de ambas siendo preferibles las conexiones AC ya que en las DC existen pequeños acoplos que pueden inducir a confusión en el sistema de reconstrucción de trazas.

Con el tiempo, los efectos de la radiación cambian. Mediante el *annealig* acelerado de los sensores podemos estudiar este fenómeno. Para ello se emplea una cámara climática. En este tipo de detectores se espera ver un incremento en la eficiencia de recolección de carga con el tiempo de *annealing*. Dos de los sensores analizados presentaron comportamientos extraños. No se observaron incrementos en la carga recolectada sino un descenso. La corriente de fugas y el ruido resultaron además extremadamente elevados imposibilitando el análisis de las medidas por encima de 65 mintos de *annealing* controlado. El comportamiento de los otros dos sensores medidos fue normal, detectando el incremento de carga (de unos (3-4) ke^{-}) despues de 300 minutos de *annealing* controlado.
Estos estudios muestran una mejora, en cuanto al *annealing* se refiere, frente a los sensores tipo n que actualmente se encuantran funcionando en *ATLAS*.

En la segunda parte de este trabajo de tesis se introdujo el proyecto Petalet. El Petalet es un prototipo del Pétalo a pequeña escala que utilizamos para verificar los distintos pasos del proceso de fabricación y elegir el mejor sistema de electrónica de lectura asociada. Los sensores del Petalet fueron fabricados por el *CNM* de Barcelona (miniaturas y de tamaño real). Se utilizaron para estos estudios detectores no irradiados, algunos de los cuales incluyen adaptadores *interstrip* construídos en el propio sensor (*embedded PA's*). Estos adaptadores permiten solventar el problema de gran ángulo de bondado que aparece en los sensores del Pétalo. Se hizo la

caracterización eléctrica de estos sensores siguiendo el mismo procedimiento que en el caso de los sensores *ATLAS12A*. Todos los detectores, tanto miniatura como de tamaño real, mostraron buen funcionamiento en términos de corriente de fugas, capacidad y recolección de carga. No se observó ruptura por debajo de los 200 V (voltaje marcado por las especificaciones) y se alcanzó la desertización completa alrededor de los (50-60) V de media, obteniendo valores dentro de lo establecido. La recolección de carga con los sensores completamente desertizados rondó los 21.93 ke^{-}, valor que es compatible con el esperado para este tipo de sensores. Debido a la adición de la segunda capa de metal en los *embedded PA's* efectos de acoplo (*pick-up* and *cross-talk*) pueden aparecer. Estos efectos se estudiaron mediante técnicas láser análogas a las utilizadas con los sensores *ATLAS12A*.
Únicamente se detectaron acoplos entre la segunda capa de metal y el subtrato del sensor (*pick-up*) pero en un pequeño porcentaje de *strips*. El área que ocupan los *embedded PA's* es además bastante reducida comparada con el tamaño total del sensor por lo que la influencia de estos efectos en el sistema total es prácticamente despreciable. Los sensores analizados mostraron, en general, buen funcionamiento eléctrico.

De todos los sensores de tamaño real, se eligieron los que mejor comportamiento tuvieron (en términos de corriente de fugas y capacidad) para construir el *Petalet* y verificar los distintos sitemas de electrónica de lectura. Las dos propuestas fueron las llamadas *Split* y *Common readout*. La diferencia más destacable entre ellas es el número de híbridos que se utilizan en los dos sensores externos. La configuración *Split readout* utiliza un único híbrido para los dos sensores. Con este sistema se distribuyen las líneas de alimentación y datos cada una a un lado del Petalet. Utlizar un único híbrido hace más complicado el montaje de los módulos. En la configuración *Common readout* se utilizan dos híbridos independientes para los sensores externos facilitando así el proceso de montaje. Por el contrario las líneas de alimentación y datos van juntas a un lado del Petalet. Los tests eléctricos incluyen la determinación del ruido de entrada y ganancia del sistema. Diferentes institutos evaluaron las distintas propuestas obteniendo resultados similares (ruido en torno a los 600-700 ENC y distribución plana de ganacia) por lo que ambas configuraciones resultaron factibles. La configuración *Split readout* permite sinergias directas con la parte Barril del detector, aunque el montaje de los módulos es más sencillo con la solución *Common readout*. Después de varias discusiones, la colaboración decidió utilizar una solución combinada

de las dos configuraciones. De modo que la electrónica de lectura de los Pétalos se basará en la configuración *Split readout* pero utilizando dos híbridos para los sensores externos, como en la configuración *Common readout*.

Finalmente, los estudios presentados en esta tesis han formado parte de resultados definitivos presentados por la colaboración *ITK* de *ATLAS* que sientan las bases del desarrollo de los detectores que se utilizarán en los futuros Pétalos en el *HL-LHC*.

References

[1] D. Perkins. *Introduction to High Energy Physics*. Cambridge University Press, 4th edition, 2000. 3

[2] Elliott D. Bloom, D.H. Coward, H.C. DeStaebler, J. Drees, Guthrie Miller, et al. High-Energy Inelastic e p Scattering at 6-Degrees and 10-Degrees. *Phys.Rev.Lett.*, 23:930–934, 1969. 4

[3] F. Abe et al. Observation of top quark production in $\bar{p}p$ collisions. *Phys.Rev.Lett.*, 74:2626–2631, 1995. 4

[4] P.M. Watkins. DISCOVERY OF THE W AND Z BOSONS. *Contemp.Phys.*, 27:291–324, 1986. 4

[5] Observation of a new particle in the search for the Standard Model Higgs boson with the ATLAS detector at the LHC. *Phys.Lett.*, B716:1–29, 2012. 4

[6] Observation of a new boson at a mass of 125 GeV with the CMS experiment at the LHC. *Phys.Lett.*, B716:30–61, 2012. 4

[7] Peter W. Higgs. Broken symmetries, massless particles and gauge fields. *Phys.Lett.*, 12:132–133, 1964. 4

[8] Steven Weinberg. A Model of Leptons. *Phys.Rev.Lett.*, 19:1264–1266, 1967. 6

[9] Peter W. Higgs. Broken Symmetries and the Masses of Gauge Bosons. *Phys.Rev.Lett.*, 13:508–509, 1964. 6

[10] H. Georgi and S.L. Glashow. Unity of All Elementary Particle Forces. *Phys.Rev.Lett.*, 32:438–441, 1974. 7

[11] D.I. Kazakov. Beyond the standard model: In search of supersymmetry. pages 125–199, 2000. 7, 8, 10

[12] Howard E. Haber and Gordon L. Kane. The Search for Supersymmetry: Probing Physics Beyond the Standard Model. *Phys.Rept.*, 117:75–263, 1985. 8

[13] E. Komatsu et al. Five-Year Wilkinson Microwave Anisotropy Probe (WMAP) Observations: Cosmological Interpretation. *Astrophys.J.Suppl.*, 180:330–376, 2009. 9

[14] Stephen P. Martin. A Supersymmetry primer. 1997. 10

[15] N. et al. Brett. Black hole production at the LHC: the Discovery reach of the ATLAS experiment. pages 125–199, 2007-2008. 11

[16] G.C. Branco, P.M. Ferreira, L. Lavoura, M.N. Rebelo, Marc Sher, et al. Theory and phenomenology of two-Higgs-doublet models. *Phys.Rept.*, 516:1–102, 2012. 12

[17] *ATLAS Collaboration: technical proposal for a general-purpose pp experiment at the Large Hadron Collider at CERN*. LHC Tech. Proposal. CERN, Geneva, 1994. 12, 18, 235

[18] *CMS Collaboration: CMS, the Compact Muon Solenoid : technical proposal*. LHC Tech. Proposal. CERN, Geneva, 1994. 12, 19, 235

[19] J Beringer et al. Review of Particle Physics. *Journal of Physics G*, 33:1+, 2006. 12

[20] Thomas Sven Pettersson and P Lefèvre. The Large Hadron Collider: conceptual design. Technical Report CERN-AC-95-05 LHC, CERN, Geneva, Oct 1995. 13

[21] Lyndon Evans and Philip Bryant. LHC Machine. *JINST*, 3:S08001, 2008. 13, 16

[22] M.Lamont. The first years of LHC operation for luminosity production. *Proceedings IPAC2013, Session: MOYAB1 - 13 May 2013*. 17, 305

[23] Lhc experiments. *http://home.web.cern.ch/about/experiments*. 19, 20, 236, 285, 302

[24] *LHCb Collaboration: Technical proposal*. Tech. Proposal. CERN, Geneva, 1998. 20, 235

[25] *ALICE: Technical proposal for a Large Ion collider Experiment at the CERN LHC*. LHC Tech. Proposal. CERN, Geneva, 1995. 20, 235

[26] *TOTEM, Total Cross Section, Elastic Scattering and Diffraction Dissociation at the LHC: Technical Proposal*. Tech. Proposal. CERN, Geneva, 1999. 20, 235

[27] O. Adriani et al. The LHCf detector at the CERN Large Hadron Collider. *JINST*, 3:S08006, 2008. 20

[28] R. L. Gluckstern. Uncertainties in track momentum and direction, due to multiple scattering and measurement errors. *Nucl. Instrum. Meth.*, 24:381–389, 1963. 28, 29

[29] ATLAS inner detector: Technical design report. Vol. 1. 1997. 31

[30] G. Gorfine. Tracking performance of the ATLAS pixel detector in the 2004 Combined Test Beam. *Nucl.Instrum.Meth.*, A565:43–49, 2006. 32

[31] Norbert Wermes and G Hallewel. *ATLAS pixel detector: Technical Design Report*. Technical Design Report ATLAS. CERN, Geneva, 1998. 33

[32] A. Abdesselam, T. Akimoto, P.P. Allport, J. Alonso, B. Anderson, et al. The barrel modules of the ATLAS semiconductor tracker. *Nucl.Instrum.Meth.*, A568:642–671, 2006. 33

[33] W. Dabrowski, J. Kaplon, and R. Szczygiel. SCT128B: A prototype chip for binary readout of silicon strip detectors. *Nucl. Instrum. Meth.*, A421:303–315, 1999. 34

[34] F. Campabadal et al. Design and performance of the ABCD3TA ASIC for readout of silicon strip detectors in the ATLAS semiconductor tracker. *Nucl. Instrum. Meth.*, A552:292–328, 2005. 34

[35] A. Abdesselam et al. The ATLAS semiconductor tracker end-cap module. *Nucl.Instrum.Meth.*, A575:353–389, 2007. 34

[36] G. Aad et al. The ATLAS Experiment at the CERN Large Hadron Collider. *JINST*, 3:S08003, 2008. 37

[37] Academic training. *The LHC machine experiment interface. CERN, April, 2005*. 40, 287

[38] F. Gianotti, M.L. Mangano, T. Virdee, S. Abdullin, G. Azuelos, et al. Physics potential and experimental challenges of the LHC luminosity upgrade. *Eur.Phys.J.*, C39:293–333, 2005. 40, 41

[39] Collaboration ATLAS. Letter of Intent for the Phase-II Upgrade of the ATLAS Experiment. Technical Report CERN-LHCC-2012-022. LHCC-I-023, CERN, Geneva, Dec 2012. Draft version for comments. 41, 45, 47, 51, 54, 236

[40] J. Ellis. Particle physics at future colliders. 2002. ICFA Nanobeam Workshop, Lausanne, September 2002. 41

[41] G. Azuelos, D. Benchekroun, O. Cakir, E. Elfgren, F. Gianotti, et al. Impact of energy and luminosity upgrades at LHC on the physics program of ATLAS. *J.Phys.*, G28:2453–2474, 2002. 41

[42] Albert De Roeck, John R. Ellis, and Fabiola Gianotti. Physics motivations for future CERN accelerators. 2001. 41

[43] L Rossi and O Brüning. High Luminosity Large Hadron Collider A description for the European Strategy Preparatory Group. Technical Report CERN-ATS-2012-236, CERN, Geneva, Aug 2012. 41

[44] T Flick. Overview of the Insertable B-Layer (IBL) Project of the ATLAS Experiment at the Large Hadron Collider at CERN. Technical Report ATL-INDET-PROC-2013-006, CERN, Geneva, Jun 2013. 43

[45] Letter of Intent for the Phase-I Upgrade of the ATLAS Experiment. Technical Report CERN-LHCC-2011-012. LHCC-I-020, CERN, Geneva, Nov 2011. 44

[46] Mark S. Neubauer. A Fast Hardware Tracker for the ATLAS Trigger System. In *Particles and fields. Proceedings, Meeting of the Division of the American Physical Society, DPF 2011, Providence, USA, August 9-13, 2011*, 2011. 44

[47] Alfredo Ferrari, Paola R. Sala, Alberto Fasso, and Johannes Ranft. FLUKA: A multi-particle transport code (Program version 2005). 2005. 47

[48] P S Miyagawa and I Dawson. Radiation background studies for the Phase II inner tracker upgrade. Technical Report ATL-UPGRADE-PUB-2013-012, CERN, Geneva, Feb 2013. 47

[49] ATLAS Collaboration. Charged-particle multiplicities in pp interactions measured with the atlas detector at the lhc. *New Journal of Physics*, 13(5):053033, 2011. 48

[50] M Capeans, G Darbo, K Einsweiller, M Elsing, T Flick, M Garcia-Sciveres, C Gemme, H Pernegger, O Rohne, and R Vuillermet. ATLAS Insertable B-Layer Technical Design Report. Technical Report CERN-LHCC-2010-013. ATLAS-TDR-19, CERN, Geneva, Sep 2010. 49

[51] G Beck, T Jones, D Lynn, and G Viehhauser. Phase 2 LOI Backup Document: Thermo-mechanical Local Support - Barrel Stave. Technical Report ATL-UPGRADE-PUB-2013-010, CERN, Geneva, Feb 2013. 52, 53

[52] NP Hessey. Building a Stereo-angle into strip-sensors for the ATLAS-Upgrade Inner-Tracker Endcaps. Technical Report ATL-UPGRADE-PUB-2013-002, CERN, Geneva, Feb 2013. 56

[53] Y.P. Varshni. Temperature dependence of the energy gap in semiconductors. *Physica*, 34(1):149 – 154, 1967. 59

[54] S.M. Sze. *Physics of Semiconductor Devices*. Wiley-Interscience publication. 1981. 59, 64, 65, 69, 72

[55] Claude A. Klein. Bandgap dependence and related features of radiation ionization energies in semiconductors. *Journal of Applied Physics*, 39(4):2029–2038, 1968. 61, 288

[56] K Nakamura and Particle Data Group. Review of particle physics. *Journal of Physics G: Nuclear and Particle Physics*, 37(7A):075021, 2010. 60, 61

[57] International Commission of Radiation Units. *Stopping powers and ranges for protons and alpha particles*. icru report no. 49, 1993. 60

[58] L. Landau. On the energy loss of fast particles by ionization. *J. Phys.(USSR)*, 8:201–205, 1944. 62

[59] W.R. Leo. *Techniques for Nuclear and Particle Physics Experiments: A How-To Approach*. Springer-Verlag, 1987. 63

[60] G Lutz. *Semiconductor Radiation Detectors*. Springer-Verlag, 1999. 67

[61] Michael Moll. *Radiation damage in silicon particle detectors: Microscopic defects and macroscopic properties*. PhD thesis, Hamburg U., 1999. 71, 88, 89, 93, 94, 95, 188, 241, 290, 302

[62] H. Spieler. Semiconductor detector systems. *Oxford University press*, 2005. 72, 84

[63] K. Kano. *Semiconductor Devices*. Prentice Hall, 1998. 73, 242

[64] G. Casse, P.P. Allport, and A. Greenall. *Response to minimum ionising particles of p-type substrate silicon microstrip detectors irradiated with neutrons to LHC upgrade doses*. *Nucl. Instr. and Meth. A*, 581:318 – 321, 2007. 77, 91

[65] Y. Unno, T. Kohriki, T. Kondo, S. Terada, T. Ohsugi, Y. Iwata, R. Takashima, I. Nakano, K. Yamamura, and K. Yamamoto. Novel p-stop structure in n-side of silicon microstrip detector. *Nuclear Instruments and Methods in Physics Research Section A: Accelerators, Spectrometers, Detectors and Associated Equipment*, 541(1–2):40 – 46, 2005. 78

[66] G. Pellegrini, C. Fleta, F. Campabadal, S. Díez, M. Lozano, J.M. Rafí, and M. Ullán. Technology development of p-type microstrip detectors with radiation hard p-spray isolation. *Nuclear Instruments and Methods in Physics Research Section A: Accelerators, Spectrometers, Detectors and Associated Equipment*, 566(2):360 – 365, 2006. 79

[67] A. Peisert. *Silicon microstrip detectors*. volume Instrumentation on High Energy Physics. ed. F. Sauli, 1992. 82

[68] V.A.J. Van Lint. The physics of radiation damage in particle detectors. *Nuclear Instruments and Methods in Physics Research Section A: Accelerators, Spectrometers, Detectors and Associated Equipment*, 253(3):453 – 459, 1987. 85

[69] C. Kittel. *Introduction to Solid State Physics*, volume 8th Edition. John Wiley and Sons, 2005. 85

[70] J. W. Corbett and G. D. Watkins. Production of divacancies and vacancies by electron irradiation of silicon. *Phys. Rev.*, 138:A555–A560, Apr 1965. 85

[71] A. Vasilescu. The NIEL scaling hypothesis applied to neutron spectra of irradiation facilities in the ATLAS and CMS SCT . Technical Report ROSE/TN/97-2, CERN-RD48 Collaboration, 1997. 86

[72] E. Fretwurst M. Moll and G. Lindström. Leakage current of hadron irradiated silicon detectors – material dependence. *Nuclear Instruments and Methods in Physics Research Section A: Accelerators, Spectrometers, Detectors and Associated Equipment*, 426(1):87 – 93, 1999. 88

[73] R. Wunstorf. PhD thesis, Hamburg U. DESY, FHIK9201, 1992. 90, 243, 290, 302

[74] E. Fretwurst et al. Proceedings of the third international symposium on the development and application of semiconductor tracking detectors. *Melbourne*, 1997. 92, 243

[75] Adrian Driewer. *Messungen an planaren, bestrahlten Silizium-Streifendetektoren für den HL-LHC*. PhD thesis, Universitat Freiburg, 2011. 92, 188

[76] Georg Waadt. *Characterization of Radiation-hard Silicon Detectors for the ATLAS Experiment at the Large Hadron Collider (LHC)*. PhD thesis, Universitat Freiburg, 2015. 92, 188, 194, 299

[77] E. Fretwurst M. Moll and G. Lindström. Investigation on the improved radiation hardness of silicon detectors with high oxygen concentration. *Nuclear Instruments and Methods in Physics Research Section A: Accelerators, Spectrometers, Detectors and Associated Equipment*, 439(2–3):282 – 292, 2000. 92, 94, 244, 290, 303

[78] H.-J. Ziock et al. Temperature dependence of the radiation induced change of depletion voltage in silicon {PIN} detectors. *Nuclear Instruments and Methods in Physics Research Section A: Accelerators, Spectrometers, Detectors and Associated Equipment*, 342(1):96 – 104, 1994. 94

[79] E. Fretwurst et al. Reverse annealing of the effective impurity concentration and long term operational scenario for silicon detectors in future collider experiments. *Nuclear Instruments and Methods in Physics Research Section A: Accelerators, Spectrometers, Detectors and Associated Equipment*, 342(1):119 – 125, 1994. 94

[80] Semiconductor equipment and material international standards. http://www.semi.org/en/Standards/. 96

[81] J. E. García. *Probe++*. http://ific.uv.es/sct/activities/detectors/software, 2001. 100, 101, 290

[82] E Barberis, N Cartiglia, D Hutchinson, J Leslie, C Le Vier, J T Rahn, W Rowe, H F W Sadrozinski, K Yamamoto, K Yamamura, T Ohsugi, Y Unno, T Aso, H Miyata, and N Tamura. Measurement of interstrip and coupling capacitances of silicon microstrip detectors. Technical Report SCIPP-92-14, Calif. Univ. Santa Cruz. Inst. Part. Phys., Santa Cruz, CA, Oct 1992. 102

[83] A. Chilingarov. *IV and CV measurements in Si diodes*. RD50 Technical Note, 2004. 102

[84] Mercedes Miñano. *Irradiated Silicon Detectors for HL-LHC: Characterization and Simulations*. PhD thesis, Valencia U., 2012. Presented 18 Jul 2012. 106

[85] E.D. Palik. *Handbook of Optical Constants of Solids II*. Academic Press handbook series. Academic Press, 1991. 109

[86] I. Abt, S. Masciocchi, B. Moshous, T. Perschke, Rainer Helmut Richter, K. Riechmann, and W. Wagner. Characterization of silicon microstrip detectors using an infrared laser system. *Nucl. Instrum. Meth.*, A423:303–319, 1999. 109, 110, 292

[87] R. Marco. *Design, development and implementation of a readout system for microstrip silicon sensors. Upgrade for test beam measurements*. PhD Thesis, 2012. 112, 250

[88] S Lochner and M Schmelling. The Beetle Reference Manual - chip version 1.3, 1.4 and 1.5. Technical Report LHCb-2005-105. CERN-LHCb-2005-105, CERN, Geneva, Nov 2006. 113

[89] C. Lacasta. *Alibava-gui documentation (https://twiki.ific.uv.es/twiki/bin/view/Atlas/ALiBaVa)*, November, 2009. 114, 117

[90] Philips semiconductors. *The I2C-bus specification and user manual. Version 3.0*, UM10204 2007. 116

[91] R. Brun and F. Rademakers. ROOT: An object oriented data analysis framework. *Nucl. Instrum. Meth.*, A389:81–86, 1997. 117

[92] Glenn F. Knoll. *Radiation Detection and Measurement. Fourth Edition*. John Wiley & Sons, 2010. 118

[93] Web: http://www.ansys.com/. 129

[94] Bart Verlaat and Auke-Pieter Colijn. CO(2) cooling developments for HEP detectors. *PoS*, VERTEX2009:031, 2009. 130, 131, 294

[95] C. Lacasta. *Petal Design and Prototypes*, (Talk on the ATLAS Endcap Strips Upgrade Week), March 2010. 135, 294

[96] T.L. Bergman, F.P. Incropera, D.P. DeWitt, and A.S. Lavine. *Fundamentals of Heat and Mass Transfer*. Wiley, 2011. 136

[97] Afroditi Koutoulaki . *Petal Studies, latest update*, (Talk presented on the ITK Week), September 2016. 137, 306

[98] ASTM International (https://www.astm.org/). 140

[99] Hamamatsu photonics, *http://www.hamamatsu.com/*. 150, 246

[100] L. B. A. et al. Hommels. Detailed studies of full-size ATLAS12 sensors. *Nucl. Instrum. Meth.*, A831:167–173, 2016. 150, 158

[101] ATLAS Upgrade Strip Sensor Collaboration. *Supply of Silicon Microstrip Sensors of ATLAS12EC Specification*. Technical report, CERN, September 2015. 150, 306

[102] Y. Unno et al. *Development of $n^+ - in - p$ large-area silicon microstrip sensors for very high radiation enviroments. ATLAS12 design and initial results. Nuclear Instruments and Methods in Physics Research Section A: Accelerators, Spectrometers, Detectors and Associated Equipment*, 765:80 –

90, 2014. HSTD-9 2013 - Proceedings of the 9th International *Hiroshima* Symposium on Development and Application of Semiconductor Tracking Detectors. International Conference Center, Hiroshima, Japan, 2 - 5 September 2013. 150, 151, 153, 154, 295, 306

[103] A. Chilingarov. Temperature dependence of the current generated in si bulk. *Journal of Instrumentation*, 8(10):P10003, 2013. 162

[104] H. Bichsel. Straggling in Thin Silicon Detectors. *Rev. Mod. Phys.*, 60:663–699, 1988. 164, 250

[105] K. Hara et al. Charge collection and field profile studies of heavily irradiated strip sensors for the ATLAS Inner Tracker Upgrade . *Nuclear Instruments and Methods in Physics Research Section A: Accelerators, Spectrometers, Detectors and Associated Equipment*, 2016. 169, 170, 195, 196, 297, 300

[106] J. Jiménez. *Laboratory test of silicon microstrip detectors*, (Master's Thesis), 2013. 175, 180, 297, 298

[107] R. Mori et al. Evaluation of the performance of irradiated silicon strip sensors for the forward detector of the ATLAS Inner Tracker Upgrade . *Nuclear Instruments and Methods in Physics Research Section A: Accelerators, Spectrometers, Detectors and Associated Equipment*, 2016. 184

[108] F. Hartmann. *Evolution of Silicon Sensor Technology in Particle Physics*. Springer-Verlag, 2009. 187, 256, 299, 303

[109] D. Briglin, on behalf of the UK Irradiation Team . *Update of irradiation at Birmingham cyclotron*, (Talk on the ATLAS Upgrade Week), February 2016. 193, 195, 300

[110] Miguel Ullán et al. Sensors for the End-Cap Prototype of the Inner Tracker in the ATLAS Detector Upgrade . Technical Report ATL-COM-UPGRADE-2015-027, CERN, Geneva, Sep 2015. 205, 307

[111] Miguel Ullan, Victor Benitez, Giulio Pellegrini, Celeste Fleta, Manuel Lozano, Carlos Lacasta, Urmila Soldevila, and Carmen Garcia. Embedded pitch adapters for the ATLAS Tracker Upgrade. *Nucl. Instrum. Meth.*, A732:178–181, 2013. 218, 264

[112] M. Ullán et al. Embedded pitch adapters: A high-yield interconnection solution for strip sensors. *Nucl. Instrum. Meth.*, A831:221–228, 2016. 221, 226

[113] Carlos Garcia-Argos. The ATLAS ITk Strip Detector. Status of R&D. Technical Report ATL-UPGRADE-PROC-2016-001, CERN, Geneva, Mar 2016. 230

[114] P.P. Allport et al. Radiation tests of ATLAS full-sized n-in-n prototype detectors . *Nuclear Instruments and Methods in Physics Research Section A: Accelerators, Spectrometers, Detectors and Associated Equipment*, 418(1):110 – 119, 1998. 242

List of Figures

1.1 The fundamental matter particles of the Standard Model. 4

1.2 Running coupling constants of the three Standard Model interactions. It is shown the inverse of the three Standard Model couplings α_i with i =1, 2, and 3 for the U(1)Y, SU(2)L and SU(3)C symmetry groups respectively as a function of the sliding scale Q (in GeV) in left for the StandardModel and in right for the minimal supersymmetric extension of the StandardModel (*MSSM*). The gauge couplings meet almost exactly in one point, somewhere around 10^{16} GeV, usually referred to as the *GUT* scale (*Gran Unification Theory*). 8

2.1 Cross section of a LHC dipole magnet design showing its components . 16

2.2 Layout of the full CERN accelerator complex and locations of the four LHC experiments 18

2.3 Representation of the LHC ring with its detectors and all its services . . 19

2.4 Detectors deployed at the four LHC interaction points [23] 19

2.5 General view of the ATLAS detector (25 m in height and 44 m in length). The overall weight of the detector is approximately 7000 *tons* 22

2.6 Inside a magnetic field the trajectories of the particles are deflected due to the Lorentz force describing a helical path. 24

2.7 Three-dimensional view of the bare windings of the ATLAS magnet system: the central solenoid, the 8 coils of the barrel toroid and the 2×8 coils of the end-cap toroids. 24

2.8 Magnetic field (B) inside a solenoid. 25

2.9 Field lines inside a solenoidal magnetic field. 25

2.10 Schematic bird's eye view of the ATLAS central solenoid. 25

2.11 Schematic view of the ATLAS toroid magnet system design. It consists of two inserted end-cap toroids and a long barrel toroid that comprises eight separate cryostats. 26

2.12 Magnetic field (B) inside a toroid. 26

2.13 Field lines inside a toroidal magnetic field. 26

2.14 Simulation of the magnetic field lines generated by the magnet system. The magnet system provides an optimised magnetic field configuration for particle bending in the inner detector and the muon spectrometer. . . 27

2.15 Endcap toroid system inserted in ATLAS. It consists of eight flat coils assembled radially and symmetrically around the beam axis. The magnet system provides a peak field of 4.1 T. 28

2.16 Barrel toroid system inserted in ATLAS. It consists of eight flat coils assembled radially and symmetrically around the beam axis. The magnet system provides a peak field of 3.9 T. 28

2.17 The sagitta *s* of the curvature of the track is often measured on collider experiments. The precision of the sagitta measurement is a direct measure for the precision of the muon momentum *p*. 29

2.18 Sketch of two muon tracks bending under the presence of the ATLAS magnet system. 29

2.19 A sketch of the ATLAS Inner Detector, showing the various subdetectors 31

2.20 Drawing showing the sensors and structural elements traversed by a charged track of 10 GeV p_T in the barrel inner detector (η = 0.3). The track traverses successively the beryllium beam-pipe, the three cylindrical silicon-pixel layers with individual sensor elements of $50 \times 400\ \mu m^2$, the four cylindrical double layers (one axial and one with a stereo angle of 40 mrad) of barrel silicon-microstrip sensors (SCT) of pitch $80\ \mu m$, and approximately 36 axial straws of 4 mm diameter contained in the barrel transition-radiation tracker modules within their support structure 33

2.21 Drawing showing the sensors and structural elements traversed by two charged tracks of 10 GeV p_T in the end-cap inner detector (η = 1.4 and 2.2). The end-cap track at η = 1.4 traverses successively the beryllium beam-pipe, the three cylindrical silicon-pixel layers with individual sensor elements of $50 \times 400\ \mu\ m^2$, four of the disks with double layers (one radial and one with a stereo angle of 40 mrad) of end-cap silicon-microstrip sensors (SCT) of pitch $\sim 80\ \mu\, m$, and approximately 40 straws of 4 mm diameter contained in the end-cap transition radiation tracker wheels. In contrast, the end-cap track at η = 2.2 traverses successively the beryllium beam-pipe, only the first of the cylindrical silicon-pixel layers, two end-cap pixel disks and the last four disks of the end-cap SCT. The coverage of the end-cap TRT does not extend beyond $|\eta|$ = 2 34
2.22 A 3D model of the Pixel Detector and it's framework. 35
2.23 Schematic of the ATLAS inner detector 36
2.24 TRT barrel, just before SCT barrel insertion 36
2.25 Charge hadron fluence rates in the inner detector. 38
2.26 Total neutron fluence rates in the inner detector. 39
2.27 Higgs event: $H \rightarrow 2e\ 2\mu$. In the upper part a "clean" event is shown. In the picture below, the same event is shown with the expected background for LHC design luminosity (from [37]). 40
2.28 Cumulative luminosity versus day delivered to (green), and recorded by ATLAS (yellow) during stable beams and for pp collisions in 2011 (left) and 2012 (right). The delivered luminosity accounts for the luminosity delivered from the start of stable beams until the LHC requests ATLAS to turn the sensitive detector off to allow a beam dump or beam studies. Given is the luminosity as determined from counting rates measured by the luminosity detectors. These detectors have been calibrated with the use of the van-der-Meer beam-separation method, where the two beams are scanned against each other in the horizontal and vertical planes to measure their overlap function. 41
2.29 Mid-term planning for increasing luminosity at LHC 43
2.30 The baseline layout of the replacement tracker showing the active areas of silicon detectors arranged on cylinders and disks. 46
2.31 Channel occupancies (in percent) with 200 pile-up events. 46

2.32 *RZ-map* of the 1 MeV neutron equivalent fluence in the Inner Tracker region, normalised to $3000\ fb^{-1}$ of 14 TeV minimum bias events generated using PYTHIA8. 48

2.33 Amount of tracks expected in LHC (left) and HL-LHC (right) scenarios. . 48

2.34 The material in X_0 as a function of η for the Phase-II tracker layout. . . 49

2.35 Barrel stave (a) and Petal stave (b) components. The basic unit is a module. Each module is composed by a silicon sensor and a hybrid above. The hybrids are made by application specific front-end chips ("ABC130") mounted on kapton circuits. 51

2.36 (a) Drawing of a stave core. (b) Photo of a stave core with a kapton bus co-cured into facing. 52

2.37 Stave being end inserted onto five carbon fibre/peek brackets. 53

2.38 Arrangement of staves in barrels. Staves are tilted 10 degrees. 53

2.39 Exploded view of a Petal (left) and a fully populated Petal with sensors, bus cable and hybrids (right). 55

2.40 In the castellated layout the Petals are arranged on either side of a disk, with services on one ear only. 55

3.1 Band structures of (a) an insulator, (b) a semiconductor and (c) a conductor. 60

3.2 Ionization energy as a function of the band gap energy in different materials. Silicon has a band gap of 1.12 eV and an ionization energy of 3.6 eV. Picture taken from [55]. 61

3.3 Bethe-Bloch distribution for different elements. The minimum of the Bethe-Bloch function correspond to values of $\beta\gamma \sim 3$. 62

3.4 The extra levels in the band model created by the impurity atoms are shown for *n-type* and *p-type* silicon. In *n-type* material there are electron energy levels near the top of the band gap so that they can be easily excited into the conduction band. In *p-type* material, extra holes energy levels in the bandgap allow excitation of valence band electrons, leaving mobile holes in the valence band. 65

3.5 Interface region of a pn-junction, each subdiagram shows a variable as a function of distance with $x = 0$ just in the junction. (a) P-type and n-type silicon. (b) Free charge carriers concentration with N_a holes in the p-type side and N_d electrons in the n-type one; note the depletion of carriers in the depletion region. (c) Fixed space charge density. (d) Electric field, E. (e) Electric potential, ϕ. 68

3.6 Applying an external potential to the pn junction the electron-hole pairs created by passing an ionizing particle through the material are moved rapidly and the dimension of the depletion region is therefore enlarged. 69

3.7 Ideal current-voltage characteristics of a pn-junction. The forward and the reverse bias regions can be distinguised. In the case of silicon tracker detectors the sensors operate in the reverse bias region where the total current density is very low. 70

3.8 Schematic view of a silicon microstrip detector. The bulk is p-type silicon and the electrodes are n^+ implants. Holes drift towards the p^+ back-plane, while electrons towards the n^+ implants. An insulator (SiO_2) is used to protect the silicon of the wafer. The strips are connected to the readout electronics through an aluminum layer. With this configuration electrons are registered by the readout. 75

3.9 Drawings of two p-on-n silicon microstrip sensors. The bulk sensor is n-type while the strip implants are p^+ doped silicon. The AC configuration uses a SiO_2 layer as a capacitor between the aluminium traces and the implants (left) while the DC uses a direct connection between them (right). 76

3.10 Sketch of an n-on-n silicon microstrip sensor. The bulk sensor is n-type while the strip implants are n^+ doped silicon. The pn junction is created at the backplane with a p^+ implant. 77

3.11 Schematic transversal view of a n^+p silicon sensor. The bulk is p-type silicon and the electrodes are n^+ implants. As in figure 3.8 SiO_2 is used to protect the silicon of the wafer and an aluminium layer is used to connect the strips to the readout electronics. With this configuration electrons are registered by the readout. 78

3.12 *P-stop* isolation technique for adjacent n^+ implants. The maximum field regions are located at the lateral pn-junctions. High dose of p^+ boron implant is used. 78

3.13 *P-spray* isolation technique for adjacent n^+ implants. The maximum field regions are located at the lateral pn-junctions. Low dose of p^+ boron implant is used. 79
3.14 Microscope view of a silicon microstrip detector. There are pointed the strips, the bias resistance, the bias line and the guard rings. 81
3.15 Block-diagram of a typical front-end circuit. 83
3.16 Schematic diagram of some defects in a silicon crystal lattice. 85
3.17 Deep defect levels acting as generation centres. On the left the defect level generates a electron-hole pair. On the right the electron in the valence band is promoted to the conduction band by a deep level. . . . 88
3.18 Scaling of the leakage current with the equivalent fluence. The leakage current presents a linear dependence with the fluence. The parametrization constant corresponds to the damage constant α. Image from [61]. . . . 89
3.19 Variation of the depletion voltage with the absolute effective doping concentration versus the normalized fluence [73]. 90
3.20 Deep defect levels acting as traps for charge carriers. When the charge carrier is held is not mobile and stayed trapped. At some later time the electron (hole) is released to the conduction (valence) band. 91
3.21 Annealing (for n-type substrates) of the irradiation-induced changes of ΔN_{eff} at 60°C after irradiation with a fluence of 1.4 $\times 10^{13}$ $n_{eq}cm^{-2}$ [77]. 92
3.22 Panoramic view of the clean room facility at *IFIC*. 96
3.23 Probe station inside a Faraday cage used for IV and CV measurements in a clean room. A zoom to the needle and a microscope image can also be seen. 98
3.24 Sketch of the IV measurement system used on a $n^+ - p$ sensor. The power supply and the metal chuck can also be distinguised. 98
3.25 Typical IV curves obtained during irradiated sensor measurements. Sensor $W639$-EC-SP-E-$P18$ presents normal behaviour with low and constant leakage current. Sensor $W609$-EC-SP-C-$P17$ shows increasing leakage current with the bias voltage and breakdown around 900 V. . . 99
3.26 Detail of the thermal chuck used inside the Faraday cage in the case of irradiated sensors where dry air and chiller tubes can be distinguised. . 100
3.27 Example of the IV measurements with the data adquisition system used (*Probe++*) [81]. 101

3.28 Sketch of the CV measurement system used. 101
3.29 Equivalent diagram of a $p-type$ silicon microstrip sensor. The strip detector can be treated as an extended network of resistors and capacitors.102
3.30 Frequency study to determine the proper value where the capacitance remains almost independent on the applied voltage (top). Zoom of the results obtained for the frequency analysis (bottom). A frequency value of $30\ KHz$ will be used in all the CV tests unless explicitly mentioned otherwise. 103
3.31 Full depletion voltage extracted from a typical Capacitance-Voltage curve in a silicon microstrip sensor. The inverse of the square of the capacitance is plotted versus the bias voltage of the sensor. 104
3.32 β source setup used for charge collection measurements (left). The source is placed above the silicon microstrip sensor. Below the detector two photomultipliers (right) are placed to provide external trigger. 105
3.33 Scheme of the complete radioactive source setup. 106
3.34 Typical charge-voltage curve obtained with a not irradiated barrel sensor using the beta setup. 106
3.35 Charge collection measurement system placed inside a vertical freezer for measuring irradiated sensors. The temperature is maintained to $-35°C$. 107
3.36 Motion controller (Newport MM4005) included in the laser setup. It controls three high-precision stages that move the laser in the perpendicular direction to the strips (X), along the strip (Y) and near/far from the strips (Z). This motion controller includes a GPIB interface and can be controlled from the PC or manually. 108
3.37 Thermal base made of aluminium to be used during laser measurements on irradiated sensors. Coolant liquid from a chiller machine circulates inside the base. A support for a dry air tube is included to avoid condensation over the sensor. 109
3.38 Sketch of the thermal base shown in figure 3.37. The coolant liquid circulates through a cooling coil. The aluminium parts are depicted in grey color. To contain the liquid two viton gaskets are used (pieces in black color). 109

3.39 Dependence of the light penetration depth in silicon as a function of the wavelength. Picture taken from [86]. 110

3.40 Laser cluster width as a function of the distance between laser and sensor surface. The distance at the minimum width is considered to be the proper focus. 111

3.41 Sketch of the signal as seen in a given channel during a laser scan. The picture also shows the parameters of the function fit. 111

3.42 Signal per channel obtained in a laser scan with a selected sensor region (around $8\ mm$). The color bar on the right represents the amount of charge in ADC counts. 112

3.43 Projection of the data obtained in 3.42 in the direction of the laser movement (X direction). All the strips show similar distribution and amount of charge achieved (around 300 ADC counts) 113

3.44 Block diagram of the ALiBaVa system with its different components. . . 114

3.45 ALiBaVa software main window. 114

3.46 Examples of a Landau distribution (a), and a Landau convoluted with a Gaussian distribution (b). 115

3.47 Time profile obtained for a $p-type$ microstrip silicon sensor biased to 1000V. The average of the collected charge (in ADC counts) as a function of the TDC measurement (in ns) is plotted. 116

3.48 Charge calibration scan to get gain and offset. 116

3.49 Pedestals level (ADC counts) versus the channel number (left) and noise level (ADC counts) versus the channel number (right). The noise value showed is computed as the RMS (Root Mean Square) of the pedestal distribution. 117

3.50 Spectrum of the signal acquired with a time cut between 13 ns and 23 ns. The number of events as a function of the absolute value of the collected charge (in ADC counts) is represented. 118

3.51 Collected charge usig the ALiBaVa system versus the bias voltage for a microstrip $p-type$ sensor. 119

4.1 Machining of the POCO foam (left) and the resulting piece (right). The modelling of the base material piece goes first with a roughing down using a handsaw and then with a milling process. A custom-made milling cutter of circular cut is needed to mechanize the internal radius of contact with the pipes. 122
4.2 Tool used to bend the pipe using two guide discs, one to check the length and the final diameter and the other to correct the opening angle to the final measurement. 122
4.3 Aluminum platform used to glue the POCO foam and the pipes. 123
4.4 POCO foam and stainless steel pipes glued with CGL adhesive. 123
4.5 Honeycomb with final dimensions placed over honeycomb plate. 123
4.6 Handle attached to the aluminum base in order to manage the honeycomb structure easily. 124
4.7 Tool used to control the height of the glue deposited on the POCO foam in the process of gluing to the carbon facing. 124
4.8 The foam is positioned on the facing using the aluminum sheets as guide (left) and then the central aluminum sheet is also placed (right). . 124
4.9 First carbon facing finally glued to the POCO foam and pipes. 125
4.10 Second carbon facing placed on the vacuum base. 125
4.11 Polythene sheet with isolating tape which create a facing mould. This structure is used to contain the glue where the honeycomb will be immersed. 126
4.12 Once the closeouts are covered with epoxy they are placed on the facings of the Petal. 126
4.13 A thermal blanket is used to avoid any curvature in the honeycomb. A heat-resistant and anti-adhesive plastic is put between the honeycomb and the thermal blanket. 127
4.14 The honeycomb is positioned close to the vacuum base. 127
4.15 Honeycomb plate assembled to the vacuum base. 127
4.16 Petal core finished and ready for mechanical tests. 128
4.17 Myself holding the two Petal cores at *IFIC*. 129

4.18 Petal core thermal *FEA* model. The temperature distribution on the Petal surface for a nominal temperature of the coolant (-30°C) is shown. For this simulation the air temperature was set to $T^{air} = 20°$C and the heat transfer coefficient to $h = 5\ W/(m^2K)$. 130
4.19 Petal CO_2 cooling system based on the open system developed by *NIKHEF* [94]. 130
4.20 Metal support used to fix the Petal to the methacrylate box. 131
4.21 Setup used for the thermo-mechanical tests. 131
4.22 Diagram of the different sensor locations along the Petal surface. The *PT100*'s are labeled as CH_i and B_i. The capacitive sensors are labeled as S_i. 132
4.23 Mollier diagram for CO_2. Isothermal lines are shown as a function of the pressure and the enthalpy. 132
4.24 Variation of the temperature on the Petal surface registered by the *PT100* sensors as a function of the CO_2 input temperature. 133
4.25 Temperature distribution on the Petal surface at 10 bar of CO_2 pressure as seen with the IR camera. Thermal uniformity is achieved along the cooling pipes. Note that the values are not corrected for emissivity. . . . 134
4.26 Minimum temperature along the pipe at 10 bar of CO_2 pressure registered by the *IR* image. Values corresponding to figure 4.25 and corrected using carbon fibre emissivity. 134
4.27 Highest temperature on silicon sensor as a function of its power. Coolant temperature of -30 °C (-27 °C in the return pipe). Considering a chip power around 0.3 $W/chip$, below -20 °C no thermal runaway is present [95]. 135
4.28 Heat transfer of a system composed by different materials. 136
4.29 Petal materials considered to obtain the silicon temperature. 137
4.30 Deflections and strains obtained with the *FEA* model for the Petal structure. 138
4.31 Strain gauge detail for measuring longitudinal strain on the bottom face of the Petal (left) and measuring process of the deflection on the top face of the Petal with a vision machine 139
4.32 Plots of deflections (top) and strains (bottom) for the Petal prototype. . . 140
4.33 Maximum deflections (normalized to maximum load and distance) (δ/PL) as a function of the square of the distance (L^2). 141

4.34 Longitudinal strains on the Petal measured with the gauge. 142
4.35 Transversal deflections measured by the capacitive sensors. 142
4.36 Optical system used to measure the surface of the Petal 145
4.37 Petal surfaces as measured by the optical system. Left column shows the *3D* representation and the right column the projection on the *Z-X* plane. 146
4.38 Coordinate measuring machine with a touch trigger probe where we measured the Petal in a "flag-like" configuration. 147
4.39 Petal measurements on the CMM with touch probe and 4 high stiffness constrains. 148
4.40 Results with 2 high stiffness constrains on the wide side and 2 low stiffness constrains in the narrow side of the Petal. 149
4.41 Plot combining the data points from the front and back sides of the Petal. The points come from the CMM and are all referred to the front side plane. 149
4.42 Mask layout of the ATLAS12A sensor in 6-in. wafer. The miniature sensors are labeled with the position numbers 1-24 and the $8 \times 8mm^2$ diodes as P1-P4 [102]. 151
4.43 "Square" trapezoid sensor design with orphan strips (in red) near the sensor edges. These orphan strips do not reach the bonding pads. A proposed solution was to gang these *orphan strips* to the neighbouring ones. 152
4.44 Possible solutions for connecting the *orphan strips*. *AC-ganging* connection (left) is made to the AC readout metals and *DC-ganging* (right) is made between the strip implants. 152
4.45 (Left) Picture of an ATLAS12A sensor with "square" design. In this sensor the strips are not parallel to the sensor edges and *orphan strips* appear. (Right) Picture of an ATLAS12A sensor with "skewed" design. In this case the strips are parallel to sensor edges and the perimeter has circular shape. 153
4.46 Leakage current as a function of the bias voltage measured with the probe station for the not irradiated sensors. No breakdown voltage was registered below 600 V. 157

4.47 Capacitance as a function of the bias voltage measured with the probe station for the not irradiated sensors. Plotted as $1/C^2$. Full depletion voltage achieved around 350 V. 157
4.48 Leakage current as a function of the bias voltage measured with the probe station for the neutron (top) and proton (bottom) irradiated sensors. A thermal chuck was used to maintain the sensors cold enough during measurements. No breakdown voltage was registered below 600 V. . . 159
4.49 Capacitance as a function of the bias voltage measured with the probe station for the neutron (top) and proton (bottom) irradiated sensors. Plotted as $1/C^2$. 160
4.50 $I-V$ results for two different irradiated sensors (one with neutron irradiation an the other with proton irradiation). 160
4.51 $C-V$ results for two different irradiated sensors (one with neutron irradiation an the other with proton irradiation). 161
4.52 Leakage current as a function of the fluence for neutron irradiated sensors. An increase in the fluence affects directly to the leakage current of a sensor. 161
4.53 Leakage current as a function of the fluence for proton irradiated sensors. An increase in the fluence affects directly to the leakage current of a sensor. 162
4.54 Charge Collection of a not irradiated barrel sensor. The curve is fitted to a function defined by 4.16. Parameters $p0$ and $p1$ indicate the full depletion voltage and the collected charge on average respectively. . . 164
4.55 Collected charge resistered for the three not irradiated sensors. The full depletion voltage is around 370 V which is close to the value extracted from the $C-V$ curve. All the sensors collected a charge above 21 ke^- at full depletion. 165
4.56 Collected charge measured for the irradiated sensors (irradiated with proton, neutron and gamma particles). The not irradiated sensor results are also included as reference. 167
4.57 Charge collection as a function of the fluence for neutron irradiated sensors. 168
4.58 Charge collection as a function of the fluence for proton irradiated sensors. 168

4.59 Summary of the collected charge measurements for the neutron irradiated ATLAS12A sensors by the seven groups involved. These results were published at [105]. 169

4.60 Summary of the collected charge measurements for the proton irradiated ATLAS12A sensors by the seven groups involved. These results were published at [105]. 170

4.61 Signal amplitude (in ADC counts) as a function of the laser position (direction perpendicular to the strips) for two not irradiated microstrip sensors. Measurements taken at 200 V for sensor $W628$-$BZ3C$-$P15$ and 400 V for sensor $W634$-EC-LP-C-$P19$. 171

4.62 Signal amplitude (in ADC counts) as a function of the laser position (X direction) for three consecutive strips of two not irradiated microstrip sensors. Measurements taken at 200 V for sensor $W628$-$BZ3C$-$P15$ (top) and 400 V for sensor $W634$-EC-LP-C-$P19$ (bottom). 172

4.63 Signal amplitude (in ADC counts) as a function of the laser position (in the direction perpendicular to the strips) for the border strips of sensor $W628$-$BZ3C$-$P15$ (left and right respectively). Measurements taken at 200 V. 173

4.64 Signal amplitude (in ADC counts) as a function of the laser position (X direction) for the border strips of sensor $W634$-EC-LP-C-$P19$ (left and right respectively). The last strip of the right border (red strip) appears in two different X positions and with less collected charge. This is due to the DC ganging of the sensor (see section 4.4.3.2). Measurements taken at 400 V 173

4.65 Signal amplitude (in ADC counts) and laser position as a function of the channel number for sensor $W628$-$BZ3C$-$P15$ (not irradiated). Measurements taken at 200 V. 174

4.66 Signal amplitude (in ADC counts) and laser position as a function of the channel number for sensor $W634$-EC-LP-C-$P19$ (not irradiated). Measurements taken at 400 V 174

4.67 Charge sharing between channels 67, 68 and 69 of barrel mini sensor $W628$-$BZ3C$-$P15$. Measurements taken at 200 V. *Root* macro taken from [106]. 175

4.68 Amplitude signal as a function of the laser position for sensor $W616$-$BZ3C$-$P04$. Measurements taken at 150 V and 22 °C. 176
4.69 Amplitude signal as a function of the laser position for sensor $W626$-$BZ3C$-$P02$. Measurements taken at 150 V and 22 °C. 177
4.70 Signal amplitud versus laser position for sensor $W628$-EC-SP-E-$P10$. Sensor irradiated with protons at 5×10^{14} n_{eq}/cm^2. Measurements taken at 200 V and -8°C. Good laser signal uniformity and strip integrity. The laser focusing was properly set and the aluminium reflection can be seen clearly. 178
4.71 Signal amplitud versus laser position for sensor $W645$-EC-LP-E-$P20$. Sensor irradiated with protons at 5×10^{14} n_{eq}/cm^2. Measurements taken at 300 V and -8°C. Low aluminium reflection due to poor laser focusing. Nevertheless, good laser signal uniformity and strip integrity. 178
4.72 Signal amplitud versus laser position for sensor $W782$-EC-SP-C-$P07$. Sensor irradiated with protons at 1×10^{15} n_{eq}/cm^2. Measurements taken at 150 V and -10°C. Good laser signal uniformity and strip integrity. Last strip appeared doubled (green) and with lower amplitude due to AC ganging (see 4.4.3.2). 179
4.73 Signal amplitud versus laser position for sensor $W782$-EC-SP-C-$P17$. Sensor irradiated with protons at 1×10^{15} n_{eq}/cm^2. Measurements taken at 100 V and -8°C. Good laser signal uniformity and strip integrity. Last strip appeared doubled (green) and with lower amplitude due to DC ganging (see 4.4.3.2). 179
4.74 Charge sharing between channels 123, 124 and 125 of an end-cap irradiated mini sensor ($W782$-EC-SP-C-$P07$). Measurements taken at 100 V. *Root* macro taken from [106]. 180
4.75 Laser movement over sensor $W782$-EC-SP-C-$P17$ (DC-gang) with channel numbers also drawn (left). Signal amplitude as function of the laser position (right). 181
4.76 Signal coupling from channel 128. The strip signal appears also in channel position *127-gang*. 182
4.77 Laser position as a function of the channel number and the collected charge for sensor $W782$-EC-SP-C-$P17$ (DC-gang). Measurements taken at 100 V. 183

4.78 Laser movement over sensor $W782$-EC-SP-C-$P07$ (AC-gang) with channel numbers also drawn (left). Signal amplitude as function of the laser position (right). 183
4.79 Laser position as a function of the channel number and the collected charge for sensor $W782$-EC-SP-C-$P07$ (AC-gang). Measurements taken at 150 V. 184
4.80 Comparison of signal amplitude as a function of the laser position results for DC-ganging sensors measured at *IFIC* (top) and *Freiburg* (bottom) institutes. 185
4.81 Comparison of signal amplitude as a function of the laser position results for AC-ganging sensors measured at *IFIC* (top) and *Freiburg* (bottom) institutes. 186
4.82 Behaviour of trapping for holes and electrons as a function of the annealing time. Picture extracted from [108]. 187
4.83 Climate chamber used for annealing procedure. The temperature and the humidity can be selected. 189
4.84 Charge collection as a function of the bias voltage at different annealing times (top). Charge collection for two selected bias voltages as a function of the annealing time (bottom). 190
4.85 Charge collection as a function of the bias voltage at different annealing times (top). Charge collection for three selected bias voltages as a function of the annealing time (bottom). 191
4.86 Charge collection as a function of the bias voltage at different annealing times (top). Charge collection for two selected bias voltages as a function of the annealing time (bottom). 192
4.87 Charge collection as a function of the bias voltage at different annealing times (top). Charge collection for two selected bias voltages as a function of the annealing time (bottom). 193
4.88 Signal spectrum at 700 V for sensors $W609$-EC-SP-E-$P08$ (left) and $W648$-EC-SP-E-$P18$ (right). In both cases the signal is almost covered by noise and it is difficult to distinguised. 194
4.89 Reconstructed pulse shape of a Birmingham irradiated sensor with a fluence of $1\times10^{15}\ n_{eq}/cm^{-2}$ tested at *Freiburg University*. Picture taken from [76]. 194

4.90 Signal distribution registered with ALiBaVa system at 1000 V for an irradiated sensor from Birmingham. Two channel regions are clearly detecting more signal. 195
4.91 Sensors attached to frame with threads. They protected the sensors from irradiation and this caused non-uniformity of the applied dose during the procedure. This results in high charge collection on different sensor regions [109]. 195
4.92 Comparison of obtained results in terms of charge collection as a function of the annealing time at *IFIC* (top) and the ones published at [105] (bottom). 196

5.1 Each Petal face has 6 different module shapes (R_i). Each module can hold one or two sensors (S_0, S_1) and one or two of hybrids (H_0, H_1), with a total of 9 different sensors and 13 different hybrids per Petal face. 199
5.2 The central region of the Petal is selected to be built as Petalet. 200
5.3 Schematic view of a Petalet with all its components and dimensions. . . 200
5.4 Petalet core based on the Petal core design. Titanium pipes surrounded by carbon foam are used to provide cooling. Stifness is achieved filling the empty space with honeycomb made of carbon fibre (left). The surface is covered by two carbon facings (right). 201
5.5 The maximum bonding angle possible is limited by the size of the smallest bonding pad size. 202
5.6 Maximum bonding angle calculation. A strip pitch of 100 μm leads to 40 $^\circ$ of bonding angle. 202
5.7 Petalet big sensor wafer with standard pads (left) and with embedded pitch adaptors in a second metal layer (right). Miniature sensors for testing purposes are also included in both wafers. 202
5.8 Detailed view of the embedded pitch adaptors design (left) and a microscope view where the wire bonds can also be appreciated (right). 204
5.9 Scheme of cross-talk and pick-up effects. Cross-talk can appear between the first and the second metal layers. However, pick-up is a coupling effect between the second metal layer and the silicon bulk. 204
5.10 Standard and embedded pitch adaptors scheme distribution in a Petalet big sensor. 205
5.11 I-V curves obtained for the Petalet miniature sensors. 207

5.12 C-V curves obtained for the Petalet miniature sensors. 208
5.13 Histogram of the full depletion voltages obtained with the Petalet miniature sensors. The average value is also included. 209
5.14 I-V curves obtained for the full-size big sensor manufactured by *CNM*. . 210
5.15 C-V curves obtained for the full-size big sensor manufactured by *CNM*. 210
5.16 I-V curves obtained for the full-size top right sensor manufactured by *CNM*. 211
5.17 C-V curves obtained for the full-size top right sensor manufactured by *CNM*. 212
5.18 I-V curves obtained for the full-size top left sensor manufactured by *CNM*.213
5.19 C-V curves obtained for the full-size top left sensor manufactured by *CNM*. 213
5.20 Histogram of the depletion voltage values obtained with the full size Big sensors. The depletion voltage average is also included. 215
5.21 Histogram of the depletion voltage values obtained with the full size Top Right and Top Left sensors. The depletion voltage average is also included. 215
5.22 Collected charge as a function of the bias voltage for Petalet mini sensors.217
5.23 Collected charge as a function of the bias voltage for Petalet top right sensor. The wire bonding was stablished using the embedded pitch adaptors. 217
5.24 Scheme of laser movement (left) and example of obtained results (right) after a laser scan along X direction on sensor SP-6214-$W01$. Each color corresponds to the signal registered by each channel. 219
5.25 Scheme of laser movement (left) and example of obtained results (right) after a laser scan along X direction on sensor SP-6271-$W06$. All the strips presented signal uniformity and no presence of *cross-talk* was registered. 219
5.26 Scheme of sensor region under study and laser movement (left). Laser signal degradation due to high number of metal bands where the laser reflects (right). 220
5.27 Signal amplitude as a function of the laser position. *Pick-up* effect is detected between channels 250, 251 and 256. 220

5.28 Connections sketch of the strips and the *PA*s of channels under study. *pick-up* effect is detected between channels 250, 251 and 256. 221

5.29 *Split readout* configuration scheme where two hybrids are used for sensors (one hybrid for the lower and one hybrid for the two upper sensors). Data and power lines are separated in two different sides (right and left) in this configuration. 222

5.30 *Common readout* configuration scheme where three hybrids are used for sensors (one hybrid for the lower and two hybrids for the two upper sensors). With this configuration data and power lines are built in the same side of Petalet bus cable. 223

5.31 Channel occupancy as a function of the threshold for three different charge values. The threshold value where the occupancy is the 50 % is known as V_{th50} parameter. 224

5.32 V_{th50} threshold values as a function of the injected charge. 224

5.33 Input noise (top) and gain (bottom) as a function of the channel number for a lower module of a *Common readout* Petalet. 225

5.34 Input noise as a function of the channel number for standard (top) and embedded (bottom) modules. 226

6.1 Detectores localizados en los cuatro puntos de colisión del *LHC* [23] . . 236

6.2 Diseño base del futuro sistema de trazas en el que se muestran las áreas activas de los sensores dispuestos en cilindros y discos. 237

6.3 Componentes del *Stave* del barril (a) y los Pétalos (b). 238

6.4 Esquema de los materiales que componen un Pétalo (izquierda) y dibujo de todos sus componenetes externos (sensores, cable *bus* e híbridos) (derecha). 238

6.5 Esquema de un sensor de *microstrip*. El *bulk* es de tipo p y los electrodos son implantes n^+. 240

6.6 Dependencia de la corriente de fugas con la dosis de irradiación equivalente. Imagen extraída de [61]. 241

6.7 Variación del voltaje de desertización con la concentración efectiva de dopantes en función de la dosis normalizada [73]. 243

6.8 Comportamiento típico de *annealing* (en detectores tipo n) de cambios en la concentración efectiva de dopantes debido a los defectos introducidos por la radiación. Temperatura de 60°C después de irradiación a una dosis de 1.4 $\times 10^{13}\ n_{eq}cm^{-2}$ [77]. 244
6.9 Diseño de un sensor con forma de trapezoide cuadrado con los *strips* huérfanos en los laterales. 246
6.10 Soluciones posibles para conectar los *strips* huérfanos a sus vecinos. Conexión *AC* que se realiza entre los *strips* de aluminio del *readout* (izquierda) o conexión *DC* que se realiza entre los implantes. 247
6.11 Corriente de fugas en función del voltaje aplicado medido con la caja de puntas para los detectores no irradiados. No existe ruptura por debajo de los 600 V. 248
6.12 Capacidad en función del voltaje aplicado medido en la caja de puntas para los detectores no irradiados dibujado como $1/C^2$. El voltaje de desertización completa se alcanza sobre los 350 V. 249
6.13 Carga recolectada medida para tres detectores no irradiados. El voltaje de desertización completa se encuentra en torno a los 370 V, valor próximo al extraído de las curvas $C-V$. Todos los detectores recolectan carga por encima de los 21 ke^-. 250
6.14 Carga recolectada para los sensores irradiados (con protones, neutrones y pratículas gamma). El resultado para el sensor no irradiado es también incluído como referencia. 252
6.15 Amplitud de la señal (en cuentas de ADC) en función de la posición del láser para tres *strips* consecutivos de dos sensores no irradiados. . . . 253
6.16 Amplitud de la señal (en cuentas de ADC) en función de la posición del láser para tres *strips* consecutivos de dos sensores no irradiados. . . . 254
6.17 Amplitud de la señal (en cuentas de ADC) en función de la posición del láser para el sensor $W626$-$BZ3C$-$P02$. 254
6.18 Amplitud de la señal en función de la posición del láser para dos detectores irradiados con *DC-ganging* (izquierda) y *AC-ganging* (derecha). 255
6.19 Comportamiento de las trampas en agujeros y electrones en función del tiempo de *annealing*. Figura extraída de [108]. 256
6.20 Carga recolectada en función del tiempo de *annealing*. 257
6.21 Carga recolectada en función del tiempo de *annealing*. 258

6.22 Región central del Pétalo seleccionada para construir el Petalet. 259
6.23 Curvas I-V (izquierda) y C-V (derecha) obtenidas para los sensores miniatura. 260
6.24 Curvas I-V (izquierda) y C-V (derecha) obtenidas para los detectores de tamaño real tipo *big*. 261
6.25 Curvas I-V (izquierda) y C-V (derecha) obtenidas para los detectores de tamaño real tipo *top-right*. 262
6.26 Curvas I-V (izquierda) y C-V (derecha) obtenidas para los detectores de tamaño real tipo *top-left*. 263
6.27 Carga recolecctada en función del voltaje aplicado en los sensores miniatura del Petalet. 263
6.28 Amplitud de la señal en función de la posición del láser. El efecto de *pick-up* es detectado entre los canales 250, 251 y 256. 264
6.29 Ocupancia de canales en fución del umbral para tres valores de carga diferentes. El valor umbral en el que la ocupancia es del 50 % se conoce como paránetro V_{th50}. 266
6.30 Ruido de entrada (arriba) y ganancia (abajo) en función del número de canal para un módulo *lower* en la configuración *Common readout*. . . . 266

List of Tables

2.1 LHC general parameters at the high luminosity of 10^{34} cm^{-2} s^{-1} 14
2.2 Design accelerator parameters of the LHC collider 17
2.3 LHC parameters for proton-proton collisions for nominal design and for 2010 and 2011 runs at 7 TeV and 2012 runs at 8 TeV. Source:[22] . . . 17
2.4 Main parameters of the CMS and ATLAS magnet systems. CMS uses strong solenoidal magnets on a compact structure while ATLAS combines lighter solenoidal and toroidal magnetic fields in an open structure. . . . 30
2.5 Summary of the expected combined and stand-alone performance at two typical pseudorapidity values (averaged over azimutal) of the CMS and ATLAS experiments. 30
2.6 Main parameters of the Inner Detector 32
2.7 Design accelerator parameters of the HL-LHC collider 42
2.8 Inner tracker active area and channel count. 50
2.9 Performance of the existing ID with IBL, and of the Phase-II tracker for transverse momentum and impact parameter resolution. $\sigma_x(\infty)$ refers to σ_x for $p_T \to \infty$, to remove the contribution due to material. 50
2.10 Summary of the number of rows of strips and hybrids per sensor. Each hybrid is designed to read out one pair of strip rows. 57

3.1 Relevant properties of silicon at room temperature. 61
3.2 Mobilities for electrons and holes at $300\ K$ for silicon and germanium materials. 65
3.3 General features of the laser used in the setup. 110

4.1 Major differences between the Petal prototypes built at Berkley. 128
4.2 Average obtained values of temperature along the Petal measured with the *PT100* sensors and the *IR* camera for different CO_2 pressures. . . . 135

4.3 Properties of Petal materials from coolant to CO_2. Values taken from [97]. . . . 137
4.4 Results acquired with thermo-mechanical *FEA* simulations on Petal prototype. 139
4.5 Deflections and strains obtained for different applied loads on the Petal prototype. . . . 140
4.6 Results for the deflections and longitudinal strains on the Petal. . . . 143
4.7 Comparison of the mechanical results obtained for the *FEA* simulation and the laboratory tests. . . . 143
4.8 Comparison of the thermal results obtained for the *FEA* simulation and the laboratory tests. . . . 144
4.9 Hamamatsu ATLAS12A large-area silicon microstrip sensor technical specifications. Values taken from [101] and [102]. . . . 150
4.10 Principal parameters of the “square” trapezoid design for small and large pitch sensors [102]. . . . 153
4.11 Principal parameters of the “skewed” trapezoid design [102]. . . . 154
4.12 Hamamatsu sensor inventory with the different not irradiated sensors tested in this thesis. . . . 155
4.13 Hamamatsu sensor inventory with the different irradiated sensors tested in this thesis. . . . 156
4.14 Parameters used during $I-V$ and $C-V$ curves measurements with not irradiated sensors. . . . 156
4.15 Parameters used during $I-V$ and $C-V$ curves measurements with irradiated sensors. . . . 158
4.16 Alpha factors calculated from neutron and proton iradiated sensors results. The theoretical value is also listed. . . . 162
4.17 Summary of the results obtained from the $I-V$ and $C-V$ curves for not irradiated and irradiated sensors and the comparison with the sensor specifications. The values for not irradiated sensors meet the specifications while in the case of irradiated sensors the influence of radiation is clearly reflected on the electrical properties. . . . 163
4.18 Summary of the collected charge and full depletion voltage for the not irradiated sensors measured. . . . 166
4.19 Summary of the collected charge measured for the irradiated sensors. . 169

4.20 Sensors used with the laser setup. Not irradiated and irradiated sensors are included. . . . 171
4.21 Summary of used paremeters during laser measurements with irradiated sensors. . . . 176
4.22 Summary of used irradiated sensors for ganging studies and their setup parameters during laser measurements. . . . 181
4.23 Summary of the used sensors for AC and DC ganging laser measurements comparison. . . . 185
4.24 List of analyzed irradiated sensors for annealing studies and their characteristics. 188
4.25 Summary of obtained results for the annealing studies with *ATLAS12A* irradiated sensors. . . . 196

5.1 Fabrication properties of *CNM* sensors. . . . 203
5.2 Summary of *CNM* Petalet miniature sensors measured. Parameters extracted from [110]. . . . 205
5.3 Summary of *CNM* Petalet miniature sensors measured. . . . 206
5.4 Summary of *CNM* Petalet full-size sensors measured. *BS*, *TR* and *TL* correspond to big sensor, top right sensor and top left sensor respectively. 206
5.5 Parameters used during $I-V$ and $C-V$ curves measurements with miniature and full-size sensors. . . . 207
5.6 Full depletion voltage values for miniature sensors extracted from their C-V curves. . . . 209
5.7 Summary of results and comments for Petalet full-size big sensors. . . . 211
5.8 Summary of results and comments for Petalet full-size top right sensors. 212
5.9 Summary of results and comments for Petalet full-size top left sensors. . 214
5.10 Petalet sensors grouped by their capacitance and depletion voltage characteristics. These three groups correspond to similar run numbers. 214
5.11 Sensors selected for Petalet fabrication with their electrical characteristics. 216
5.12 Summary of *CNM* Petalet miniature sensors used for charge collection studies. . . . 216
5.13 Summary of *CNM* Petalet miniature sensors used for charge collection measurements. . . . 217
5.14 Summary of *CNM* Petalet miniature sensors measured with the laser system for cross-talk and pick-up effects studies. . . . 218
5.15 Petalets characteristics and testing sites. . . . 225

5.16 Summary of input noise results for the different Petalets tested by the collaboration institutes. Each setup conditions are also included. 226

6.1 Comparación de los resultados mecánicos obtenidos para las simulaciones *FEA* y en laboratorio. 245
6.2 Comparación de los resultados térmicos obtenidos para las simulaciones *FEA* y en laboratorio. 245
6.3 Resumen de los resultados obtenidos para las curvas $I-V$ y $C-V$ de los detectores irradiados y no irradiados y su comparación con las especificaciones establecidas. 248
6.4 Resumen de los resultados obtenidos para los detectores no irradiados en cuanto a carga recolectada y voltaje de desertización completa se refiere. 251
6.5 Resumen de las medidas de recoleción de carga en detectores irradiados. 253
6.6 Sensores seleccionados para construir el Petalet y sus características eléctricas. 261
6.7 Resumen de los resultados de ruido de entrada para los diferentes Petalets construidos por la colaboración. Se incluyen además, las condiciones particulares de cada sistema. 267